PFC/RR-79-9

A SOLID BREEDER TOKAMAK BLANKET DESIGNED FOR FAILURE MODE OPERATION

Franklin Chen
Peter Griffith
Thomas McManamy
Neil Todreas
Gary Was

FUSION TECHNOLOGY PROGRAM

Massachusetts Institute of Technology
Cambridge, MA 02139

May 1977

ABSTRACT

The objective of this study was to evaluate a new concept for a Tokamak type fusion reactor blanket. The design was based on using a packed bed of lithium aluminate as the breeding material with helium gas cooling. The unique aspect of the design was the assumption that small coolant leaks were inevitable and should not necessitate major maintenance. A modularized design was chosen with cylindrical breeder rods and graphite shim rods. Redundancy was provided by designing the blanket such that if a module failed it could be depressurized and its heat load shared by the neighboring operating modules. The thermal hydraulic analysis evolved analytical and computational methods for determining the temperature profiles of all components and the pumping power requirements. A computer program TRIPORT was developed to evaluate the tritium retention and transport. A one dimensional ANISN code was used to determine the breeding ratio for different configurations. The thermal hydraulic, neutronic and mechanical aspects of the Breeder Rod Shim Rod (BRSR) design were combined to determine a design window, that is the allowable range of system parameters. Unfortunately adequate breeding could not be demonstrated so that there was no open window. Basically the low breeding was caused by the inherently poor breeding potential of $LiAlO_2$ combined with the additional structure required for failure mode operation. However, this conclusion is based on a specific design concept (BRSR) and further research in the area may prove more fruitful.

ACKNOWLEDGEMENT

The financial support of ERDA (DCTR) for this work is gratefully acknowledged.

This study is basically an integration and extension of a Doctor's Thesis by Franklin Chen and a Master's Thesis by Gary Was.

Franklin's thesis was a thermal hydraulic analysis of the initial configurations which was conceived by Franklin and Professor Ardent Bement. Gary's thesis was based on the same design and included the breeding ratio calculations, tritium inventory calculations, and a study of the material properties.

To combine their results and to gain a better insight into the desirability of a reactor based on this scheme Professor Neil Todreas introduced the idea of forming a design window and helped to guide its development.

Franklin and Gary cooperated with me in extending their results to obtain data needed to define a window.

A large number of people gave valuable advice and guidance to Franklin and Gary during their thesis work which they acknowledged and also to myself during the integration of the results. Professor Peter Griffith in particular was a valuable critic and helped shape the final report. Professor Bora Mikic helped in both the very beginning of the project and at the end. Professor Larry Lidsky's continued interest and support was also appreciated.

Finally Ms. Barbara Rose is to be thanked for her typing of the manuscript.

Thomas J. McManamy

TABLE OF CONTENTS

TABLE OF CONTENTS cont.

TABLE OF CONTENTS cont.

TABLE OF CONTENTS cont.

LIST OF FIGURES

LIST OF TABLES

LIST OF TABLES cont.

NOMENCLATURE

SYMBOLS	DEFINITION	UNITS
A	- total heat transfer area	cm^2
A_1	- surface area between regions 1 and 2 of Figure 3.1	cm^2
A_2	- same as A_1	cm^2
A_c	- free flow area	cm^2
Al	- aluminum	
A_c	- concentration of parent substance (Li)	Ci/cm^3
A_{eff}	- effective atomic mass	g/mole
a	- $LiAlO_2$ pellet radius (r=a)	cm
B	- Tritium generate rate in pellets	Ci/cm^3-sec
B_{eff}	- effective stopping number	
BR	- breeding Ratio	
b_1	- energy generation decay constant in region 1 of Figure 3.1	cm^{-1}
b_2	- energy generation decay constant in region 2 of Figure 3.1	cm^{-1}
b_3	- energy generation decay constant in region 3 of Figure 3.1	cm^{-1}
b_s	- energy generation decay constant in the niobium wall	cm^{-1}
b_w	- energy generation decay constant in graphite shield	cm^{-1}

C,c	- carbon	
C(r,t)	- concentration of tritium in $LiAlO_2$	Ci/cm^3
C_a	- tritium concentration at pellet surface (r=a)	Ci/cm^3
C_{crit}	- critical impurity concentration in the plasma above which ignition is impossible	at/cm^3
C_o	- tritium concentration in pellet at t=0	Ci/cm^3
C_p	- specific heat capacity of helium coolant	Btu/lbm °F
C(J)	- concentration of T_2 in coolant in segment J	Ci/cm^3
CC	- tritium concentration in the coolant that diffused out of the pellets	Ci/cm^3
D	- diffusion coefficient	cm^2/sec
D_o	- frequency factor for diffusion	cm^2/sec
d_e	- diameter of equivalent sphere	cm
E	- modulus of elasticity	psi
$E_{ij}(E)$	- energy released per reaction i at neutron energy E in element J	mev
E_p	- photon energy	mw cm^2
e	- electronic charge	coulomb
$\frac{dE}{dx}$	- stopping power	MeV/cm
F	- conversion factor from CC(STP) to Ci of T_2	323.6 Ci/CC(STP)
f	- friction factor	
G	- flow stream mass velocity	kg cm^{-2} sec^{-1}
g	- gravitational acceleration	9.8m sec^{-2}

G(r)	- gaussian distribution function	
H	- effective conductance between flow passages	w $cm^{-2}{}^{\circ}C^{-1}$
HC	- contact conductance	w $cm^{-2}{}^{\circ}C^{-1}$
H_g	- parameter in gaussian distribution function	cm^{-1}
h	- heat transfer coefficient	w $cm^{-2}{}^{\circ}C^{-1}$
I	- tritium inventory in pellets	Ci
J	- module segment indicator	
J_f	- tritium flux out of pellets	Ci/cm^2-sec
K	- Boltzmann constant	1.38×10^{-23} J°C^{-1}
K_c	- contraction coefficient	
K_e	- expansion coefficient	
k	- conductivity	w $cm^{-1}{}^{\circ}C^{-1}$
k_b	- effective conductivity of breeder rod	w $cm^{-1}{}^{\circ}C^{-1}$
k_c	- conductivity of graphite	w $cm^{-1}{}^{\circ}C^{-1}$
$k_{ij}(E)$	- kerma factor for reaction i with neutron of energy E in element j	mev cm^2
k_n	- conductivity of niobium	w $cm^{-1}{}^{\circ}C^{-1}$
k_γ^j	- gamma kerma factor for element j	mev cm^2
L	- breeder rod center to center distance	cm
LOSS(J)	- T_2 that permeated through the walls of segment J	Ci/cm^3
LN(r)	- log normal distribution function	

ℓ	- segment length	cm
MR	- minor radius plus graphite shield thickness	cm
$\dot{m}$	- mass flow rate	kg sec^{-1}
m_e	- electron mass	g
m_o	- rod void fraction	
Nb, nb	- niobium	
n	- ion density	cm^{-3}
NP	- number of pellets/unit of volume	cm^{-3}
N_a	- Avagadro's number	at/mole
P	- pressure	psi, torr
PF	- tritium permeation rate	Ci/sec
PO	- permeation coefficient	Ci $mm/cm^2 atm^{1/2}$ hr
PP	- pumping power	kw
P_1	- T_2 partial pressure inside module	atm
P_2	- T_2 partial pressure outside module	atm
PROD(J)	- T_2 that diffused into the coolant from the pellets in segment J	Ci/cm^3
P_1	- inlet pressure	kgf cm^{-2}
P_2	- outlet pressure	kgf cm^{-2}
P	- porosity	
Q	- total heat removal rate	w
q'''(r)	- volumetric heat generation rate at	r mev cm^{-3} sec^{-1}
q'''	- heat generation rate	w cm^{-3}

q_1'''	- heat generation rate in region 1	w cm^{-3}
q_{10}'''	- heat generation rate in region 1 at x=0	w cm^{-3}
q_2'''	- heat generation rate in region 2	w cm^{-3}
q_{20}'''	- heat generation rate in region 2 at x=0	
q_3'''	- heat generation rate in region 3	w cm^{-3}
q_{30}'''	- heat generation rate in region 3 at x=0	w cm^{-3}
q_b'''	- heat generation rate in breeder rod	w cm^{-3}
q_c'''	- heat generation rate in graphite shim	
q_n'''	- heat generation rate in niobium wall	w cm^{-3}
q_w'''	- heat generation rate in graphite shield	w cm^{-3}
q_{wo}'''	- heat generation rate in graphite shield at y=0	w cm^{-3}
q_{SO}'''	- heat generation rate in the niobium wall at x=0	w cm^{-3}
q_{c3}'''	- heat generation rate in carbon of zone 3	w cm^{-3}
q_{c4}'''	- heat generation rate in carbon of zone 4	w cm^{-3}
q_{nb4}'''	- heat generation rate in niobium of zone 4	w cm^{-3}
$q_{LiAlO_2 4}'''$	- heat generation rate in $LiAlO_2$ of zone 4	w cm^{-3}

q_4'''	- heat generation rate in all of zone 4	w cm^{-3}
q_{1-2}''	- surface heat flux from regions 1 to 2	w cm^{-2}
q_{2-1}''	surface heat flux from regions 2 to 1	
q_α''	surface heat flux on graphite shield	w cm^{-2}
$q(r)$	- fraction of atoms formed within dr of the surface which escape by recoil	
Q_D	- activation energy for diffusion	cal/mole
Q_p	activation energy for permeation	cal/mole
Q_s	- activation energy for solubility	cal/mole
R_a	- radius of point a	cm
R_b	- radius of point b	cm
R_c	- radius of point c	cm
R_e	- radius of point e	cm
R_i	- radius of the inner passage of the breeder rod heat exchanger	cm
R_o	- radius of the outer passage of the breeder rod heat exchanger	cm
R_t	- spatial solution to the triport equation	Ci/cm^3

RR	- recoil range of a tritium atom	cm
r	- radius in $LiAlO_2$ pellets	cm
r_i	- inner radius of module end cap	cm
r_m	- mean pellet radius for the gaussian distribution	cm
S	- solubility coefficient	Ci/cm^3(STP)
S_H	- sputtering yield	at/incident particle
SO	- Frequency factor for solubility	$Ci/cm^3 atm^{1/2}$
s	- Laplace transformation variable	$x=e^{-s}$
T	- temperature	°C
T_1	- temperature of coolant in region 1	°C
T_2	- temperature of coolant in region 2	°C
T_a, T_b	- dummy variable in the solution for the off-normal graphite shield temperature	°C
T_{an}	- temperature of the niobium annulus wall of the breeder rod	°C
T_b	- temperature of breeder rod	°C
T_c	- temperature of the graphic shim	°C
T_{cy}	- temperature of the breeder rod cylinder	°C
T_f	- coolant temperature in region 1	°C

T_n	- temperature of the niobium annulus	°C
T_i	- inlet coolant temperature	°C
T_o	- maximum coolant temperature at x=o	°C
t_{lw}	- thickness of graphite shield	cm
T	- time solution transport equation	sec
T_m	- melting temperature	°F, °R, °C, °K
T_s	- pellet surface temperature	°F, °R, °C, °K
t	- module wall thickness	cm
u	- concentration x radius	Ci/cm^2
v	- helium coolant velocity	cm/sec
Vol_1	- volume of region 1	cm^3
Vol_2	- volume of region 2	cm^3
Vol_3	- volume of region 3	cm^3
VF	- void fraction	
WA	- wall area of segment	cm^2
W_m	- volumetric heat generation rate in structure	W/cm^3
w_f	- free velocity	cm sec^{-1}
XT	- breeder rod length	cm
x	- distance measured from bottom of the breeder rod	cm
x'	- distance measured from top of the breeder rod	cm
Y	- graphite shield thickness	cm
y	- distance measured from the surface of the graphite shield	cm

z	- horizontal axis of Figure 3.5	
z_1	- inlet elevation	cm
z_2	- exit elevation	cm
Z	- atomic number	
α	- linear coefficient of thermal expansion	cm/cm °C
γ_m	- helium coolant density	lbm/ft^3
ε	- pellet radius/cylinder radius	
ε_r	- fraction of bred tritium atoms that leave the pellet by recoil	
ξ	- mean pellet radius for log normal distribution	cm
ξ_{LN}	- logrithmic transformation of ξ	cm
γ	- ratio of specific heat	
ΔP	- pressure drop through breeder rod	$kg\ f\ cm^{-2}$
ΔT	- coolant temperature difference between region 2 and 1	°C
η	- efficiency in energy conversion	
λ_f	- friction factor	
§	- bremsstrahlung radiation coefficient	$J\ cm^3\ sec^{-1}\ °C^{-1/2}$
ρ	- density	$kg\ cm^{-3}$
ρ_1	- inlet density	$kg\ cm^{-3}$
ρ_2	- exit density	$kg\ cm^{-3}$
ρ_m	- density of mean temperature velocity ratio	$kg\ cm^{-3}$

σ	- Stefan Boltzmann's constant	5.67×10^{-12} w $cm^{-2}{}^{\circ}K$
σ_{cs}^{j}	- compton scattering microscopic cross section with element j	cm^2
$\sigma_{ij}(E)$	- microscopic neutron cross section for reaction i with neutron of energy E in element j	cm^2
σ_{pe}^{j}	- photoelectric microscopic cross section with element j	cm^2
σ_{pp}^{j}	- pair production microscopic cross section with element j	cm^2
$\overline{\sigma_f v}$	- fusion reaction-rate parameter	$cm^3 sec^{-1}$
$\phi(r,E)$	- flux at r with energy E	$mev^{-1} sec^{-1} cm^{-2}$
ψ	- shape factor	
ε_c	- emissivity of carbon	
ε_{nb}	- emissivity of niobium	
Λ	- decay constant of parent substance (Li)	sec^{-1}
λ	- decay constant of tritium	sec^{-1}
λ_n	- $\frac{n\pi}{a}$, argument in concentration equation	cm^{-1}
λ_p	- constant depending on the Reynolds number	
ν	- kinematic viscosity	ft^2/sec
ν_p	- Poisson's ratio	

-2°K

τ	- tritium holdup time	sec
τ_m	- coolant transit time through module	sec
τ_p	- time for tritium leakage through module wall	sec
ϕ	- particle shape factor	
ϕ_1	- square root of particle shape factor	
ω	- ω_f/m_o, mean stream velocities between particles	ft/sec
ω_f	- superficial helium velocity	ft/sec

1. INTRODUCTION

1.1 Background

Considerable attention has been given to the engineering problems associated with the design of a thermonuclear power reactor. At this time, the principal merits of design studies are: the identification of problem areas previously not realized, proposed solutions, and eventually, the generation of enough information to make rational decisions concerning which approaches to pursue further.

One of the most difficult problems is the design of the "blanket" region surrounding the plasma. The blanket region must extract the energy of the neutrons at a usefully high temperature and also produce sufficient tritium to fuel the D-T fusion reactions while subject to a large number of difficult constraints.

Most designs investigated to date, employ either helium as the coolant or liquid lithium which is both the coolant and breeding material. The use of helium has both advantages and disadvantages. The most obvious advantages are the elimination of MHD effects, and the inert chemical nature of the coolant. Some disadvantages are that an increased void fraction in the blanket is required for coolant passages and additional structural material is needed to accomodate the higher pressures needed with helium. The helium cooled solid breeder does, however, appear as a viable alternative to liquid lithium systems and several design studies have been accomplished, such as the Japanese pebble bed design[1], the BNL MAMI module[2] and the UWMAK II design[3].

One aspect of helium cooled designs which has received little attention is the problem of coolant leakage into the plasma chamber through a failed region of the first wall, such as a cracked weld with a pin hole size fault.

Even a very small hole could allow enough helium into the vacuum region to quench the plasma. Considering the large surface area of the first wall, typically on the order of $1500m^2$, and the large number of welds which must maintain their integrity in an exceedingly harsh environment, it seems virtually impossible that a reactor could operate for one to two years without experiencing a number of leaks. If every time such a pinhole sized leak occured, the torus had to be disassembled, the leak located, and the damaged section reparied or replaced, the design probably would not be acceptable from a practical viewpoint because of a high percentage of down time for repair.

The UWMAK II report did address this question and proposed two possible modifications to their original design. One suggestion was a "sacrificial" first wall composed of cooling tubes welded together to form a second "first wall" which would prevent any helium leaking from a module to enter the plasma (Fig. 1.1a). They noted the problem with this suggestion was that while it could be designed to significantly lower the likelihood of leakage into the plasma, the additional structural material would probably lower their breeding ratio to below one and in addition, the manufacture of such a structure would "tax the ingenuity of the industry". The other idea was to make a double wall. In the basic design, the thermal stress on the first wall was uncoupled from the pressure stress by adding thin semi-circular coolant tubes facing the plasma to a thicker backing structure. By making the thin semi-circular tubes double walled, Fig. 1.1b, the likelihood of leakage is proportedly reduced. The major drawback is that there is no redundancy for the case of a leak at the weld which is the most likely point of failure.

The blanket design concept investigated in this report was conceived by F. Chen and A. L. Bement and provides for redundancy by having a modularized solid breeder in which any given module that fails can be depressurized and the reactor operated in this manner with the heat load generated in a failed module conducted to its neighbors. The objective of this study was to develop a design envelope for this concept to determine if a viable window exists and in the process evolve a systematic approach which could be used in the analysis of other solid breeder designs.

1.2 DESIGN LIMITS

The design limits in this report will be taken to be the maximum material temperatures and total stresses to which we can design structural components while all other restrictions on choices will be called constraints.

The materials considered were helium coolant, graphite moderator, lithium aluminate breeding material, and both 316SS and Nb-1Zr as the structural material. The design limits taken for these materials were as follows:

MATERIAL	MAXIMUM TEMPERATURE	MAX. TOTAL STRESS
GRAPHITE	2000°C	
$LIAlO_2$	1800°C	
316 SS	650°C	10^4 PSI
Nb-1Zr (w/He coolant)	600°C	10^4 PSI
Nb-1Zr (no coolant; unstressed)	2000°C	

1.21 Graphite Design Limit

The use of carbon and other low-Z first wall materials was studied in

a report by the General Atomic Co.[4] The calculated equilibrium vapor densities in 10^{-5} atm H_2 for several materials as given in this report is shown in Fig. 1.2. Their analysis of the energy loss rates for a typical plasma indicated that ignition could be sustained in a plasma containing an ionized carbon impurity level of up to 10% of the electron density. The plasma densities expected for our design should be close to 6×10^{13} cm^{-3}. To allow for uncertainties we introduced a safety factor of 4 which gives a maximum carbon impurity density of $1.5 \times 10^{12} cm^{-3}$. This impurity density in the plasma is reached at a carbon surface temperature of approximately 2000°C which is what has been taken as the design limit.

1.2.2 Lithium Aluminate Limit

The lithium aluminate melting point is approximately 1900°C[5] and a limit of 1800°C was taken to allow for uncertainty in the data.

1.2.3 316 Stainless Steel Limits

The limits taken on 316SS correspond to 1% creep in 10,000 hours as given by Fraas[6] (Figure 1.3).

1.2.4 Niobium- 1% Zirconium Limits

For Nb-1Zr the maximum temperature for 1% creep in 10,000 hours at 10^4 PSI is approximately 850°C (Fig. 1.3), but it appears that corrosion from trace impurities in the helium coolant will lower the maximum operating temperature. Fraas recommends a maximum operating temperature of approximately 600°C and that is what we have taken. It does not appear possible to remove this constraint by purifying the helium stream. In the 1950's Pratt-Whitney conducted the CANEL PROGRAM in which they examined various helium purification processes to protect certain Nb-1Zr loops from corrosion.

All attempts were unsuccessful.[7] More recently the Jet Propulsion Laboratory operated Nb-1Zr loops using argon with an O_2 and H_2O content of 1ppm and below respectively. After 1000 hours of operation the combined impurity content was 4480ppm.[8] Studies show that the contamination of Nb-1Zr in high vacuum at high temperature requires that the total residual gas pressure be held to below 10^{-6} Torr (1.33×10 N/m^2) to avoid serious deterioriation of mechanical properties in periods as short as weeks at 1000°C[(9)]. With a helium coolant at 40 atmospheres this would require a maximum impurity content of .00003 PPM ($^nc/^nHe=P_c/P_{He}=10^{-6}$TORR/(40)(760)TORR $\simeq 3 \times 10^{-11}$) and it does not appear possible to achieve such high purity in any large scale system. Also, all attempts to develop a suitable coating for the Nb-ZR have failed.

For cases where the Nb-1Zr is not under stress and no coolant is present, a limit of 2000°C has been taken to simply stay safely below the melting point.

1.3 Design Constraints

The design constraints are basically the same as those identified by Fraas as applied to the blanket portion of a reactor. It is assumed that the reference reactor will be a Tokomak type. The following are the principal constraints which the design attempted to meet.

1) Breeding Ratio

The design constraint on the minimum acceptable breeding ratio depends on a number of factors. First, if a fusion economy is postulated it is desirable that the initial reactors breed an excess of tritium over their fueling requirements to generate an inventory of tritium to be used in the initial fueling of a new reactor. A fuel doubling time can be defined as[10]

$$\tau_2 = \frac{\text{INVENTORY}}{(\text{B.R.} - 1)r}$$

where

B.R. = BREEDING RATIO

r = TRITIUM BURNING RATE

The size reactor postulated (1450 m^2) under a steady state total wall loading of 1.2 MW/m^2 would consume .27kg of tritium per day. Taking the reactor inventory to be 10kg, which is probably an upper bound, a doubling time of 2 years can be attained with an overall breeding ratio of 1.05.

The breeding ratios calculated in this report are based on an average module. An actual reactor would also require some portion of the blanket to be used for access. Such access regions would be required for the vacuum pumping system, the fueling system, diagnostic ports and divertors if employed. Abdou gives an estimate of 10% for neutron loss due to streaming and parasitic adsorption in such access regions[11]. There also exists the possibility of some small loss rate of tritium from the fuel processing system and due to decay. Adopting an estimate of 10% for all loss mechanisms would raise the required breeding ratio to 1.15.

There is also some uncertainty in the calculated breeding ratios due to uncertainties in the basic cross section data and due to the calculational method itself. Steiner and Tobias have investigated the effects of uncertainties in cross-sections of ^6Li, ^7Li and ^{93}Nb on the tritium breeding of a particular type of blanket[12]. For a liquid lithium, graphite moderated blanket breeding in the range of 1.5 they concluded that uncertainties in the $^7Li(n,n'x)t$ reaction attach an uncertainty in excess of 5% to the tritium-breeding ratio. When the cross sections of the $^6Li(n,x)t$, the

$^{7}Li(n,n'x)t$, and the 93Nb(n,2n) reactions were varied simultaneously and the uncertainties in the secondary-neutron energy distribution of the $^{7}Li(n,n'x)t$ was included, the uncertainty in the breeding ratio approached 10%.

The computation of the breeding ratio for this design was accomplished using a 1D ANISN S_8P_3 code in a slab geometry. The use of a 1D code and the homogenization required by it will introduce some additional uncertainty as will be discussed later.

For the purpose of this preliminary analysis it was decided to set the minimum breeding ratio at 1.15 with the understanding that the uncertainties present in the calculated breeding ratio would have to be reduced for a more refined design by using a 3-D code and, if available at a future time, more accurate cross section data.

2. Blanket Inventory

There is a strong motivation to have a small tritium inventory in the blanket. Some reasons for this are as follows:

1. Cost: Estimates for the price of tritium vary from $2,000,000[6] to $7,000,000[13] per kg. A large inventory in the blanket would be quite expensive and would serve no useful purpose.

2. Doubling time[6]: For a reactor at a given power level, the fuel doubling time will be proportional to the reactor inventory and it is desirable to have this time short enough so that tritium availability will not restrict the growth of a fusion based economy.

3. Hydrogen Embrittlement: With a lower inventory the tritium concentration seen by the structural components will generally be less and therefore the effectsof hydrogen embrittlement should also be lessened.

4. Availability : Fraas has indicated that it would be difficult to obtain more than about 10 kg of tritium for starting-up the first power reactor[6].

5. Safety: It is desirable to reduce the amount of tritium available for release in the event of an accident and to keep the amount of tritium leakage to the environment at a very low level. Fraas has indicated that there is a strong incentive in a lithium blanket to keep the tritium concentration on the order of 1 ppm.

What is desired for a design constraint is the maximum inventory allowable in the blanket beyond which the design is not viable. It will be assumed that the capital cost for inventories of 10 kg or less will be acceptable. If the overall breeding ratio of the blanket was exactly equal to one, then the total inventory in the reactor would be limited to the amount available for start-up which we will assume to be 10 kg. This inventory would be distributed between the blanket, the fuel processing and injection system, and whatever amount of tritium has been absorbed in the structural components. The availability of tritium therefore places a limit on the total reactor tritium inventory and to obtain a limit for the for the blanket inventory an estimate must be made of the fraction of the inventory which is required outside of the blanket region. Without a model for the fuel reprocessing system and the plasma parameters only a rough guess can be made.

A 1.2 MW/m^2 total loading on the first wall corresponds to 1740 MW_t fusion power for a 1450 m^2 reactor. This represents a consumption of .27 kg of tritium per day for steady state operation. Typical functional burnup in a Toiamak type reactor is on the order of 5%[3,10]. Therefore

a reasonable figure for the amount of tritium which must be recirculated through the plasma chamber is 5 kg per day. We next estimate the number of kg necessary in the fuel system to achieve this 5 kg per day flowrate. Some tritium inventories should be kept in reserve to permit operation in case of temporary fuel reprocessing system failures. In addition, some tritium will reside within the reprocessing system, the amount depending on the time required to reprocess the fuel. A reasonable guess for the total inventory outside of the blanket seems to be 5 kg. This could be broken down to a 2.5 kg reserve (a 12 hr reserve), 2 kg in the fuel system corresponding to a turnaround time of approximately 10 hours, and 0.5 kg absorbed in the structure. For a rough approximation therefore it will be assumed that availability limits the blanket inventory to 5 kg.

For a total reactor inventory of 10 kg the doubling time with a breeding ratio of 1.05 is 2 years which appears acceptable and would therefore not restrict the blanket inventory further.

For the solid breeder design employed here the steady state tritium concentration in the coolant is independent of the amount of tritium bound in the breeding material and the amount of hydrogen embrittlement should not be a strong function of the blanket inventory.

Safety and environmental concerns do not seem to limit the blanket inventory to less than 5 kg. It is assumed that the entire reactor will be enclosed by a redundant wall system to prevent accidental leakage of tritium to the outside since one study[14] has shown that under certain circumstances an airborne release of as little as 23 grams of tritium could exceed allowable radiation levels at the plant boundaries. If a suitable confinement system is possible to handle accidents in the fuel processing and storage

system, which probably would have amounts of tritium in the range of kilograms, it should be possible to contain tritium released from the blanket in an accident. The problem should be easier since the tritium will be bound in solid material and the diffusivity appears to be extremely small at temperatures below 500°C. Within the reactor hall itself it also appears feasible to cope with accidental releases of tritium on the order of several kg. The study by Lawrence Livermore Laboratory of a mirror reactor system indicated that with careful design, allowable worker dosage levels would not be exceeded even with the release of several kilograms of tritium within the hall[15].

3. The capacity to sustain a small number of leaks and to continue operation without major maintenance. Since even a pin-hole size leak would be a major problem (see Appendix D) it is assumed that there must be some way of preventing the leaking coolant from entering the plasma, or stopping the flow to the area of the leak.

4. A reasonably high thermal efficiency

5. High vacuum integrity

6. A blanket thickness of one meter was assumed, similar to other reference designs. Thinner blankets would make shielding the magnets more difficult and possibly hurt the breeding while a thicker blanket would increase the cost of the magnet system.

7. Good accessibility to all blanket elements to permit remote maintenance

8. A projected lifetime for major components of approximately 2 years

9. A pumping power to heat removal ratio of not greater than 5%

10. A low first wall sputtering rate.

Economic constraints have not been evaluated nor is this meant to be a complete reactor design. What has been done is an investigation of the effects of imposing the constraint of designing a blanket from the beginning with the assumption that leaks are inevitable and the blanket must be able to maintain operation with them.

CHAPTER 2

Breeder Rod - Shim Rod Design Overview

2. General Blanket Arrangement

If a small section of the first wall fails, in order to continue operation either the failed section must be replaced or the flow of coolant to it stopped. The design approach taken here was to have a modularized blanket where if one module failed, it could be isolated from the coolant circuit and the machine operation could be continued with the failed module depressurized. Since any given module could be operating next to or surrounded by depressurized modules, it was also decided to design each module essentially as a separate pressure vessel. This together with the desire to have easily replaceable components led to cylindrical breeder rods. To accomodate the space between cylindrical rods in a torroidal geometry required the use of shim rods. Besides simply filling the space these also had to have a high thermal conductivity to allow the heat generated in a failed module to be conducted to its neighbors. To prevent neutron streaming the shim rods material also should have a high scattering cross section and for neutron economy a low absorption cross section. The material found which best fulfilled these requirements was carbon. If a module is not cooled by helium the first wall structural temperature can be kept low by conducting most of the surface energy flux to the surrounding modules by using a graphite shield in front. The shield also is helpful in reducing plasma contamination by high Z impurities. Additionally, by lowering the energy spectrum of the neutrons seen by the first wall, the rate of irradiation damage to the metal should be reduced and the breeder rod effective lifetime increased.

The breeding material selected was lithium aluminate arranged in a packed bed of spherical pellets. To cool the packed bed and remove the bred tritium the breeder rod was divided into two concentric cylindrical regions of equal area forming a single stream counter flow heat exchanger with two possible routings which give a symmetric temperature distribution for the blanket.

The general arrangement is shown in Fig. 2.1. The blanket modules together with the supporting back structure form the vacuum boundary. As conceived the modules would be replaced from inside the torus by being screwed-mounted onto the backing structure with a double high vacuum seal of soft metal. The shim rods are also mechanically connected to the back structure but have no vacuum boundary, and are allowed to have radial freedom to accomodate swelling of the blanket elements. It is highly desirable from a thermal viewpoint to have the shims in good physical contact with the breeder rods since they must conduct the heat away from a failed module, but this is a difficult mechanical problem. The possibility exists, that the breeder rods and the shim rods would swell enough due to thermal expansion and radiation induced swelling to generate sufficient normal force to prevent any relative sliding. In that case, the higher thermal linear expansion of the metal can would probably overstress the carbon. In consideration of this problem, the design was also investigated with a gap between the shim rods and breeder rods and a radiative boundary condition for heat transfer.

For the given arrangement the breeder rods would all be identical but the shim rods would vary because of the toroidal geometry. The shim rods along a fixed major perimeter would all have the same size. There would

therefore be as many types of shim rods as there are rows of breeder rods along the minor perimeter.

Irradiation of the blanket by the fusion neutron results in substantial amounts of long-lived radioactivities (10^{10} C_i/5000 MW_T for a niobium blanket after 18 years of operation[16]). It appears therefore, that remote machine maintenance will be required. The BRSR modularized design would be compatible with this. Any portion of the blanket could be replaced by remote manipulations. Virtually no repair work would be required to be done within the torus. Also, the backing structure would not be exposed to energetic neutron radiation and should have a lifetime comparable to the rest of the reactor.

The blanket is designed for a Tokamak type reactor and the assumed dimensions for the torridal vacuum wall are a major radius of 10.5 meters and a minor radius of 3.5 meters. Additionally, the wall loading has been fixed at 1MW/m^2 of neutrons and a surface flux of .2 MW/m^2 from plasma radiation and particle flux. If a complete reactor design could incorporate a diverter, the percentage of surface energy flux would be less, but this alternative has not been considered. For a complete reactor study also an analysis should be done to find the optimum wall loading based on material lifetimes, replacement cost and efficiencies gained by higher loading. The thickness of the blanket also has been arbitrarily fixed at one meter which should allow enough space for breeding and moderating the neutron flux so that the shielding requirements for the magnets are not excessive.

2.2 Development of Design Window

Rather than developing a fixed point design, the effort here has been to establish a design window to see what range of variables are possible

for module sizes, operating pressure, pellet sizes, inlet temperature and temperature drop through the module. The manner in which this was done was to postulate a given geometry and then to find the relationships between the different variables as the geometry and operating conditions varied.

The use of both Nb-1Zr and 316 SS was investigated. The neutronic calculations were performed for Nb-1Zr and it was assumed that the use of 316 SS would not significantly change the results. The principal change resulting from the use of 316 SS was a much higher thermal stress in the first wall which had to be accomodated in the design.

The design geometry initially evaluated is given in Table 2.1. The breeder rod outer diameter was taken to be 8cm, the thickness of the can 2mm, the graphite shield thickness 5cm, and the diameter of the $LiAlO_2$ spheres 4mm. The wall separating the cooling passages was one mm thick. For this geometry the atom fraction is given in Table 2.2. The void fraction within a breeder rod for this geometry is approximately .36 but when this is homogenized with the shim rod for a one dimensional neutronic study, the resulting void fraction is .13.

For this geometry a one dimension homogenized calculation was done to determine the heating rates (Appendix B). A three-dimensional Monte-Carlo neutron calculation would have been more accurate, but it was felt that for a first approximation the 1-D calculation was sufficient. The energy generation rates (q''') are reasonably approximated by the following exponential functions:

$$q'''_{c_3} = 3.68e^{-.103y} \qquad (2.1)$$

$$q'''_{C_4} = 2.296e^{-.043x} \quad (2.2)$$

$$q'''_{Nb_4} = 4.1e^{-.084x} \quad (2.3)$$

$$q''_{LiALO_2} = 2.1e^{-.035x} \quad (2.4)$$

Where x is the distance from the first wall and y is the distance from the surface of the graphite shield (Figures 2.2 and 2.3).

The relatively low energy generation rate in $LiAlO_2$ is to be expected. This is partly because of the large void fraction (.36) in the breeder rod, and partly because of the choice of $LiAlO_2$ which decreases the lithium concentration even further. It is the exothermic ^6Li (n,α)t reaction which is the primary source of energy multiplication. The relatively low lithium concentration is evidenced in Table 2.2. At 5 cm from the can wall, the total energy generation rates in ^6Li and ^7Li are .21 w/cc and .31 w/cc respectively, relatively low when compared to .71 w/cc in oxygen, .47 w/cc in Al, 1.8 w/cc in C and 3.16 w/cc in Nb. In the low energy intervals (i.e. far from the first wall), the same is true. For example, at 95 cm from the first wall, the energy generation rates are .0117 w/cc in ^6Li, .0028 w/cc in ^7Li, .0074 w/cc in Al, .0099 w/cc in oxygen, .0217 w/cc in C and .1053 w/cc in Nb.

For a first wall loading of $1MW/M^2$ and first wall heat flux of 20 W/cm^2, the postulated blanket as represented by equations 2.1 to 2.4 has an energy multiplication of ~1.0 resulting in the total energy removal from the blanket approximately equal to the energy content of the neutron first wall loading. The low energy multiplication (and as later calculations will show a low breeding ratio also) is a reflection of the lack of optimization in the

neutronic design of the blanket at this point. To represent the case of a neutronically well designed BRSR blanket, the following q''', representing an energy multiplication of ~1.7 (energy removal from blanket is ~1.7 times the first wall loading), is assumed for the thermal/hydraulic calculation in addition to those of equations 2.1 to 2.4.

$$q'''_{c3} = 3.68\ e^{-.103y} \tag{2.5}$$

$$q'''_{4} = 5.2\ e^{-.042x} \tag{2.6}$$

TABLE 2.1

BRSR INITIAL DESIGN SPECIFICATIONS

Item	Breeder Rod	Shim Rod
Length	100.0 cm	100.0 cm
Outer cylinder OD	8.0 cm	-
Outer cylinder thickness	0.2 cm	-
Inner cylinder OD	2.74 cm	-
Inner cylinder thickness	0.1 cm	-
Outer cylinder material	Nb-1Zr	-
Inner cylinder material	Asbestos, Nb-1Zr sandwich	-
Shim material	-	Graphite
Breeding material	$LiAlO_2$	-
Pellet diameter	0.4 cm	-
Void fraction	0.36	0.0
Graphite shield thickness	5.0 cm	-
Volume % of blanket	43.0	57.0

TABLE 2.2

ATOM FRACTIONS OF ELEMENTS IN THE BREEDER ROD AND SHIM ROD

Zone	C	Nb	He	^6Li	^7Li	O	Al
1	-	-	-	-	-	-	-
2	-	-	-	-	-	-	-
3	1	-	-	-	-	-	-
4	.643	.045	.001	.006	.072	.155	.078

CHAPTER 3

BLANKET RESPONSE UNDER NORMAL OPERATING CONDITIONS

3.1.1 THEORY OF THE SINGLE STREAM COUNTER FLOW HEAT EXCHANGER WITH INTERNAL GENERATION (THE BREEDER ROD HEAT EXCHANGER)

A schematic of the breeder rod heat exchanger is included as Figure 3.1. For the purpose of illustrating the derivation of the coolant temperature solution, the case where the coolant enters through the outer cylinder and exits through the inner cylinder is treated.

In the x' direction,

$$\dot{m}\, c_p\, dT_1 = q_1'''\, dVol_1 + q_3'''\, dVol_3 + q_{2-1}''\, dA_1 \tag{3.1}$$

In the x direction,

$$\dot{m}\, c_p\, dT_2 = q_2'''\, dVol_2 + q_{1-2}''\, dA_2 \tag{3.2}$$

The boundary conditions are

$$T_1 \Big|_{x' = 0} = T_i \text{(inlet helium temperature)} \tag{3.3}$$

$$T_2 \Big|_{x=0} - T_1 \Big|_{x=0} = (L^2\, q_\alpha'' - L^2 q_{wo}'''(e^{-b_w\, t_{1w}} - 1)/b_w)/(c_p \dot{m}) \equiv \Delta T_o \tag{3.4}$$

Boundary condition (3.3) represents the inlet condition of the coolant while the condition of equation (3.4) reflects the coolant temperature change at the bottom of the breeder rod due to the energy input from the graphite shield.

In equations 3.1 and 3.2, the geometrically determined quantities are

$$dVol_1 = \Pi(R_o^2 - R_i^2)\, dx' \tag{3.5}$$

$$dVol_3 = (L^2 - \Pi R_o^2)\, dx' + \frac{L^2}{MR}\, XT\, dx' - \frac{L^2}{MR}\, x'\, dx' \tag{3.6}$$

$$dA_1 = 2\Pi R_i\, dx' \tag{3.7}$$

$$dA_2 = 2\Pi R_i\, dx \tag{3.8}$$

$$dVol_2 = \Pi R_i^2\, dx \tag{3.9}$$

With the substitution of Equations (3.5) to (3.9), and the internal generation rates as depicted in Figure 6, Equations (3.1) and (3.2) becomes

$$\frac{dT_1}{dx'} = a\, e^{-b_1(XT-x')} + c\, e^{-b_3(XT-x')} - \varepsilon\, x'\, e^{-b_3(XT-x')} + f\,(T_2 - T_1) \tag{3.10}$$

$$\frac{dT_2}{dx} = g\, e^{-b_1 x} + f\,(T_1 - T_2) \tag{3.11}$$

where $a = q'''_{10}\, \Pi(R_o^2 - R_i^2)/\dot{m}\, C_p$ (3.11a)

$$c = q'''_{30}\, (L^2 - \Pi R_o^2 + \frac{L^2}{MR}\, XT)/\dot{m}\, C_p \tag{3.11b}$$

$$\varepsilon = q'''_{30}\, L^2/MR/\dot{m}\, C_p \tag{3.11c}$$

$$f = 2\, H\, \Pi\, R_i/\dot{m}\, C_p \tag{3.11d}$$

$$g = q'''_{10}\, \Pi\, R_i^2/\dot{m}\, Cp \tag{3.11e}$$

Transformation of Equation (3.10) from x' to x yields

$$\frac{dT_1}{dx} = -\, a\, e^{-b_1 x} - c\, e^{-b_3 x} + \varepsilon(XT-x)e^{-b_3 x} - f(T_2 - T_1) \tag{3.12}$$

Subtraction of (3.12) from (3.11) gives

$$\frac{d\Delta T}{dx} = \alpha\, e^{-b_1 x} + \beta\, e^{-b_3 x} + \varepsilon\, x\, e^{-b_3 x} \tag{3.13}$$

With the boundary condition of

$$\Delta T \Big|_{x=0} = \Delta T_o \tag{3.14}$$

The solution of Equation (3.13) is

$$\Delta T = C_1 - \frac{\alpha}{b_1}\, e^{-b_1 x} - \gamma\, e^{-b_3 x} - \frac{\varepsilon}{b_3}\, x\, e^{-b_3 x} \tag{3.15}$$

Where $\Delta T = T_2 - T_1$ (3.15a)

$$\alpha = q'''_{10}\, \Pi R_o^{\,2}/\dot{m}\, C_p \tag{3.15b}$$

$$\beta = c - \varepsilon\, XT \tag{3.15c}$$

$$\gamma = \beta/b_3 + \varepsilon/b_3^{\,2} \tag{3.15d}$$

$$C_1 = \alpha/b_1 + \beta/b_3 + \varepsilon/b_3^{\,2} + \Delta T_o \tag{3.15e}$$

With the substitution of Equation (3.15), Equation (3.11) becomes

$$\frac{dT_1}{dx} = -\,a\, e^{-b_1 x} - \beta\, e^{-b_3 x} - \varepsilon\, x\, e^{-b_3 x} - C_1\, f + \frac{\alpha f}{b_1}\, e^{-b_1 x} + \gamma\, f\, e^{-b_3 x} + \frac{\varepsilon f}{b_3}\, x\, e^{-b_3 x} \tag{3.16}$$

The boundary condition for this equation is

$$T_1 \Big|_{x=XT} = T_i \tag{3.16a}$$

Integration of equation (3.16) with the boundary condition of (3.16a) gives the following result.

$$T_1 = T_i + c_1 f\,(XT - x) + (a/b_1 - \alpha f/b_1^2)(e^{-b_1 x} - e^{-b_1 XT})$$

$$+ (\beta/b_3 - \gamma f/b_3 + \varepsilon/b_3^2 - \varepsilon f/b_3^3)(e^{-b_3 x} - e^{-b_3 XT})$$

$$+ (\varepsilon/b_3 - \varepsilon f/b_3^2)(x\, e^{-b_3 x} - XT\, e^{-b_3 XT}) \tag{3.17}$$

With the substitution of Equation (3.15), Equation (3.10) becomes

$$\frac{dT_2}{dx} = -c_1 f + (g + \frac{\alpha f}{b_1})\, e^{-b_1 x} + \gamma f\, e^{-b_3 x} + \frac{f\varepsilon}{b_3}\, x\, e^{-b_3 x} \tag{3.18}$$

with the boundary condition of

$$T_2 \Big|_{x=XT} = T_i + \Delta T \Big|_{x=XT} \tag{3.18a}$$

The solution of equation (3.18) by integration with the condition of (3.18a) is

$$T_2 = T_i + \Delta T\Big|_{x=XT} + c_1 f(XT - x) + (g/b_1 + \alpha f/b_1^2)(e^{-b_1 XT} - e^{-b_1 x})$$

$$+ (f/b_3)(\gamma + \varepsilon/b_3^2)(e^{-b_3 XT} - e^{-b_3 x})$$

$$+ (f\varepsilon/b_3^2)\,(XTe^{-b_3 XT} - xe^{-b_3 x}) \qquad (3.19)$$

Equations (3.17) and (3.19) then completely determine the thermal behavior of the coolant for the case of entering through the outer cylinder and exiting through the inner cylinder. For the sake of completeness, but simultaneously avoiding redundant derivation, only the final expressions for the temperature of the case where coolant enters through the inner cylinder and exits through the outer are included here.

ΔT is the same as Equation (3.15).

$$T_2 = T_i + C_1 f\,(XT - x) + (\alpha\, f/b_1^{\,2} - g/b_1).$$

$$(e^{-b_1 XT} - e^{-b_1 x}) + \frac{f}{b_3}\,(\gamma + \frac{\varepsilon}{b_3^2})\,(e^{-b_3 XT} - e^{-b_3 x})$$

$$+ \frac{\varepsilon f}{b_3^2}\,(XT\, e^{-b_3 XT} - x\, e^{-b_3 x}) \qquad (3.20)$$

$$T_1 = T_i + \Delta T\Big|_{x=XT} + C_1 f\,(XT - x) +$$

$$(a/b_1 + \alpha f/b_1^2)\,(e^{-b_1 XT} - e^{-b_1 x}) \qquad (3.21)$$

$$+(\beta/b_3 + \gamma f/b_3 + \varepsilon/b_3^2 + \varepsilon f/b_3^3)(e^{-b_3 XT} - e^{-b_3 x})$$

$$+ (\varepsilon/b_3 + \varepsilon f/b_3^2)\,(XT\, e^{-b_3 XT} - x\, e^{-b_3 x})$$

All the constants are the same as those defined for equations (3.17) and (3.19) with only the following exception of

$$c = q'''_{30}\,(L^2 - \pi R_o^2)/\dot{m}\, C_p \qquad (3.22)$$

which can be attributed to the difference in $dVol_3$ of the two cases.

A careful investigation of equation (3.15) reveals the interesting absence of the effective conductance, H. This absence of H infers the indifference of the ΔT profile to either the choice of partitioning materials or the flow conditions on either side of the heat exchanger. This mathematical phenomenon can be explained as that of a feedback of the temperature from the high temperature side to the low temperature side. The effective conductance is the resistance for heat transfer, whereas the temperature difference is the driving force. Together, the effective conductance and ΔT govern the amount of heat transfer as can be seen from equations (3.11) and (3.12). However, being a single stream counter flow heat exchanger, the temperature at any arbitrary point A prescribed by the heat generated and the heat transferred up to point A eventually gets to a point B of the same axial position as point A on its return pass. The doubling back of the same fluid stream to the same axial position means that the temperature

difference of point A and point B is a function of the energy released between the two points and not a function of the heat transfer between the two streams. Therefore, it is not surprising that H is not a factor affecting the ΔT profile as mathematically demonstrated by equation (3.15).

3.1.2 Evaluation of the Breeder Rod Coolant Temperature

Before the evaluation of equations (3.17), (3.19), (3.20) and (3.21) for the coolant temperature profile, several parameters are first to be calculated. The initial geometry of the breeder rod investigated is given in Chapter 2. In the following,the hydraulic and thermal conditions are postulated and certain parameters calculated.

For the case of equations (2.1) to (2.4), the flow rate is .008 kg/sec. For the case of equations (2.5) and (2.6), the flow rate is .011 kg/sec. The flow rates are different for these two cases and represent values selected to maintain the pumping power to energy extraction ratio below 4.0% for a system pressure of 49.3 kgf/cm^2. This interaction of pumping power requirments and other thermal/hydraulic parameters is discussed durther in Section (3.4). Both cases have a helium inlet temperature of 300°C and an inlet pressure of 49.3 kgf/cm^2. Correspondingly, the temperature drops through the blanket are determined by the first law to be 230°C and 300°C for the two cases. The heat transfer coefficients of coolant/wall for a packed bed are assumed equal to that ofthe coolant/bed. For the stated conditions of the case corresponding to equations (2.5) and (2.6), the heat transfer coefficient is calculated to be ~.28 w/cm^2 °C (~490 Btu/hr ft^2 °F) with the Coppage and London's Correlation[17], ~.37 w/cm^2 °C (~650 Btu/hr ft^2 °F) with the Eckert's equation[18], and .27 w/cm^2 °C (~480 Btu/hr ft^2 °C)

with the correlation suggested by Kunii and Levenspiel[19]. With an average of these calculated heat transfer coefficients (.3067 w/cm^2 °C) and the insulation equivalent to 1 mm of asbestos (the importance of insulation is discussed later), the effective conductance (or overall heat transfer coefficient) is calculated to be .016 w/cm^2 °C and .018 w/cm^2 °C for the two cases[20].

For the stated geometry and thermal/hydraulic conditions, the coolant temperature profiles were calculated[21] and plotted on Figures 3.2 and 3.3, with the effective conductance as a parameter. Both figures reveal interesting interactions between the peak coolant temperature and the effective conductance. Interestingly, the peak coolant temperature occurs before the exit from the breeder rod, and furthermore shows an upward tendency with increased effective conductance. Physically, this convexed temperature profile on the return pass represents trapped energy in the breeder rod heat exchanger showing up as a higher coolant temperature. As the effective conductance increases, it becomes more difficult to get the generated energy out of the heat exchanger, and subsequently a bigger portion of the generated energy is recirculated which manifests as a higher temperature of the coolant. This relationship is demonstrated as the upper curve of Figure 3.4, in which the maximum coolant temperature is shown to increase almost linearly at the rate of ~6000°C per w/cm^2-°C with the effective conductance between the flow passages. Consequently, at and above the effective conductance of ~.016 w/cm^2-°C, the coolant peak temperature will exceed 600°C for niobium with this geometry and flow rate. This interesting result serves to point out another important constraint in the engineering of the breeder rod heat exchanger,

i.e. the peak temperature in the heat exchanger is dictated by the amount of insulation as well as flow rate, q''' and geometry. The lower curve of Figure 9 further shows the other factor of mass flow rate which affects inversely the coolant temperature and can be utilized to place the coolant temperature at a level not exceeding the material limits, but concurrently compatible with the requirement of thermal conversion efficiency.

3.2 GRAPHITE SHIELD TEMPERATURE PROFILE

In an effort to protect the first wall from the high energy neutron irradiation, various concepts such as ISSEC[22], radiation shield[23] and first wall bumper[24] were proposed as a way to relax the stringent material requirements on the first wall. In these concepts, sacrificial moderator placed in front of the blanket down shifts the incoming energy spectrum under normal operating conditions and acts as a thermal damper under the conditions of a plasma dump[25]. However, the down shifting of the incoming neutron spectrum also reduces the high energy (n, 2n) reaction as well as the tritium producing ^{7}Li reaction, the synergistic effect of which is a decline of the breeding ratio. To remedy this, beryllium as a neutron multiplier is required in the high energy zone of the blanket. For the initial thermal design calculation, a graphite shield of 5 cm is postulated, representing a deduction by a factor of ~2.5 in the hydrogen and helium production rate, and a reduction by a factor of ~2 in the displacement damage rates in the first wall.

3.2.1 Theory and Approximations

The graphite shield has an internal volumetric heat source,

boundary heat addition from the plasma and boundary heat rejection to the breeder rod. The shield representation is approximated by a two dimensional geometry in rectangular coordinates, as shown in Figure 3.5. The small temperature drop through the breeder rod is assumed to be negligible. The problem definition and its solution are stated in the following. The derivation of the solution to a similar, but more interesting problem is included in the later section (4.2.1). In a rectangular coordinate system with the two variables of y and z, this problem is described as

$$\nabla^2 T + q'''/k = 0 \tag{3.23}$$

with the following boundary conditions

$$\left.\frac{\partial T}{\partial z}\right|_{z=0} = 0 \tag{3.23a}$$

$$\left.\frac{\partial T}{\partial z}\right|_{z=L} = 0 \tag{3.23b}$$

$$\left.\frac{\partial T}{\partial y}\right|_{y=0} = -\, q''_{\alpha}/k \tag{3.23c}$$

$$\left.\frac{\partial T}{\partial y}\right|_{y=Y} = 0 \qquad ,0 \leq z \leq \frac{L}{2} + R_o \tag{3.23d}$$

$$= -h(T-T_o)/k \qquad , \frac{L}{2} - R_o < z < \frac{L}{2} + R_o$$

$$= 0 \qquad , \frac{L}{2} + R_o \leq z \leq L$$

It should be pointed out that, in the boundary condition of (3.23d), the temperature drop in niobium (can wall) is neglected and the graphite shield is assumed to be in perfect contact with the structure. The heat transfer coefficient was obtained as discussed in Section (3.1.2) with the choice of a higher value than the average without asbestos to partially account for the effect on heat transfer when the flow impinges on the bottom of the breeder can. The solution to equation (3.23) subject to the given boundary conditions is as the following

$$T = q_\alpha''/h + q_{wo}'''(1-e^{-b_w Y})/(b_w h) + q_{wo}''' (e^{-b_w Y} - e^{-b_w y})/(b_w^2 k)$$

$$+ (q_\alpha''/k + q_{wo}'''/b_w/k)(Y-y) + Co$$

$$+ \sum_{n=1}^{\infty} C_n \cos \alpha_n z \cosh \alpha_n y \qquad (3.24)$$

where

$$\alpha_n = n\pi/L$$

$$C_o = T_o + \frac{(q_\alpha''+q_{wo}'''(1 - e^{-b_w Y})/b_w)\ (L - 2R_o + 2hE)}{2\ hR_o - 2h^2 E} \qquad (3.24a)$$

$$E = \sum_{n=1}^{\infty} \frac{2 \cos \alpha_n \frac{L}{2} \sin \alpha_n R_o \cosh \alpha_n Y \cos \frac{1}{2}\alpha_n \sin \alpha_n R_o}{\alpha_n (\frac{1}{2}kL\alpha_n^2 \sinh \alpha_n Y + h\ (\alpha_n R_o + \frac{1}{2} \cos \alpha_n L \sin 2\alpha_n R_o)\cosh \alpha_n Y)}$$

(3.24b)

$$C_n = \frac{2(h\ (T_o - C_o) - q_\alpha'' - q_{wo}'''(1 - e^{-b_w Y})/b_w)\cos \alpha_n \frac{L}{2} \sin \alpha_n R_o}{\frac{1}{2}kL\alpha_n^2 \sinh \alpha_n Y + h(\alpha_n R_o + \frac{1}{2} \cos \alpha_n L \sin 2\alpha_n R_o) \cosh \alpha_n Y}$$

(3.24c)

3.2.2 Evaluation of the Graphite Shield Temperature

For the case of a breeder rod with R_o = 3.8 cm, L = 10.2 cm, Y = 5 cm, h = 3407 w/m^2/°C, k = 86.5 w/m/°C, q''_α = 20 w/cm^2, $q''' = 3.68\ e^{-.103y}$ w/cc and T_o = 544 °C corresponding to the inner to outer flow case with H = .018 of Figure 3.3, Equation (3.24) was evaluated[21] and the result was plotted in Figure 3.5b. The convergence of the equation is discussed in Section (4.2.1) along with the derivation of the solution.

As shown in Fig. 3.5b, for this geometry the maximum temperature is 852°C which is considerably below the 2000°C limit imposed on carbon by its partial pressure. The maximum temperature of the module fi wall is approximately 700°C which in in a range where corrosion could be a problem. However increasing the module size and lowering ΔT can solve this problem.

The treatment of the problem as two dimensional in rectangular coordinate tends to lower the peak graphite temperature, whereas the use of maximum coolant temperature affects the temperature profile in just the opposite direction. The assumption of perfect contact between graphite and niobium also lowers the graphite temperature. At present accurate values for the contact resistance between carbon and metals under vacuum conditions are not known. Reference 4 has a discussion of this problem and concludes that for vacuum operation and relatively low contact pressure, the thermal resistance would be high and would probably fall in the range of 10^{-2} to 10^{-3} $W^{-1}m^2$-°C. For our design if a value of $10^{-3}W^{-1}m^2$-°C were taken for the thermal resistance between the shield and breeder rod, the overall coefficient of

heat transfer would become

$$U = \frac{1}{1/h_1 + 1/h_2} = \left(\frac{1}{3407} + 10^{-3}\right)^{-1} \simeq 773 \text{ w/m}^2\text{-°C}$$

The effect of this would be to increase the average shield temperatures by approximately 350 °C for normal operation. Even with this increase the graphite shield temperatures would still be well below the design limit of 2000°C and it seems reasonable to assume safe operation.

In addition to the contact resistance, it is possible that only part of the shield would actually be in contact with the metal can, but this effect has not been considered because it would depend strongly on the actual attachment method and geometry which has not been addressed in this report.

3.3 SHIM ROD TEMPERATURE PROFILE

The graphite shim rod has a maximum operating temperature of 2000°C. Energy generated within the shim is assumed to be conducted to the interface with the breeder rods where it is removed either through conductance or by thermal radiation across a gap. For the case of contact, a conductance of .4 W/cm^2-°C (700 BTU/hr-ft^2 °F) has been assumed at the interface. For the analysis with a gap the shim and breeder rods have been treated as parallel plates with assumed emissivities of 0.6 for niobium and 1 for graphite. This assumes that the surfaces have been treated to enhance their emissivities.

3.3.1 Methods of Analysis and Results

The shim's thermal profile is analyzed by an adiabatic cylinder wall method. The shim and breeder matrix is represented by a two

region annulus,the inner region being the niobium can and the outer region being the graphite shim. The outer region boundary is at a radius equal to half the center to center distance between breeder rods. The following boundary conditions are imposed:

1) an adiabatic condition at the outer radius of the graphite region, i.e. point a of Figure 3.6,

2) a heat transfer coefficient and a coolant temperature at the inner radius of the niobium region, i.e. point c. The inner to outer flow arrangement with the coolant temperature profiles of Figures 3.2 and 3.3, and a heat transfer coefficient of 0.35 w/cm^2 was used.

Point b is the boundary of the graphite shim. Quantitatively, the niobium annulus is expressed as

$$\frac{1}{r}\frac{\partial}{\partial r}\left(r\, k_n \frac{\partial T_n}{\partial r}\right) + q_n''' = 0 \tag{3.25}$$

with the boundary conditions of

$$-k_n \left.\frac{\partial T_n}{\partial r}\right|_{R_c} = h\left(T_f - \left.T_n\right|_{R_c}\right)$$

$$= \frac{-q_c'''\,(L_x^2 - \Pi R_b^2) - q_n'''(R_b^2 - R_c^2)\Pi}{2\Pi R_c} \equiv -h\, a_1 \tag{3.25a}$$

$$+ k_n \left.\frac{\partial T_n}{\partial r}\right|_{R_b} = + \frac{q_c'''\,(L_x^2 - \Pi R_b^2)}{2\Pi R_b} \equiv a_2 \tag{3.25b}$$

where $L_x = L\ (MR+x)/MR$ (3.25c)

The graphite annulus is expressed as

$$\frac{1}{r}\ \frac{\partial}{\partial r}\ (k_c\ r\ \frac{\partial T_c}{\partial r}\ ) + q'''_{cm} = 0 \qquad (3.26)$$

$$\text{where } q'''_{cm} \equiv \frac{q'''_c\ (L_x^{\,2} - \Pi R_b^{\,2})}{\Pi\ (o.5\ L_x^{\,2} - R_b^{\,2})} \qquad (3.26a)$$

with the boundary conditions for contact of

$$T_c\Big|_{R_b} = T_n\Big|_{R_b} + a_2/HC = a_3 \qquad (3.26b)$$

$$\frac{\partial T_c}{\partial r}\Big|_{R_a} = 0 \qquad (3.26c)$$

When a gap is present the boundary condition of equation (3.26b) becomes

$$T_c\Big|_{R_b} = [T_n\Big|_{R_b}^{\,4} + \frac{a_2}{\bar{\varepsilon}\sigma}]^{1/4} = a_3 \qquad (3.26d)$$

where

$$\bar{\varepsilon} = \frac{\bar{\varepsilon}_c\,\bar{\varepsilon}_{nb}}{\bar{\varepsilon}_c + \bar{\varepsilon}_{nb} - \bar{\varepsilon}_c\bar{\varepsilon}_{nb}}$$

$\bar{\varepsilon}_c$ = Emissivity of carbon

$\bar{\varepsilon}_{nb}$ = Emissivity of niobium

σ = Stefan Boltzmann constant (5.67×10^{-8} w/m^2(°K)$^{-4}$

$$\text{where } C_1 = \frac{q'''_n R_b^2}{2} + a_2 R_b \tag{3.28a}$$

$$C_2 = T_f + a_1 + \frac{q'''_n R_c^2}{4 k_n} - \frac{C_1}{k_n} \ln R_c \tag{3.28b}$$

$$C_3 = \frac{q'''_{cm} R_a^2}{2} \tag{3.28c}$$

and $a_3 \equiv$ equation 3.26b or 3.26b' for the contact and gap geometries respectively.

For the conditions already stated, and the geometry postulated in Chapter 2, Equations (3.27) and (3.28) were evaluated[21]. The resulting temperatures at points a, b and c were plotted on Figure 3.6 and 3.7 for the two sets of boundary conditions. With a contact conductance at the interface the temperature rise across the interface is small and T_b follows the shape of the curve for the coolant temperature. With a gap present, however, the temperature rise is much greater and the curve in the vicinity of the first wall tends to follow the exponential decrease in energy generation within the carbon shim. Again, reasonable operating temperature is evidenced and safe operation can be expected. A parametric study of the dependence of the maximum shim temperature on conductivity, heat transfer coefficient and contact conductance was plotted on Figure 3.8 revealing a comfortable margin for safe operation even in the presence of fairly large parameter variations.

3.4 HYDRAULIC ANALYSIS

The viability of any reactor design depends strongly on its efficiency in producing net power, which is a further function of the amount of recirculated power needed for the operation of the reactor. In this respect, the pumping power to heat removal ratio is one important factor in the design of the breeder rod shim rod blanket. The use of gas coolant bypasses the difficulties associated with the MHD pumping of a conductive material in a high field environment. However, the porous breeder rod presents itself to the coolant with a tremendously large surface area. The effect of which is high pressure drop through the breeder and consequently high pumping requirements.

3.4.1 Pressure Drop

The pressure drop through a porous bed has contributions from factors such as skin friction, acceleration, elevation, entrance and exit effect. These effects can be expressed as equation (3.29) in terms of the momentum equation[26], friction factor, area ratio, contraction coefficient and expansion coefficient[26,27].

$$-\Delta P = \frac{G^2}{2\rho_1}\left[f\,\frac{A}{A_c}\,\frac{\rho_1}{\rho_m} + \left(\frac{\rho_1}{\rho_2} - 1\right) + \left(1 + K_c - \sigma^2\right) + \left(K_e + \sigma^2 - 1\right)\frac{\rho_1}{\rho_2}\right] + \rho_m g\,(z_2 - z_1) \qquad (3.29)$$

For matrix surface with $K_c = K_e = 0$, equation (3.29) becomes

$$-\Delta P = \frac{G^2}{2\rho_1}\left[f\,\frac{A}{2A_c}\left(1 + \frac{P_1}{T_1}\,\frac{T_2}{P_2}\right) + \left(\frac{\rho_1}{\rho_2} - 1\right)\sigma^2\right] + g\,\rho_m(z_2 - z_1) \qquad (3.30)$$

However, the pressure drop through a packed bed can also be calculated by various empirical equations[27,28]. One of these suggested by Leva is[27]

$$\Delta P = \frac{\lambda_f XT}{2r_p} V_f^2 \rho_m \left[\frac{(1-m_o)^{3-n}}{m_o^3}\right] \qquad (3.31)$$

Where XT is the length of the breeder rod, r_p is the breeder pellet radius, V_f the free stream velocity before entrance to the bed, $_m$ is the mean fluid density, m_o is the bed porosity ($m_o = .32 + .45\ r_p/r_{im}$ where r_{im} is the inner flow channel radius which for our case yields equal cross sectional area for the inner and outer flow channels), and λ_f and n are functions of the Reynolds number as illustrated in reference 27. P was evaluated using Equations 3.30 and 3.31 for several cases and the results are tabulated in Table 3.

3.4.2 Pumping Power

The pumping power to heat removal ratio is calculated by[29]

$$\frac{PP}{Q} = \frac{\dot{m}\Delta P}{Q} \qquad (3.32)$$

where $\dot{m}$ is the mass flow rate, is the inlet coolant density and Q = the total heat removal rate from the breeder rod module.

For an ideal gas and isotropic condition this can be expressed as

$$\frac{PP}{Q} = \frac{\dot{m}}{Q}\left(\frac{\gamma}{\gamma-1}\right)\frac{P1}{\rho_1}\left[\left(\frac{P_2}{P_1}\right)^{\gamma-1}-1\right]0.098 \qquad (3.33)$$

The results of pumping power to heat removal ratio for the cases of Table 3 were plotted in Figures 3.9, 3.10, and 3.10. For the geometry under consideration the PP/Q were found to be 2.8 %.

and 3.9% corresponding to Equations 2.1 to 2.4 and Equations 2.5 and 2.6 respectively.

From Equations 3.31 and 3.32, assuming an ideal gas, and that Q is proportional to r_o^2 (the module radius) it can be shown that

$$\frac{PP}{Q} = \frac{C}{r_p} \frac{\lambda}{\Delta T^3} \frac{T_{inlet} T_m}{P^2} \left[\frac{(1-m_o)^{3-n}}{m_o^3}\right] \qquad (3.34)$$

where ΔT is the temperature rise through the module, T inlet is the inlet helium temperature in °K, Tm is the average coolant temperature (°K), P is the average helium pressure kgf/m^2), and C is a constant related to Q. Thus, from a hydraulic point of view the desired system is one with large ΔT, large particles, low inlet temperature and high pressure.

TABLE 3. Pressure drop through the Breeder Rod With Inlet Temperature of 300 °C

Q/module (kw)	$\dot{m}$ (kg/sec)	ΔT (°C)	γ_p (mm)	ΔP (nt/cm^2) P_1 = 49.3 kgf/cm^2 (700 psia) by Eq. (3.31)	ΔP (nt/cm^2) P_1 = 49.3 kgf/cm^2 (700 psia) by Eq. (3.30)	ΔP (nt/cm^2) P_1=42.3 kgf/cm^2 (600 psia) by Eq. (3.30)
18.12	.0242	300	1	80.	-	-
Eqs. (2.4) and (2.5)			2	27.	24.9	-
			3	22	-	-
10.276	.0176	230	— 2	15.1	-	-
Eqs. (2.1) to (2.4)						
12.59	.0122	200	1	82.4	-	95.9
			2	26.3	24.8	30.6
			3	17.7	14.7	20.6
			4	9.8	-	-
12.59	.0081	300	1	44.6	-	52.1
			2	16.1	13.5	17.1
			3	8.9	-	10.5

CHAPTER 4

BLANKET RESPONSE UNDER OFF-NORMAL OPERATING CONDITIONS

4.1 Module Conditions Considered

This chapter will examine the thermal response of the blanket components when a module is depressurized and cooled only indirectly by the surrounding modules which are operating. For the geometry postulated in Chapter 2, shield, shim, failed module and operating module temperatures are determined for both the case where the shim rods are in contact with the breeder rods and for the case where a gap is required between them to accomodate different thermal expansion. For the second case it was found that the peak $LiAlO_2$ temperature within a failed module was considerably higher than our design limit.

In addition the peak structural temperature was found to exceed 600°C under off-normal conditions. Means to alleviate these problems are considered in Chapter 5 where the geometry was varied in an attempt to meet the thermal constraints.

One facet of the design important to failure mode operation is the valving and header arrangement. With a first wall area of 1450 m^2 and a center to center distance of 10.2 cm 140,000 modules would be required. For such a large number it obviously is desirable to have less than one inlet valve per module. The blanket would be divided into sections. Within each section, modules are arranged in groups fed by independent supply headers. If each section had two supply headers, then if one module fails the corresponding header would be depressurized and half the modules in the

section would be isolated and the other half would have twice the normal heat load. If five supply headers per section were used, then this additional heat load in failure mode operation would be 1/4 of normal; with nine supply headers the additional load could be reduced to 1/8. The remaining thermal analysis will assume a 5 header arrangement so that the heat load of a failed module is shared between the four adjacent breeder rods. It should be noted that the number of modules is proportional to $1/L^2$ so it is desirable to go to larger modules. For L = 13 m the total number of modules would drop to 85,800.

In the event of a coolant failure, the solution for the coolant temperature is modified slightly to account for the additional heat input from the failed module. The results were plotted as Figure 4.1, showing a higher level of coolant temperature than the normal case by ≈70°C with the same mass flow rate.[21] These temperature profiles were later used as input to the structure temperature calculation.

4.2 STRUCTURE TEMPERATURE PROFILE

4.2.1 Graphite Shield

The description of the graphite shield temperature in two dimensional rectangular geometry can be formulated as (see section 3.2)

$$\nabla^2 T + q'''/k = 0 \qquad (4.1)$$

with the following boundary conditions

$$\left.\frac{\partial T}{\partial z}\right|_{z=0} = 0 \qquad (4.2)$$

$$\left.\frac{\partial T}{\partial z}\right|_{z=3L/2} = 0 \qquad (4.1b)$$

$$\left.\frac{\partial T}{\partial y}\right|_{y=o} = -q''_{\alpha}/k \qquad (4.1c)$$

$$\left.\frac{\partial T}{\partial y}\right|_{y=Y} = 0 \qquad o \leq z \leq \frac{L}{2} - R_o \qquad (4.1d)$$

$$= -\frac{h}{k}\left(T\Big|_{y=Y} - T_o\right) \qquad \frac{L}{2} - R_o \leq z \leq \frac{L}{2} + R_o$$

$$\frac{L}{2} + R_o \leq z \leq \frac{3}{2} L$$

where for a first approximation 4.1c neglects thermal radiation from the surface to the rest of the interior of the torus.

This problem is separated into two problems in T_a and T_b where $T = T_a + T_b$. The first problem is dependent on y only, and is as the following

$$\frac{\partial^2 T_a}{\partial y^2} + q'''/k = 0 \qquad (4.2)$$

with the following boundary conditions

$$\left.\frac{\partial T_a}{\partial y}\right|_{y=0} = -q''_\alpha / k \tag{4.2a}$$

$$\left.\frac{\partial T_a}{\partial y}\right|_{y=Y} = -h\, T_a \Big|_{y=Y} \Big/ k \tag{4.2b}$$

The second problem is a function of y and z as in the following

$$\nabla^2 T_b = 0 \tag{4.3}$$

with the following boundary conditions

$$\left.\frac{\partial T_b}{\partial z}\right|_{z=0} = 0 \tag{4.3a}$$

$$\left.\frac{\partial T_b}{\partial z}\right|_{z=\frac{3}{2}L} = 0 \tag{4.3b}$$

$$\left.\frac{\partial T_b}{\partial y}\right|_{y=o} = 0 \tag{4.3c}$$

$$\left.\frac{\partial T_b}{\partial y}\right|_{y=Y} = \frac{h}{k} T_a \Big|_{y=Y} \qquad 0 \le z \le \frac{L}{2} - R_o \tag{4.3d}$$

$$= -\frac{h}{k} \left(T_b\Big|_{y=Y} - T_o\right) \qquad \frac{L}{2} - R_o < z < \frac{L}{2} + R_o$$

$$= \frac{h}{k} T_a \Big|_{y=Y} \qquad \frac{L}{2} + R_o \le z \le \frac{3}{2} L$$

The solution to equation (4.2) with only y dependence is obtained by integration with the boundary conditions of (4.2a) and (4.2b).

$$T_a = q''_\alpha /h + q'''_{wo} (1 - e^{-b_w Y}) / (b_w h) + q'''_{wo} (e^{-b_w Y} - e^{-b_w y})/ (b_w^2 k) + (q''_\alpha/k + q'''_{wo} / (b_w k)) (Y-y) \quad (4.4)$$

With the expression for T_a, equation (4.3) was solved using the method of separation of variables . Applying boundary conditions of (4.3a) and (4.3c), the solution becomes

$$T_b = C_o + \sum_{n=1}^{\infty} C_n \cos \alpha_n z \cosh \alpha_n y \quad (4.5)$$

where $\alpha_n = 2n\pi/3L$ is obtained by applying the boundary condition of (4.3b). The constants of C_o and C_n are obtained by satisfying the remaining boundary condition of (4.3d), and are defined as the following.

$$C_o = T_o + \frac{h T_a\big|_{y=Y} (\frac{3}{2} L - 2 R_o + 2 h E)}{2 h R_o - 2 h^2 E} \quad (4.5a)$$

$$C_n = 2D_n (h(T_o - C_o) - h T_a\big|_{y=Y}) \quad (4.5b)$$

$$D_n = \frac{\cos(\alpha_n \frac{L}{2}) \sin (\alpha_n R_o)}{\frac{3}{4} kL\alpha_n^2 \sinh(\alpha_n Y)+h \cosh(\alpha_n Y)(\alpha_n R_o + \frac{1}{2} \cos (\alpha_n L)\sin(2\alpha_n R_o))} \quad (4.5c)$$

$$E = \sum_{n=1}^{\infty} \frac{2D_n}{\alpha_n} \cosh(\alpha_n Y) \cos(\alpha_n \frac{L}{2}) \sin(\alpha_n R_o) \qquad (4.5d)$$

Equations (4.4) and equation (4.5) then define the off-normal graphite shield temperature profile. The convergence of equation (4.5) is rather rapid as can be seen from the $1/n^2$ in C_n and $1/n^3$ in E. The solution was computer coded. With the maximum coolant temperature of 598°C at the bottom of the module obtained from Figure 4.1, the resulting profile was plotted as Figure 4.2. The maximum graphite temperature is estimated at 1227°C, whereas the maximum operating can wall temperature is estimated at 900°C. This high wall temperature is a problem and ways of reducing it will be discussed later. Maximum can wall temperature of the failed (depressurized) module is 1145°C which is much below the 2000°C design unit for unstressed niobium with no He coolant present.

4.2.2 Shim Rod

The modelling of the off-normal shim temperature is the same as that discussed in section (3.3). However, the geometry of the graphite annulus is different and is defined in Figure 4.3 with point a denoting the adiabatic boundary. Within the graphite annulus bounded by point b of Figure 4.3, a volumetric heat generation equivalent to twice of the normal heat load is assumed instead of the 1 1/4 due to the sharing of the energy of the failed module by the four adjacent operating modules. With this new arrangement, the off-normal shim temperature is described by equation (3.27) and (3.28), just the same as that of the normal shim temperature, but with the following new definitions reflecting the differently assumed q''' in graphite.

$$a_1 \equiv \frac{2\, q_c''' \,(L_x^2 - \pi R_b^2) + 2\pi q_n''' \,(R_b^2 - R_c^2) + q_b''' \,\pi R_c^2}{2\pi\, R_c h} \quad (4.6)$$

$$a_2 \equiv \frac{2\, q_c''' \,(L_x^2 - \pi R_b^2) + q_b''' \,\pi R_c^2 + q_n''' \,\pi(R_b^2 - R_c^2)}{2\pi\, R_b} \quad (4.7)$$

$$q_{cm}''' = \frac{2\, q_c''' \,(L_x^2 - \pi R_b^2) + q_b''' \,\pi R_c^2 + q_n''' \,\pi(R_b^2 - R_c^2)}{\pi\,(R_a^2 - R_b^2)} \quad (4.8)$$

With the higher off-normal coolant temperature profile as input, the shim temperature profiles were calculated using equations (3.27) and (3.28) and plotted as Figure 4.3 for conduction at the interface and 4.5 for the radiative boundary condition.

From the results of Figures 4.3 and 4.4, continued operation of the blanket element is reasonably predicted, though the differential expansion of the shim will cause additional stress on the surrounding as well as the failed blanket elements when in contact with the breeder rods. A parametric variation of the effect of heat transfer coefficient, the contact conductance and the graphite conductivity was performed and is on the peak shim temperature, plotted as Figure 4.5.

4.2.3 Failed Module

The failed module is analyzed as a cylinder surrounded by an annulus. Two cases will be examined. For the first case the shim will be assumed to be in contact with both the failed module and with the surrounding operating modules with an interface contact conductance of .4W/cm^2-°C. In

the second case it will be assumed that there exists a small gap around the entire shim. The boundary conditions for the annulus at point a consist of a surface flux equivalent to the total heat generated in the cylinder and annulus, a shim temperature as calculated in the previous section for the two cases, and either a contact conductance of the same value as above or a parallel plate radiative boundary condition.

With the annulus temperature profile, the cylinder than has the boundary conditions of finite temperature at point d of Figure 4.6, and a surface temperature at point e from the annulus temperature profile. The temperature solutions for these two regions are

$$T_{an} = a_3 + \frac{q_n'''}{4k_n} (R_a^2 - r^2) + \frac{C_1}{k_n} \ln \frac{r}{R_a} \tag{4.9}$$

$$T_{cy} = T_{an}\Big|_{r=R_e} + \frac{q_b'''}{4k_b} (R_e^2 - r^2) \tag{4.10}$$

where

$$a_3 = \frac{T_a + q_n''' (R_a^2 - R_e^2) + q_b''' R_e^2}{2 R_a HC} \quad \text{(Case (1))} \tag{4.10a}$$

$$a_b = \left[T_a^4 + \frac{q_n''' (R_a^2 - R_e^2) + q_b R_e^2}{2 R_a \bar{\varepsilon} \sigma}\right] \quad \text{(Case (2))} \tag{4.10b}$$

$$\bar{\varepsilon} = \frac{\varepsilon_c \varepsilon_{Nb}}{\varepsilon_c + \varepsilon_{Nb} - \varepsilon_c \varepsilon_{Nb}}$$

$$C_1 = \frac{q_n''' R_e^2}{2} - \frac{q_b''' R_e^2}{2}$$

and, T_a is from the shim rod temperature calculation for either case 1 or 2. For the conditions of HC = .40 w/cm^2/°C, k_n = .69 w/cm/°C, k_b = .05 w/cm/°C, and the geometry postulated in section (2.3), the failed module temperature was plotted for case 1 and case 2 with $\varepsilon_c = 1$, $\varepsilon_{Nb} = .6$ as figures 4.6 and 4.7. The effective conductivity of the failed module was based primarily on the effective conductivity of porous material corresponding to the geometry of the packed breeder rod at elevated temperature[30]. The effective conductivity of the packed bed was assumed based on only the contribution from radiation at elevated temperature and therefore is subject to slight variations. The maximum temperature in the failed module is inversely proportional to the effective conductivity and safe temperature levels exist for case 1 for effective conductivity of as low as .02 w/cm/°C. It should also be pointed out that the temperature of the niobium annulus is independent of the value of the effective conductivity and therefore the off-normal maximum can wall temperature will vary little even under extremem variation in the packed bed effective conductivity. Furthermore, Figure 4.6 serves to illustrate the exponential nature of the spatial heat generation rate which raised only a small region of the breeder to a temperature of 1000°C or above for the case of contact. In view of the melting temperature of 1900°C of $LiAlO_2$, the structure of the failed breeder rod is reasonable guaranteed in this case.

From Figure 4.7 it can be seen that for this geometry and with an energy generation rate corresponding to Equations 2.5 and 2.6 a portion of the packed bed close to the first wall would exceed the melting point

of $LiAlO_2$ if a gap is required around the shim rods. Obviously this is not acceptable. The next chapter will investigate the effects on the peak temperature of reducing the module size and going to a closer packing arrangement.

CHAPTER 5

EFFECT OF SHIELD THICKNESS AND MODULE SIZE ON TEMPERATURE PROFILE

The results of breeding ratio calculations, to be presented later, indicated a strong incentive to decrease the thickness of the graphite shield and also the amount of graphite in the shim rods. In addition the results of the thermal analysis indicated a need to reduce the peak temperature of the module's first and side walls when operating under off-normal conditions and also the peak temperature of the $LiAlO_2$ in a failed module when a gap is required around the shim rods. This chapter examines the effects on these peak temperatures of reducing the shield thickness, going to a closer packing arrangement of the breeder rods and varying the module side wall radius.

For the same geometry as discussed so far the effect of reducing the shield thickness on various critical temperatures was first investigated. The results for failed mode operation are shown in Figure 5.1 for Tinlet = 300°, ΔT = 300. These curves are based on the assumption that all heat transfer is by conduction and illustrate that the temperatures go through a minimum near a thickness of 3 cm. For thicknesses less than 2 or 3 cm, the temperatures increase as the thickness decreases because the effective conductance from the failed module to its neighbors is decreasing but the same surface energy flux is present. For thicknesses greater than 2 or 3 cm the additional energy generated within the shield becomes important and the temperatures tend to increase again.

The closest packing in a rectangular array is where the center to center distance between adjacent modules at the first wall equals twice the module side wall radius. This arrangement was assumed and also a 1 cm shield thickness to evaluate the effect of changing module radius. One cm was taken as a minimum shield thickness because of the steep rise in the maximum structural temperature of the operating module first wall for smaller thicknesses. In order to approximate the additional heating in a blanket containing Be as a multiplier and more $LiAlO_2$, an assumed heating rate was taken for which the total energy removed from a breeder rod divided by the first wall surface area of a unit cell, equalled 1.5 Mw/m^2 or a total energy multiplication of 1.25. The corresponding energy generation rates are

$$q_4''' = 5\ e^{-.042x}\ \text{w/cm}^3 \qquad (5.1)$$

$$q_3''' = 3.68e^{-.103y} \qquad (5.2)$$

For the conditions given in Table 5.1 and an inlet temperature of 300°C and a temperature rise in the module (ΔT) equal to 200°, the maximum temperature of the graphite shield, the operating module side wall, the first wall, and the coolant are plotted versus module radius in Figure 5.2 for normal operation.

For the same temperature drop between inlet and outlet with different module radius, the coolant mass flow rate per unit volume of the module must be approximately constant assuming volume energy generation rates do not change.

The fraction of heat which is trapped because of the finite thermal conductivity of the insulating wall is expected to be proportional to the surface area of the wall divided by the volume of the flow passages and therefore inversely proportional to the module radius and this is the type of variation found as shown in Figure 5.2 for normal operation.

OFF NORMAL RESPONSE

For the same condition as above, the blanket thermal response was evaluated for failure mode operation and the results are shown in Figure 5.3 and Figure 5.4. Two curves were calculated for $LiAlO_2$. One assuming the same contact conductance between the shim rod and breeder rods as before ($h = .4$ W/cm^3/°C) and one based on the radiative boundary condition with emissivity of the niobium assumed to be enhanced by surface treatment to yield a value of 0.6. The lithium aluminate temperature shown is the peak temperature which occurs at the point closest to the first wall in the center of the failed module. It can be seen that the introduction of the gap raises the $LiAlO_2$ temperature profile by over 600°C and places a restriction on the maximum allowable module size. For normal operation however, the gap would only increase the shim rod temperature and this would not be close to the design limit.

Figure 5.4 is the same as 5.3 on a magnified scale to show the variation of maximum structural temperature. The maximum temperature calculated for the first wall of an operating module under off-normal conditions is considerably above 600°C, varying between approximately 780° to 750°C. The calculations however, are quite conservative since they do not include radiation from the failed module shield to the rest of the enclosure. For the off normal case the maximum shield temperature was calculated to be 945°C for a 5 cm radium module while the rest of the enclosure would be at 587°C, the normal shield temperature. For those temperatures and an emissivity of .3

the failed module shield would radiate at 8.4 watts/cm^2 if the temperature was uniform. This is a very significant fraction of the incident 20 w/cm^2 and indicates that equilibrium would be reached at a signficantly lower temperature. Also, simply increasing the shield thickness to 2.75 would lo the maximum temperature by 65°C although this would be detrimental to the breeding. A three-dimensional calculation to represent the spherical cap and allowing radial heat conduction down the shim rod from the shield would also lower this calculated peak first wall temperature. A quantitative calculation of these effects has not been accomplished but it is felt that this were the only design problem, it would not be difficult to resolve. For the present therefore, it will be assumed that the first wall maximum temperatures are approximately equal to the maximum side wall temperatures and if a viable design window can be found based on this then the assumptio will have to be justified or the window altered.

TABLE 5.1

REVISED GEOMETRY

$L = 2\ Rm$

shield thickness = 1 cm

$Q/L^2 = 1.5\ Mw/m^2$

$$\frac{\dot{m}}{L^2} = \frac{1.5\ Mw/m^2}{(\Delta T)_{normal} C_p} = \text{constant}$$

$H = .016\ w/cm^2$

CHAPTER 6

ANALYSIS OF THE BREEDING MATERIAL AND TRITIUM TRANSPORT IN THE BRSR

6.1 INTRODUCTION

The selection of the breeding material and the analysis of tritium transport in the BRSR will be the subject of this chapter. At first it may seem odd to include these two subjects in a single chapter. However, as it will soon become clear, they are closely linked and perhaps inseparable. After the basic design requirements for material selection such as thermal stability, material compatibility, strength, etc., have been established, the single most important consideration is the transport of tritium in the breeding material and throughout the blanket module. The mere existence of large quantities of tritium is a potential hazard. Thus, a fusion reactor blanket must be designed to breed tritium and facilitate separation from the bred material to keep the inventory low.

6.2 BREEDING MATERIAL

6.2.1 Selection of Breeding Material

A solid breeding material must display certain characteristics to be acceptable for use in a fusion reactor blanket. The most important points are as follows:

1) High melting point
2) High lithium content
3) Low tritium rententivity
4) Chemical stability
5) Compatibility with structural material
6) No resource limitation
7) Low vapor pressure

Several possible lithium compounds are listed along with their characteristics in Table 6.1. Due to the requirement that the BRSR design be able to sustain a faiulre, failed module temperatures in the range of 1000°C must be expected, and therefore, the melting point of the breeding material is of prime importance. Of those compounds presented, this requirement leaves $LiAlO_2$, Li_2SiO_3, Li_2BeO_3, Li_2O and $Li_2B_4O_7$ for consideration. Next, the compound must have a significant lithium content ($\geq$ 25% lithium atom fraction) as the rod is already 36% void volume due to the packing geometry. This requirement eliminates $Li_2B_4O_7$. Of the remaining four compounds, all have both positive and negative points. However, due to the large amount of information available on lithium aluminate relative to the other compounds, $LiAlO_2$ was selected for use in the BRSR study. A serious drawback of $LiAlO_2$ (lithium aluminate) is the low lithium content, indicating a possible need for a neutron multiplier. However, this drawback is somewhat countered by a favorable margin of safety in the melting point (1900°C). Nevertheless, the main determining factor is that it is the only lithium compound on which tests have been performed for the purpose of exploring its possible use in a fusion reactor blanket. These experiments are being performed at Brookhaven National Laboratory[31, 32] and form the data base for all computations involving $LiAlO_2$ in this report.

Additional features of lithium aluminate are that it is readily available, inexpensive, inert and not resource limited. Other drawbacks of $LiAlO_2$ are that lithium aluminate obtained commerically contains 21.4% Li_2O (lithia) which is quite volitile at high temperatures and displays

Table 6.1a

CHARACTERISTICS OF SOLID LITHIUM COMPOUNDS FOR TRITIUM BREEDING *

Lithium alloy or compound	M.P. °C	Tritium retentivity	Neutron multiplier needed	Low residual radioactivity	Reacts with air	Sintering problems	Chemically stable	Resource Limitation
LiAl	718	very low	yes	yes	slowly	maybe	yes	no
$LiAlO_2$	1910	very low	yes	yes	no	probably not	yes	no
Li_2SiO_3	1204	very low	yes	yes	no	probably not	yes	no
$Li_2Be_2O_3$	1150	unknown	no	yes	no	unknown	yes	Be(?)
Li_7Pb_2	726	very low	no	yes	slowly	unknown	yes	no
Li_3Bi	1145	unknown	no	some Po^{210}	probably slowly	unknown	yes	Bi
Li_4Si	635	unknown	no	yes	probably slowly	unknown	probably	no
Li_3N	800	unknown	no	yes	probably slowly	unknown	probably requires N_2 gas	no
Li_4Sn	765	unknown	no	no	probably slowly	unknown	probably	no
$Li_2B_4O_7$	930	unknown	yes	yes	probably not	unknown	yes	requires separated B^{11}
Li_2O	1200	high	no	yes	probably not	unknown	?	no

* ref. 32

Table 6.1b*

Potential Non-Mobile Breeder Materials

Material	M. pt. °C	Vapor Pressure	Li atoms $10^{22}/cm^3$
Li (liq.)[a]	180	1342°C(B. pt.)	4.2
LiAl	718	-	2.7
Li_3Bi[b]	1145	-	4.0
Li_2O[c]	1700	10^{-1} torr (1400°C)	8.2
LiOH[c]	471	5 torr H_2O(500°C)	3.7
$LiAlO_2$[e]	1700	Li_2O (1400°C)	2.3
Li_4SiO_4[f]	1256	Li_2O (1256°C)	4.8
Li_2C_2[g]	>1000	Li (1000°C)	4.1
LiF[d]	848	b. pt. (1693°C)	6.1
LiH[a,c]	686	24 torr H_2(686°C)	5.9

a. V. A. Moroni, E. J. Cairns, and F. A. Cafasso, "A Review of the Chemical, Physical and Thermal Properties of Lithium that are Related to Its Use in Fusion Reactors," Argonne National Laboratory, ANL-8001 (1973).

b. M. Hansen, Constitution of Binary Alloys, McGraw-Hill, New York (1958).

c. T. Kikuchi, Japan Atomic Energy Research Institute Memo - 5837 (1974).

d. W. A. Hart and O. F. Beumel, Jr., Comprehensive Inorganic Chemistry, Vol. I, A. F. Tnrutman-Dickenson, Ed., pp. 340-361, Pergamon Press, Oxfor

e. D. W. Streckler and Rustum Roy, J. Am. Ceramic Soc., 44, 225 (1961).

f. F. C. Kracek, J. Phys. Chem., 34, 2645 (1930).

g. T. Ya. Kosolapova, Carbides, pp. 61-63, Plenum Press, New York (1971).

* Table IV-B-2 Reference 3

high tritium rententivity.[32] Additionally, $LiAlO_2$ undergoes a phase change at 900°C from a rhombohedral structure to a more open tetragonal structure resulting in a 30% volume increase. This is an important point which may limit the use of $LiAlO_2$ to lower temperature systems. However, all things considered, $LiAlO_2$ appears to be an acceptable starting point.

6.2.2 Pellet Size Effects on Breeding Ratio

The breeding capability of this design is affected by the pellet size through the void fraction. Clearly, the optimum breeding arrangement is one in which the blanket consists of perfectly dense breeding material. However, a packed bed of pellets yields a fertile material number density that falls far short of the optimum, and is therefore, an inherently difficult design with which to achieve breeding. For spherical pellets packing into a cylindrical tube, the void fraction can be related to the ratio of the pellet diameter to tube diameter, ε, through Figure 6.1. As one can see, for a given tube diameter, a reduction in the pellet radius (and hence ε) results in a reduction of the void fraction.

The breeding ratio increases with an increase in the ratio of fertile material (Li) to total blanket material. In this design, an increase in the void fraction means a decrease in the fertile to total material ratio resulting in a breeding ratio that varies inversely with the void fraction. Therefore, since the optimum void fraction is zero (which is impossible in this design) one can only say that the void fraction should be kept to an absolute minimum implying a pellet radius as small as possible. The calculations of the breeding ratio are presented in detail in Chapter 7.

6.2.3. Effect on Inventory

If the tritium that is bred inside the pellet is unable to escape into the coolant stream, an inventory will accumulate that may exceed the maximum acceptable level. The possible mechanisms limiting tritium escape are the surface reaction of tritium to form T_2, the diffusion of tritium through the pellet and the solubility of tritium in $LiAlO_2$. Studies performed at Brookhaven National Laboratory indicate that diffusion is the rate limiting mechanism.[32] Therefore, an inventory of tritium will be present due to slow diffusion. The amount of inventory buildup is a function of the temperature, crystal size and the pellet size as discussed in Section 6.3.1. These relations are discussed in detail later, and it will suffice to state that the pellet size will influence the tritium inventory. Hence, from an inventory standpoint, one would like to keep both the crystal and pellet size as small as possible.

6.3.1 Diffusion of Tritium in $LiAlO_2$

The diffusion of tritium in $LiAlO_2$ can be expressed by the well known equation[33]

$$D = D_o \exp(-Q_D/RT) \qquad (6.1)$$

where

D_o = Diffusion coefficient in cm^2/sec

Q_D = Activation energy for diffusion in cal/mole

R = Gas content, 1.987 cal/mole °K

T = Temperature, °K

The determination of the tritium diffusivity in $LiAlO_2$ is essential to any study of tritium transport in a breeding material. Drs. J.R. Powell, R.H. Wiswall, and E. Wrising of BNL have tried to determine the diffusivity of tritium in several lithium compounds one of which was $LiAlO_2$.

Their experiment consisted of crushing and screening $LiAlO_2$ to an approximately uniform particle size of 150-210μ in diameter. A one-half gram sample was then exposed for one hour to a thermal neutron flux of 10^{13} n/cm^2-sec in the Brookhaven Medical Reactor. After irradiation, 250 mg was transferred to an extraction tube where the tritium was carried away by a flowing helium stream. The stream then flowed into a mixing device where one part of helium was mixed with 10 parts of P-10 counting gas (90% argon, 10% methane). Since a significant fraction of the tritium was released from $LiAlO_2$ as T_2O or HTO, an oxygen reducing step was inserted before the gas reached the counter. Tritium disentegrations were recorded on standard counting equipment that could measure instantaneous counting rates or the total number over a period of time.

The diffusion coefficient was extracted by relating the fraction of tritium released to the time, through the solution of the time dependent diffusion equation.[34]

$$\frac{\partial C}{\partial t} = D\left(\frac{\partial^2 C}{\partial r^2} + \frac{2}{r}\frac{\partial C}{\partial r}\right) \qquad (6.2)$$

For $Dt/a < 0.5$ the solution to Eq. (3.4) can be approximated by

$$f = \frac{6}{a\sqrt{\pi}} \sqrt{Dt} \qquad (6.3)$$

where

C = Tritium concentration in pellet, Ci/cm^3

D = Diffusion coefficient, $cm^2/sec.$

a = Pellet radius, $0 < r \leq a$, cm.

t = Time, sec.

f = Fraction of tritium released.

A plot of Eq. (6.2) as compared to the exact solution is presented in Fig. 6.2 which indicates good accuracy for small times. Thus, given the particle radius and the fraction removed at a given time, the diffusion coefficient can be calculated.

From the diffusion coefficient, a tritium retention time or hole up time can be calculated by solving the steady state inhomogeneous concentrat equation for a sphere.

$$D \frac{1}{r^2} \frac{\partial}{\partial r} \left(r^2 \frac{\partial C}{\partial r}\right) = -B \qquad (6.4)$$

where B = Tritium generation rate in $Ci/sec\text{-}cm^3$

with boundary conditions,

$$\frac{\partial C}{\partial r}(0) = 0$$

$$C(a) = C_a$$

The solutions to this equation is

$$C(r) = \frac{B}{6D}(a^2 - r^2) + C_a \text{ Ci/cm}^3 \qquad (6.5)$$

Integration over the volume of a sphere results in the inventory

$$I = \frac{4\pi a^5 B}{45D}$$

which can be separated into 2 terms

$$I = \left(\frac{4}{3}\pi a^3 B\right)\left(\frac{a^2}{15D}\right) \text{ Ci} \qquad (6.6)$$

where

$\frac{4}{3}\pi a^3 B$ is the tritium generation rate in Ci/sec and $\frac{a^2}{15D}$ is in units of sec and is known as the holdup time, τ.

Substitution of τ for t in Eq. (6.3) gives

$$f = \frac{6}{a\sqrt{\pi}}\sqrt{D}$$

$$f = \frac{6}{a\sqrt{\pi}}\sqrt{\frac{Da^2}{15D}}$$

$$f = \frac{6}{\sqrt{15\pi}} = .874$$

The holdup time as defined in Eq. (6.6) is the time for 87.4% of the bred tritium to diffuse out of the sphere. Results obtained from the BNL experiments are presented in Table 3.2. Performing a "once through" regression on these results yields average values of

$D_o = 3.899 \times 10^6$ cm^2/sec, and

$Q_D = 64055$ cal/mole °K

TABLE 6.2

TRITIUM DIFFUSIVITY IN $LiAlO_2$

Material	Diameter (μm)	Temperature (^{o}C)	Holdup time, τ (hrs.)	Diffusion coefficient (cm^2/sec)
$LiAlO_2$	150-200	500	500	3.0×10^{-12}
$LiAlO_2$	150-200	600	4	3.8×10^{-10}
$LiAlO_2$	120-177	650	1	1.0×10^{-9}

resulting in the following diffusion equation for $LiAlO_2$.

$$D = 3.899 \times 10^{6} \exp\left(\frac{-64055}{RT}\right) \text{ cm}^2/\text{sec} \qquad (6.7)$$

These results will be used in all subsequent calculations involving tritium transport in $LiAlO_2$.

One further point must be briefly discussed. Although this design deals with pellet radii on the order of .2 cm, experimental results are based on .0075 cm radius particles. These results do not indicate whether the particles used in the experiment are single or polycrystalline. If these particles are crystals, then the 0.2 cm pellet can be thought of as being composed of $\left(\frac{.2}{.0075}\right)^3$ single crystals. Now, since the grain boundary diffusion will most probably be much greater than the grain (solid state) diffusion, the pellet inventory will be the inventory of a single .0075 cm radius particle times the number of particles/pellet, $\left(\frac{.2}{.0075}\right)$. However, if the particles analyzed are polycrystalline, then the grain boundary diffusion has already been accounted for and the pellet inventory will be that of a 0.2 cm radius pellet. Since the inventory varies as the 5th power of the radius (see equation 6.6) and the number of particles/pellet is $\left(\frac{.2}{.0075}\right)^3$, the inventories for the 2 cases will differ by a factor of 711. This is a significant point in that it may very well determine the feasibility of gas-cooled blankets from the standpoint of tritium inventory and release.

Because the nature of this diffusion coefficient is presently unknown, both cases will be examined. Therefore, in subsequent sections, where the word particle appears in place of pellet, this will indicate that the 0.2 cm pellet is composed of $\left(\frac{.2}{.0075}\right)^3$ particles each with an inventory proportional to $(.0075)^5$ as opposed to one pellet with an inventory proportional to $(.2)^5$.

6.3.3 Tritium Transport Dynamics

In order to accurately calculate the tritium inventory of the BRSR blanket design, a computer code, TRIPORT, was written. A description of this code is given in reference [21]. It calculates the amount of time needed for the tritium concentration in the blanket material to reach steady state assuming steady state reactor operation. Then, using the steady state conditions, it calculates the tritium inventory of the blanket. Thus, the solution to the time dependent inhomogeneous differential equation for the concentration at any point along the BRSR and for any time t forms the basis of TRIPORT. This differential equation[33] is

$$\underset{1}{\frac{\partial C}{\partial t}} = \underset{2}{D \frac{1}{r^2} \frac{\partial C}{\partial r} \left(r^2 \frac{\partial C}{\partial r}\right)} + \underset{3}{B} - \underset{4}{\lambda A_c} - \underset{5}{\Lambda A_c q(r)} \qquad (6.8)$$

where

B = Tritium generation rate in Ci/cm^3 sec

λ = Decay constant for tritium, sec^{-1}

Λ = Decay constant for parent substance, (Li^6), sec^{-1}

A_c = Concentration of parent substance (Li) Ci/cm^3

$q(r)$ = Fraction of atoms formed within dr of the surface which escape.

This equation can be simplified without loss of accuracy. Term number 5 gives the loss of tritium from a sphere due to recoil. The amount of bred tritium that is lost from a 0.2 cm pellet due to recoil is less than 1.0%. Similarly, term number 4 is the tritium loss due to radioactive decay. If after 2 years, the entire steady state inventory

was assumed to be present from time t=0, the loss would be at most 10%. These two terms are neglected in the solution. The remaining equation is

$$\frac{\partial C}{\partial t} = D \frac{1}{r^2} \frac{\partial}{\partial r} \left(r^2 \frac{\partial C}{\partial r}\right) + B \qquad (6.9)$$

Substituting $u = C \cdot r$ gives

$$D \frac{\partial u}{\partial t} = \frac{\partial^2 u}{\partial r^2} + \frac{B}{D} \qquad (6.10)$$

The boundary conditions are

$u = 0$	$r = 0$	$t \geq 0$
$u = aC_a$	$r = a$	$t \geq 0$
$u = 1\ f(r)$	$0 < r < a$	$t = 0$
	$f(r) = C_o$	

This equation is the basis of TRIPORT and is most easily solved by separation of variables (Appendix E) with the final solution

$$C(r,t) = \frac{B}{6D}(a^2 - r^2) + C_a + \frac{2}{r} \sum_{n=1}^{\infty} \frac{(-1)^n}{\lambda_n} \left(C_a + \frac{B}{D\lambda_n^2}\right) e^{-D\lambda_n^2 t} \sin \lambda_n r \ \frac{Ci}{cm^3} \qquad (6.11)$$

where

$$\lambda_n = \frac{n\pi}{a}$$

$$C_a = C(a)$$

At this point it will be helpful to explain the operation of TRIPORT so that the presentation of subsequent equations and their interactions can be more easily understood.

6.3.3.1 TRIPORT Overview

Given the diffusion coefficient of tritium in $LiAlO_2$, the tritium production rate and other system parameters, TRIPORT evaluates the solution of the concentration equation for each x cm length of the breeder rod every N seconds. Figure 6.6. The time step should be chosen such that significant changes will not occur in the tritium concentration of a pellet over any one time step. A safe rule of thumb for Δt is $0.1\ a^2/(D\pi^2)$ where $D \geq .75$ times the smallest value of D over the length of the rod. The segment length should be fine enough such that the temperature and tritium production rate do not change appreciably between segments. One one-hundredth of the total length (down and back) or 2.0 cm is satisfactory.

Each time step, TRIPORT calculates the tritium concentration and release from the pellets in each segment of the rod. The tritium concentration in the coolant is then calculated for each segment. The T_2 concentration of segment J is equal to the cocentration of segment J-1 plus the amount produced in segment J minus the amount lost through the walls in the Δt necessary for the coolant to travel 1 segment.

$$C(J) = C(J-1) + PROD(J) - LOSS(J) \qquad (6.12)$$

This is done for each segment after which the concentration is converted to a partial pressure and used to calculate the boundary condition of the concentration equatio (6.10); the T_2 concentration at the boundary of the sphere, from which the T_2 solubility in $LiAlO_2$ is determined. This T_2 concentration is then used to evaluate the solution to the concentration equation in the next time step.

This entire process is performed each time step (evaluating the solution based on the boundary condition of the previous time step and updating theboundary condition for the next time step) until a convergence criteria is reached. This criteria is that the fractional change in the T_2 concentration in a pellet between two time steps,

$$\frac{C_{t+1} - C_t}{C_{t+1}} ,$$

doe not exceed 0.001. A more accurate convergence criteria is to ensure that the fractional difference between the pellet release rate at the time t and the steady state release rate,

$$\frac{\frac{\partial C}{\partial r_s} - \frac{\partial C}{\partial r_t}}{\frac{\partial C}{\partial r_s}} ,$$

is less than 0.001.

When this condition is satisfied, steady state has been reached. However, since the temperature in the rod varies from segment to segment, steady state will be reached at different times for each segment. A safe solution is to monitor a segment with a lower temperature than most of the blanket ($\sim$ 80%), as the time to reach steady state varies inversely with the temperature.

After steady state is reached, the inventory is ready to be calculated. It is calculated by integrating the tritium concentration over the volume of the pellet in each segment for the given particle/pellet size distribution as specified by the user. The inventory of each pellet is multiplied by the number of modules/reactor to arrive at a total blanket inventory. It should be noted that experiments have shown that most of the tritium released from the pellets is in the form of T_2O or HTO. This is accounted for by assuming that 90% of the tritium released from the pellets is in the form of T_2O while the balance is released as T_2.

Each of the steps described above will be analyzed below with a presentation of results of computer runs.

6.3.3.2 Analytical Treatment in TRIPORT

As discussed in Section 6.3.2, the tritium concentration at a point r in a pellet at time t is given by

$$C(r,t) = \frac{B}{6D}(a^2 - r^2) + C_a$$

$$+ \frac{2}{r} \sum_{n=1}^{\infty} \frac{(-1)^n}{\lambda_n} \left(C_a + \frac{B}{D\lambda_n^2}\right) e^{-D\lambda_n^2 t} \sin \lambda_n r \ \frac{Ci}{cm^3} \qquad (6.11)$$

The release of tritium from the sphere is calculated by multiplying D times the derivative of C(r,t) at the pellet/particle boundary r=a, giving

$$D \left.\frac{\partial C}{\partial r}\right|_{\substack{r=a \\ t=t}} = J_f = D\left[-\frac{aB}{3D} + \frac{2}{3} \sum_{n=1}^{\infty} \left(C_a + \frac{B}{D\lambda_n^2}\right) e^{-D\lambda_n^2 t}\right] Ci/cm^2\text{-sec} \qquad (6.12)$$

Multiplying by the pellet surface area, A cm^2, the number of pellets/cm^3 in the rod and dividing by the void fraction gives the Ci/cm^3-sec released into the coolant stream per segment. Next, multiplying by the segment length and dividing by the coolant velocity gives the concentration in Ci/cm^3 added to the segment in t sec.

$$CC = \frac{(NP)AD}{VF} \frac{\ell}{V} \ J_f \ Ci/cm^3 \qquad (6.13)$$

where

CC = Tritium concentration added to coolant, Ci/cm^3.

NP = Number of pellets/cm^3.

VF = Rod void fraction.

ℓ = Segment length, cm.

v = Coolant velocity, cm/sec.

The corresponding pressure in torr is

$$P(torr) = 1.065(CC\ C_i/cm^3)T(°K) \qquad (6.14)$$

$$P(atm) = P(torr)/760.0$$

From this pressure, the solubility of tritium in $LiAlO_2$ in Ci/cm^3 can be calculated from[41]

$$S = SO \exp(-Q_s/RT)\sqrt{P(atm)} \qquad (6.15)$$

where

S = Solubility of tritium in $LiAlO_2$ in Ci/cm^3.

SO = Solubility coefficient, $Ci/cm^3\text{-}atm^{1/2}$.

Q_s = Activation energy in cal/mole °K.

Similarly, the permeation of tritium through the module walls can be calculated by[41]

$$PF = \frac{PO(\sqrt{P_1} - \sqrt{P_2})WA}{d} \exp(-Q_p/RT) \qquad (6.16)$$

where

PF = Tritium permeation in Ci/sec.

PO = Permeation coefficient in Ci mm/cm^2-sec-$atm^{1/2}$.

P_1 = T_2 Pressure inside module, atm.

P_2 = T_2 Pressure outside module, atm.

WA = Wall area of segment, cm^2.

d = Wall thickness, mm.

Q_p = Activation energy for permeation, cal/mole °K.

Finally, the inventory can be calculated based on a specified particle/pellet size distribution. The options available are the uniform size distribution, the gaussian distribution and the log normal distribution, included due to the frequency with which sieved particles fit this type of distribution. The inventory distribution for each distribution will be briefly explained below.

The inventory calculation for the uniform pellet/particle size distribution is simply the integral over the volume of the pellet resulting in a segment inventory of

$$I_j = \frac{4}{3}\pi a^3\left(\frac{B_j a^2}{15D_j} + C_{a_j}\right)NP \quad \text{curies} \tag{6.17}$$

and a module inventory of $I_M = \sum_{j=1}^{100} I_j$

The inventory for a segment containing particles/pellets that fit a gaussian distribution is more complicated. The gaussian distribution can be described as[35]

$$G(r) = H_g \exp\left[-h^2(r - r_m)^2\right] \tag{6.18}$$

where

$$H_g = \frac{2h}{\sqrt{\pi}}\left[1 + \text{erf}\,(hr_m)\right]^{-1}$$

and h is related to the standard deviation σ, by

$$\sigma^2 = \overline{(r - r_m)^2} = \int_o^\infty (r - r_m)G(r)dr = \frac{1}{h^2\sqrt{\pi}}\left[\frac{\sqrt{\pi}}{2} - \frac{hr_m \exp\,(-h^2r_m^2)}{1 + \text{erf}\,(hr_m)}\right] \tag{6.19}$$

Table 6.3 provides an easy determination of h given σ and r_m. Based on this, the inventory is given as

$$I_j = \int_o^\infty G(r)\left[\frac{4}{3}\pi r^3\left(\frac{B_j r^2}{15D_j} + C_{a_j}\right)\right]dr \tag{6.20}$$

$$= \frac{2h}{\sqrt{\pi}[1+\text{erf}(hr_m)]}\left\{\frac{4}{45}\frac{\pi B_j}{D_j}\int_o^\infty r^5 \exp\left[-h^2(r-r_m)^2\right]dr\right.$$

$$\left. + \frac{4}{3}\pi C_a \int_o^\infty r^3 \exp\left[-h^2(r-r_m)^2\right]dr\right\}NP \tag{6.21}$$

with $I_M = \sum_{n=1}^{100} I_j$

TABLE 6.3

COMPUTATIONAL PARAMETERS FOR THE GAUSSIAN DISTRIBUTION*

σ/r_m	hr_m
0.10	14.1421
0.20	7.0711
0.30	2.6316
0.40	1.7227
0.50	1.3145
0.60	1.0459
0.70	0.8698
0.80	0.7490
0.90	0.6611
1.00	0.5939

*ref. 35

Finally, the inventory for a segment containing pellets/particles that fit a log normal distribution can be described as follows. If σ is the standard deviation of the distribution and ξ the mean radius, the particle size distribution is given as[35]

$$LN(r) = \frac{1}{\sigma_{LN}\sqrt{2}\,\pi}\,\frac{1}{r}\,\exp\left\{\frac{-[\ell n(r/\xi_{LN})]^2}{2\sigma_{LN}^2}\right\} \qquad (6.22)$$

where

$$\sigma_{LN} = \log\,(\sigma/\xi)^2 + 1$$
$$\xi_{LN} = \xi\,\exp\,(-\sigma_{LN}^2/2)$$

are the logarithmic transformations of σ and ξ respectively. Now, the segment inventory is given by

$$I_j = \int_o^\infty LN(r)\left[\frac{4}{3}\,\pi r^3\left(\frac{B_j r^2}{15D_j} + C_{a_j}\right)\right]dr \qquad (6.20)$$

$$= \frac{1}{\sigma_{LN}\sqrt{2}\,\pi}\left[\frac{4}{45}\,\frac{\pi B_j}{D_j}\int_o^\infty r^4\,\exp\left\{\frac{-[\ell n(r/\xi_{LN})]^2}{2\sigma_{LN}^2}\right\}dr\right.$$

$$\left. + \frac{4}{3}\,\pi C_{a_j}\int_o^\infty r^2\,\exp\left\{\frac{-[\ell n(r/\xi_{LN})]^2}{2\sigma_{LN}^2}\right\}dr\right]NP \qquad (6.23)$$

with $I_M = \sum_{j=1}^{100} I_j$

Two important points should be noted. First, the tritium generation rates used in TRIPORT are based on the output from ANISN.

Second, the diffusivities in a pellet were assumed to be constant across the pellet diameter. This is a valid assumption as the temperature gradient across a 0.4 cm diameter pellet is expected to be quite flat. The temperature profile in a sphere is given by

$$T = T_s + \frac{q'''}{6k}(a^2 - r^2) \qquad (6.24)$$

where

T_s = Pellet temperature at surface, °C

q''' = Heat generation rate, w/cm^3

k = Thermal conductivity of pellet, w/cm°C

Therefore, the maximum ΔT occurs between the pellet surface and center r=0.

$$\Delta T = \frac{q'''}{6k} a^2 \qquad (6.25)$$

Calculations indicate that the maximum heat generation rate in $LiAlO_2$ will occur at the plasma end of the module and will be approximately 4.0 w/cm^3 [21]. Now, since the thermal conductivity of $LiAlO_2$ is unknown, an estimate must be made. Based on the thermal conductivities of alumina (Al_2O_3) and lithia (Li_2O), a reasonable estimate of k is 0.04 w/cm°C[36]. This conductivity coincides with that of UO_2 and will probably represent a conservative estimate on which calculation can be based. Results for ΔT pellet vs pellet radius are presented in Figure 6.4.

6.3.4 TRIPORT Results on Tritium Inventory

In calculating the tritium inventory for the BRSR design, the first interesting result noted was that in all computer runs with uniform 0.2 cm radius pellets, steady state was reached only when the temperature profile

ranged from 600 - 900°C. All runs with module temperature profiles of lower magnitude did not converge in 10^8 seconds or 3.2 years (64% of the life of the module). This slow transient is not unreasonable judging from the extremely low tritium generation rates. Nevertheless all parameters were well stabilized and slowly changing by 10^8 seconds so that a steady state inventory calculation based on these parameters remained valid.

This finding, however, indicates that the calculated steady state inventories can grossly overestimate the actual inventory if the steady state condition is not reached in the lifetime of the module. For the 0.2 cm radius pellet composed of uniform 0.0075 cm radius particles, the steady state will have been reached by the 5 yr. module lifetime in all cases except the one where the temperature profile ranges from 300-600°C. These results are presented in detail later but are alluded to here to caution against the use of steady state calculations when this condition may in fact never be reached. All parametric calculations were performed at temperatures at which steady state will be reached within one year of operation. An example of the inventory profile along the breeder rod is given in Figure 6.5 for a module consisting of uniform 0.2 cm radius pellets and a coolant profile shape as given in Figure 6.3 for H = .018 and inner to outer routing but with an inlet temperature of 500°C and ΔT = 300°C. This is for the design with BeO at the plasma end of the rod as can be noted by the low tritium inventory between 95-100 c Also note the higher inventory in the inner cylinder where the helium temperature is much lower, Figure 6.7.

6.3.4 Reference Design Results

The inventory calculated for the uniform 0.2 cm radius pellets under steady state conditions for the initial reference design (T_{in} = 300°C, ΔT = 300°C, P = 700 psia) is 6.99 x 10^{12} Ci. However, after 5 years, only a maximum of 2 x 10^{8} curies will be produced and is therefore the maximum possible inventory for the blanket. For the particulate pellet, the 5 year inventory accumulation will similarly be about 2 x 10^{8} curies while 9.88 x 10^{9} curies will be present at steady state. Therefore, both values clearly exceed 5 kg (5 x 10^{7} Ci) limit and render this temperature profile impractical from the standpoint of tritium inventory.

Since diffusion is such a strong function of temperature (see Eq. 6.7) an increase in the temperature level with constant profile shape will decrease the inventory. In order to determine what temperature level is needed to keep the inventory within the limit, a series of computer runs was made in which the temperature level was raised but the profile shape remained constant.

6.3.4.1 Temperature Level Variations

The temperature level was increased in magnitude in units of 100°C to a maximum increase of 300°C while keeping the profile constant. Figure 6.6 gives an illustration of the reference design (T = 300-600°C) temperature profile while Table 6.4 presents the effect of increasing the temperature level and Fig. 6.7 illustrates the temperature effect on the steady state inventory. In Table 6.4, columns 2 and 4 give the calculated steady state inventories while columns 3 and 5 give the probable inventories after 5 years of operation. As is evident from this table, a 200°C inlet

TABLE 6.4

EFFECT OF TEMPERATURE ON BLANKET INVENTORY

Temperature range (°C)	Uniform pellets, 0.2 cm radius			Uniform particles 0.0075 cm radius		
	Steady state inventory (Ci)	Time to reach steady state	5 year inventory (Ci)	Steady state inventory (Ci)	Time to reach steady state	5 year inventory (Ci)
Reference design 300-600	6.99×10^{12}	>1000 yr	2.0×10^{8}	9.88×10^{9}	>10 yr	2.0×10^{8}
400-700	3.62×10^{10}	190 yrs	2.0×10^{8}	5.14×10^{6}	116 day	5.14×10^{6}
500-800	1.62×10^{7}	3.5 yrs	1.62×10^{7}	2.5×10^{5}	3.9 day	2.5×10^{5}
600-900	2.86×10^{5}	45 days	2.86×10^{5}	6.5×10^{3}	2.5 hrs	6.5×10^{3}

temperature increase is necessary to keep the inventory of a blanket containing uniform 0.2 cm radius pellets below 5 kg (5×10^7 Ci) limit while a temperature increase of only 100°C is needed for the uniform 0.0075 cm radius particulate pellets. The results of varying the type of particle size distribution are presented in the following section.

6.3.4.2 Particle Size Distribution Variation

The particle size distribution can be specified as uniform, gaussian or log normal as illustrated in Figure 6.8. The effect of varying the type of pellet or particle size distribution for the 600-900°C temperature range is presented in Table 6.5 for a mean pellet radius of 0.2 cm and a mean particle radius of 0.0075 cm for T/rm (coefficient of variance) of .5.

This table shows that the inventory is greatest for the log normal distribution and smallest for the uniform distribution. Physically, this occurs because the smaller particles release the gas quickly and do not build up large inventories. However, these smaller particles represent only a small fraction of the total mass while the fewer large particles account for the balance and retain tritium to the extent that it over compensates for the small particles' quick release, resulting in an increased inventory. Thus to minimize the inventory it is desirable to use uniform size particles or a size distribution with a strict upper limiting size.

6.3.4.3 Solubility and Permeability Effect

The coolant temperature will have a direct bearing on the solubility of T_2 in $LiAlO_2$ and its permeability through the module walls. As the

TABLE 6.5

EFFECT OF PELLET/PARTICLE SIZE DISTRIBUTION ON BLANKET INVENTORY [1]

For 600-900°C range and $\sigma / r_m = .5$

Size distribution	Inventory (Ci) Mean pellet radius = 0.2 cm	Inventory (Ci) Mean particle radius = 0.0075 cm
Uniform	2.85×10^5	2.21×10^3
Gaussian	1.40×10^6	5.36×10^3
Log normal	2.04×10^6	6.24×10^3

coolant temperature rises, the percentage of the total tritium inventory that is dissolved in the $LiAlO_2$ increases. Further, tritium solubility increases with the square root of the T_2 partial pressure in the helium. Thus, two effects, temperature and pressure influence solubility.

The temperature distributions are well established while the T_2 partial pressure profile in the coolant is highly questionable. This arises from the extremely high permeability of niobium, the principal reference design material. Calculations (Appendix C) show that even for a fast moving helium stream (150 cm/sec), the tritium in the form of T_2 will permeate through the module walls faster than it can be generated. Thus, assuming the inner cylinder is not permeable, and the T_2 concentration is building up as the helium flows through this cylinder, a T_2 concentration equivalent to 10^{-4} Torr will permeate the walls of the outer cylinder (which separates the coolant from the vacuum) in the first .03 cm of exposed wall. This means that all the tritium will be lost to the vacuum surrounding the modules.

This calculation was performed assuming a vacuum outside the modules. However, Fraas has shown that this "vacuum" may contain a T_2 concentration as high as 10^{-6} to 10^{-5} Torr[4]. Assuming 10^{-5} Torr, the T_2 concentration will equalize with that outside the module instantly upon reaching the exposed wall. Although this treatment of permeation may have far reaching consequences for fusion reactor aspects such as heat exchanger design, the discussion at hand will be confined to the effect on solubility.

TABLE 6.6

TRITIUM SOLUBILITY AS A FUNCTION OF PRESSURE
For 600-900°C range

Pellet/particle radius (cm)	Solubility (Ci/cm^3)		% inventory due to solubility
	P = 0.0 torr	P = 10^{-5} torr	
Uniform pellets r = 0.2 cm	1.95×10^{8}	1.97×10^{8}	1.0
Uniform particles r = 0.0075 cm	3.61×10^{4}	1.89×10^{5}	81.0

If one compares the 2 cases; that with the outer annulus having a T_2 partial pressure of 0.0 and then 10^{-5} Torr in a module with the temperature ranging from 600°C-900°C, the solubility will behave as displayed in Table 6.6. Thus as explained earlier, the smaller particle size and higher T_2 partial pressure combine to greatly increase the inventory due to solubility in high temperature ranges. If structural considerations, however limit the maximum temperatures to approximately 600°C, the contribution to the inventory from solubility should not be significant.

6.3.4.4 Summary of Results

Pellet shape has not been considered since its effect on inventory will be minimal. However, since the sphere has the smallest surface to volume ratio, it is evident that decreasing the sphericity will decrease the inventory.

From the preceeding discussion, certain brief generalizations about tritium inventory can be made. First, the smaller the particle, the lower the inventory. Second, higher temperatures reduce the inventory. Third, uniform particle size minimizes the inventory. Last, lowering the T_2 partial pressure will lower the inventory. Table 6.7 summarizes these results. The effect on a design window will be discussed in Chapter 9.

6.4 TRITIUM RECOVERY

Several recovery schemes are possible for the recovery of tritium from the helium stream. Since most of the tritium is present as T_2O or HTO the proposed schemes will be structured toward handling such a case. Two schemes are outlined briefly below.

6.4.1 CuO Bed with a Desiccant

The easiest way to remove T_2O or HT) from a flowing helium stream is with a desiccant or molecular sieve. A fraction of the circulating helium stream (1-10%) can be diverted on each pass. The T_2 or HT present in the stream can be transformed to water by passing it through a CuO bed. Now, with all the tritium in the form of water, a desiccant or molecular sieve can be used most efficiently to remove the tritiated water from the helium stream.

6.4.2 Metal Window with a Desiccant

In place of a CuO bed, the residual T_2 or HT can be removed by a metal window consisting of a highly permeable metal such as vanadium or niobium. After permeation of the T_2 or HT through the metal window, the T_2O or HTO in the helium stream can be removed with a desiccant or molecular sieve. These recovery schemes appear to be most applicable to this type of blanket design. The next section will present a discussion on the breeding capability of the BRSR design.

TABLE 6.7

SUMMARY OF FACTORS AFFECTING TRITIUM INVENTORY IN $LiAlO_2$

Direction of change	Characteristic	Effect on inventory
Decrease	Pellet size	Decrease
Increase	Temperature	Decrease
Increase	Pellet size uniformity	Decrease
Decrease	T_2 partial pressure	Decrease

CHAPTER 7

BREEDING CAPABILITY OF THE BRSR DESIGN

As discussed previously the BRSR design will be considered potentially feasible if a gross breeding ratio of 1.15 can be demonstrated.

Since the quest for a blanket design with the ability to breed may lead to drastic changes in the base reference design, certain ground rules must be obeyed to ensure a final working design. These rules are simply that any altered design must satisfy the limits or constraints in a "first-cut" analysis imposed by the thermal/hydraulic, material strength and compatability, and tritium transport design considerations. Although the purpose of this chapter is to assess the breeding capability of the BRSR design and to perform alterations necessary to achieve breeding, it is unrealistic to ignore the effect such alterations may have on the overall feasibility and success of the blanket design. Hence, all designs presented in the following section will address this concern.

7.1 METHOD OF BREEDING RATIO CALCULATION

Early in the planning stages of a neutronic calculation, it was decided to attack the problem using a one dimensional neutronics code for reasons such as cost, time, availability of expertise and above all, the primitive stage of the design. The code selected was ANISN, a one dimensional, multigroup code that solves the neutron transport equation in slab, cylindrical or spherical geometry using the S_N method.

A glance at Figure 7.1 will immediately illustrate the problem with using a 1-D code on such an inherently three-dimensional design. ANISN, like any other 1-D code is quite valid when applied to problems with different material zones whose boundaries are parallel to the symmetry axis of the neutron source. As is evident from Fig. 7.1a, the material boundaries lie in a direction perpendicular to the symmetry axis of the plasma. Furthermore, Figures 7.1a and b show that the carbon shims vary in thickness in both the θ and ϕ directions. Hence, the BRSR design is not well suited to a 1-D calculation. Hopefully, using the homogenization technique, fairly accurate results can be obtained for a "first-cut" analysis.

7.1.1 Alternative Neutronic Treatments of the BRSR Design

There exists two basic options of handling an ANISN calculation of the BRSR design. The most attractive alternative would be to create a line source down the center of the breeder rod so that all material zones vary in the correct direction. This method has several drawbacks, most important of which is the generation of such a source. A line source must be generated from a point source and therefore cannot be more accurate than a calculation based on a point source. The point source generation is the second alternative.

The option selected will treat the plasma as a point source and account for the effect of the structure and carbon by homogenization. This treatment results in a design as pictured in Figu. 7.2. Homogenization is a common practice and will be used in determining the breeding ratio of BRSR designs. The following section will describe the process.

7.1.2 The Homogenization Technique

The homogenization process as detailed in reference [34] consists of taking the carbon shims, the niobium structure and the breeding material and homogenizing them uniformly along the blanket cross-section and as a function of blanket thickness. The solution to the transport equation is carried out in slab geometry (as the curvature of the torus wall is insignificant in a single rod and shim combination) with an isotropic neutron flux impinging on the face of the breeder rod. This treatment will account for variations in material in the r direction and will yield a neutron flux as a function of depth which can then be used for a single cell calculation as previously described. However, the consequences of homogenization must be considered.

First, in homogenizing the niobium, the probability of neutron capture by the $Nb^{93}(n,\gamma)Nb^{94}$ reaction is altered. The reason for this is that whereas a neutron may travel one or more mean free paths (mfp) in the breeder material alone without encountering the niobium structure, homogenization has insured that in every mfp, a neutron has a probability of being captured. In effect, homogenization results in a change from a high macroscopic capture cross section ($\Sigma_{a_{Nb}}$) in a discretized volume to a low macroscopic capture cross section over the entire rod volume. The same is true for the carbon shim. However, the neutron capture cross section

is small enough that it will probably not affect the results. The homogenization of the carbon may, however, alter the neutron energy spectrum due to its strong moderation.

Thus, homogenization will affect the results, and although it is hard to determine in what direction the effect will be, it appears that a 1-D calculation may tend to under-estimate the breeding ratio. This same prediction was made by the UWMAK-II group when in fact a 3-D calculation resulted in a drop from 1.18 to 1.06[3]. This effect was due to an underestimation of the amount of structural material present, differing material compositions, and neutron leakage. For the same material composition the 3-D calculation gave a BR less than one. Based on the UWMAK-II results the 1-D calculated breeding ratios will be considered as an upper bound, but a 3-D calculation would be desirable.

7.2 BREEDING CALCULATION RESULTS

Several blanket designs were tested for their breeding ability in the hope of finding a design that will breed and comply with the requirements set forth earlier in this chapter. The designs will be presented in the order they were conceived so as to show the progressive elimination of possible alterations that may enhance breeding. Each design will be illustrated by a schematic showing the material compositions and locations in the rod, followed by the results of the ANISN S_8P_3 run which will include the important breeding, multiplication and absorption reaction. This will be followed by a discussion of the results and a consideration of the effects any alterations may have on other design aspects. Finally, alterations to the design will be suggested.

7.2.1 Neutronic Reference Design 1

A schematic representation of the initial reference design is presented in Figure 7.2. Table 7.1 gives the results of the breeding, neutron multiplication, and parasitic absorption reactions occuring in the blanket. From these results, it is evident that there are three basic problems with the design. First, the Li^6 number density is too low. This can be seen from the successful competition for neutrons by the niobium (n,γ) reaction. A blanket enriched in Li^6 would raise the macroscopic cross section and thus reduce the parasitic effect of niobium. This problem can also be identified by comparing the ratio of the Li^7 to the Li^6 breeding reaction (.10), despite the large number density ratio advantage of Li^7 over Li^6 (12.33). Hence for this particular energy spectrum, the Li^6 reaction is more fruitful.

Second, there are simply not enough neutrons to breed. The low multiplication of this blanket makes breeding impossible with parasitic absorptions such as in niobium, indicating the need for a multiplying material.

Finally, the 5 cm graphite layer on the front face of the rod is degrading the neutron spectrum to a degree such that the Li^7 $(n, n\text{-}\alpha)t$ and Nb^{93} $(n, 2n)Nb^{92}$ threshold reactions are of little value. Removal of the shield would greatly enhance these reactions.

7.2.2 Neutronic Reference Design 2

The schematic of design 2 is presented in Figure 7.3 with the results of the ANISN run appearing in Table 7.2. The changes over the reference design consist of enriching the Li in $LiAlO_2$ to 90% Li^6, and adding a neutron multiplier in the form of 5 cm of beryllium oxide (BeO) pellets in the front of the module followed by one cm of alumina (Al_2O_3) pellets. The breeding problem with this blanket appears to be due to the effect of the 5 cm graphite shield. This graphite layer may account for the low neutron multiplication in the beryllium and hence the low breeding ratio of only 0.684. Thus, the recommended alteration would be to remove the graphite shield.

Concerning the other design aspects, materials compatibility may become a problem if not accounted for. Beryllium oxide (BeO) may tend to leach out Li from $LiAlO_2$. Thus, in order to reduce this reaction, a buffer layer of 1 cm of alumina pellets was placed between the BeO and $LiAlO_2$ pellets. Alumina is one of the most stable oxides known, with a heat of formation of -399 kcal/mole. A more efficient buffering technique may be to coat the BeO pellets with an inert material such as siliceous glass. Other than this concern, BeO is a stable compound with a very safe melting point of 2530°C.

7.2.3 Neutronic Reference Design 3

The schematic representation of NRD3 is shown in Figure 7.4 with the results of the ANISN run presented in Table 7.3. This design differs from NRD2 only by the removal of the 5 cm graphite shield. The results show that although the carbon was reducing the neutron multiplication of beryllium and niobium by about a factor of 2, the neutron mutliplication

is still too low to facilitate breeding. The answer to this problem is to increase the beryllium number density or change the breeding material. Before this is discussed, the effect of the alteration on other design aspects will be evaluated.

The consequence of removing the graphite shield is that the niobium now must absorb the full impact of the plasma heat load and neutron load. This will lead to sputtering of high z material, higher helium and hydrogen production rates, afterheat, induced activity and biological hazard potential, all of which are undesirable.

In addition if 316 SS is to be used, a minimum graphite shield thickness of approximately one cm is required to keep the first wall temperature of the failed and operating modules within design limits.

Returning to the problem of increasing the neturon multiplication there exists at least two possible ways in which this can be done. The first option is to extend the BeO layer for another 5 cm or so to increase the number density. This suggestion will probably not work based on the follwoing argument. From the figure given in Table 7.2, if 5 cm of BeO yields only .1 extra neutron and the breeding ratio is .77, then in order to raise the breeding ratio above 1.0, one would need about .3 more neutrons or a BeO thickness of 20 cm. Now, since the Be^9 (n,2n) 2α reaction is a threshold reaction it is important that the beryllium be "up front" in the module to capture the uncollided neutrons. Therefore, it is unlikely that a BeO thickness of greater than 10 to 12 cm will be effective in neutron multiplication.

The second possible alternative is to replace the graphite shield with a beryllium carbide (Be_2C) shield. This shield would have two advantages over BeO pellets. First, it is completely unscreened and will efficiently utilize the high energy neutrons. Second, it has over four times the beryllium number density of BeO in the module. Since the module is only 64% breeding material and the BRSR cell is 43% breeder rod, this means that the number density of a Be_2C shield is 1/(.64)(.43) or 3.6 times as great as 5 cm of BeO pellets. Adjusting this figure for both the beryllium number in the molecule and the densities gives a number density ratio of 4.56:1. This idea will be investigated in the next section.

7.2.4 Neutronic References Design 4

The schematic of NRD4 is given in Figure 7.5 and the results are presented in Table 7.4 along with a comparison of the UWMAK-II design. The difference between this design, NRD4, and NRD3 is the use of a 5 cm Be_2C shield in place of the graphite shield and BeO pellets, and the addition of 5 cm of $LiAlO_3$ pellets in the front of the module containing natural lithium. As is evident, this blanket will breed in excess of the previously stated breeding requirement of 1.15. The key to such successful breeding was the increased beryllium number density at the front of the module (as in the UWMAK-II design) whose effect is illustrated in the neutron multipli-

Consideration of other design aspects include the amount of beryllium used and the behavior of the Be_2C shield. The beryllium us ed in this desi- amounts to 8 tons or 1/5 that of the UWMAK-II requirement. Although this is a significant amount of beryllium, it is not unreasonable for a test reactor

The beryllium carbide shield is of greater concern. It has been found that Be_2C shows little resistance to thermal cracking. Experiments have revealed that Be_2C will crack when cycled 4 times between 1475 and 2000°C[37]. Although the loss of structural integrity could be compensated by blanketing the shield with a layer of graphite cloth, the thermal conductivity makes this design completely impractical. Beryllium carbide has a thermal conductivity of about 0.2 w/cm°C at 1500°C as compared with .7 w/cm°C for graphite.[36] A thermal analysis indicates that no amount of Be_2C would be able to keep the niobium wall temperature below its limit during off normal operation. Therefore, this design will be removed from consideration. The next option remaining is to pack Be_2C or BeO pellets inside the module.

7.2.5 Neutronic Reference Design 5 —

This design consists of a one cm graphite shield followed by the first wall and varying thicknesses of a Be_2C pellet zone. BeO could have been used just as well, but Be_2C was chosen due to its number density advantage (1.27) and the low absorption cross section of graphite. Fig. 7.6 shows the schematic of this design. The only materials problem with Be_2C is that it is reduced by water forming BeO and methane at low temperatures and corroded by oxygen and nitrogen at high temperatures. Since this is a concern with the T_2O and HTO release from $LiAlO_2$ and impurities in the coolant stream, the pellets can be coated with a thin layer of siliceous glass which is effective in reducing corrosion.[38]

To test this last option, a computer run was made with a 20 cm region of Be_2C resulting in a breeding ratio of .6265, neutron multiplicati of 1.3203, and parasitic absorptions of .6455. The reason for the extremel low breeding ratio is due to the presence of a high threshold reaction material, Be, a strong moderator, C and an absorber, Nb in the neutron multiplication zone. In effect, the Be was producing neutrons and the C wa moderating others for capture by the Nb before they could reach the fertile ($LiAlO_2$) zone. A reduction in the Be_2C zone thickness to 10 cm resulted in a breeding ratio of .7641, neutron multiplication of 1.2574 and parasitic absorptions of .4550. This is a definite improvement, but far from the required 1.15.

The last remaining alteration is the carbon shim rod content of the blanket (57% for reference design). This content could theoretically be reduced to 21% of the blanket. Several runs were made to test out the effect of a reduced carbon content with a 10 cm thick zone of Be_2C pellets. A summary of these results appears in Table 7.5 and Figure 7.7.

Next, the Be_2C region thickness was varied from 15 cm to 3 cm for the 21% carbon content case as given in Table 7.6 and Figure 7.8. To find the optimum Be_2C thickness as is evident from these tables and figures, the optimum carbon content is the minimum content while the optimum Be_2C thickness is 5 cm. However, the best breeding ratio attained (.91) is still .24 away from a neutronically feasible design of 1.15. Thus, the probability of breeding with a neutron multiplier inside the module appears dim.

TABLE 7.5

NEUTRONIC SUMMARY FOR VARYING BLANKET CARBON CONTENT*

Carbon % of blanket	Breeding ratio	Neutron multiplication	Parasitic absorptions
57	.7641	1.2574	.4550
27	.8355	1.4193	.5263
21	.8549	1.4787	.5598

* Be_2C pellet zone thickness = 10 cm.

TABLE 7.6

NEUTRONIC SUMMARY FOR VARYING Be_2C ZONE THICKNESS*

Be_2C thickness (cm)	Breeding ratio	Neutron multiplication	Parasitic absorptions
15	.7398	1.5455	.7341
10	.8549	1.4787	.5598
5	.9100	1.3706	.4045
3	.9037	1.3077	.4032

*Carbon content of blanket = 21%, corresponding to a hexagonal close packing rather than a rectangular array

7.2.6 Neutronic Reference Design 6

The final neutronic configuration considered was substituting a BeO shield for the carbon shield as done in reference design 4 with Be_2C. The motivation for using BeO is that the thermal conductivity is much higher at the lower range of temperatures encountered then for Be_2C. At 900°K for example the BeO thermal conductivity is .57 watt $cm^{-1}K^{-1}$ but is highly nonlinear, falling to .18 watts $cm^{-1}K^{-1}$ at 1700°K. The breeding ratio results were similar to case four although slightly lower. Figure 7.9 shows the calculated breeding ratio versus thickness of the BeO shield. For a breeding ratio of 1.15 a thickness of 6.3 cm is required.

The use of BeO as a shield still presents serious difficulties. One study [4] indicates that a BeO shield would be limited to a projected lifetime of .7 Mw-yr/m^2 and would, therefore, require frequent changing. In addition, the ability of BeO to withstand thermal stresses appears to be poor. The study defines, a quantity R' called the thermal stress resistance parameter as[4]

$$R' = \frac{S_t(1-\mu)k}{\alpha E}$$

Where S_t is the tensile strength, μ is Poisson's ratio, α is the coefficient of linear thermal expansion, E is Young's modules and k the thermal conductivity. It is a measure of the material strength relative to the thermal stress. For carbon at 1500°C R' = 250 w/cm while for BeO it equals 1 w/cm.

It appears unlikely therefore that BeO would make an acceptable shield particularly under off-normal conditions.

7.2.7 Effects of Structure and Void Fraction

All of the preceeding results were for a fixed void fraciton within the breeder rod and fraction of structural material. Since no configuration was found that met all the constraints it was decided to pick one geometry for the remainder of the report and investigate the effects of different operating conditions. Consistant with the thermal analysis a close packed rectangular array was assumed giving a carbon content of 31% and a configuration otherwise the same as reference design 5. For this case, however, the breeding ratio was calculated for 2 fractions of structural material to allow for different system pressures and also for three void fractions. The first case was for a 2 mm thick wall with 5.62% Nb and the second for a 4 mm thick wall with 11.7% Nb. The results are shown in Figure 7.10. It can be seen that the breeding ratio is much more sensitive to the amount of Nb than to small changes in the void fraction. The results are tabulated below and shown in Figure 7.10.

% Nb.	Void Fraction	Breeding Ratio
5.62	.32	.8971
5.62	.36	.8843
5.62	.40	.8705
11.69	.36	.7203

CHAPTER 8

STRUCTURAL CONSIDERATIONS

8.1 STRESS CALCULATION

A simple first order calculation of the stresses in the breeder rods was done neglecting edge effects and stresses due to mechanical attachment of the graphite shield. The pressure stress was taken to be simple hoop stress on the side walls and the thermal stress on the side walls was considered small enough to be neglected. The maximum tangential tension occurs at the inside surface and is given by

$$\sigma_{PS} = P_i \frac{r_o^2 + r_i^2}{r_o^2 - r_i^2} \qquad (8.1)$$

where P_i is the internal pressure and r_o and r_i are the outside and inside module radius respectively.

The first wall facing the plasma was assumed to be a spherical cap and the maximum stress again occurs at the inside surface but in this case it is the sum of the pressure stress and the thermal stress. The thermal stress was taken as that generated in a flat plate. The two components are both tensile on the inner surface and are given by:

$$\sigma_{Pf} = \frac{P_i}{2} \frac{2r_i^3 + r_o^3}{r_o^3 - r_i^3} \qquad (8.3)$$

$$\sigma_{\text{thermal f}} = \frac{\alpha}{2} \frac{E}{k(1-\nu)} \left(W_s t + \frac{W_m}{2} t^2\right) \qquad (8.3)$$

where

α = coefficient of thermal linear expansion

E = Young's modulus

k = Thermal conductivity

ν = Poisson's Ratio

W_S = Surface energy flux incident on metal cap

W_n = Volume energy generation rate

t = thickness of the plate

Subscripts

f = first wall

s = side wall

The stresses for both 316 SS and Nb-1Zr were calculated. The physical constants used were:

TABLE 8.1

	316 SS	Nb-1Zr
E	2.90×10^6 psi	15.2×10^6 psi
α	17×10^{-6} in/in°C	8.3×10^{-6} (in/in°C) at 500°C
k	.2 w/cm°C	.544 watts/cm°C
ν	.28	.38
W_n	4.5 w/cm^3	3.16 w/cm^3
W_s*	20 w/cm^2	20 w/cm^2

The volume heating rate for Nz-1Zr was the value calculated previously (3.6 w/cm) and for 316 SS the heating was assumed to be 30% higher based on the result of William et al[39] who calculated a heating rate 31% lower in a niobium first wall than a 304 SS first wall.

For r_i fixed at 3.8 cm and wall thickness (t) varying, the first wall and side wall stresses are shown in Figures 8.1 and 8.2. The high thermal stresses in 316 SS causes the curves to have a minimum and

*for an initial evaluation the surface flux is taken as that incident on the graphite shield. For thick shields the energy generated in the shield should be included.

restricts the use of 316 SS to thin thicknesses. The thermal stresses on Nb-1Zr are much smaller and the limiting stresses are the cylindrical wall hoop stress rather than the first wall total stress.

The design approach taken was to fix the stress σ then find the relationship between pressure, module radius and wall thickness. To minimize the amount of structural material and therefore help the breeding ratio it was decided to design to a stress of 10,000 psi for both 316 SS and Nb-1Zr. This was considered the highest allowable stress. It was also assumed that to ease fabrication both the side wall and the first wall would be the same thickness.

For 316 SS the highest stress occurs at the first wall and exhibits a sharp minimum when plotted against thickness as previously mentioned. It is highly desirable to operate at this minimum. This condition along with a fixed stress, heating rates, and a given wall thickness then determine the module size as a function of pressure.

We have the conditions:

$$\sigma_f = \sigma_{Pf} + \sigma_{tf} = 10^4 \text{ psi} \qquad (8.4)$$

$$\frac{\partial \sigma}{\partial t} = 0 \qquad (8.5)$$

where

$$\sigma_f = \frac{P_i}{2}\left(\frac{2r_i^3 + r_o^3}{r_o^3 - r_i^3}\right) + At + Bt^2$$

$$A = \frac{\alpha}{2}\frac{E}{k(1-\nu)} W_s \qquad B = \frac{\alpha}{2}\frac{E}{k(1-\nu)}\frac{W_n}{2} \qquad r_o - r_i = t$$

8.5 reduces to

$$-\frac{9r_i^2 r_o^3}{(r_o^3 - r_i^3)^2} + \frac{2A}{P_i} + \frac{4Bt}{P_i} = 0$$

or expanding this

$$r_o^2 - 2r_o t + t^2 - \frac{2A + 4Bt}{P_i} \left\{r_o t^2 - 2t^3 + \frac{5}{3}\frac{t^4}{r_o} - \frac{2}{3}\frac{t^5}{r_o^2} + \frac{t^6}{r_o^3}\right\} = 0$$

since $r_o >> t$ typically we will neglect terms of order $t^3(\frac{t}{r_o})$ and higher compared to t^3 and lower terms. We then have a quadriatic equation for r_o and the solution is

$$r_o = -\frac{b + \sqrt{b^2 - 4C}}{2} \qquad (8.6)$$

where b

$$b = -\frac{2At^2 + 4Bt^3 + 2t}{P_i}$$

$$c = \frac{4At^3 + 8Bt^4}{P_i} + t^2$$

We now have two unknowns, (r_o and t) for a given pressure and two equations (8.4 and 8.5) so the problem is determined. For the assumed values given above the optimum thickness for 316 SS was found to be nearly constant between 800 psi and 200 psi varying between .147 cm and .144 cm. This optimum choice for the first wall gives a thermal stress nearly equal to the pressure stress. Since the pressure stress on the spherical cap is roughly half the cylindrical wall stress the total first wall stress is approximately the same as the side wall stress. It was found

that the side wall stress in some cases was just slightly over 10,000 psi requiring slightly smaller module radii, but this correction was small (≃ 2%). The module radius vs. pressure for 316 SS and for several thicknesses of Nb are shown in Figure 8.3.

8.2 PERCENTAGE OF STRUCTURAL MATERIAL

Another consideration is the amount of structural material which is important because the breeding ratio is fairly sensitive to this.

For a unit cell with the first wall center to center distance between breeder rods equal to twice the outside radius the total volume is equal to

$$V_t = 2\ r_o^2 + \frac{(2r_o)^2}{2\cdot(3{:}5)} = 4.57\ r_o^2\ (m^3)$$

where the Torus minor radius is 3.5 m and the length of the cell 1m. The volume of structural material is given by

$$V_s = \pi(r_o^2 - r_i^2) + t\ \pi r_o^2$$

and therefore

$$\frac{V_s}{V_t} = .687\left(2\,\frac{t}{r_o} - \left(\frac{t}{r_o}\right)^2 + t\right) \simeq 1.37\,\frac{t}{r_o}$$

a thin cylinder approximation gives

$$\frac{t}{r_o} = \frac{P_i}{\sigma}$$

where the hoop stress is taken as a constant for our design. Therefore we should expect to percentage of structural material to be directly proportional to the pressure.

Equation 8.1 was used to determine r_o for a given t and pressure for Nb-1Zr then Vs/Vt was calculated. The resultant percentages are given in Table 8.2. There values of Vs/Vt are nearly independent of t and are within about 1% of the values for 316 SS at its optimum thickness.

If we were to design to 5×10^3 psi versus 10^4 psi to allow a large safety factor in the mechanical design, this would approximately double the percentage of structural material and would have a serious effect on the breeding ratio.

Table 8.2

P(psi)	t(cm)	r_o (cm)	Vs/Vt %
800	.2	2.60	10.3
700	..2	2.96	9.11
600	.2	3.44	7.90
500	.2	4.10	6.68
400	.2	5.10	5.47
300	.2	6.76	4.14
250	.2	8.10	3.49
200	.2	10.1	2.83

8.3 RELIABILITY

Another area of concern is the large total number of modules required for this design. For a module radius of 4 cm, 140,000 breeder rods would be required for a first wall surface area of 1450 cm^2 as postulated. An extremely high degree of component reliability is therefore required.

A potential problem is the vacuum seal made by screwing the cylinder into the backing structure. In an effort to estimate the problem, reliability data for typical pnematic components was reviewed in the literature[40,71,72]. Such components as pipe joints, unions and junctions and "0" Rings all seemed to have failure rates in the range of 10^{-6} to 10^{-7} failures per hour (Figure 8.4). If you assume a value of 5×10^{-7} failures/hr for our postulated seal and 1.4×10^{5} modules the mean time between failure for the whole blanket is only about 14 hours which is obviously unacceptable. A solution appears possible however. It would require designing a double seal such that the second seal is not stressed unless the first seal breaks. The problem of determining the average number of modules that will have both seals failed after a given time is formally the same as for a radioactive decay chain going from parent to daughter to grandaughter where you want to know the number of grandaughter products present as a function of time. From this approach it can be shown that the probability of n breeder rods surviving a time t in a double seal system, with each seal having a failure rate independent of time, is given by

$$P_s = e^{-n\lambda t} (\lambda t + 1)^n$$

for

$n = 1.4 \times 10^{5}$

$\lambda = 5 \times 10^{-7}/hr$

$t = 10^{3} hr$

this gives P = .983, that is the probability of the blanket, lasting 10^3 hours without a leak from any vacuum seal joint is 98.3%. If the failure rate were to be 5×10^6, an order of magnitude higher, then a triple seal would probably be required. In this case

$$P_s = e^{-n\lambda t}\left(1 + \lambda t + \frac{(\lambda t)^2}{2}\right)^n$$

and for the same n and t as above $P_s = .997$.

Thus, if an effective double or triple seal can be designed for the breeder rod - backing structure junction the reliability should be acceptable.

Fraas gives a rough guide to estimate the occurrance of leaks in his comparative survey of blanket concepts. Summarizing his estimate, the mean time between coolant leaks is given by

$$\text{MTBF(hr)} = \frac{10^9}{[N_o \text{ tube joints} + N_o \text{ ft weld}] \cdot A \cdot B}$$

where A = thermal stress factor = (coolant temperature rise°C/50)

B = pressure stress factor = nominal pressure stress/allowable stress

For our design with $\sigma = 10^4$ and for $\Delta T = 200$, $A = 4\ E\alpha/(E\alpha)_{SS}$ and $B \simeq 1$. For the original design assuming 2 tube to header joints per module and a circular weld around the first wall cap

No tube joints = 2.8×10^5

No ft. weld = 1.15×10^5

For a niobium structure $\frac{E\alpha}{(E\alpha)_{SS}} = .195$ and

MTBF $\simeq 3.24 \times 10^3$ hr

For 316 SS, MTBF = 633 hr.

If material considerations require the use of 316 SS this problem would have to be addressed in a much more accurate manner. Going to a large module size, lowering the design stress, and reducing ΔT would all help but would increase the pumping power. For failure mode operation the temperature in the failed module $LiAlO_2$ limits the maximum module radius to something between 6 and 7 cm which would not significantly increase the MTFB.

CHAPTER 9

DESIGN ENVELOPE

The objective of this section is to establish the allowable range of module sizes, wall thickness and system pressure. In attempting to establish the designenvelope for this concept it was assumed that the most difficult constraint to fulfill was the breeding requirement. Consequently in the process of picking certain parameters to be fixed, where a choice was possible, the value most favorable for breeding was taken. Thus the stress was fixed at 10^4 psi, our design limit and the ratio of pumping power to heat removal (PP/Q) at 5%, which is probably the highest allowable. The design also employed the smallest allowable void fraction. Despite these choices, the breeding ratio could not be demonstrated to be above one and there was therefore no open window. To illustrate the approach however, we will show a design window based on the other known constraints with the parameters optimized for breeding and assume a breeding ratio higher than calculated.

9.1 GEOMETRY AND HEATING RATE

The geometry evaluated was for a module with a one cm thick graphite sheild. The module outside radius (R_o) and wall thickness (t) were variable and the modules were arranged in a close packed rectangular array so that $L = 2R_o$ and the average volume of carbon in the blanket was 31% which is the minimum for a rectangular array. The heat rate was taken to be $q''' = 5.0\ e^{-.042x}\ W/cm^3$ within the modules. The heating rates and geometry correspond to what was assumed in Chapter 5 with $H = .016\ w/cm^2{}^\circ C$.

9.1.1 REMOVAL OF HIGH INLET TEMPERATURE CONSTRAINT DUE TO INVENTORY CONSIDERATIONS

If the inventory calculations of section 6 were used to set the minimum inlet temperature, a viable design window could not be obtained because of the high temperatures required. Several possibilities exist however, First inventory calculations are based on a sphere .2 cm in radius composed of 0.0075 cm radius particles. It may be possible to manufacture the $LiAlO_2$ with a smaller particle size and eliminate the problem entirely. Second the experimental data on diffusion in $LiAlO_2$ is quite recent and the values may not be totally accurate. Finally if indeed the diffusion is as calculated previously, a change in operational procedure might be possible to allow the use of lower inlet temperatures.

If an inlet temperature of 300°C is used, the tritium inventory will build up and based on the previous calculations should take approximately 20 days to go from 1 kg to 5 kg. At that time with the plasma quenched, the blanket heat exchanger could be bypassed and the He slowly recirculated with little or no cooling. The inlet temperature should then rise because of the afterheat. In an inlet temperature of close to 600°C could be maintained with a small temperature rise through the module, the tritium in the blanket could be "flushed" out. Based on .0075 cm particles and .2 cm spheres it would take about 2.3 hours to reduce the inventory to 1 kg and then begin the cycle again. In establishing a design window therefore it will be assumed that for one or another of the above reasons it will be possible to remove the constraint of high inlet temperature imposed by inventory considerations.

9.2 HELIUM TEMPERATURE SELECTION

The calculations of Chapter 5 showed that for an inlet temperature of 300°C and ΔT equal to 200°C, the maximum temperature of the side wall under off-normal operation varies between approximately 645°C and 605°C. To obtain an open design window, an inlet temperature of 275°C will be taken with ΔT = 200°C. The effect of lowering the outlet temperature is to decrease the thermal efficiency. The pumping power however is also reduced or for the same pumping power, smaller pellets can be used giving a slightly smaller void fraction because of wall effects. It will be assumed that the shape of the temperature profile is the same as before and the previously calculated temperature will simply be lowered by 25°C.

9.3 WINDOW CONSTRUCTION - STEP 1 - MODULE SIZE

As the size of the module increases the first component to reach a design limit temperature is the $LiAlO_2$ in a failed module. Conversely as the module radius is decreased the first component to reach a design limit temperature is the module side wall in an operating module where we have assumed that the peak first wall temperature will equal the peak side wall temperature as calculated for the reasons discussed in Chapter 5. The peak temperature of these components as a function of module radius is plotted in the upper left quadrant of Figure 9.1. Two curves are shown for $LiAlO_2$ the upper corresponding to a contact conductance of .4 $W/cm^2°C$ between shim and breeder rods and the lower to the case where a gap is present around the shim rods and the emissivity of the metal wall is taken to be .6 and the shim emissivity equal to one. For the stated conditions the $LiAlO_2$ design limit temperature of 1800°C limits the maximum module radius to 6.6 cm for contact conduction at the shim breeder rod interface. For the case of a gap around the shim rods the

maximum allowable module radius is only 4.0 cm.

The smallest allowable module size is set by the peak temperature of the module side wall which increases as module radius decreases and is limited to 600°C. This limit is reached at a radius of 4.3 cm. Therefore for the above conditions the thermal constraints allow module radii between 4.3 and 6.6 cm for contact conductance between shim and breeder rods. For the radiative boundary conditions between shim and breeder rod however there is no open window for these conditions since the maximum radius allowed is less than the minimum. To employ a gap, the inlet temperature could be lowered. This would shift the peak component temperature curves to the right, increasing the maximum and decreasing the minimum allowed module radii. If the inlet temperature were lowered 30°C with ΔT kept at 200°C, a narrow window would open around a module radius of 4 cm.

With the inlet temperature and ΔT given and the range of module radii established it is desirable to find the allowable range of operating pressure.

9.4 WINDOW CONSTRUCTION - STEP TWO - MAXIMUM PRESSURE

A maximum pressure can be determined in principal from the breeding ratio design constraint of 1.15. The logic behind this is as follows. Increasing the amount of structure decreases the breeding ratio as shown before. Increasing the design pressure also allows a small reduction in the void fraction for the same PP/Q, but the breeding ratio still decreases because of the first effect. For a given wall thickness and

9.5 MINIMUM PRESSURE

Figure 8.3 is duplicated in the upper right quadrant of Figure 9.1 for several thicknesses of Nb-1Zr. These are curves for a constant maximum stress of 10^4 psi. A minimum thickness has been set somewhat arbitrarily at .145 cm because of the difficulty of handling and fabricating large components with thinner walls. This minimum was chosen to be the same as the optimum thickness for 316 SS. The curve of minimum thickness sets the lower pressure boundary and closes the design window.

Figure 9.2 shows the corresponding window for 316 SS where it has been assumed that the only change is the additional first wall thermal stress. In this case the window degenerates to a single line at the optimum thickness going from the maximum radius to the minimum module radius.

The optimum thickness for 316 SS was based, among other factors, on a surface loading of 20 W/cm^2. If an additional loading of 3.5 W/cm^2 was added to allow for the energy generation within the shield the optimum thickness would decrease slightly to .125 cm.

The principal variable which has not beed fixed is ΔT. It would be desirable to have this as large as possible to minimize the pumping power but the upper bound will be set by reliability. The larger ΔT is the greater the thermal stress will be and the shorter the mean time between failure. To accurately fix this would require a detailed fracture mechanics analysis of the first wall and structure which was beyond the scope of this report.

pressure there will be a specific percentage of structural material and void fraction and therefore breeding ratio. The maximum pressure is then the pressure at which the breeding drops below 1.15.

The minimum void fraction to be used in the breeding calculation can be determined in the following manner. Given the wall thickness and pressure the module radius can be determined as in Figure 8.3. Then with ΔT and T_m (the average coolant temperature) known or estimated the equation for PP/Q (Eq. 3.34) can be solved for the pellet size which gives PP/Q = 5%. This will also give the void fraction which is just a function of the ratio of pellet size to cylinder radius. Estimating T_m by $T_{inlet} + \Delta T/2$ for an inlet temperature of 300°C and ΔT = 200°C gives the pellet sizes shown in Figure 9.3. The void fractions based on pellet sizes found in this manner are shown in Figure 9.4 and Figure 9.5 for the single thickness of 316 SS and for two thicknesses of Nb-1Zr for several inlet temperatures.

The calculated breeding ratio for the stated geometry shown in Fig. 7.10 was interpolated to give the solid curve (#4) of breeding ratio versus pressure shown in the lower right quadrant of Figure 9.1. Since it is never above 1.15 there is no open window. For illustration however suppose the breeding ratio followed the curve (#5) corresponding to a module with a 6.3 cm BeO shield. In this case the maximum amount of Nb is 5.69%, which is reached at a pressure of approximately 430 psi.

Time Dependent Properties

Thermal Cycling

This preliminary study has not taken into account an analysis of the effects of thermal cycling and the associated structural fatigue. It should be recognized that this could be a limiting factor. To estimate this effect however requires an accurate model of the first wall shield and module wall interface and also the time dependent thermal wall loading. At this point the necessary information is not available for the BRSR design.

Irradiation Effects

A more refined design would also have to allow for the change in parameters as a function of the cumulative radiation over an estimated module lifetime. Information is required on the changes in such parameters as the thermal conductivity of the graphite and allowable stress levels for given temperatures of the structure.

CHAPTER 10

OVERALL DESIGN REVIEW

A number of difficulties were encountered during the evolution of this design and its generalization into a design window. A review of these along with suggestions for potential solutions could help define directions for further work on solid breeders.

The most obvious and serious problem was the poor breeding ratio. Part of the reason for this was the poor blanket geometry which was required to make each module a separate pressure vessel to permit failure mode operation. The solution could be a more clever geometry that would eliminate or greatly reduce the size of the shim rods. It would also help if the structure of a depressurized module could still contribute to the support of the remaining breeder rods, allowing a smaller total amount of structure in the blanket. Also, if niobium is the structural material it may be possible to entirely eliminate the shield in front of the module although this would not be possible with 316 SS because of its lower melting point (1430°C). The breeding ratio would also be improved if an alloy of vanadium could be developed that was suitable. Aluminum has a lower absorption cross section than niobium or 316 SS and was used in the Brookhaven design but the high temperatures reached in failure mode for this design would preclude its use here.

It appears that a closer look should be made for improving the solid breeding material. For $LiAlO_2$ it would be helpful if it could be made as basically solid blocks with flow channels cut through with a

microstructure that allows sufficiently rapid diffusion. This could allow a smaller void fraction. If beryllium is needed for neutron multiplication some consideration of using a BeO shield should be given although its thermal shock resistance is poor and it would probably have to be replaced relatively frequently. Another possibility would be to develop a composite shield with both carbon and a beryllium compound that would retain a high conductivity by effectively having the thermal resistances in parallel, but would still have a high enough percentage of beryllium to satisfy the breeding requirement.

For failure mode operation in a modularized system, provision must be made for removal of the heat generated in a depressurized module. In the reference design this was done by conduction through the packed bed of the failed module to the graphite shim rods and finally to the surrounding operating modules. It is possible that because of the different thermal linear expansion of the metal can and the carbon shim that a gap would have to be provided between them and the heat transfered by radiation. As noted previously this required a large surface to volume ratio and a correspondingly small sized module. If such a gap is required, reasonably sized modules most likely could be designed by going to the closest possible packing instead of a rectangular array and coating or otherwise treating the surface of the can to raise the total hemispherical emissivity to the range of .8 to .9. It would also be highly advantageous to raise the conductivity of the breeding material. A possibility here is to utilize the phase change at 900°C in a failed, depressurized module to decrease the void fraction and

increase the conductivity. This would require very careful engineering and an accurate knowledge of the swelling of $LiAlO_2$ due to radiation. Another possibility would be to design for a gap between the breeder rods and the shim rods for normal operation but in a failure mode allow the expansion due to the higher temperatures to close the gap and permit conductive heat transfer from the failed module.

A more difficult problem than handling the volume energy generation in a failed module is absorbing the surface energy flux without exceeding any limits. In the reference design the carbon shield provides a conduction path to the surrounding modules which are operating. Within the very conservative assumptions discussed previously, the maximum first wall temperature for an operating module rises to approximately 800°C, at the point closest to the failed module. The problem at this temperature is corrosion with the coolant stream. If a more accurate calculation was done accounting for radiation from the first wall surface regions at elevated temperatures to the rest of the enclosure, a closer packed geometry, and a spherical rather than rectangular cap, this maximum temperature would undoubtedly be lower. At the expense of increasing the pumping power the coolant mass flow rate could also be increased if required. An alternative design philosophy might be to allow no conduction of the surface flux to surrounding modules and to rely entirely on radiation. For example, if the normal operating surface temperature of a graphite shield is 850°C, then for a 5 cm thick shield the entire surface flux and volume energy generation in the shield could be dissipated by radiation from the surface at a temperature of approximately 1700°C.

If niobium is the structural material it should be possible to eliminate the shield entirely and allow the surface to be cooled by radiation. An additional benefit would be that there would be a significant increase in n, 2n reactions in the niobium which would help the breeding ratio. To reduce plasma contamination a thin carbon coating or carbon curtain as in UWMAK-II could be used. For a 1 cm thick niobium wall with an emissivity of .8 (assuming a thin carbon coating), a surface load of 20 w/cm^2 and a volumetric generation of 3 w/cm^3 the surface temperature for a depressurized module would be on the order of 1300°C well below the melting point of 2468°C, assuming the rest of the enclosure is at 700°C and lateral transport of the heat generated internally in the failed module. As shown previously, however, the breeding ratio is still significantly less than desired.

A difficulty not considered in this design is the effect of swelling of the breeding material either from helium production because of radiation or the phase change at 900°C. On a small scale, radiation induced swelling would cause flow irregularities and hot spots. In a failed module the danger would be that the phase-change-induced-swelling added to whatever radiation-induced-swelling is present could cause large stresses on the structure and possible failure. More data on swelling is needed in order to evaluate these possibilities. It should be remembered also that if extra volume is provided for such swelling there still must be adequate heat transfer for failure mode operation without the coolant present.

Another design point which would have to be handled in a full reactor design is the piping and valving required. A major constraint here would be the physical space available. For a modular system such as postulated here there are a very large number of modules, on the order of 140,000. It obviously would not be desirable to have twice that number of valves which is what would be required to isolate individual modules. On the other hand, every module valved to a failed module would also have to be replaced when the time came for maintenance because the high temperatures reached when operated without coolant would cause the $LiAlO_2$ phase change discussed previously. Also, it is possible that local sintering of the lithium aluminate could occur. For a system with five headers this means 1/5 of all the modules in a section would have to be replaced which could be a large number requiring a costly and time consuming job. An invention that would help here would be some simple type of valve, similar to concept to a fuse in an electrical circuit, which would be used just once to isolate a single module permanently.

Rapid location of a leak is another requirement which remains at present an unsolved problem. A trace gas in the coolant could most likely be used to detect such a leak by looking for the presence of the given impurity in the plasma spectrum but to use such a method to determine which module it is coming from would require a very complicated additional piping and valving system. Present mass spectrometer type systems for locating the leak would require access to the inside of the torus and a time consuming search. Research is needed in this area. One avenue of investigation possible is to determine if a small leak

would cause a detectable vibration or sound in the structure. Another idea would be to see if a small coolant leak would cause a temperature change on the first wall that could be seen on an infrared type detector, after the plasma was quenched in a normal cycle.

It would be very advantageous to use 316 SS as the structural material since it is the only metal considered that has an established industry. For this particular design however, an estimate of the probable mean time between leaks using the criterion given by Fraas, indicates a very low reliability with a MTBF on the order of 600 hours. The main reasons for this are the high thermal stresses in the first wall and the extensive welding.

The results of the tritium transport calculations indicated that for reasonable steady state inventories, high coolant inlet temperatures were required. It appears possible, however, to relax this constraint by allowing the tritium to build up in the blanket to a maximum allowed level and then to flush out the blanket using high coolant temperatures with no plasma present. For example the blanket inventory could be allowed to cycle between one and five kilograms where one cycle would take about 20 days. Then without the plasma present the heat exchanger could be bypassed and the afterheat used to keep the coolant temperature high with a fairly uniform profile. For the breeder particles discussed before, 80% of the trapped inventory could then be released in 2.3 hours with a coolant inlet temperature of 600°C. If the structural material was niobium most of the tritium would diffuse into the vacuum chamber and could be recovered by the same system used to pump out the spent fuel.

It may also be possible to manufacture the $LiAlO_2$ with a small enough particle size that diffusion would not be a problem for temperatures between 300° to 600°C.

Chapter 11. Future Directions

11.1 Effects Plasma Physics On Reactor Design

The objective of fusion reactor studies is to evolve an economically attractive energy source. To achieve this end will require a compromise between what is most desirable from the point of view of the plasma physics and what engineering reality will allow. At present the engineering problems associated with conceived reactors are enormous. It may be possible through clever design to overcome the problems but it may also be worthwhile to begin looking for ways to alleviate these problems through changes on the plasma side.

As a beginning consider what a proposed plasma confinement scheme determines:

1. The general geometry as for example in a low aspect ratio Tokamak or a Mirror machine.

2. The percentage of total power which appears in the form of charged particles or radiation which becomes a surface heat flux.

3. The neutron generation rate in space and time and its energy spectrum, which is essentially a delta function at 14 Mev for $D + T \rightarrow He^4 + n$.

4. The plasma heating requirements necessary to achieve ignition as for example neutral beams or R.F. power input.

5. The allowed flux of impurities from the first wall.

6. The magnetic fields required to confine the plasma, both steady state and pulsed.

7. The fueling requirement, that is the rate at which D and T are to be injected and the proposed manner such as pellet injection.

8. The operating cycle. Tokamaks presently are considered to run in a pulsed mode for example while mirror machines could run steady state.

In each of these areas certain directions for change are more favorable to the engineering then others.

1. General Geometry. It is highly desirable to have a geometry which would permit easy access to all areas such as in a linear system or a torroidal system with a high aspect ratio. This is especially important since the blanket region will require remote maintanence. Another factor is that fabrication costs would be decreased considerably if the geometry would allow the use of simple structures such as boxes or cylinders for major components rather than requiring the use of compound curves for structural components or a very large number of small modules.

The geometry can also help decrease costs if it allows an increase in the ratio of power output to reactor volume. Finally development costs would be reduced if the geometry allowed smaller sized first generation machines.

2. Surface Flux. Large surface heat fluxes on the first wall lead to thermal stress problems and require complex cooling arrangements which also reduce the reliability of the system. As proposed neutron wall loadings increase, it becomes even more important to ensure that designs include divertors or some scheme to reduce the surface heat flux on the first wall. This is particularly true if 316 SS is to be the structural material.

3. Neutron Generation. If D and T are to be the fuels the only neutronic help would be a configuration which gives a spatial flux favorable to the engineering requirements of a specific design.

4. Heating. In evaluating alternative plasma heating schemes some consideration should be given to the effect on the overall reactor design.

schemes which require a large number of holes in the blanket will reduce the breeding, complicate the shielding requirement for the magnets and probably make access more difficult.

5. Impurities. The requirement to control the flux of impurities reaching the hot plasma is another strong factor favoring inclusion of a divertor in the design. Naturally if plasma parameters can be varied to increase the tolerance of impurities the required efficiency of the impurity control system can be relaxed, hopefully allowing the use of bare metal walls.

6. Magnetic Fields. It is well known that the costs of the magnet system can be significant. In very general terms, changes which would reduce the complexity of the field windings required and/or the amount of stored energy in the fields would be desirable.

7. Fueling. To fuel the plasma requires tritium breeding and a fuel reprocessing and injection system. An area of concern in a reactor is the tritium inventory. A considerable fraction of the inventory is tied up in the reprocessing system and in any reserve fuel stockpile. If the particle confinement time is increased and therefore the fractional burnup, then the amount of tritium which must be recirculated for a given power level is reduced and consequently the inventory could be lower.

8. Operating Cycle. Steady state operation is naturally the most desirable. Pulsing creates problems of thermal fatigue and requires additional complexity to supply a steady state output from a pulsed source.

A combination of the fueling and heating requirements strongly influence the recirculating power fraction. It is naturally desirable to have a system with a low recirculating power fraction ($\lesssim 10\%$). Tokamak reactors for example appear much more favoravle in this reguard then a simple mirror reactor.

11.2 Effect of Changes on the BRSR Design

Since this study was a blanket evaluation rather then an integrated reactor design only some of the proposed areas of change are directly applicable.

The biggest help would eome from a reduction in the surface heat flux. Thicker 316 SS first walls could be tolerated and higher pressures. This effect is shown in figure 11.1 which has curves showing the maximum module size versus pressure for different first wall heat fluxes. As before these are based on a design stress of 10^4 psi and the optimum thickness for a given pressure. With a lower heat flux the optimum thickness increases. The original design line shown for 316 SS then opens up into a window as shown. Reducing the surface heat flux will also reduce peak first wall temperatures.

While not evaluated for this design, thermal fatigue could be a significant problem. Reducing the surface flux would help here also. Naturally steady state operation would be ideal from the viewpoint of thermal fatigue.

11.3 Possible Engineering Changes in the BRSR Design

It would be desirable to increase the size of the modules in order to reduce the total number and increase the reliability. What is needed even more however, are changes to increase the breeding ratio.

To increase the breeding ratio some possibilities are:

1. Increase the lithium density in the modules, possibly with a different lithium compound.

2. Reduce the percentage of carbon in the blanket. If the structure of a depressurized module could be used to help support an operating module it may be possible to use a breeder rod shape besides cylindrical which would reduce the size shim required or perhaps eliminate it entirely.

3. Again the percentage of structural material may be decreased with a better design

4. Design a composite shield containing BeO which could satisfy all constraints.

To increase the module size:

1. Increase the thermal conductivity within a failed module

2. Eliminate or reduce the size of the shims

3. Lower T_{in} and/or ΔT although this would be at the expense of thermal efficiency.

4. Reduce the hot spot peak in the $LiAlO_2$ at the center front of a failed module perhaps with a short annular region or a high thermal conductivity path.

CONCLUSIONS

1. The design features required to meet the thermal and mechanical constraints for failure mode operation when combined with the inherently low breeding potential of the solid breeder type design reduced the breeding ratio to an unacceptable level. A thick (6.3 cm) BeO shield in front of the module would give the desired minimum breeding ratio (1.15) but the lifetime of such a shield would be short and it appears that designing a support structure that would permit it to withstand the thermal stresses would be very difficult.

It should be noted that the breeding ratio conclusion is based on the results of 1-D ANISN calculations. A 3-D Monte-Carlo calculation would be desirable but for the conclusion to be different such a 3-D calculation would have to give breeding ratios approximately 25% higher and this seems unlikely.

2. If adequate breeding could be demonstrated however, it appears that the thermal constraints imposed by requiring the blanket to be capable of operating with some modules depressurized could be met.

3. Calculations based on initial experimental values for the diffusion of T in $LiAlO_2$ indicate the possibility of unacceptably large T_2 inventories for inlet temperatures of less than 500°C. For a viable solid breeder design either the diffusivity must be increased over the initial experimental values by different fabrication techniques or the inventory content of the blanket must be periodically decreased by some high coolant temperature "flushing" technique.

4. The use of a single thickness 316SS first wall may be possible but is not desirable. It would be quite sensitive to variations in thickness produced in fabrication and allowance for stress concentration probably would require very small modules or pressures less then 200 psi.

5. The analysis of a solid breeder design should start with a preliminary one dimension estimate of the breeding ratio after the rough geometry is decided upon. This would then give an indication of the amounts of structure and void fraction that could be tolerated. Such an approach would have saved considerable effort in this study.

RECOMMENDATIONS

A number of recommendations specific to this design were made in the previous section. At this point it would be better to try to take a general view.

Part of the motivation of requiring failure mode operation was the assumption that because of the low aspect ratio torus shape and the nested magnetic coils required in a Tokamak, access to a blanket element would be quite difficult. If a plasma confinement scheme could be developed that would permit relatively easy access, the engineering problems would be eased a great deal.

The most difficult thermal problem encountered was handling the 20 w/cm^2 surface heat flux. It would be quite helpful from this point of view if the reactor design included divertors which besides removing impurities could take a significant percentage of the surface flux composed of energetic particles and spread it out over a larger surface area separate from the breeding portion of the blanket.

The UWMAK-II breeding ratio was 1.06 and to attain it required very large amounts of beryllium. In addition if a redundancy was incorporated into the first wall the breeding ratio would probably drop below 1. The breeding ratio for this design was only on the order of .9. The conclusion from this seems to be that either a more efficient neutron design, if possible, is required or a different solid breeding material with better breeding characteristics should be found.

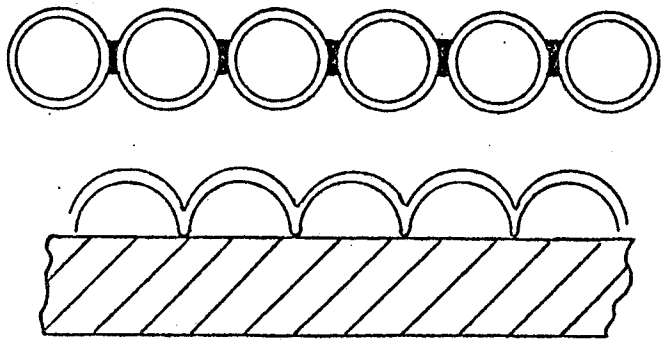

(a) Sacrificial First Wall

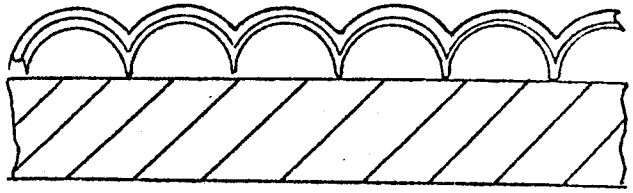

(b) Double First Wall

Fig. 1.1 Redundant First Walls (Ref. 3, Fig. IV-I-13 and IV-I-14)

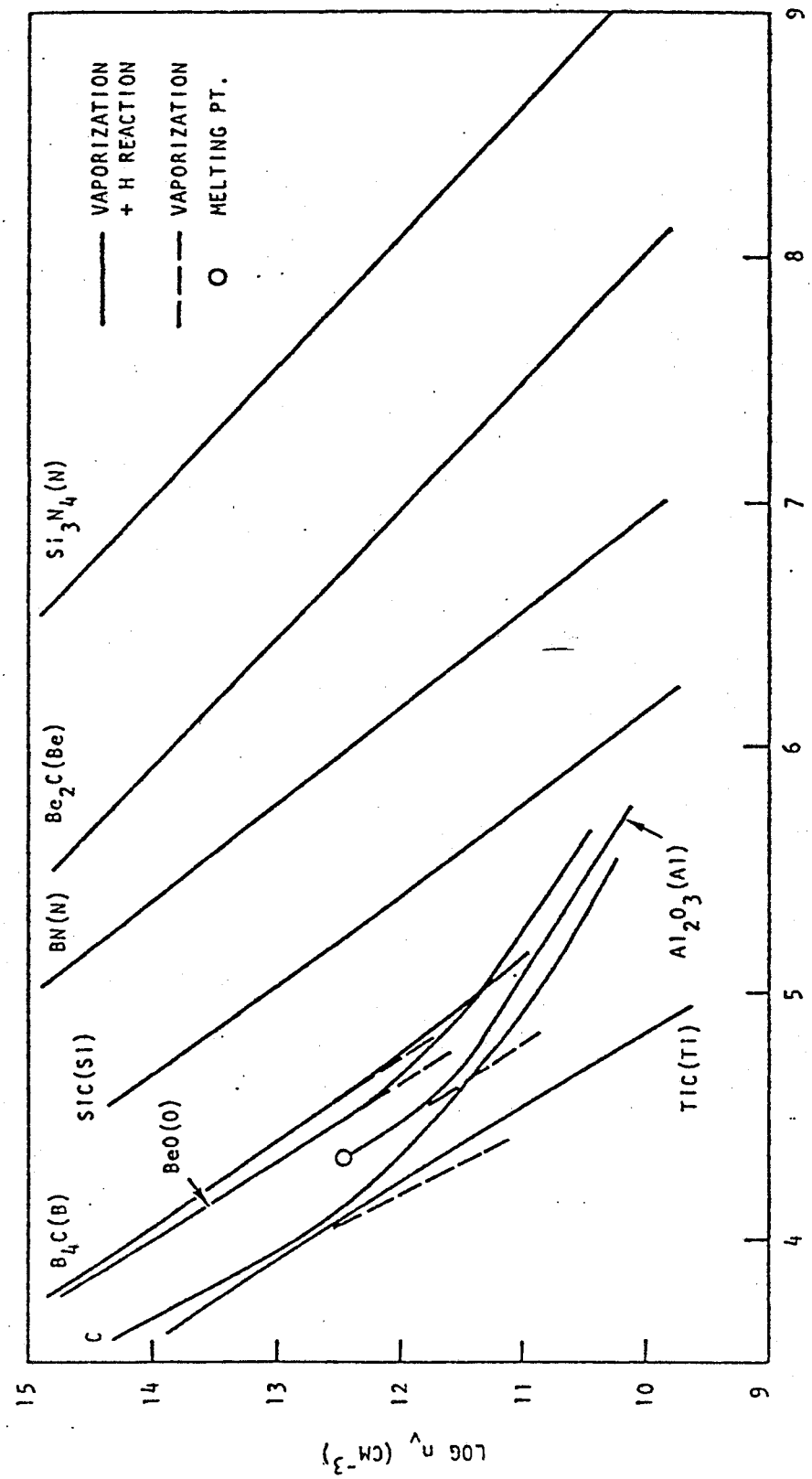

Fig. 1.2--Equilibrium vapor densities in 10^{-5} atm H_2 (Fig. 2.1, ref 4)

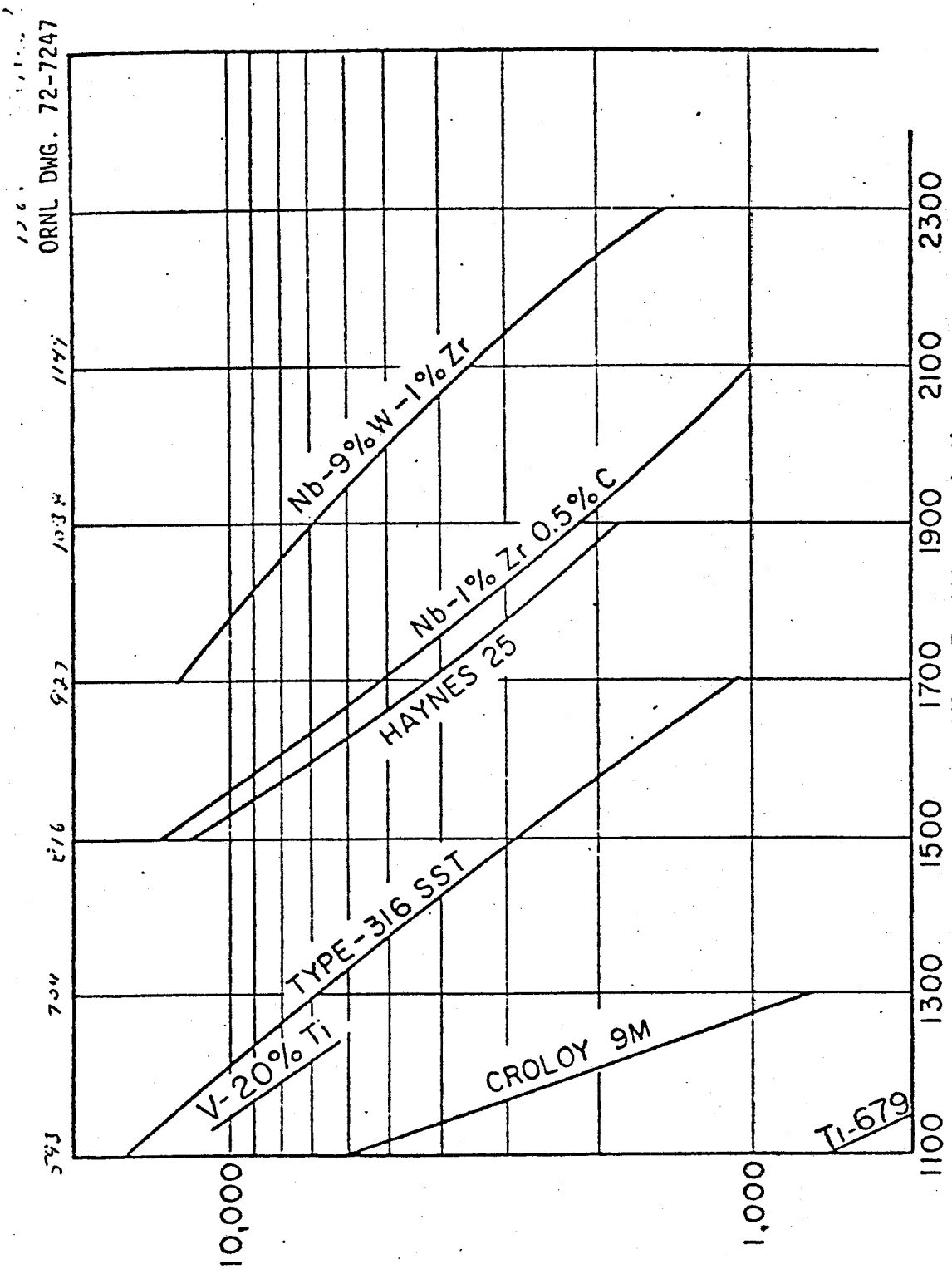

Fig. 1.3 Effects of temperature on the creep strength of typical alloys (fig. 19, ref 6)

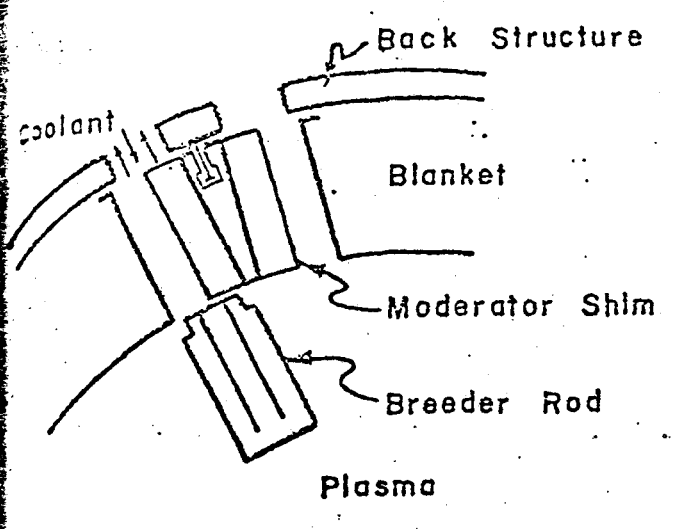

a. GENERAL ARRANGEMENT

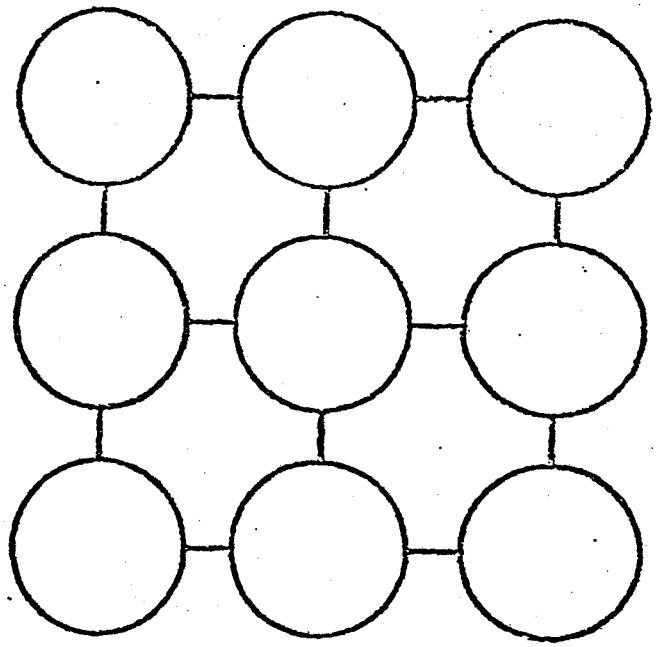

b. Spatial Arrangement

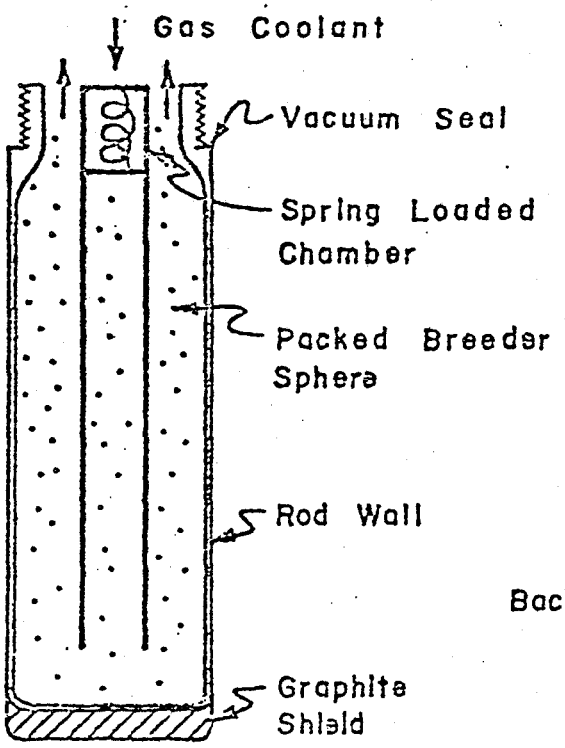

c. BREEDER ROD

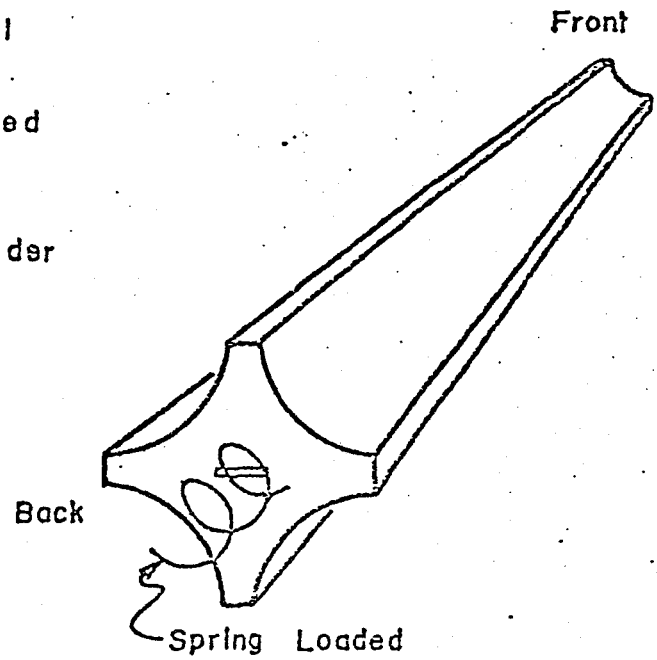

d. MODERATOR SHIM ROD

FIG. 2.1 BREEDER ROD AND SHIM ROD DESIGN

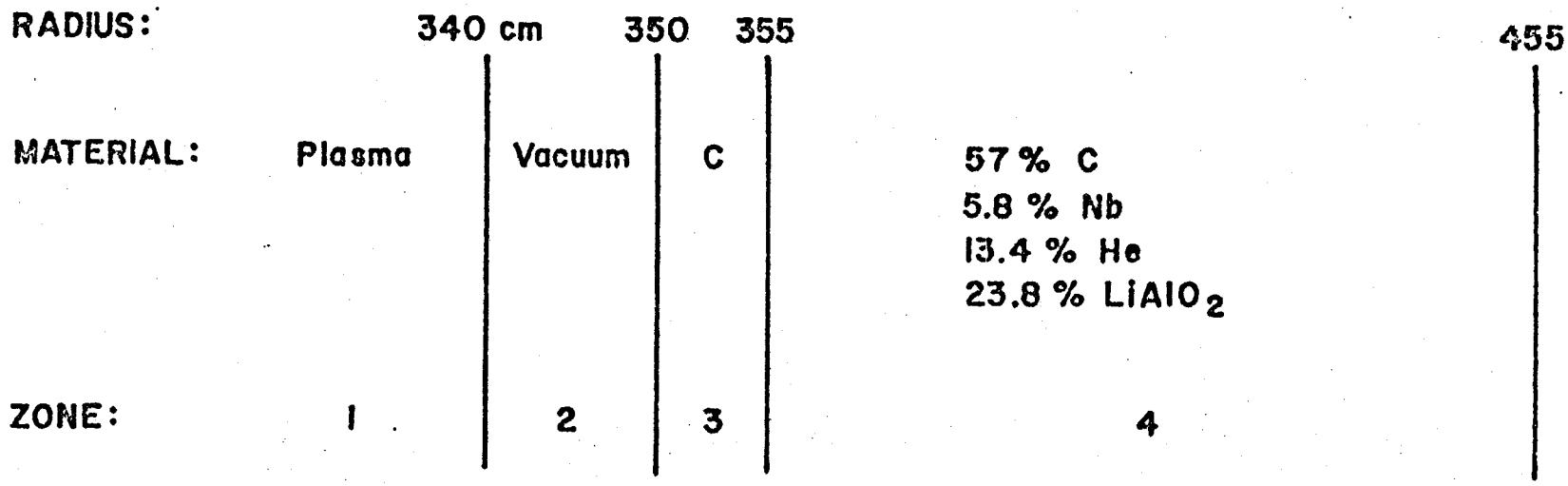

FIG. 2.2 SCHEMATIC OF BREEDER ROD AND SHIM ROD BLANKET

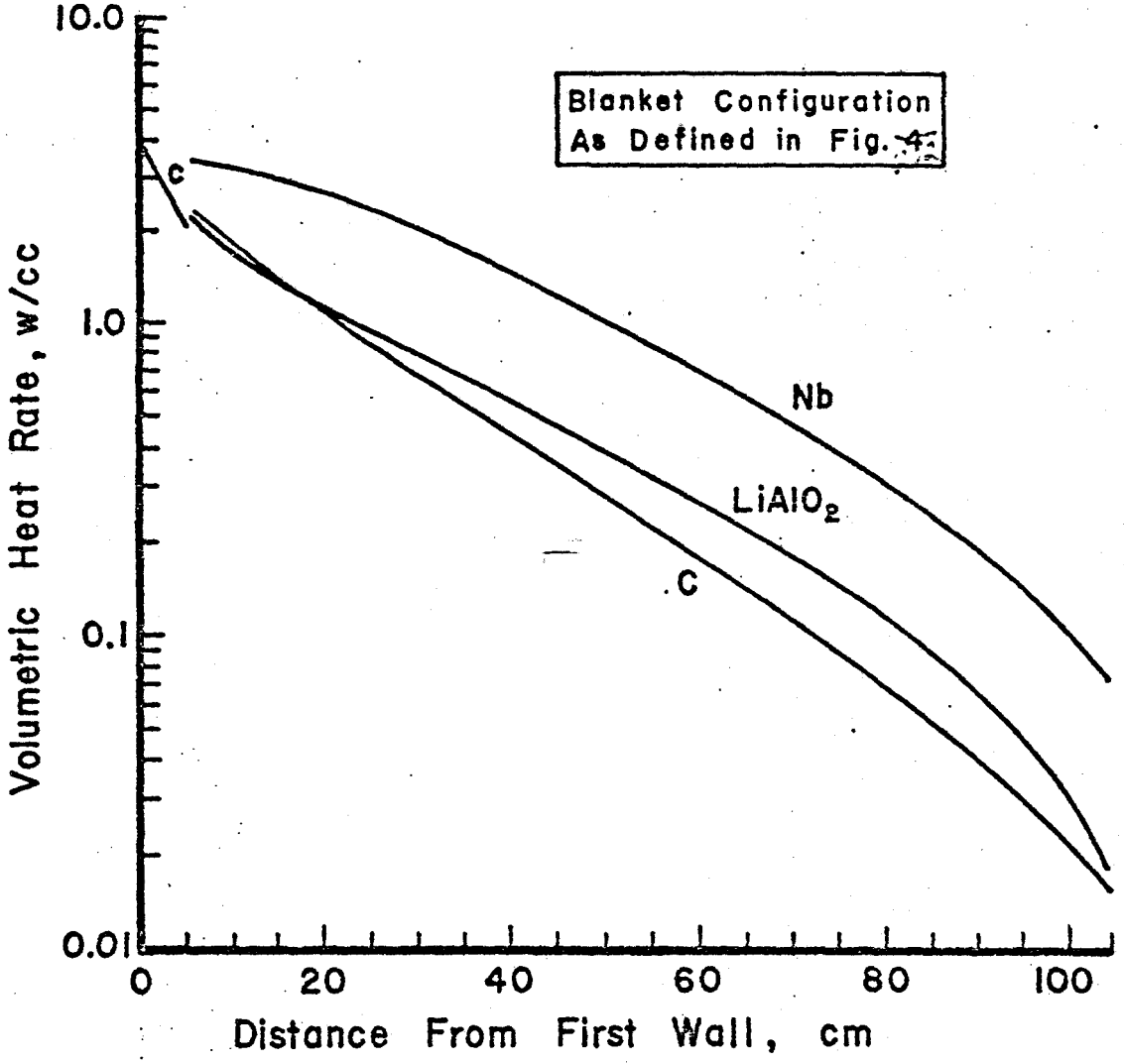

FIG 2.3 q''' vs. DISTANCE FROM FIRST WALL

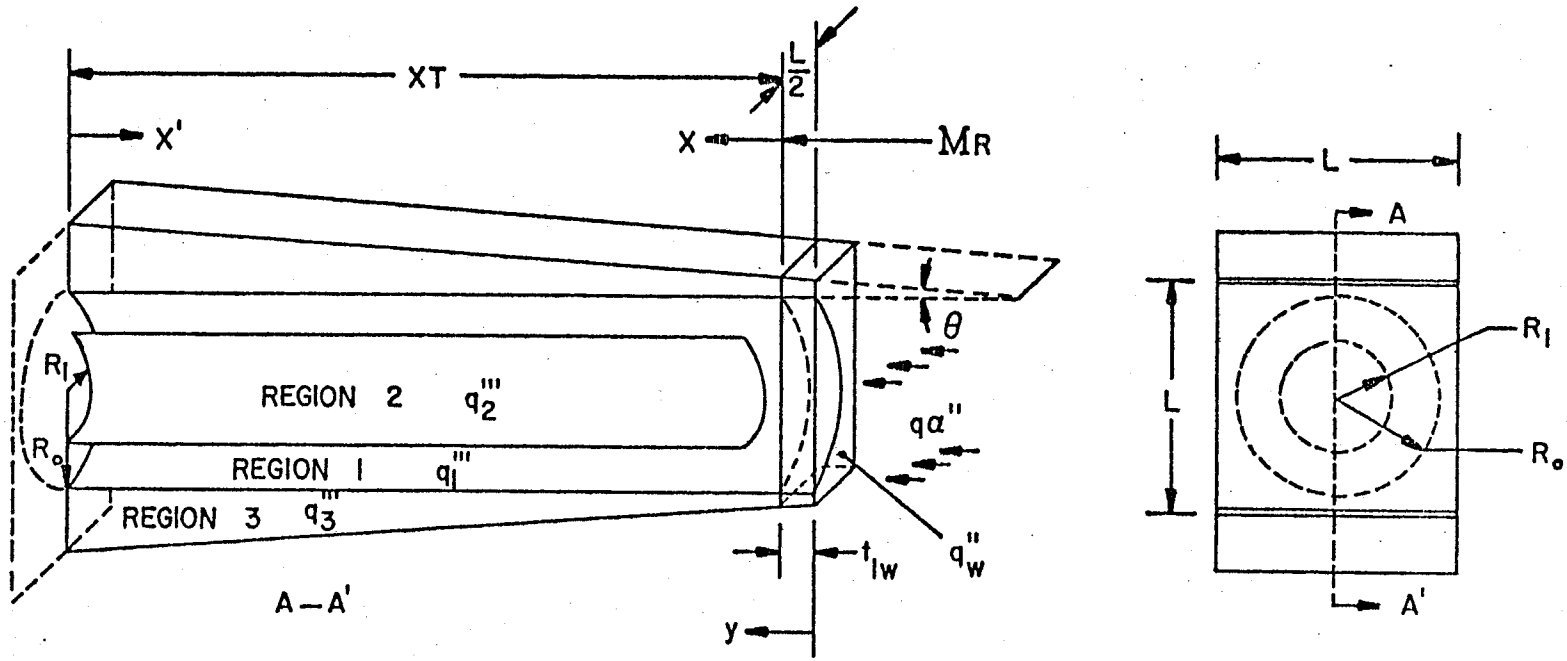

$$q'''_w = q'''_{w_o} e^{-b_w y} \ \text{W/CC}$$

$$q'''_I = q'''_{I_o} e^{-b_I x} \ \text{W/CC} \qquad I = 1, 2, 3$$

$$\theta = \tan^{-1} \frac{L}{2MR}$$

FIG 3.1 SCHEMATIC CROSS SECTION OF THE BREEDER ROD HEAT EXCHANGER

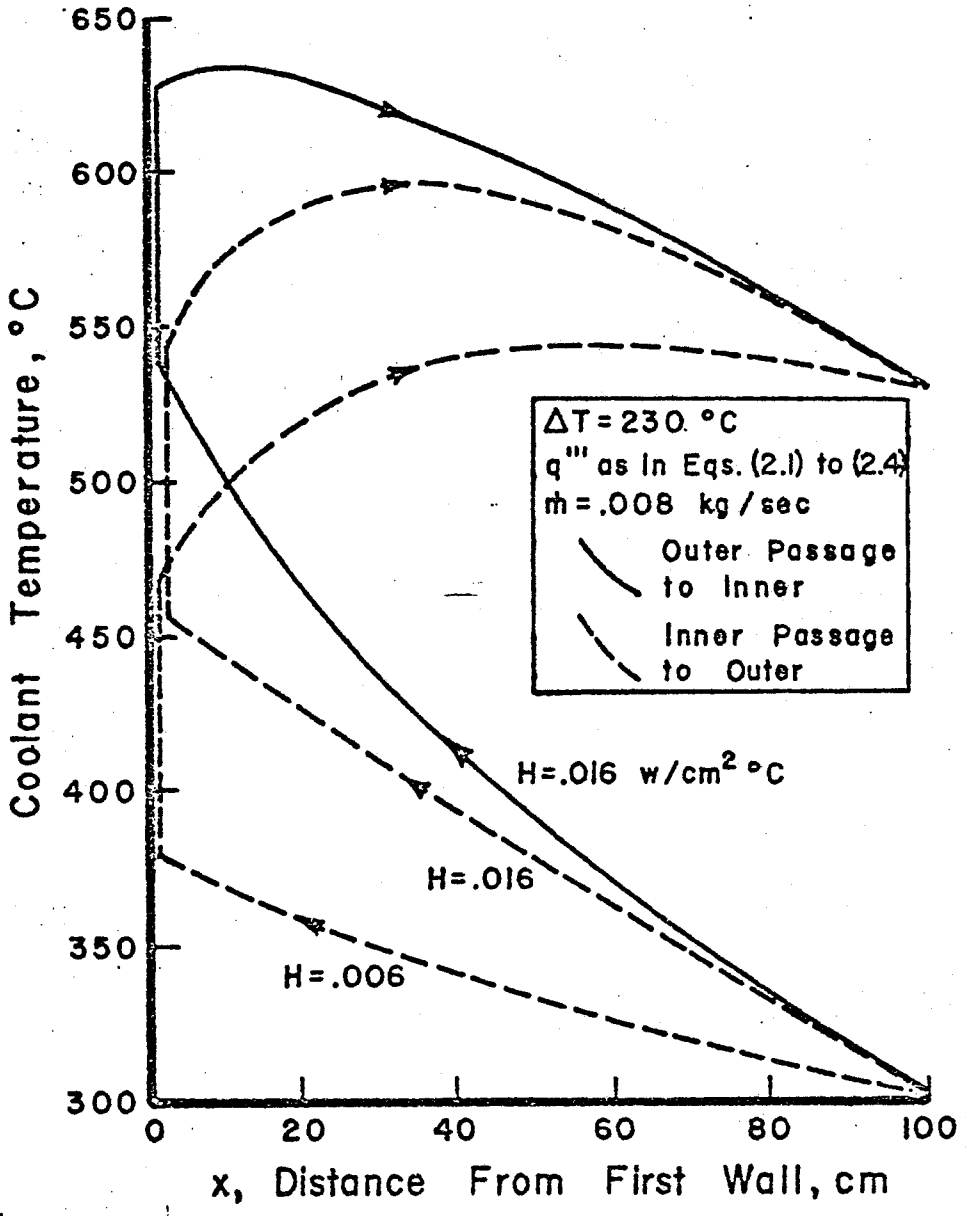

FIG 3.2 COOLANT TEMPERATURE vs. DISTANCE FROM FIRST WALL

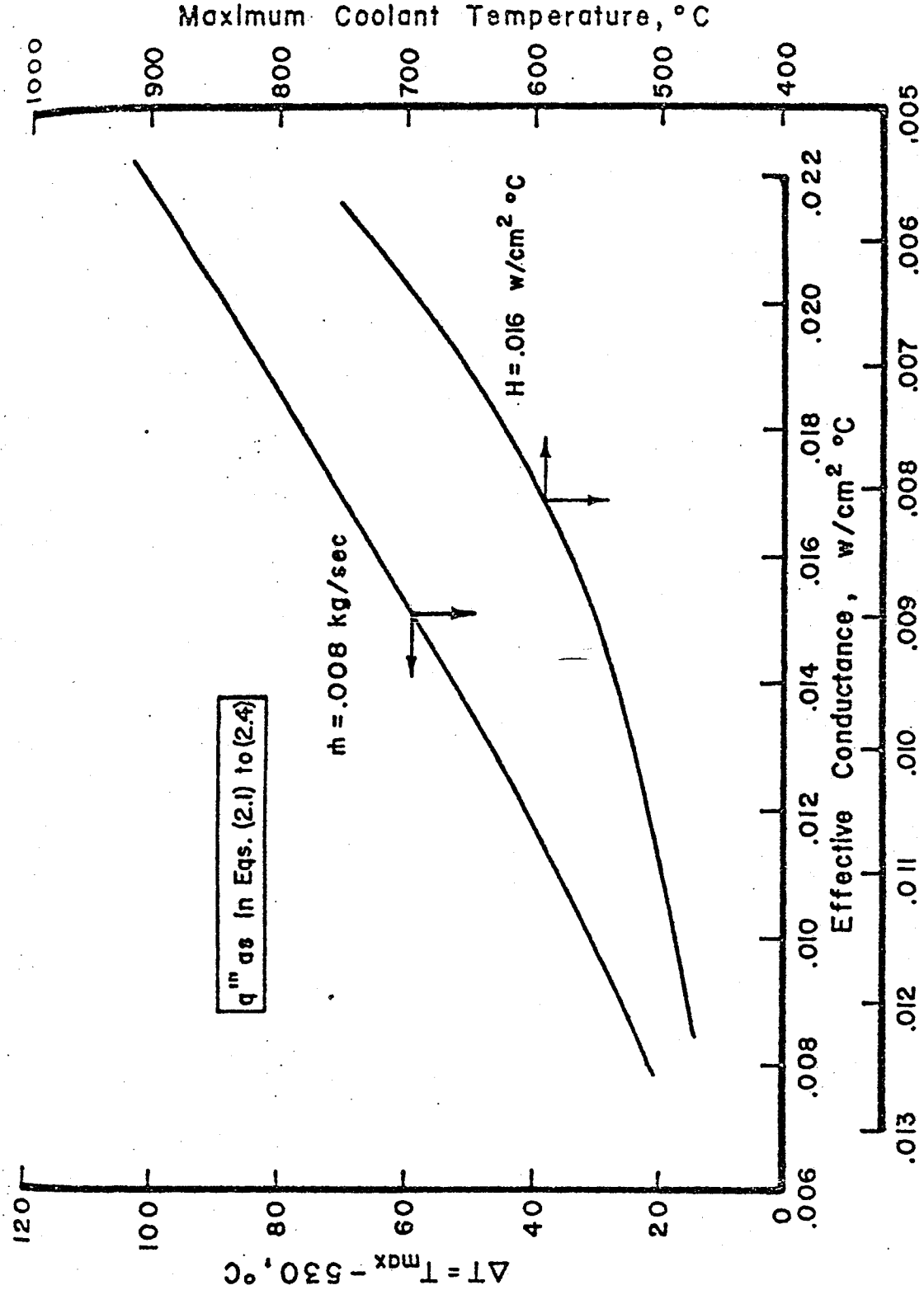

FIG. 3.4 MAXIMUM COOLANT TEMPERATURE vs. EFFECTIVE CONDUCTANCE AND MASS FLOW RATE

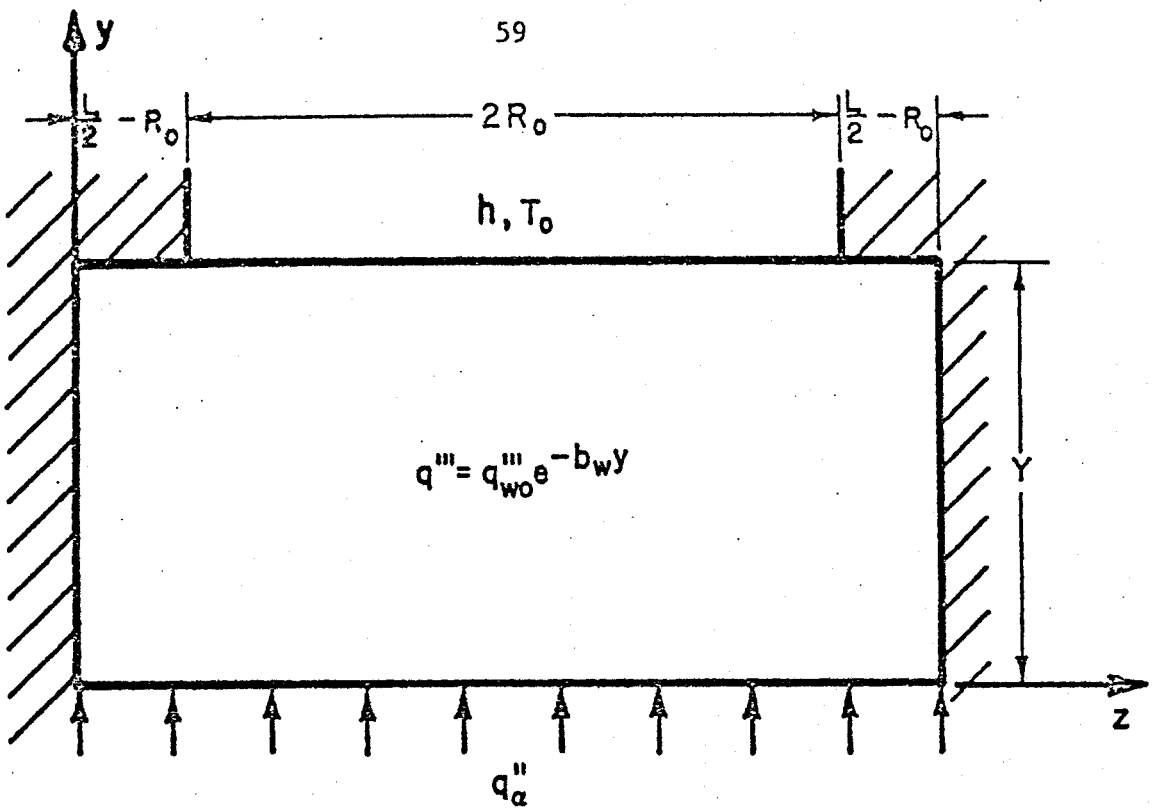

FIG. 3.5a SCHEMATIC OF THE GRAPHITE SHIELD

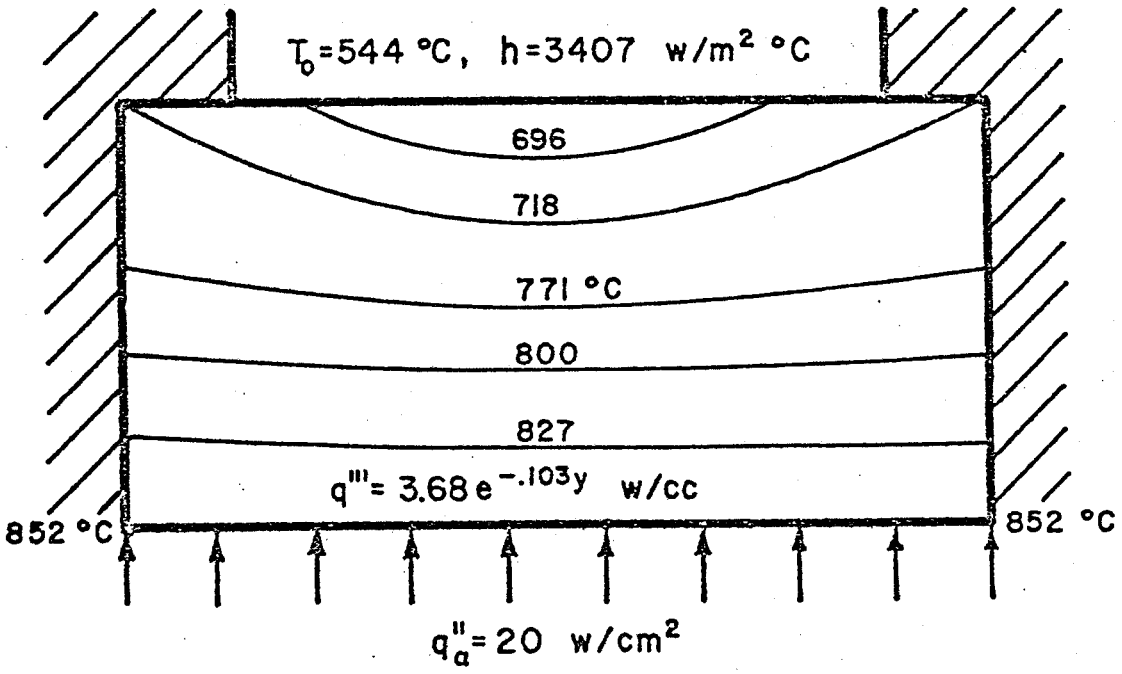

FIG. 3.5b ESTIMATED GRAPHITE SHIELD TEMPERATURE PROFILE

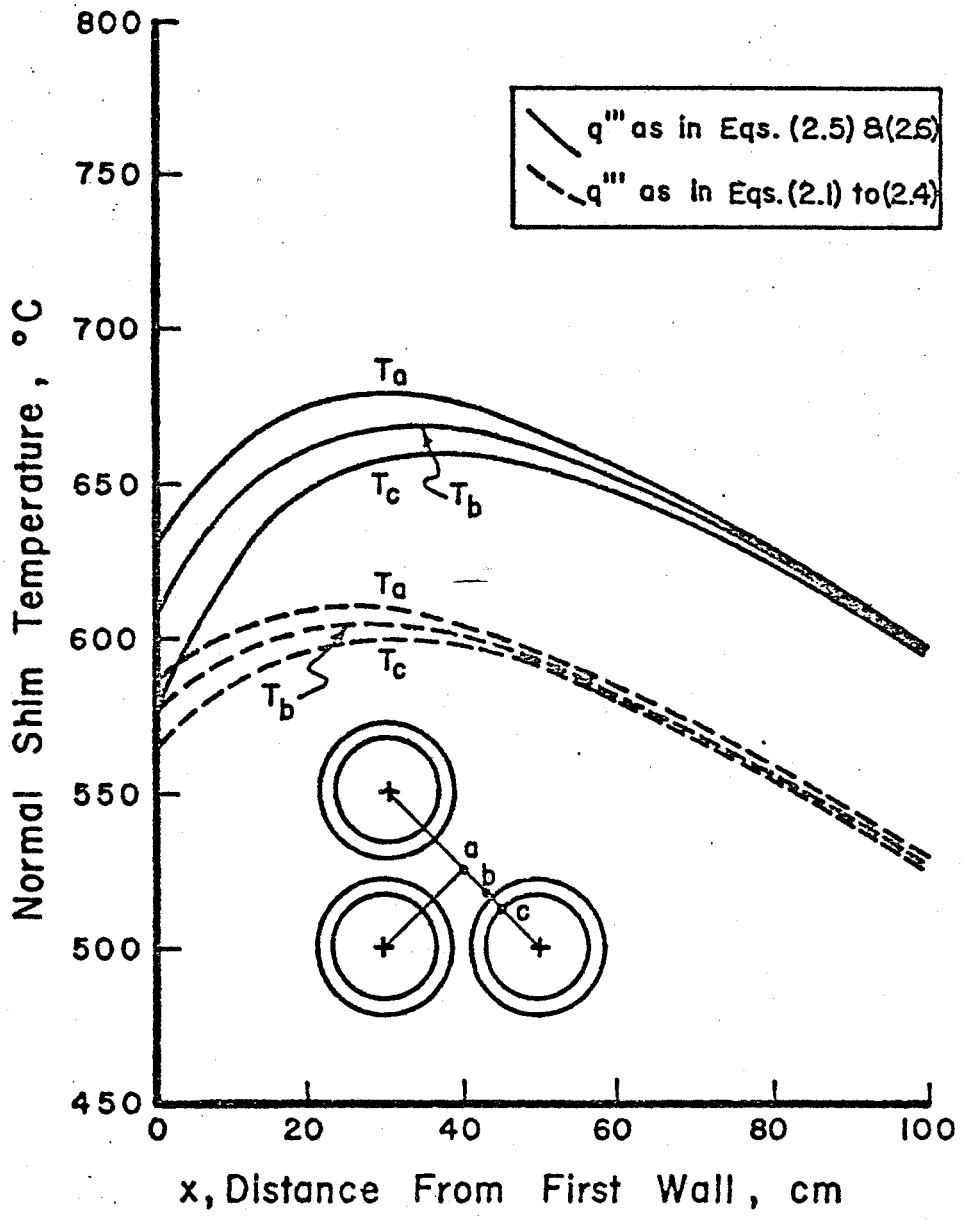

FIG. 3.6 NORMAL SHIM TEMPERATURE PROFILE vs. DISTANCE FROM FIRST WALL

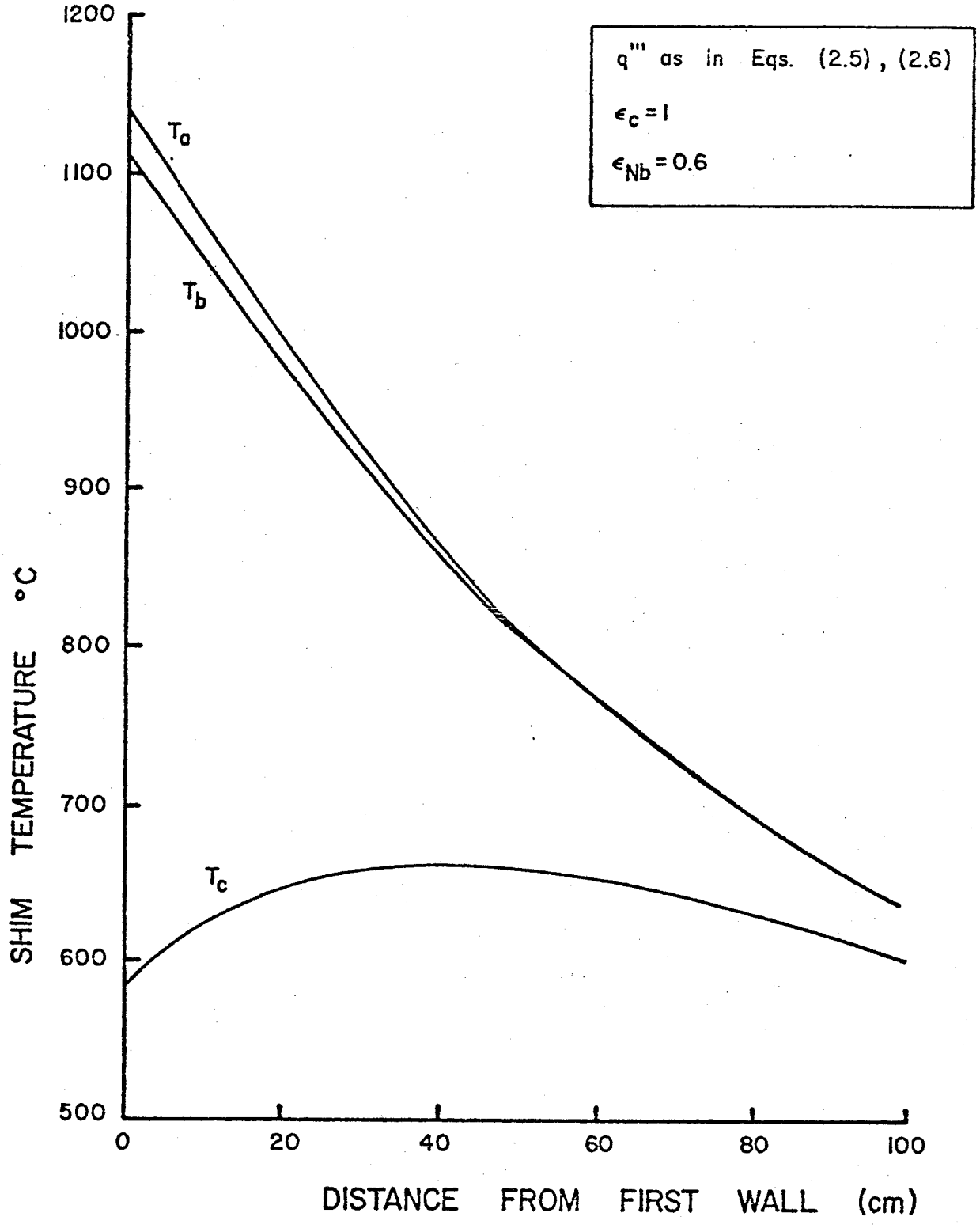

FIGURE 3.7: NORMAL SHIM TEMPERATURE PROFILE VS. DISTANCE FROM FIRST WALL (No Contact with Breeder Rod)

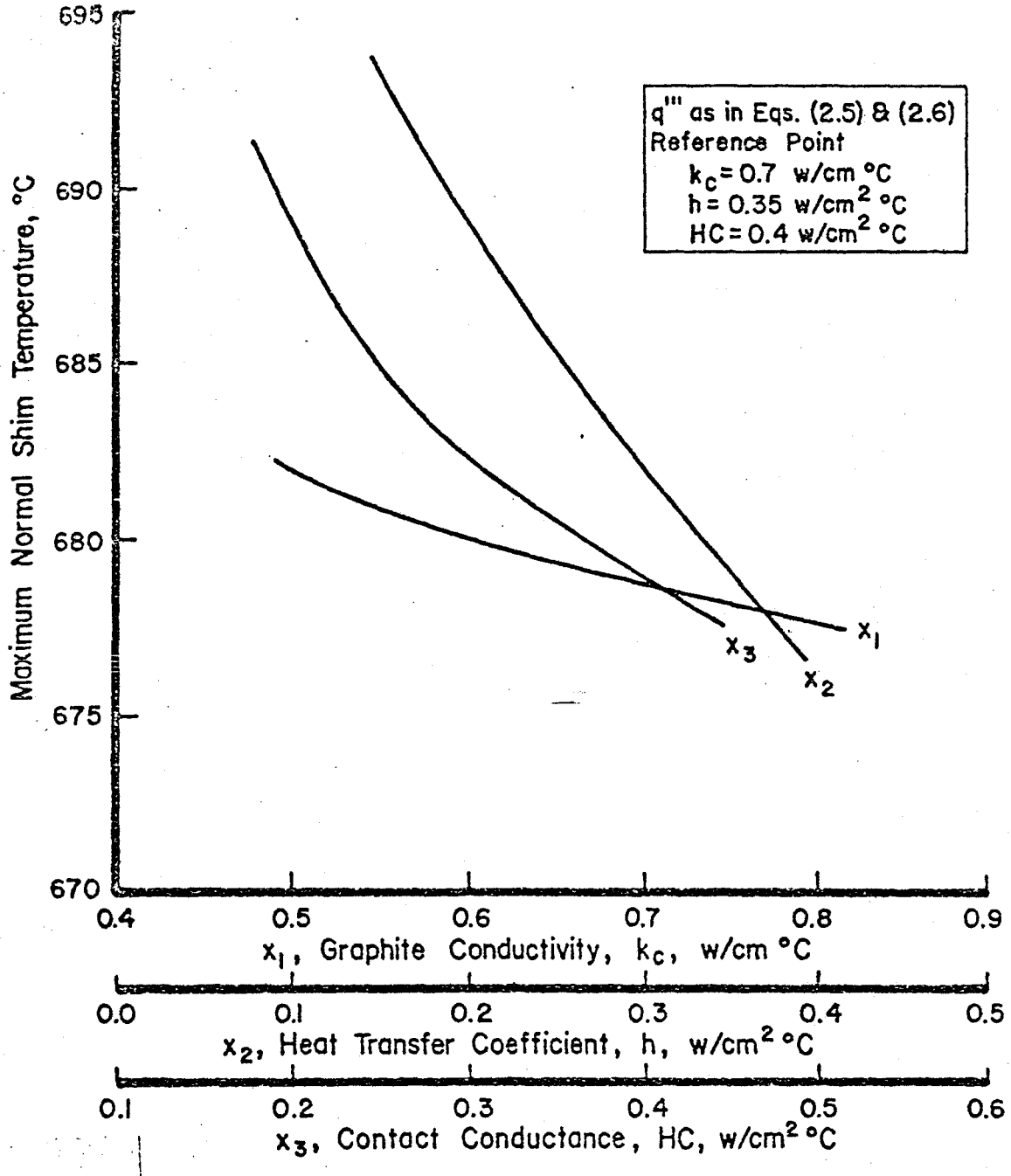

FIG 3.8 MAXIMUM NORMAL SHIM TEMPERATURE vs. k_c, h AND HC

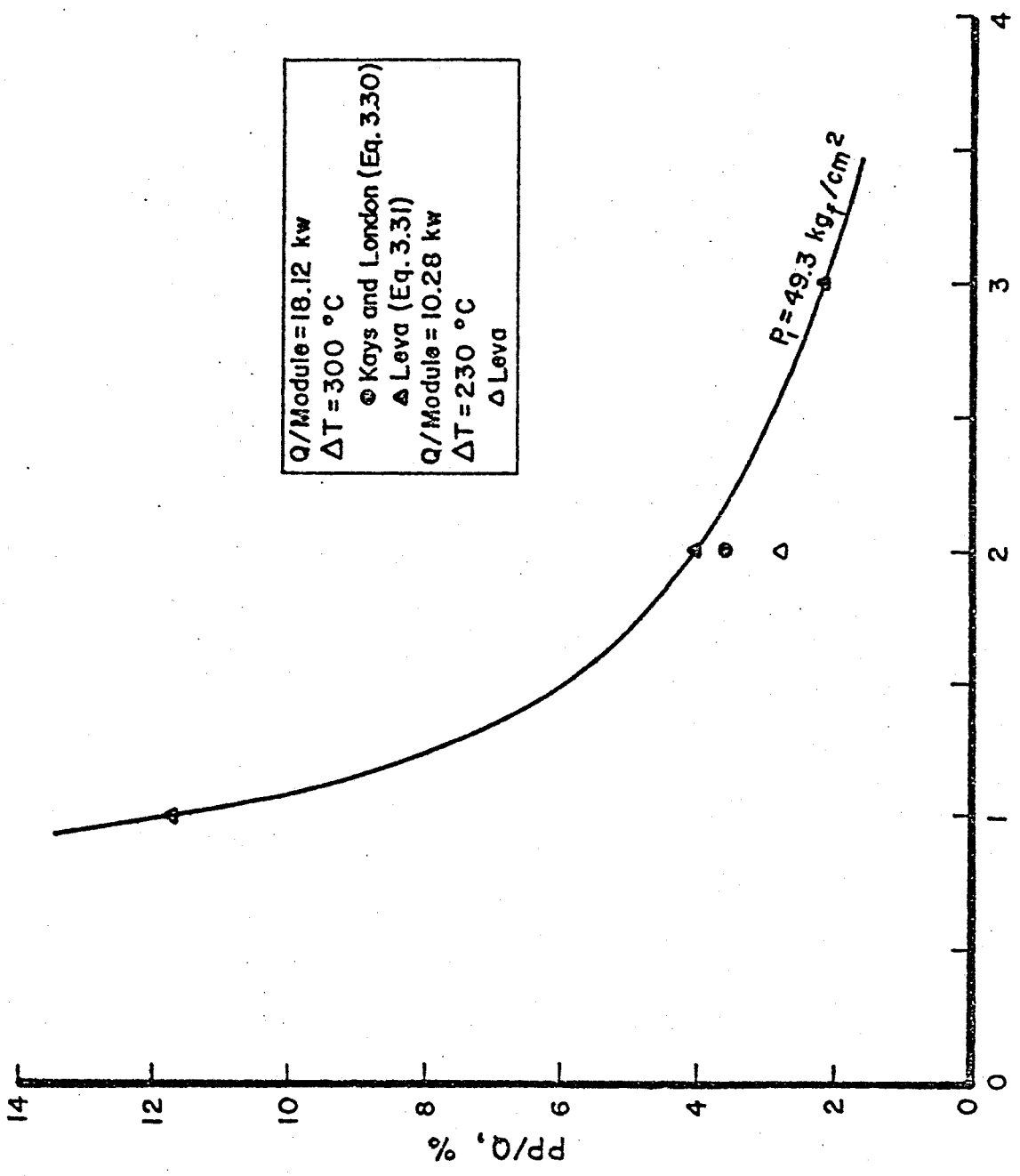

FIG. 3.9 PUMPING POWER TO HEAT REMOVAL RATIO vs. PELLET RADIUS

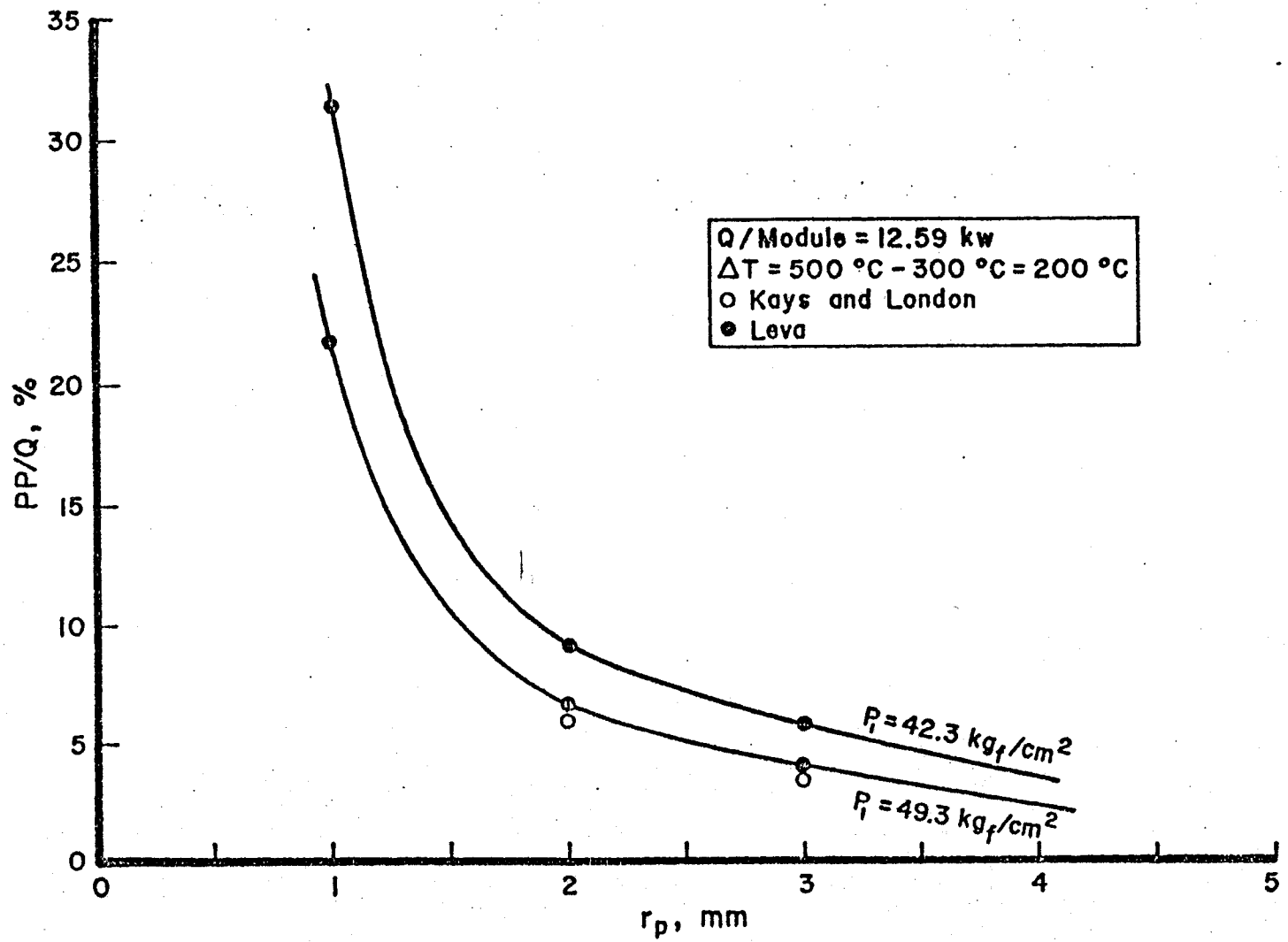

FIG.3.10 PUMPING POWER TO HEAT REMOVAL RATIO vs. PELLET RADIUS

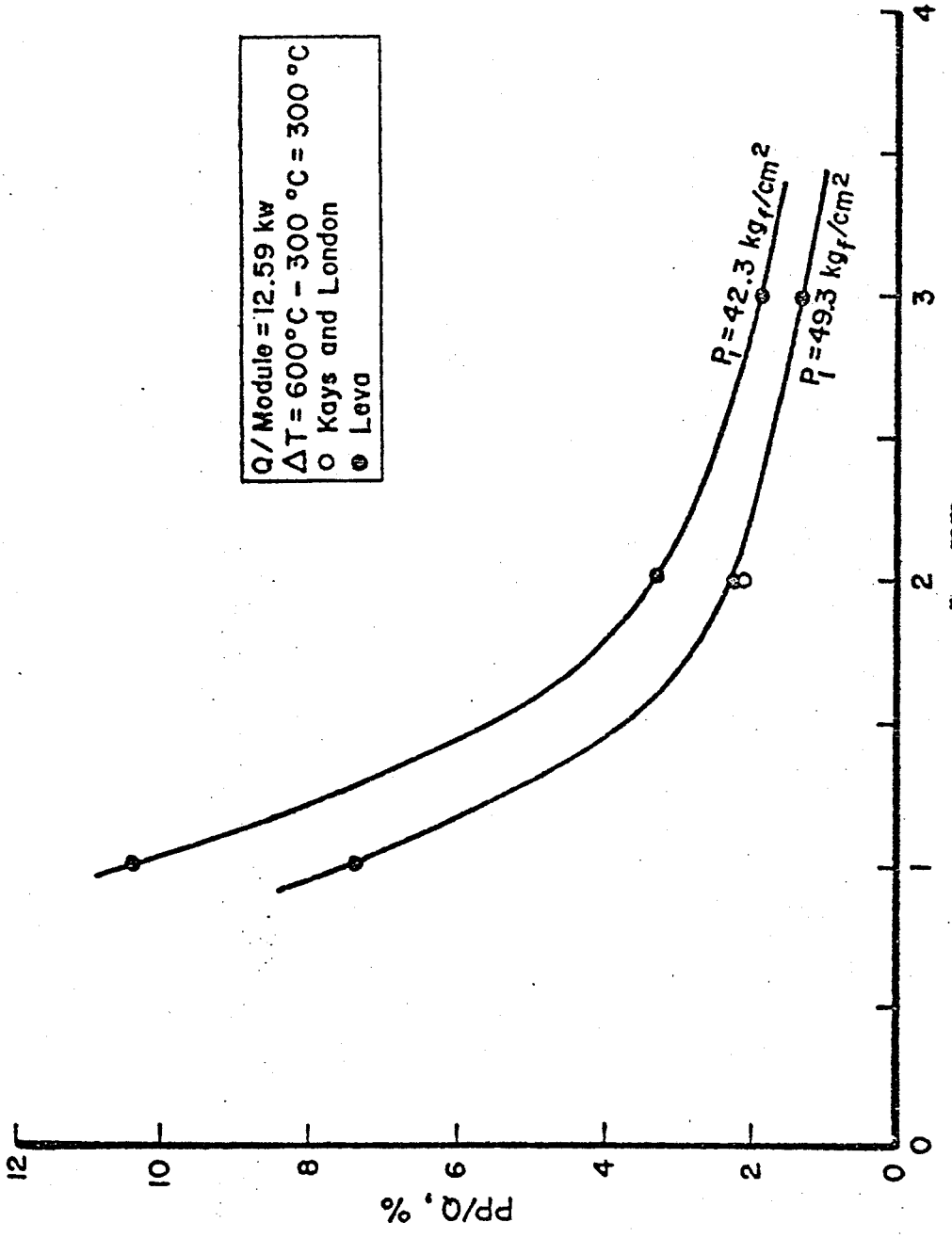

FIG. 3.11 PUMPING POWER TO HEAT REMOVAL RATIO vs. PELLET RADIUS

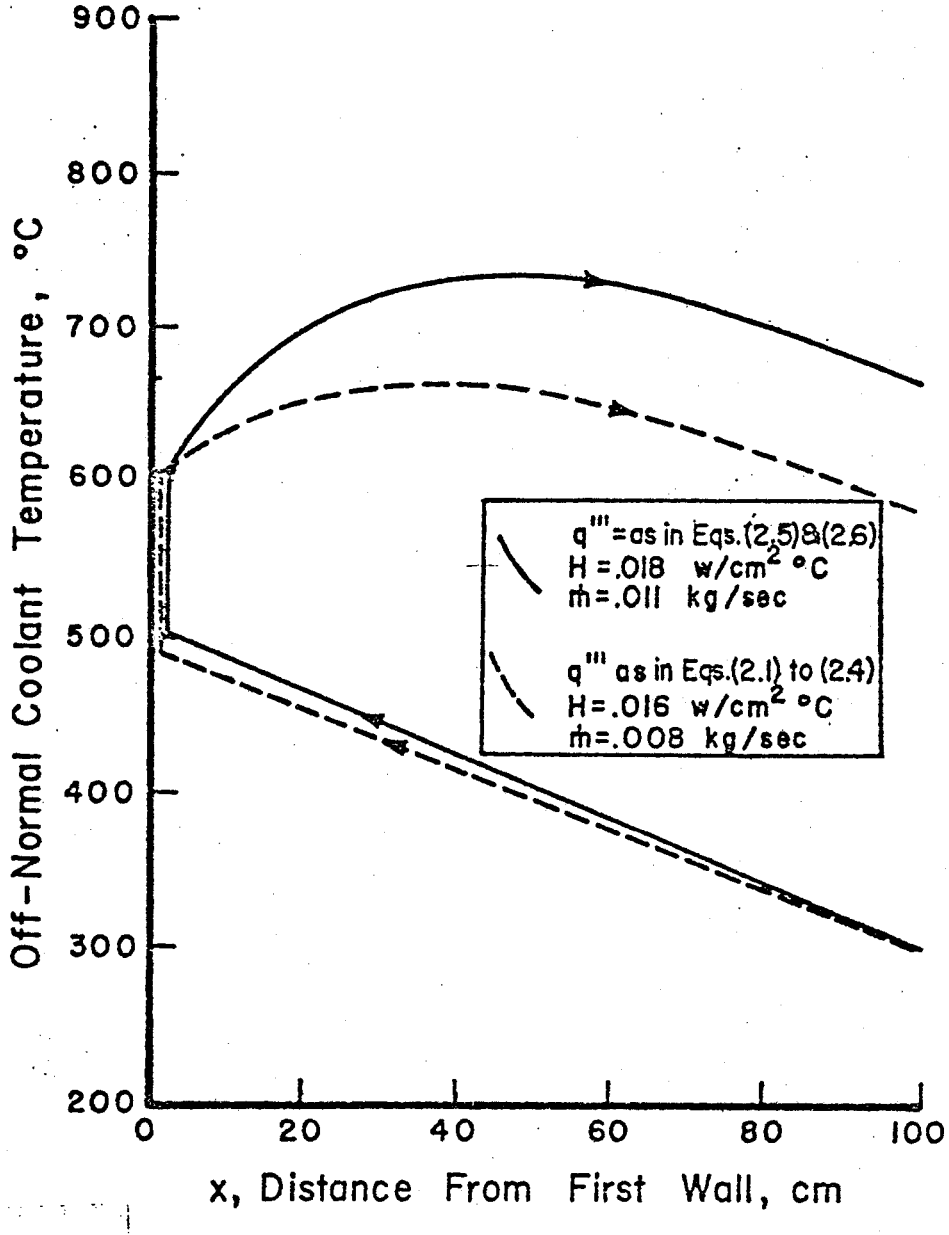

FIG. 4.1 OFF-NORMAL COOLANT TEMPERATURE PROFILE FOR THE CASE OF INNER TO OUTER PASSAGE ROUTING vs. DISTANCE FROM FIRST WALL

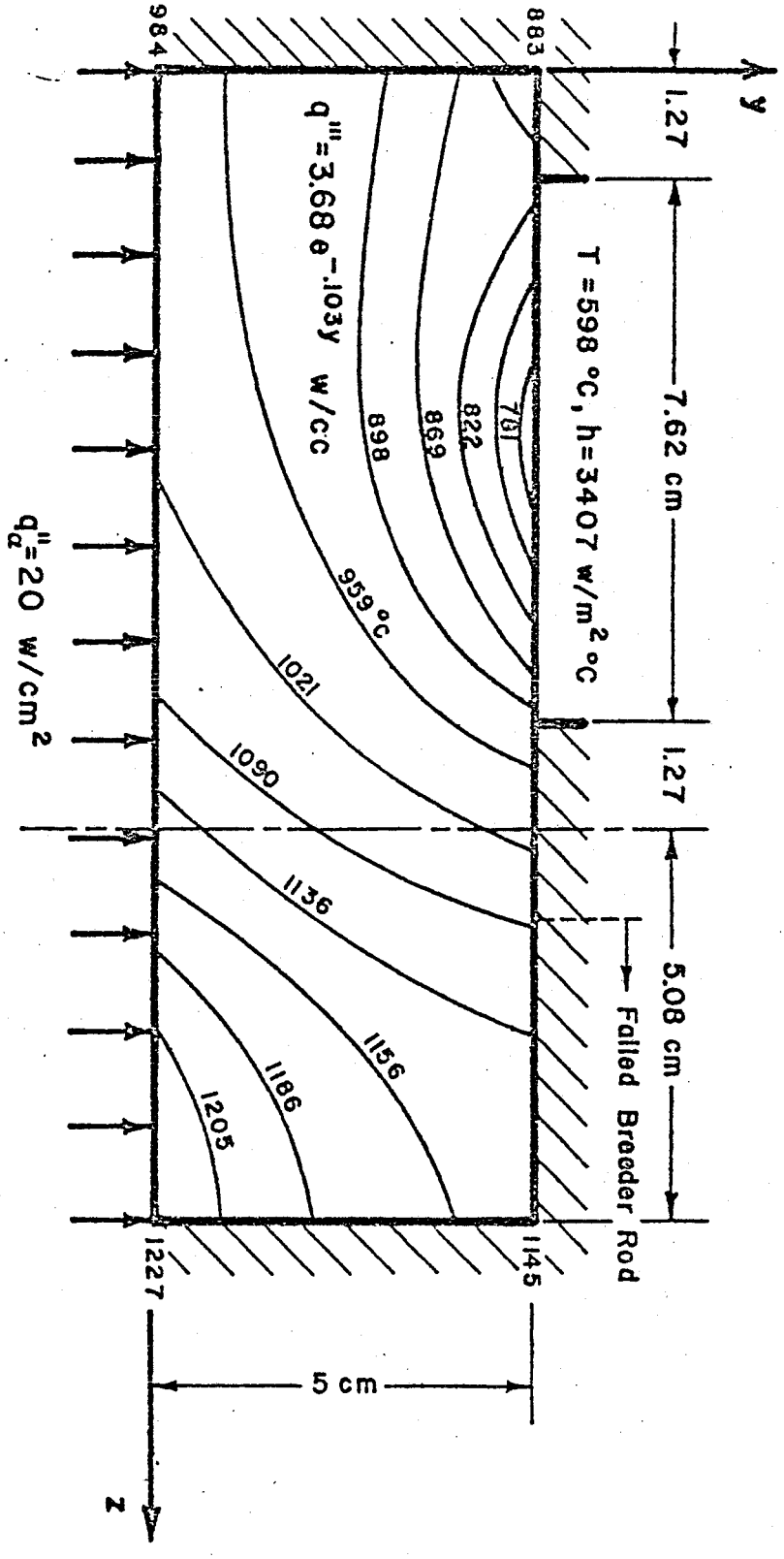

FIG. 4.2 ESTIMATED OFF-NORMAL GRAPHITE SHIELD TEMPERATURE PROFILE

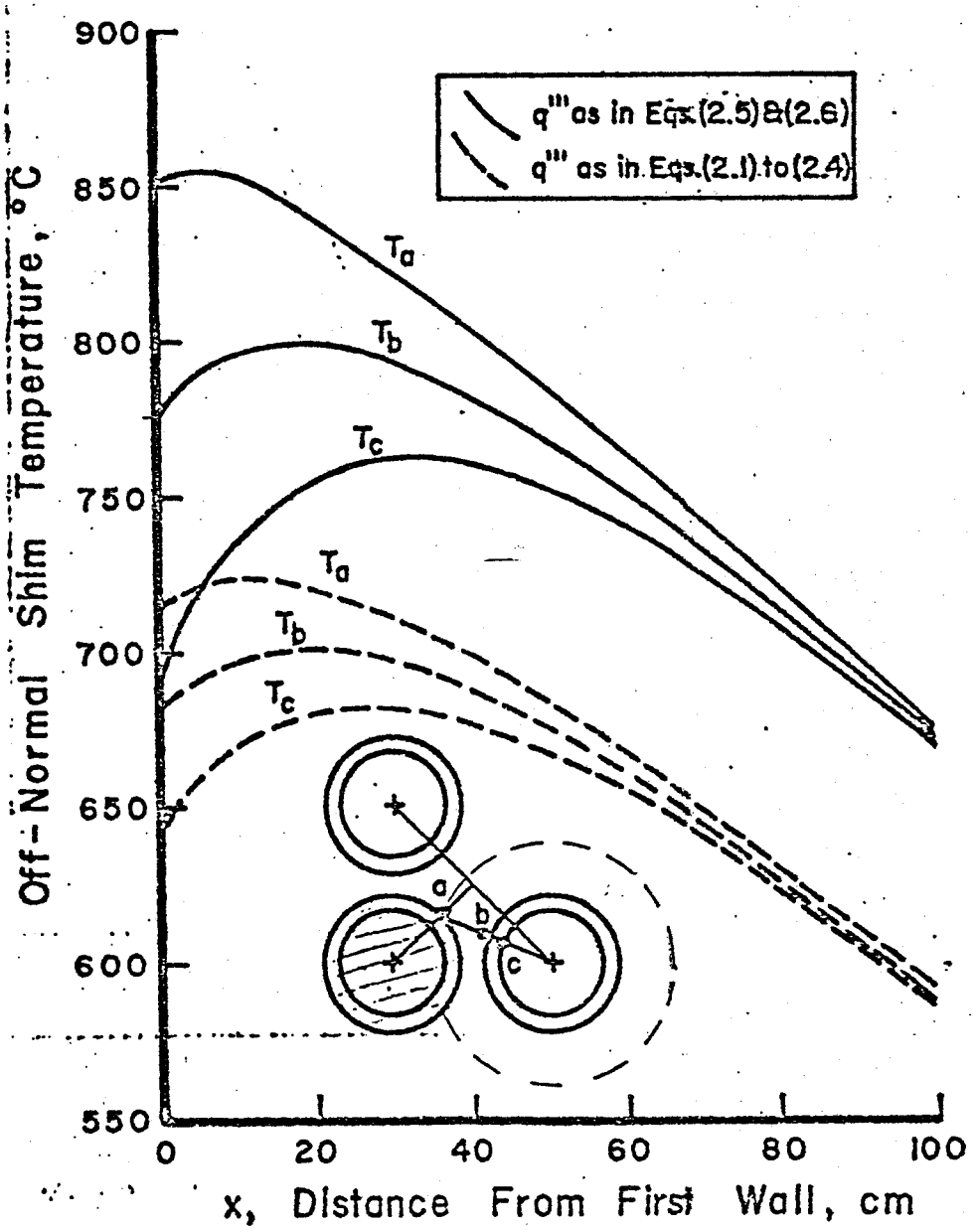

FIG. 4.3 OFF-NORMAL SHIM TEMPERATURE PROFILE vs. DISTANCE FROM FIRST WALL

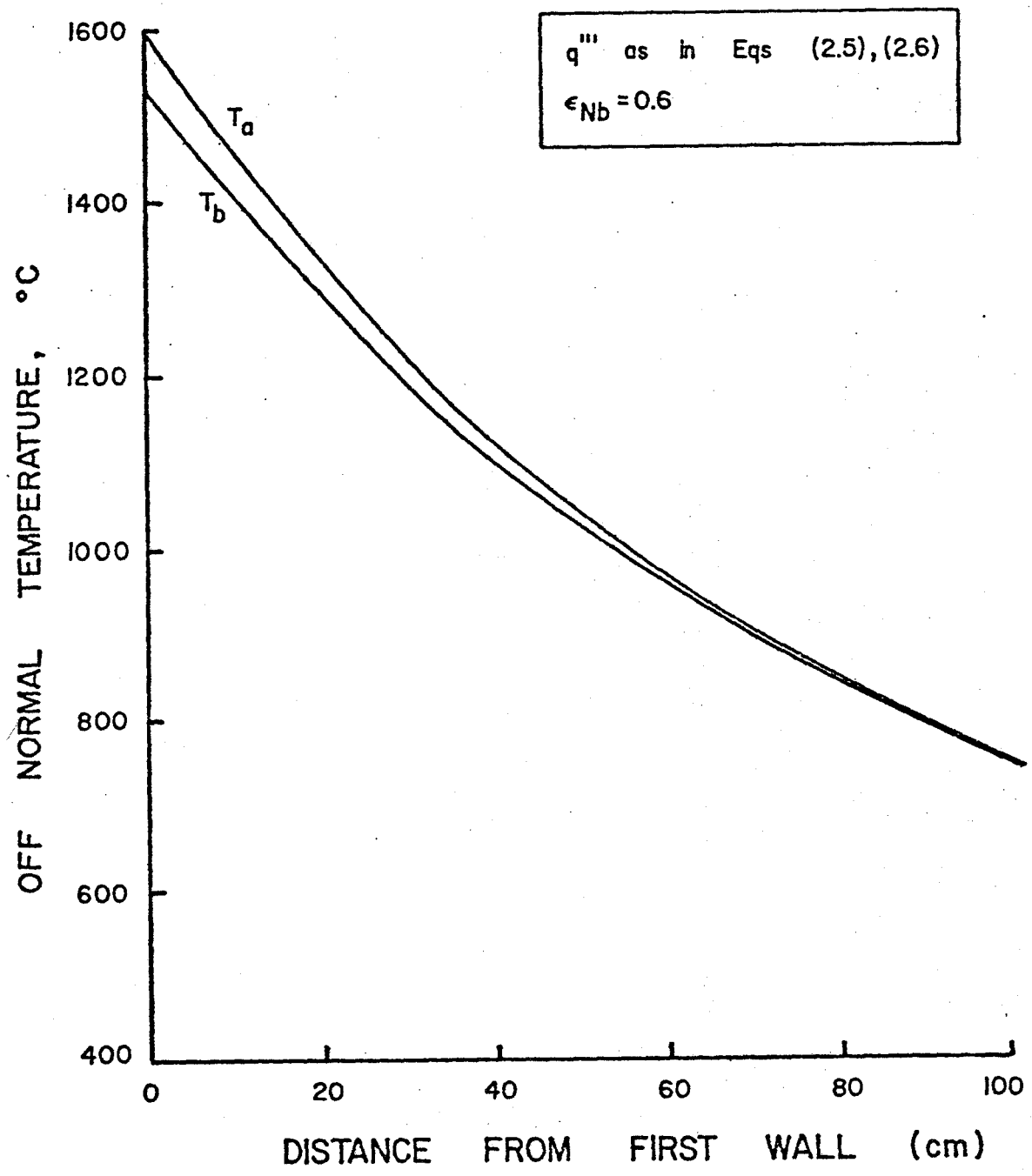

FIG. 4.4 OFF NORMAL SHIM TEMPERATURE PROFILE VS. DISTANCE FROM THE FIRST WALL (RADIATIVE BOUNDARY)

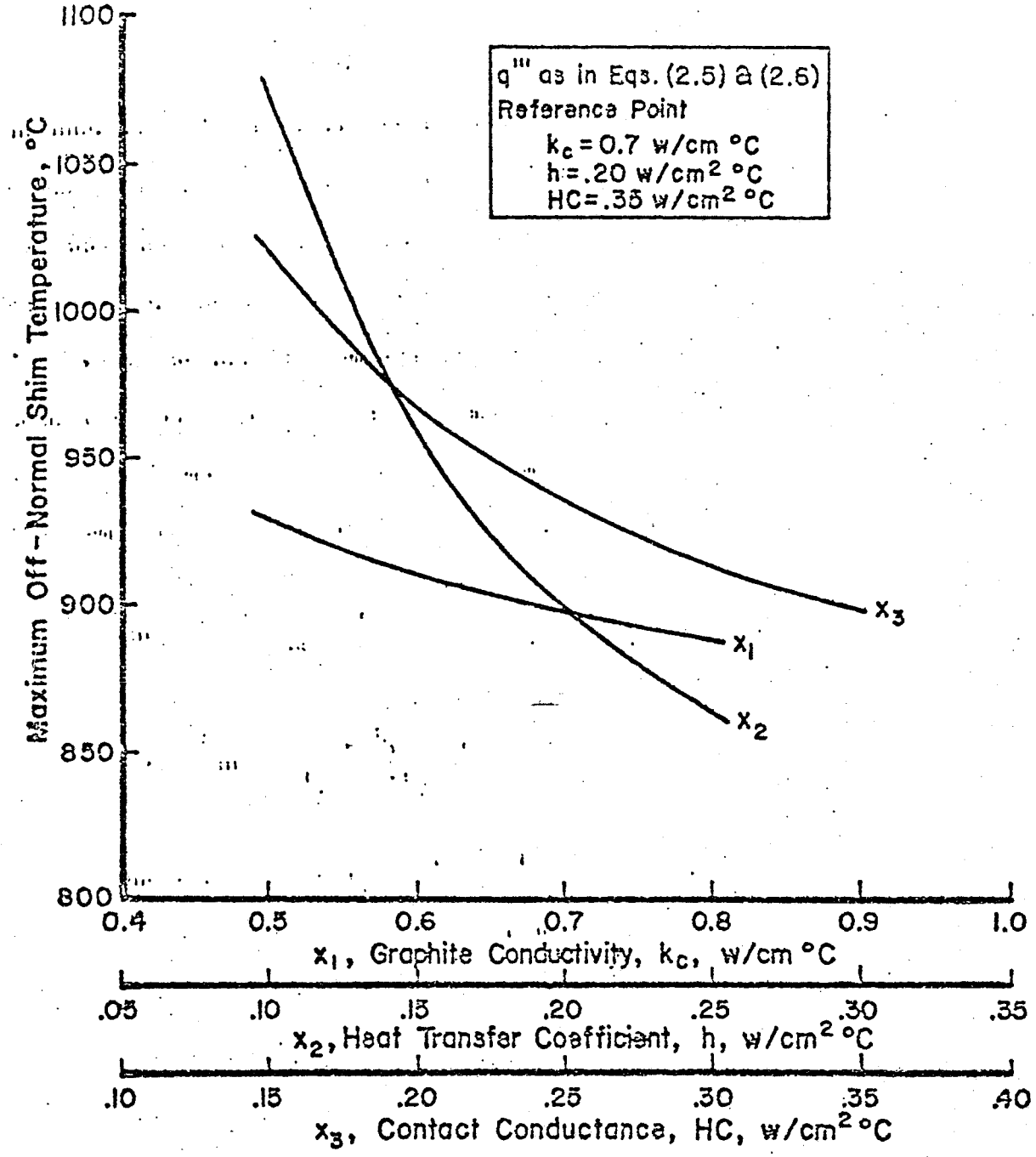

FIG. 4.5 MAXIMUM OFF-NORMAL SHIM TEMPERATURE vs. k_c, h & HC

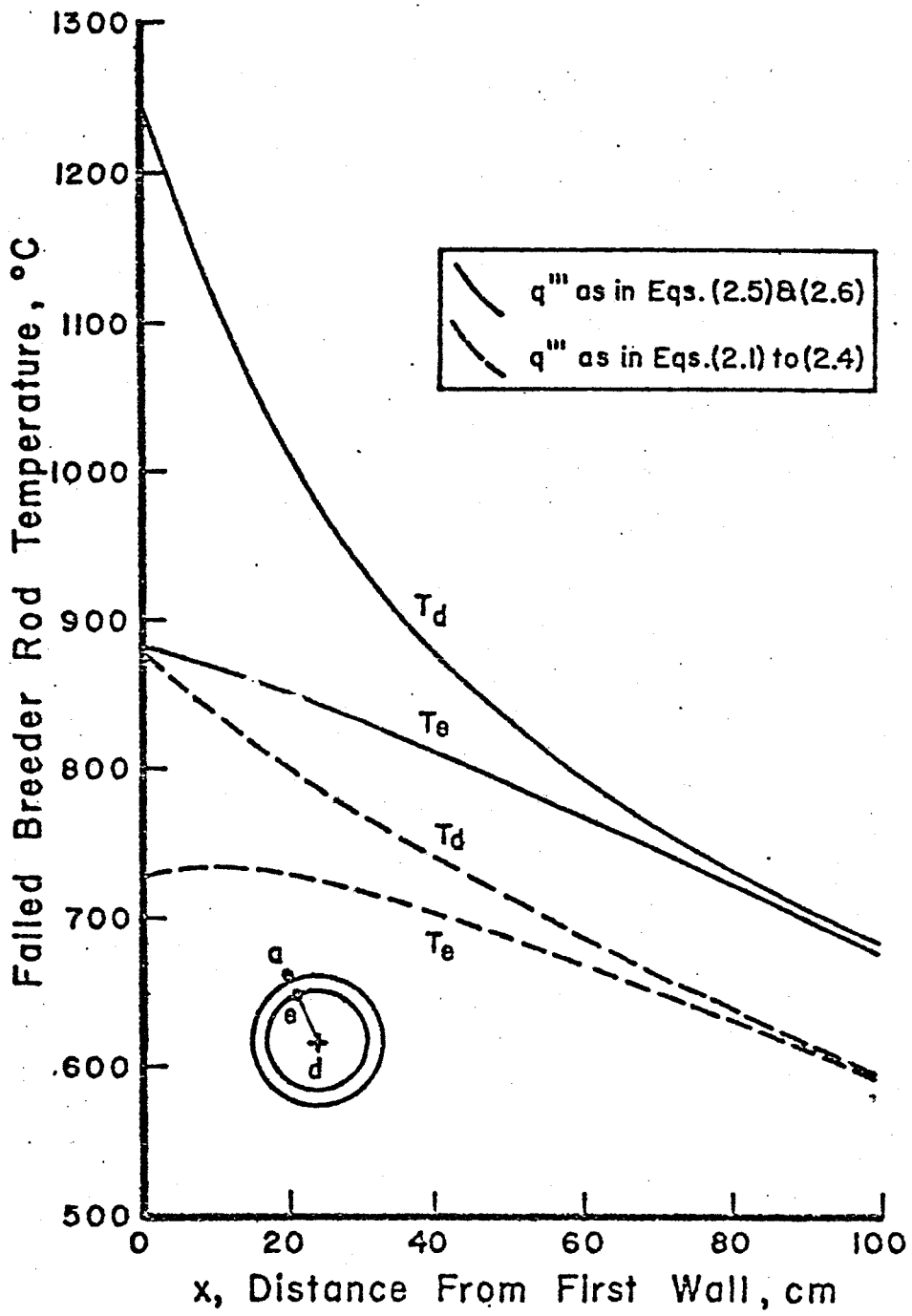

FIG. 4.6 FAILED MODULE TEMPERATURE PROFILE vs. DISTANCE FROM FIRST WALL

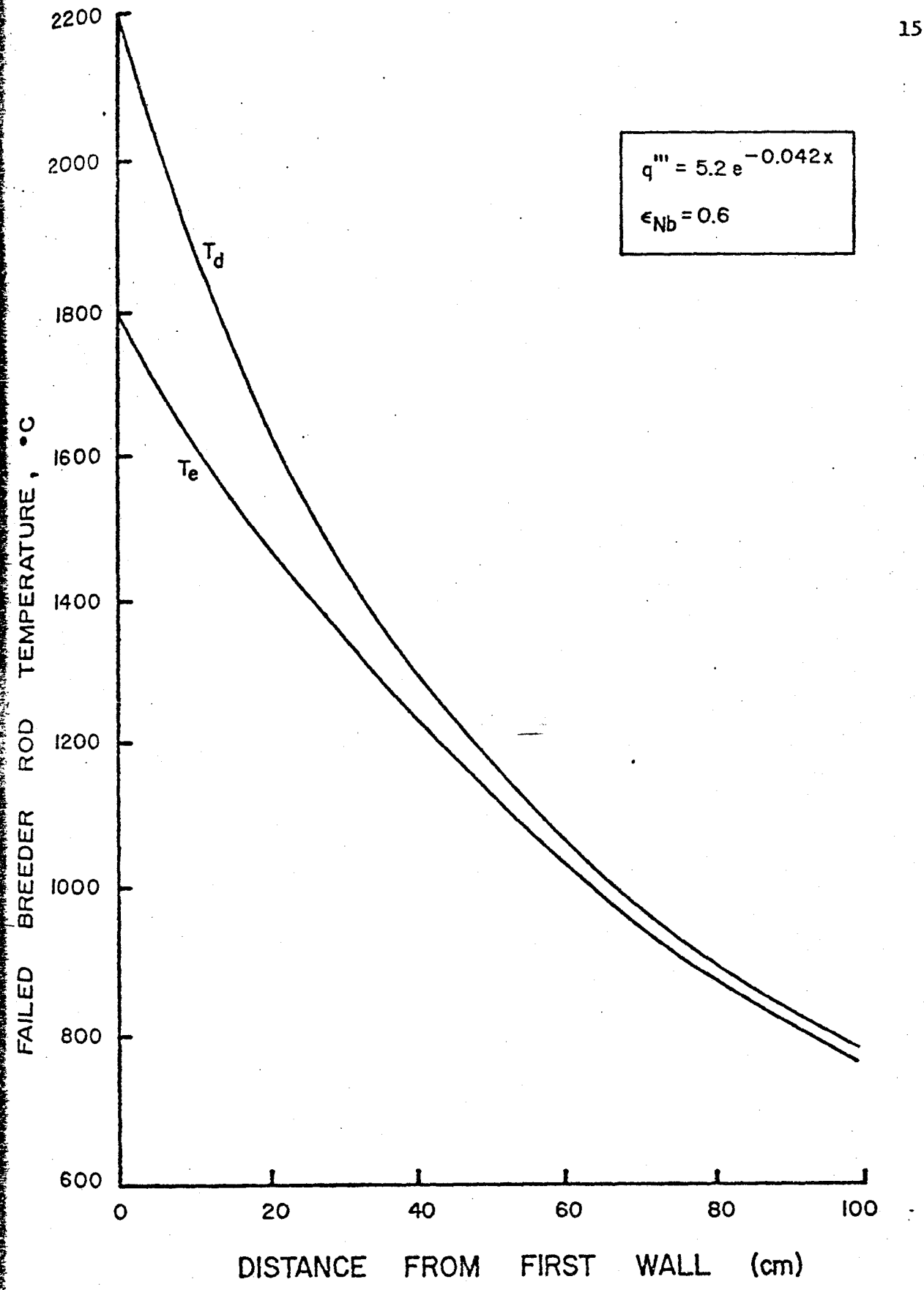

FIG. 4.7 FAILED MODULE TEMPERATURE PROFILE VS. DISTANCE FROM FIRST WALL (RADIATIVE BOUNDARY CONDITION)

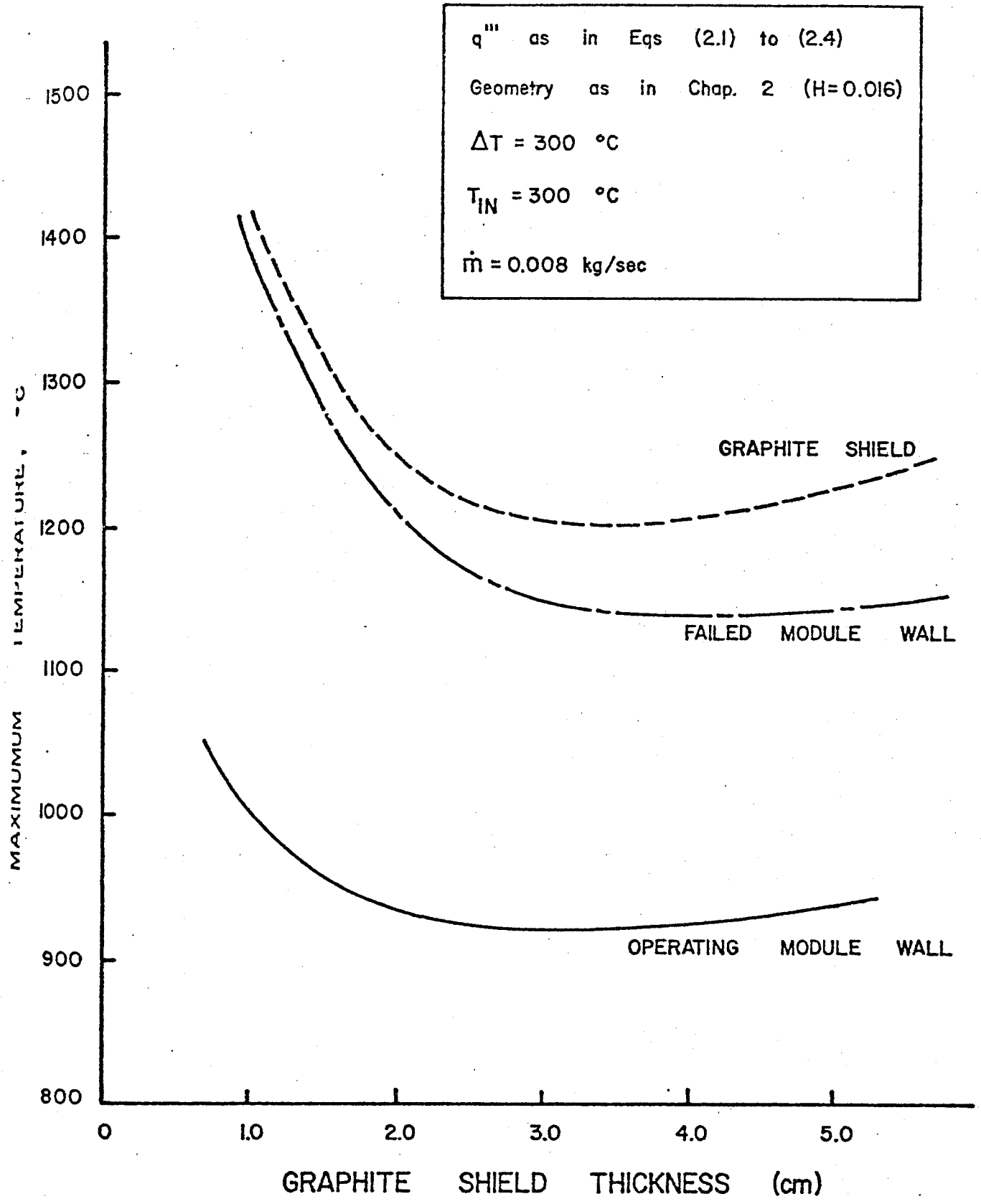

FIG. 5.1 MAXIMUM TEMPERATURES vs. GRAPHITE SHIELD THICKNESS

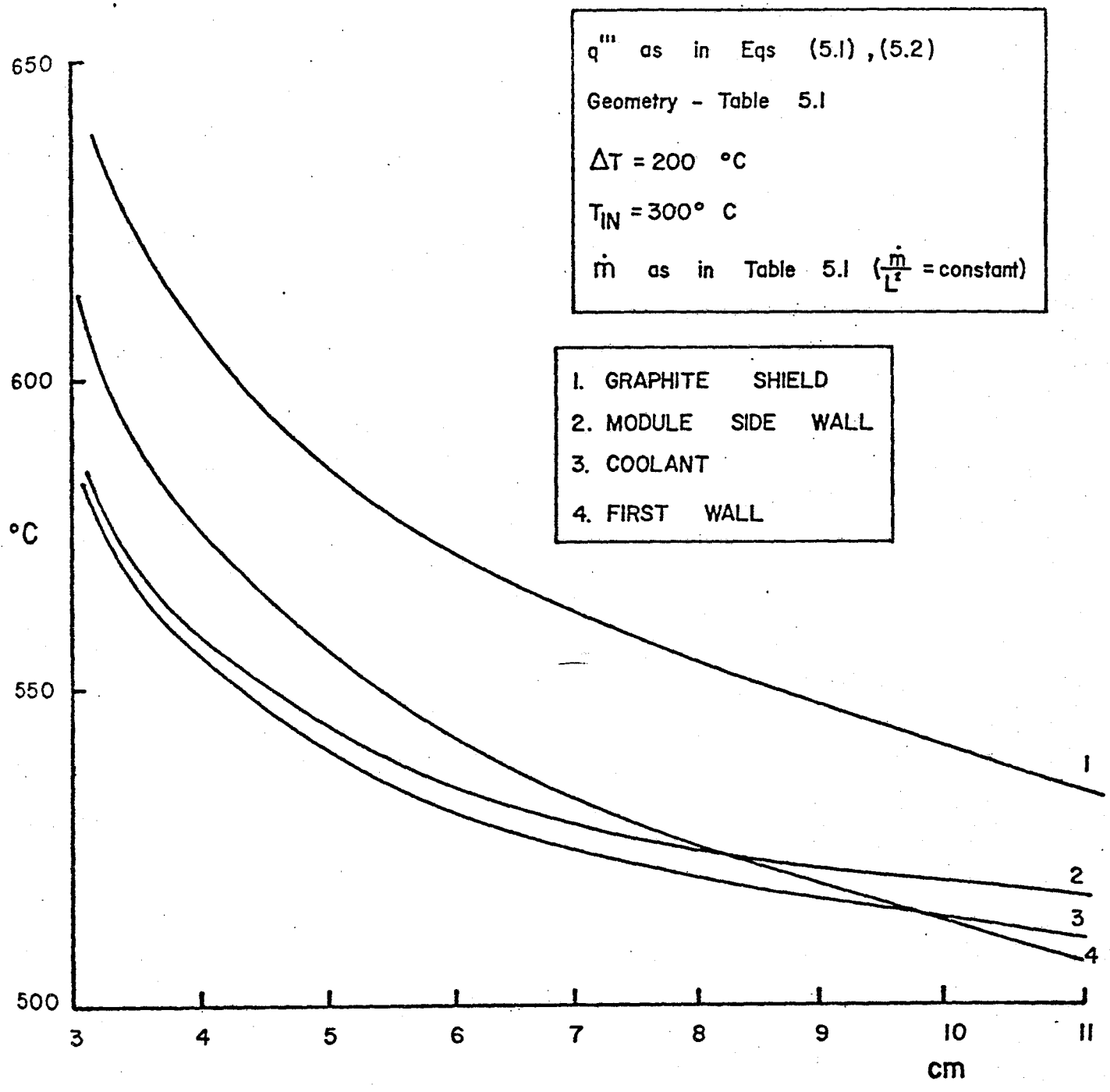

FIG. 5.2 MAXIMUM TEMPERATURE FOR NORMAL OPERATION vs. MODULE RADIUS

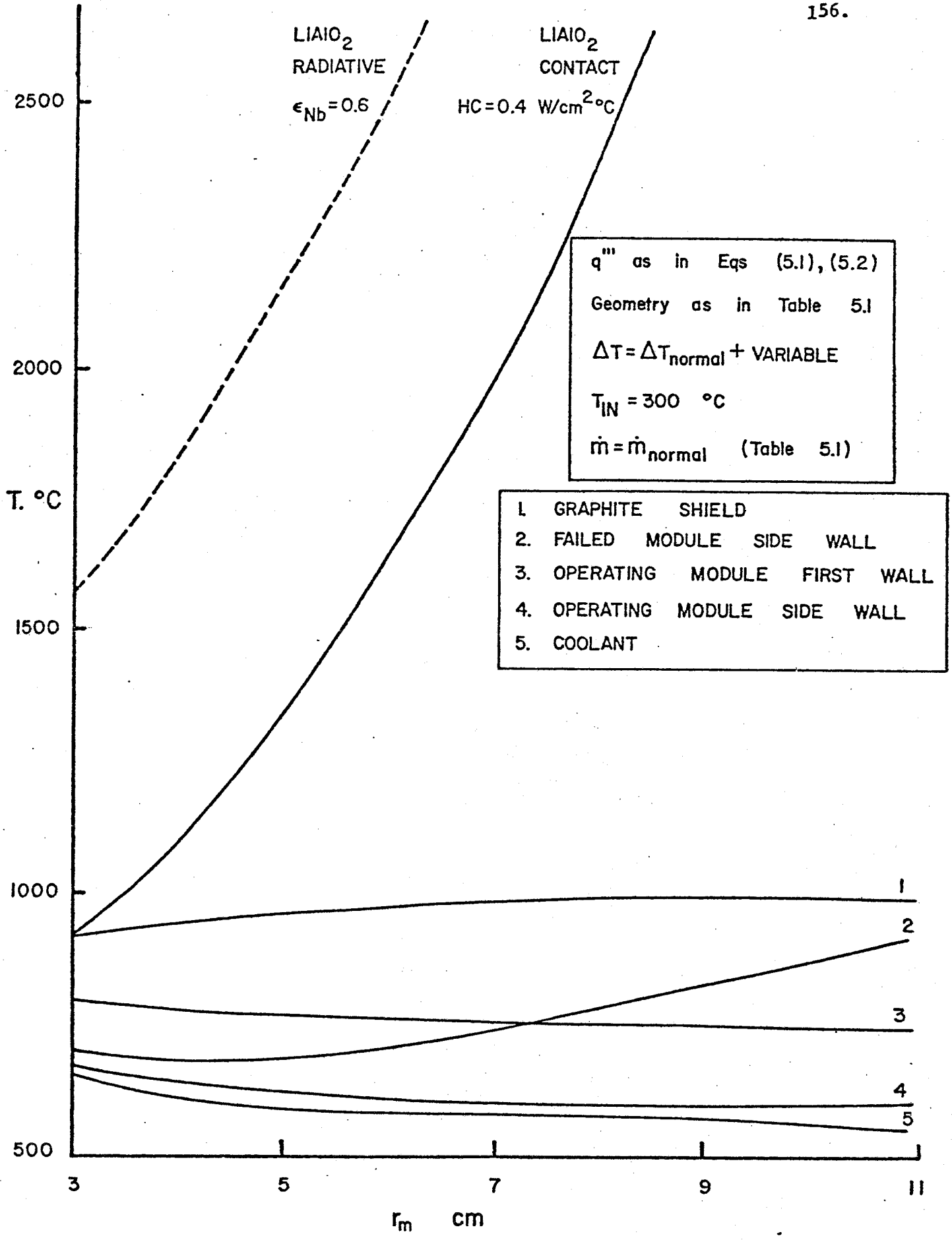

FIG. 5.3 MAXIMUM TEMPERATURES vs. MODULE RADIUS OFF NORMAL

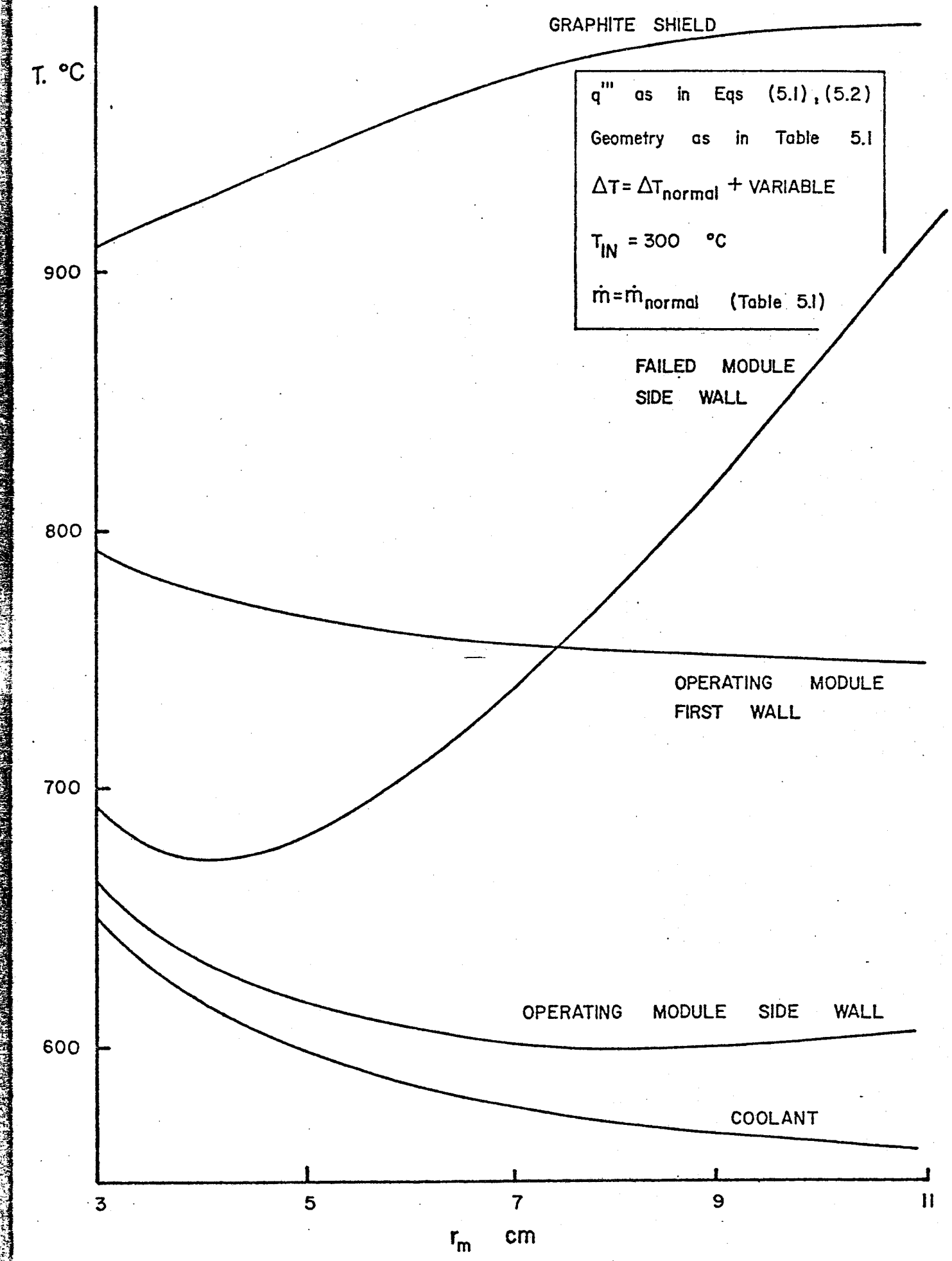

FIG. 5.4 MAXIMUM TEMPERATURES vs. MODULE RADIUS OFF NORMAL

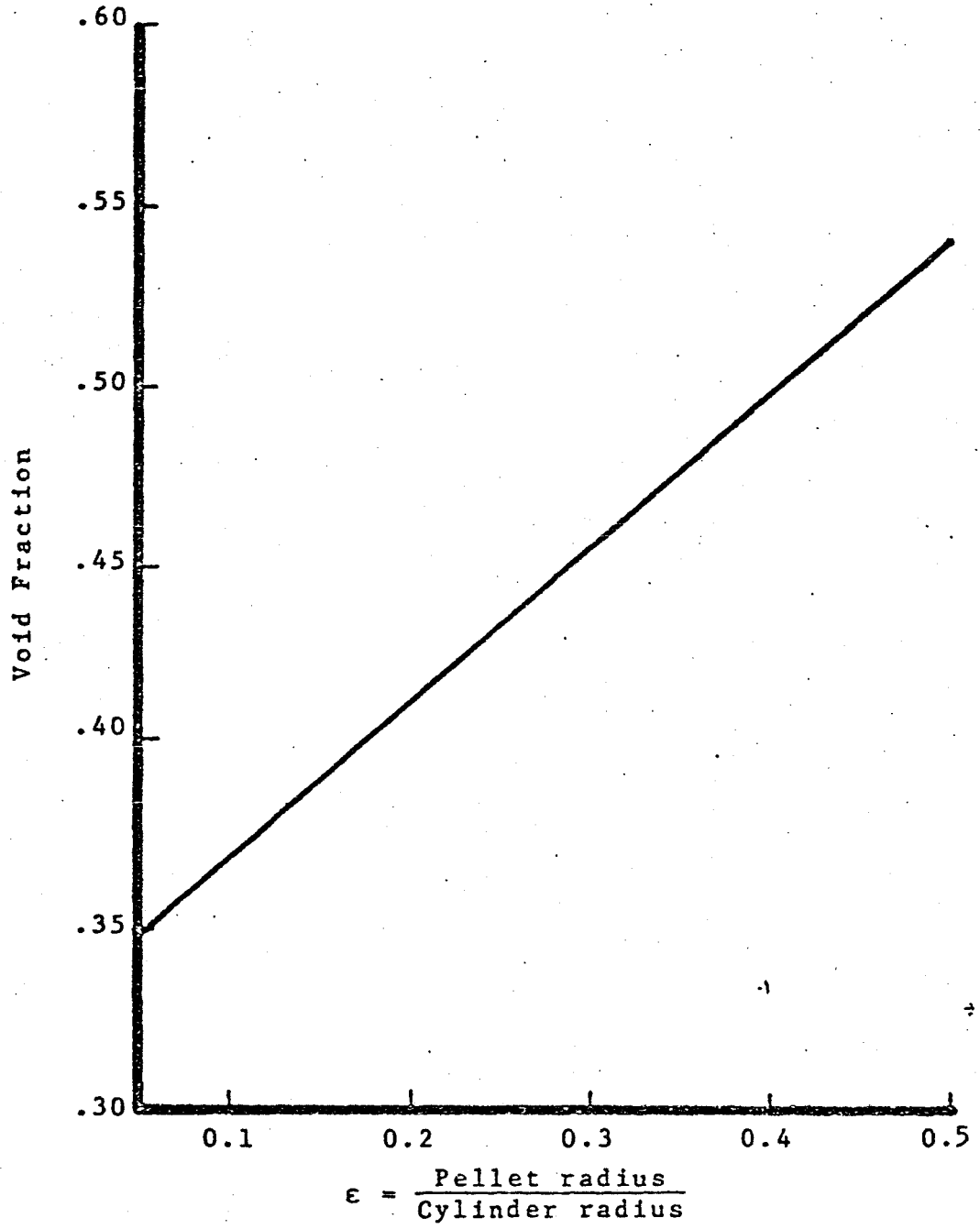

Fig. 6.1 Void Fraction vs ε.

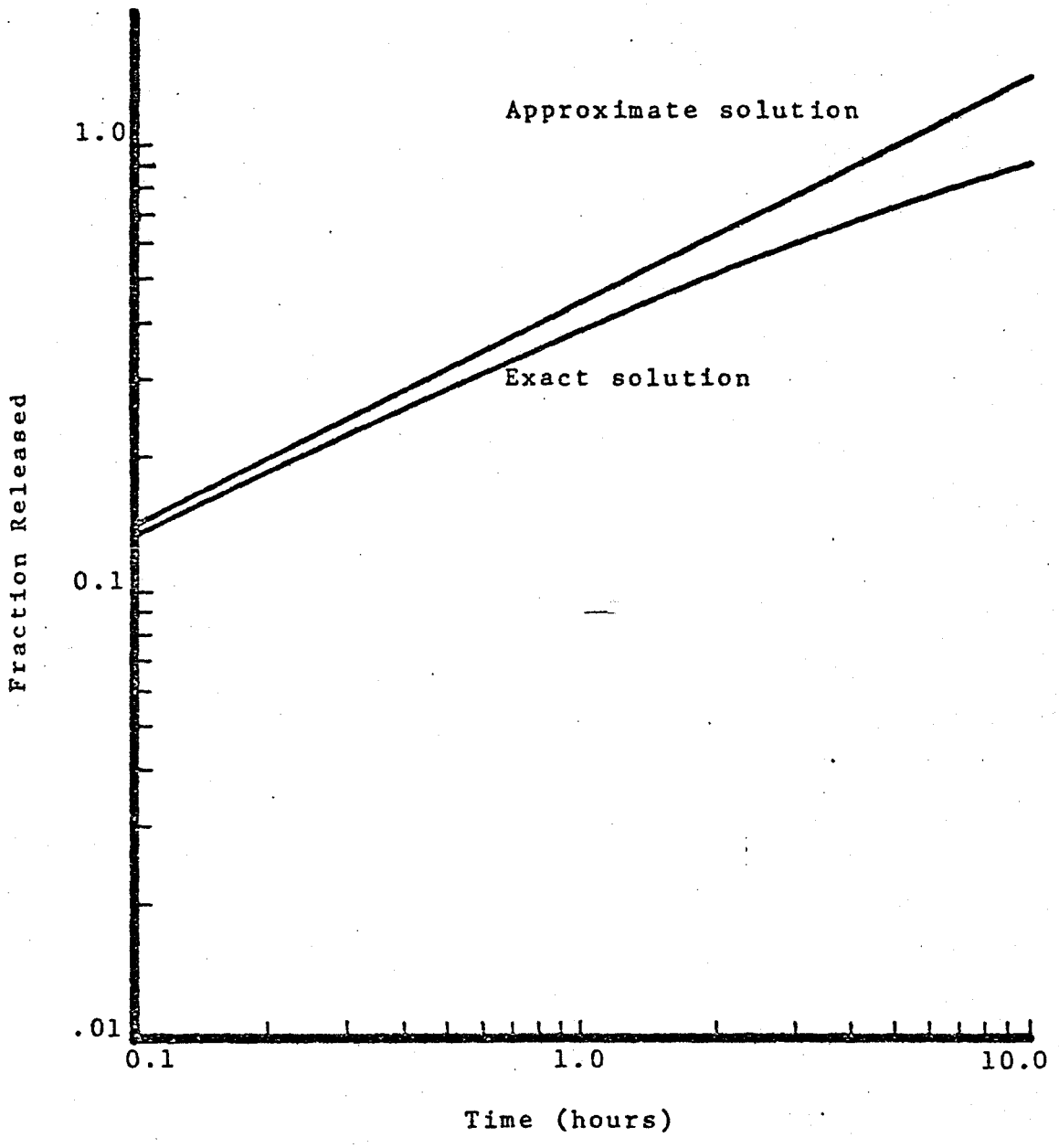

Fig. 6.2 Fractional Release of T_2 from $LiAlO_2$ vs Time

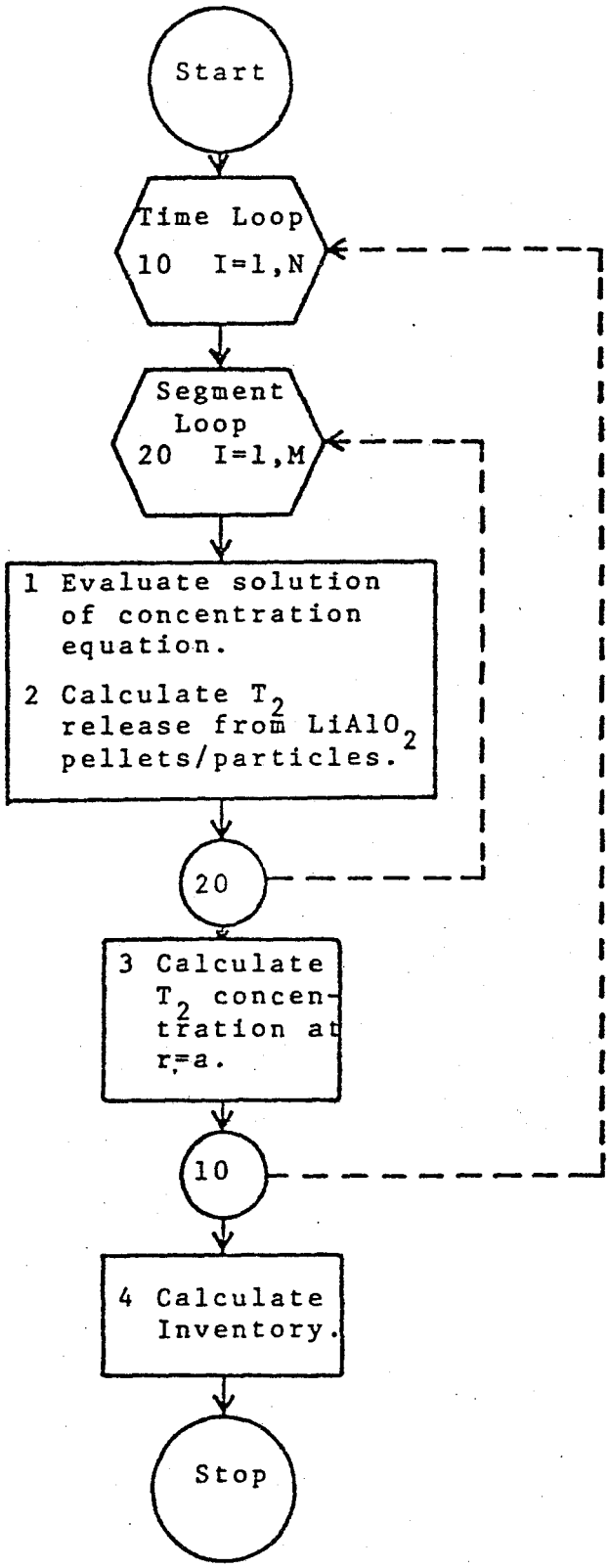

Fig. 6.3 Simplified TRIPORT Flowchart.

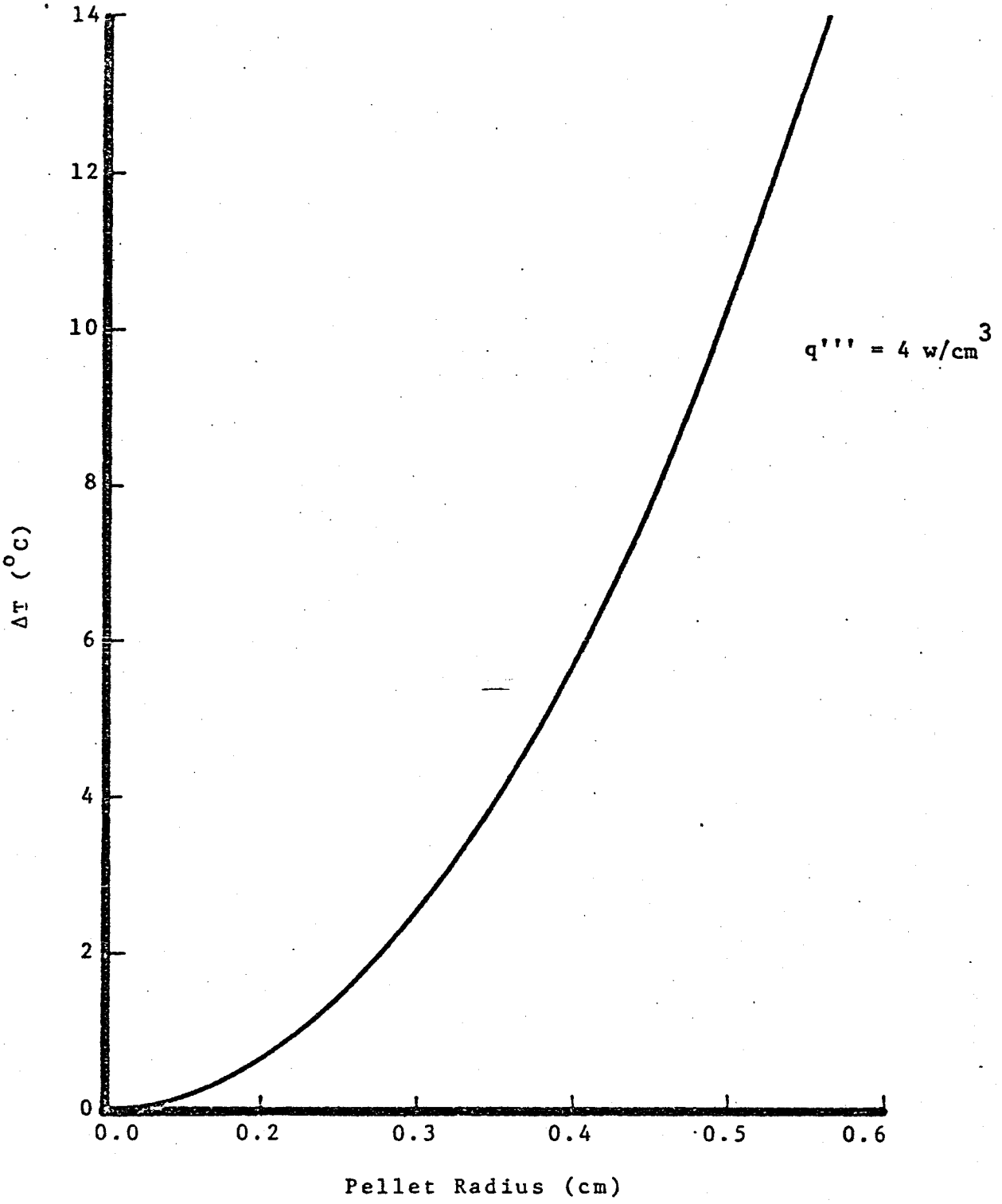

Fig. 6.4 Temperature Drop Across Pellet vs Pellet Radius.

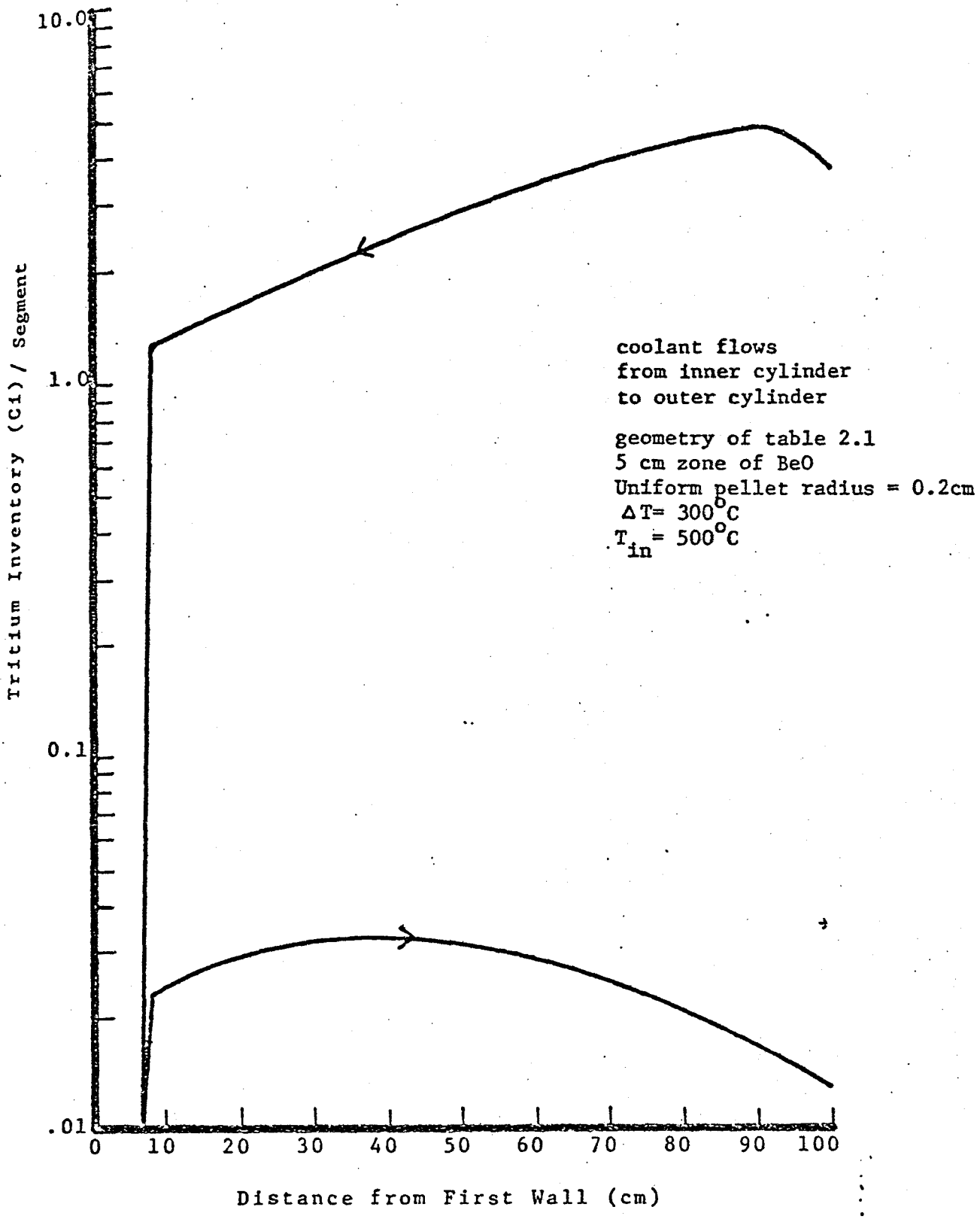

Fig. 6.5 Tritium Inventory Profile in the BRSR Module

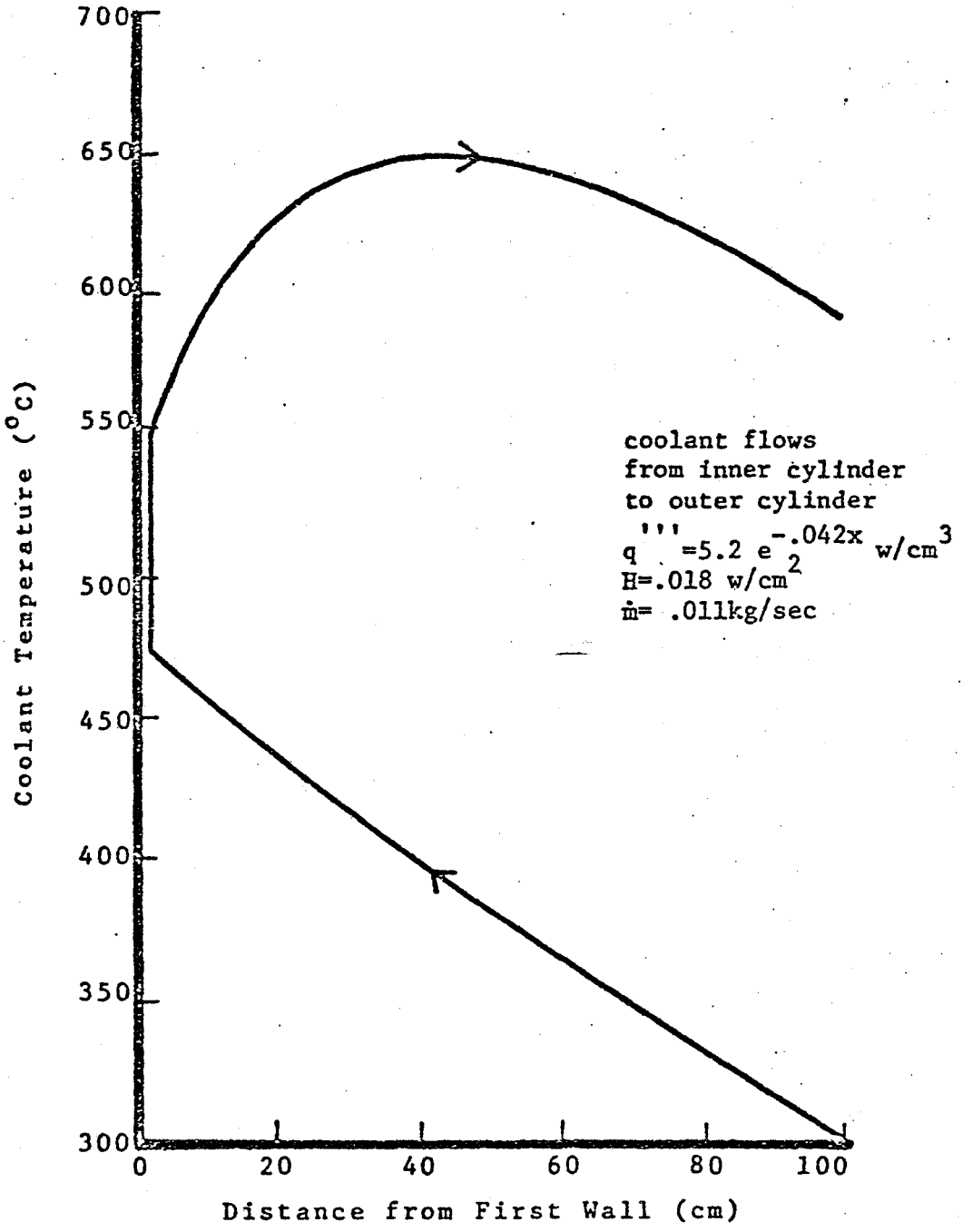

Fig. 6.6 Coolant Temperature Profile in the BRSR Reference Design Module.

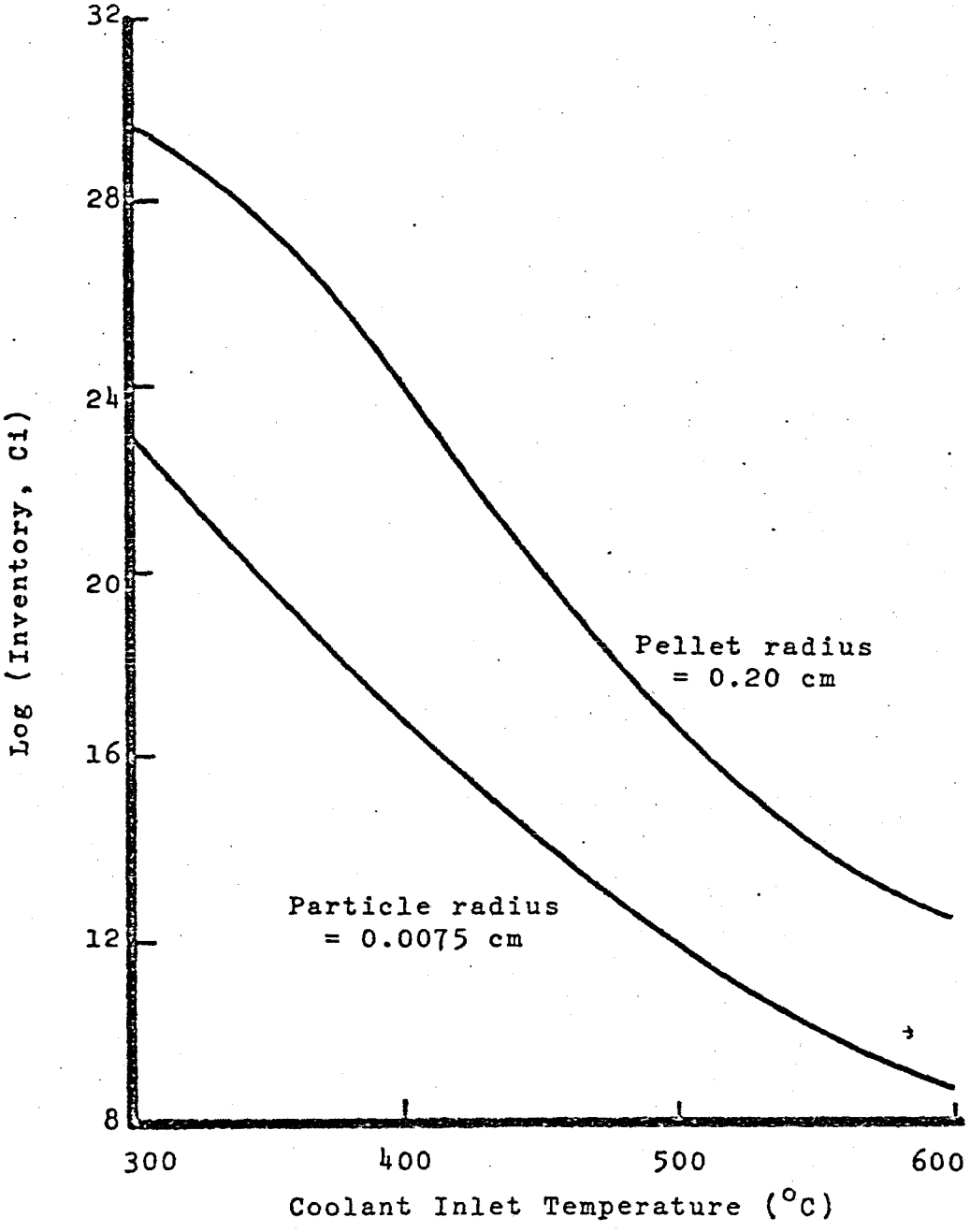

Fig. 6.7 Effect of Temperature on the Steady State Blanket Inventory.

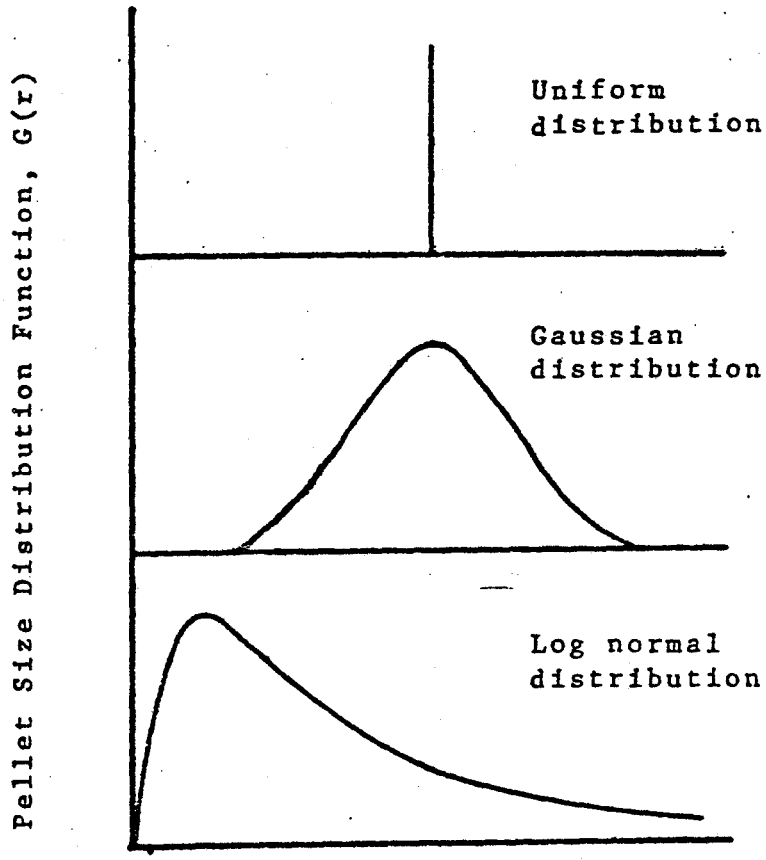

Fig. 6.8 Uniform, Gaussian and Log Normal Pellet Size Distributions.

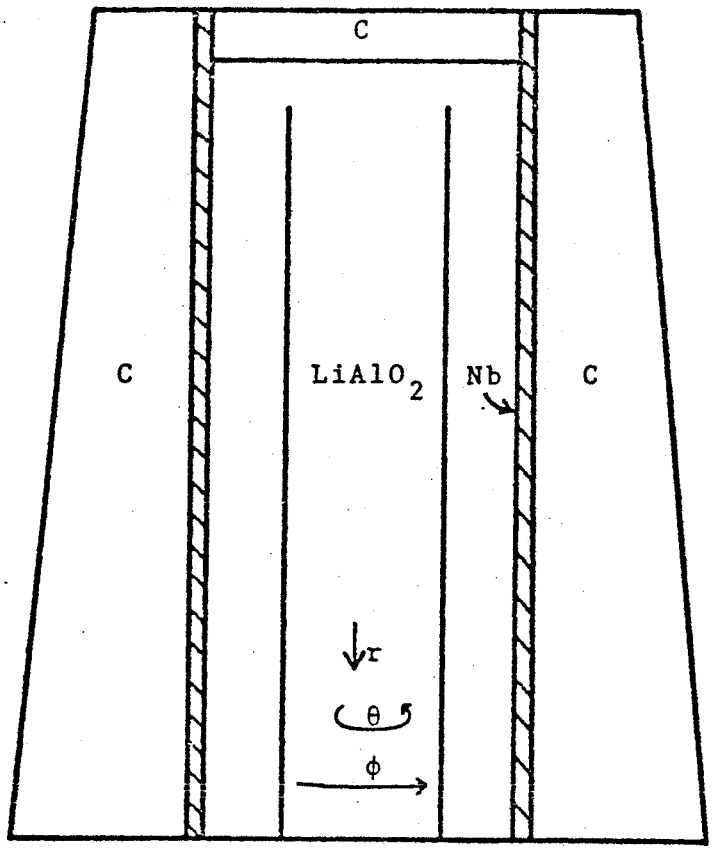

a. BRSR Cross Sectional View

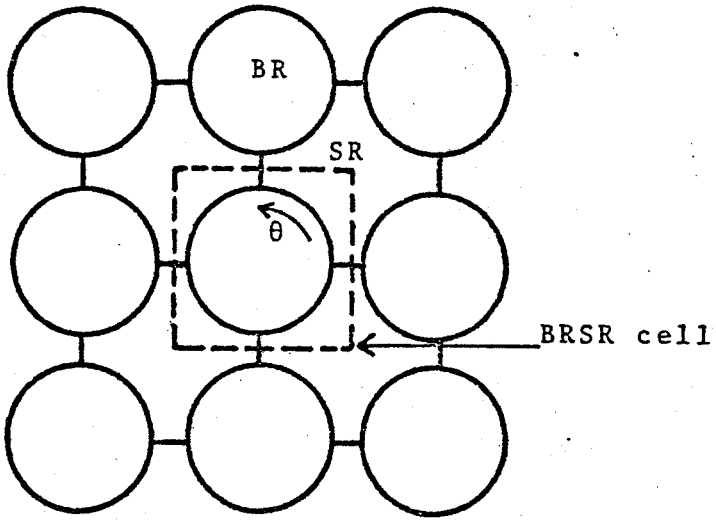

b. View from Plasma

Fig. 7.1 Schematic Views of the BRSR Reference Design

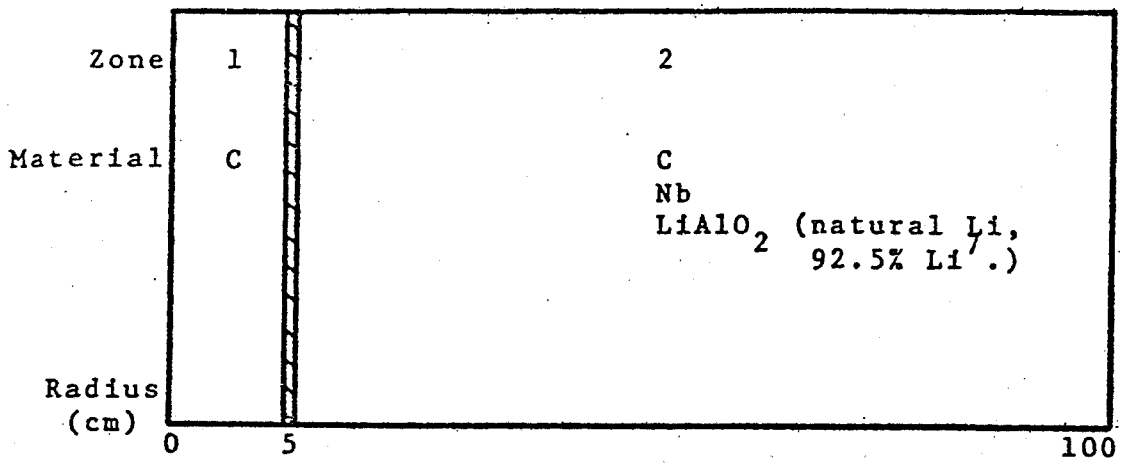

Fig. 7.2 Neutronic Reference Design 1 Schematic

TABLE 7.1

BREEDING RESULTS FOR NRD 1

Breeding reactions		Multiplication reactions		Parasitic absorptions	
$Li^6(n,\alpha)T$	.357	$Li^6(n,2n-\alpha)p$	.0003	$Nb^{93}(n,\gamma)Nb^{94}$	.595
$Li^7(n,n-\alpha)T$	.037	$Li^7(n,2n)Li^6$	.0013	$Al^{27}(n,\gamma)Al^{28}$	.0003
		$Li^7(n,2n-\alpha)H^2$	.0015		
		$Nb^{93}(n,2n)Nb^{92}$	.0723		
Breeding ratio =	.3938	Neutron Multiplication =	1.0754	Parasitic Absorptions =	.5958

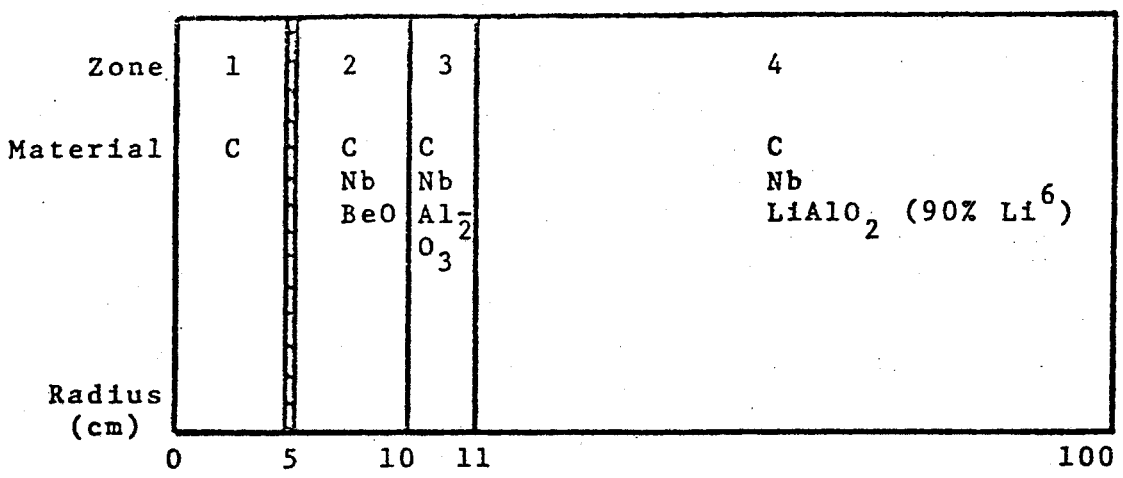

Fig. 7.3 Neutronic Reference Design 2 Schematic

TABLE 7.2

BREEDING RESULTS FOR NRD 2

Breeding reactions	Multiplication reactions	Parasitic absorptions
$Li^6(n,\alpha)T$ .6814	$Li^6(n,2n-\alpha)p$ .0018	$Nb^{93}(n,\gamma)Nb^{94}$ .1418
$Li^7(n,n-\alpha)T$ .0020	$Li^7(n,2n)Li^6$ -	$Al^{27}(n,\gamma)Al^{28}$ .0016
$Be^9(n,T)Be^7$ .0008	$Li^7(n,2n-\alpha)H^2$ -	
	$Be^9(n,2n)2\alpha$ .0539	
	$Nb^{93}(n,2n)Nb^{92}$ .0308	
Breeding ratio = .6842	Neutron multiplication = 1.0865	Parasitic absorptions = .1434

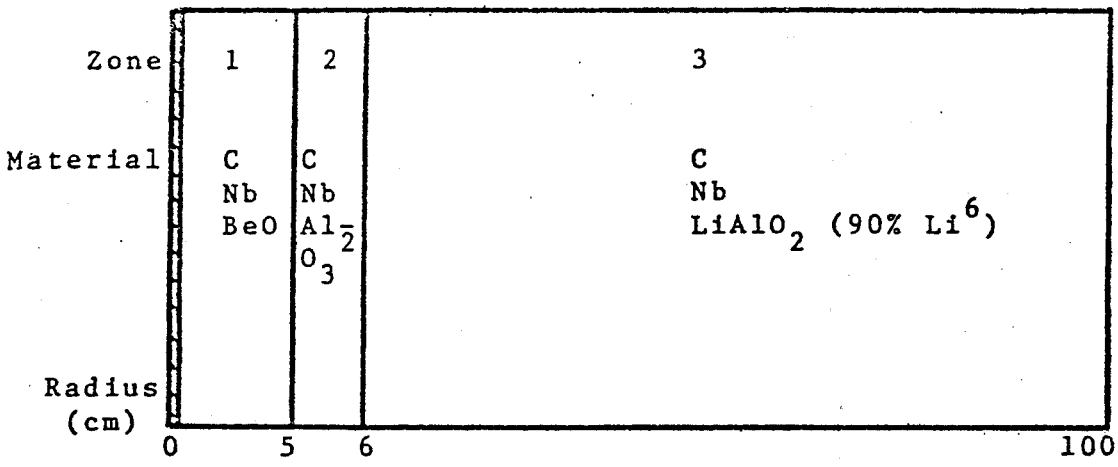

Fig. 7.4 Neutronic Reference Design 3 Schematic

TABLE 7.3

BREEDING RESULTS FOR NRD 3

Breeding reactions		Multiplication reactions		Parasitic absorptions	
$Li^6(n,\alpha)T$	.7644	$Li^6(n,2n-\alpha)T$	.0030	$Nb^{93}(n,\gamma)Nb^{94}$	.1697
$Li^7(n,n-\alpha)T$	.0030	$Li^7(n,2n)Li^6$	.0001	$Al^{27}(n,\gamma)Al^{28}$	.0019
$Be^9(n,T)Be^7$	.0023	$Li^7(n,2n-\alpha)H^2$	.0002	C^{12} $\Sigma_{a\ total}$	.1396
		$Be^9(n,2n)2\alpha$	.1048		
		$Nb^{93}(n,2n)Nb^{92}$	.0659		
Breeding ratio =	.7697	Neutron multiplication =	1.1739	Parasitic absorptions =	.3112
				minus C^{12} =	.1716

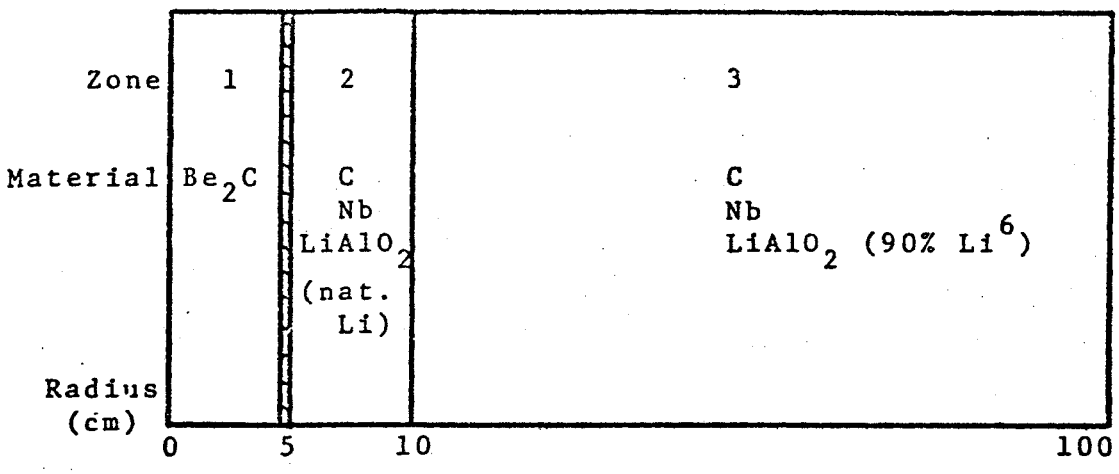

Fig. 7.5 Neutronic Reference Design 4 Schematic

TABLE 7.4

BREEDING RESULTS FOR NRD 4

Breeding reactions	Multiplication reactions	Parasitic absorptions
$Li^6(n,\alpha)T$ 1.1395	$Li^6(n,2n-\alpha)p$ .0015	$Nb^{93}(n,\gamma)Nb^{94}$ .2153
$Li^7(n,n-\alpha)T$ .0101	$Li^7(n,2n)Li^6$ .0004	$Al^{27}(n,\gamma)Al^{28}$ .0033
$Be^9(n,T)Be^7$ .0128	$Li^7(n,2n-\alpha)H^2$ .0005	C^{12} Σ_a total .1204
	$Be^9(n,2n)2\alpha$ .5563	O^{16} Σ_a total .0233
	$Nb^{93}(n,2n)Nb^{92}$ .0253	
Breeding ratio = 1.1624	Neutron multiplication = 1.5840	Parasitic absorptions = .3623 minus C^{12}&O^{16} = .2186
	UWMAK - II	
Breeding ratio = 1.18	Neutron multiplication = 1.59	Parasitic absorptions = .2173

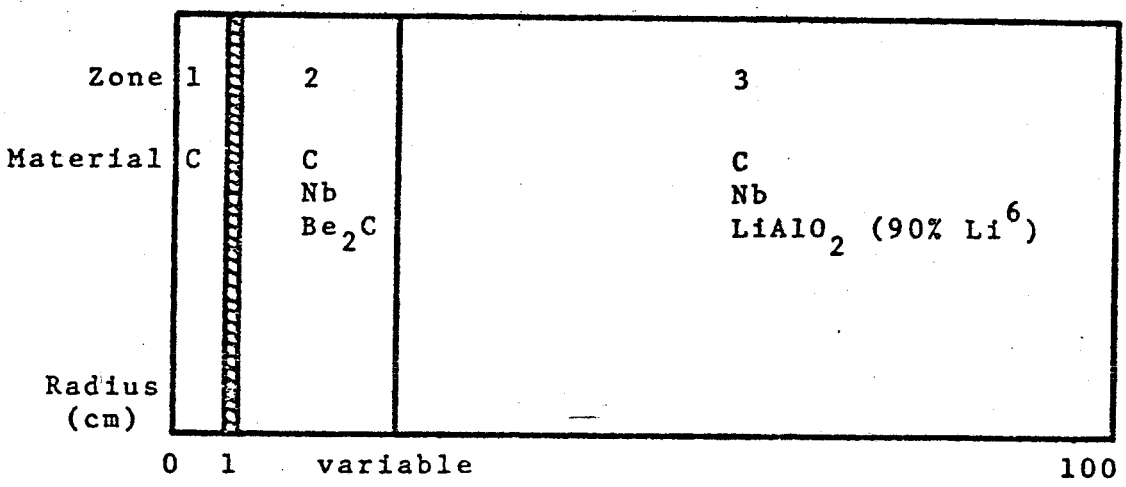

Fig. 7.6 Neutronic Reference Design 5 Schematic

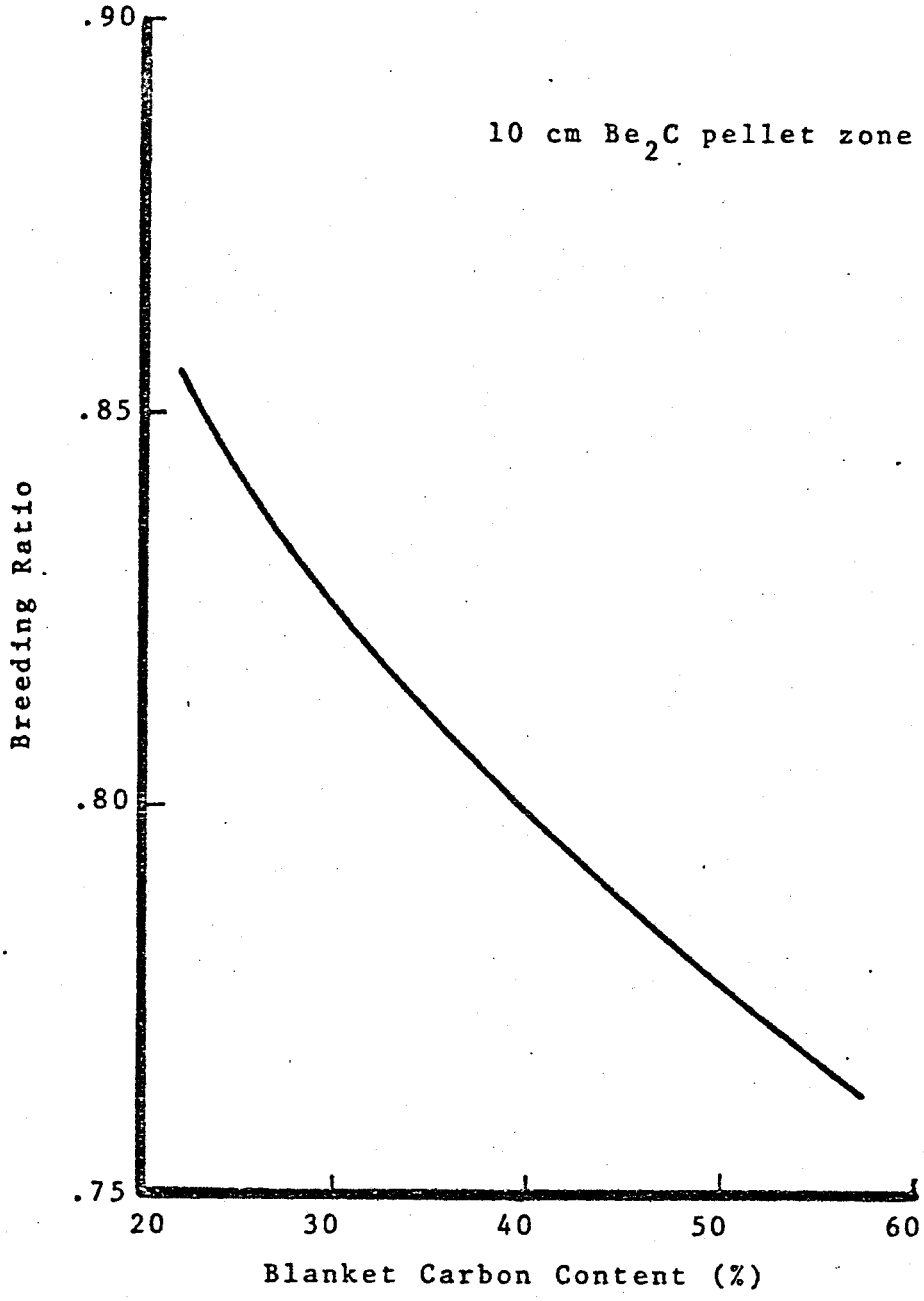

Fig. 7.7 Breeding Ratio vs Blanket Carbon Content.

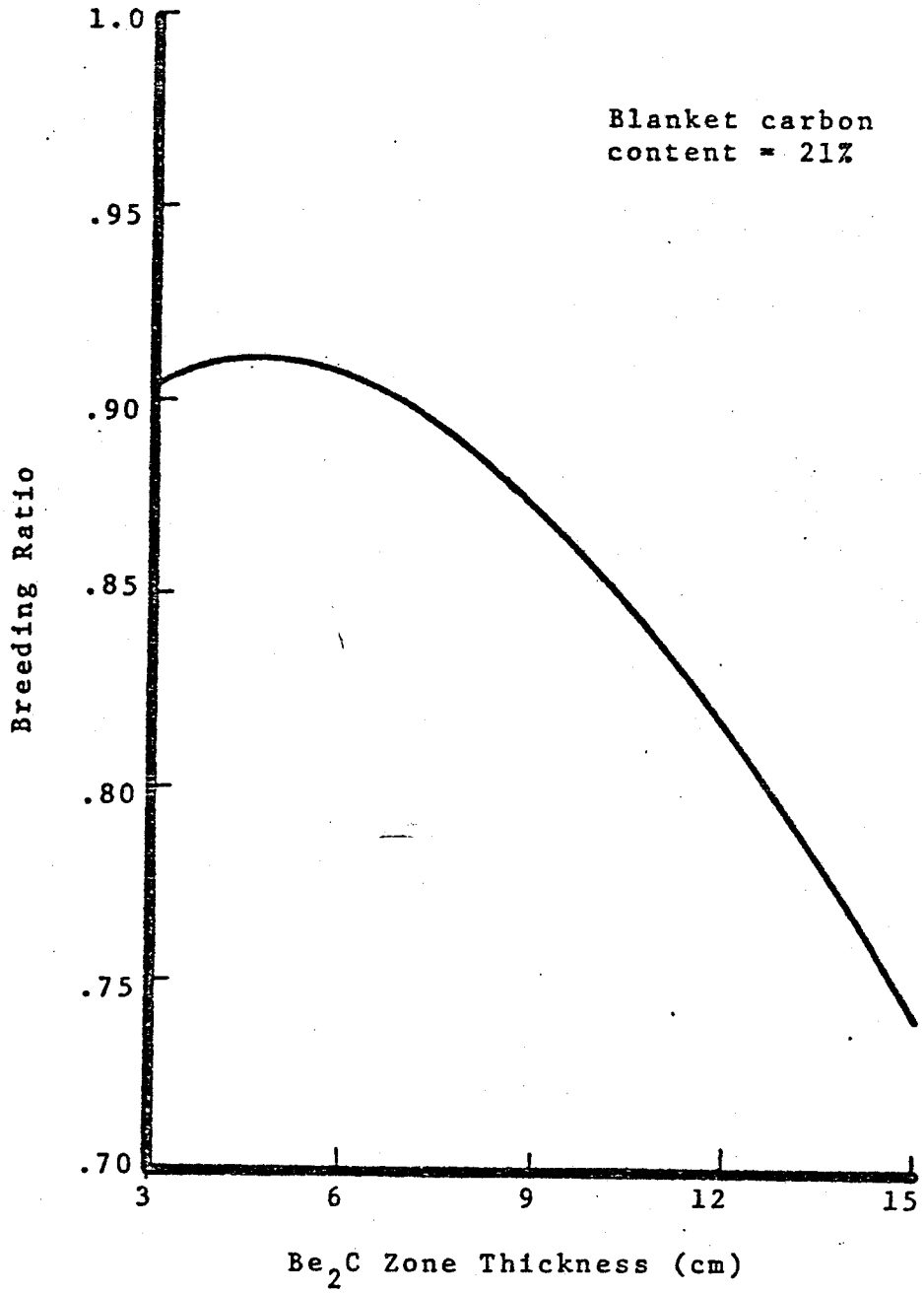

Fig. 7.8 Breeding Ratio vs Be_2C Pellet Zone Thickness.

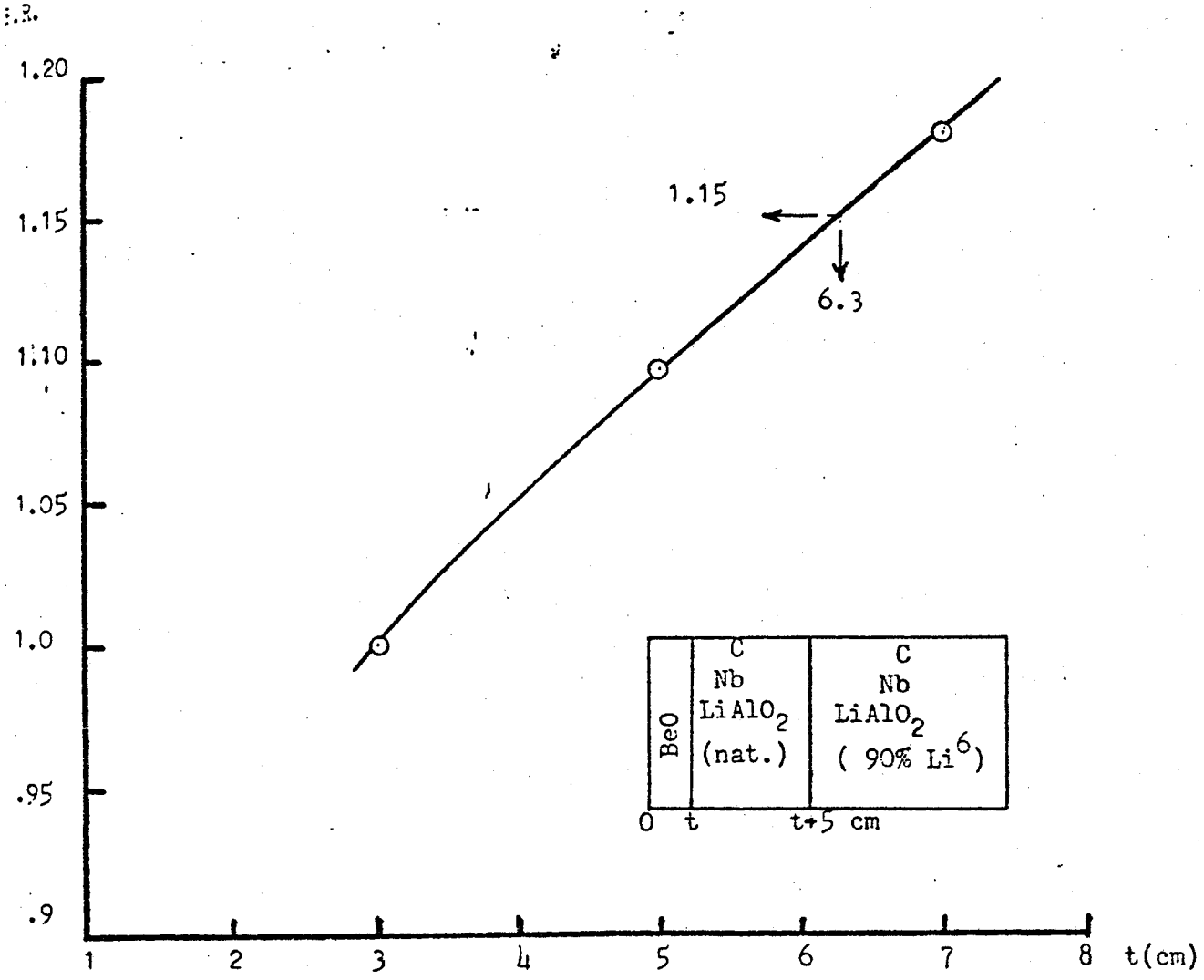

Fig 7.9 Breeding Ratio vs. BeO Shield Thickness

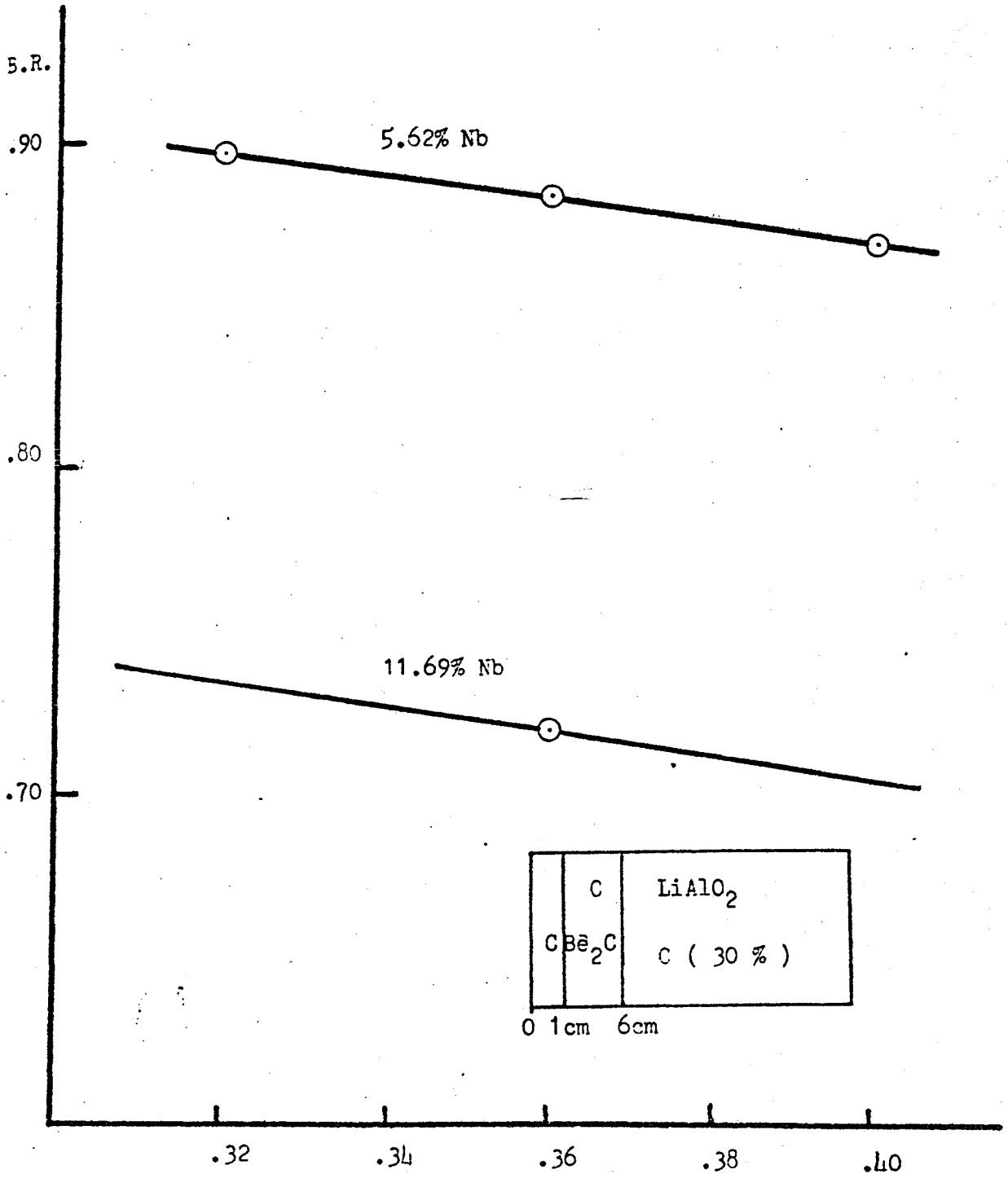

Fig. 7.10 BREEDING RATIO vs.VOID FRACTION

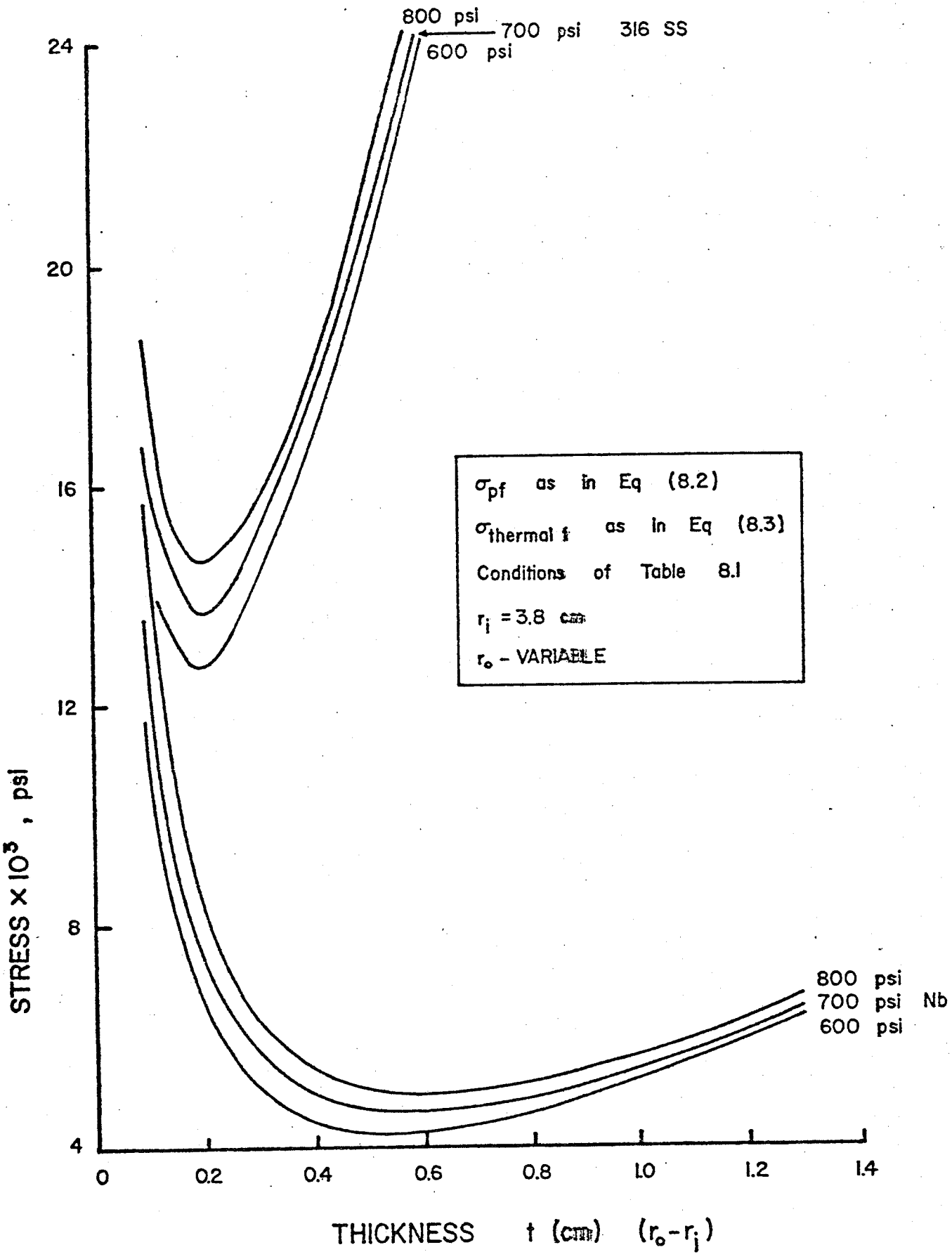

FIG. 8.1 FIRST WALL STRESS

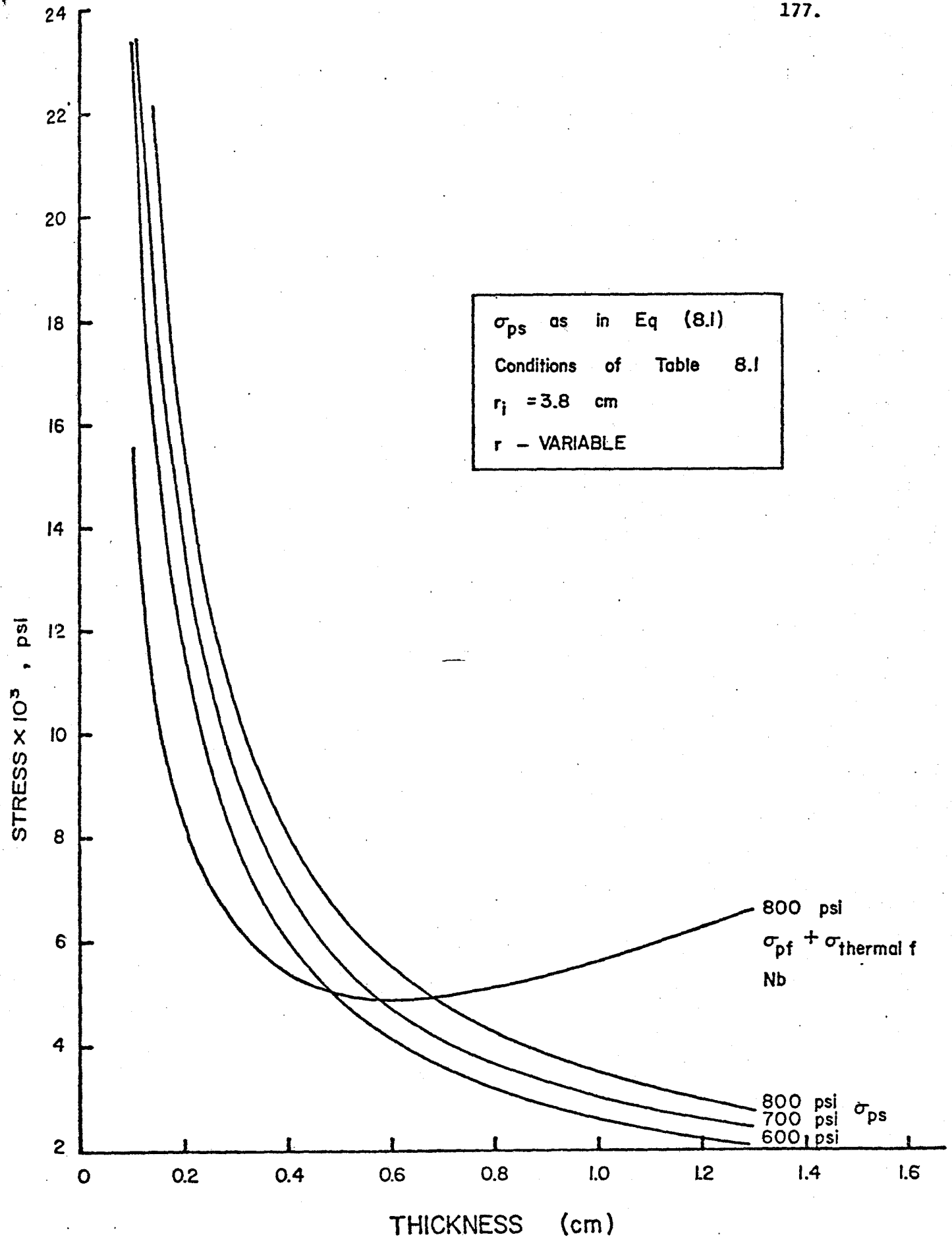

FIG. 8.2 SIDE WALL STRESS

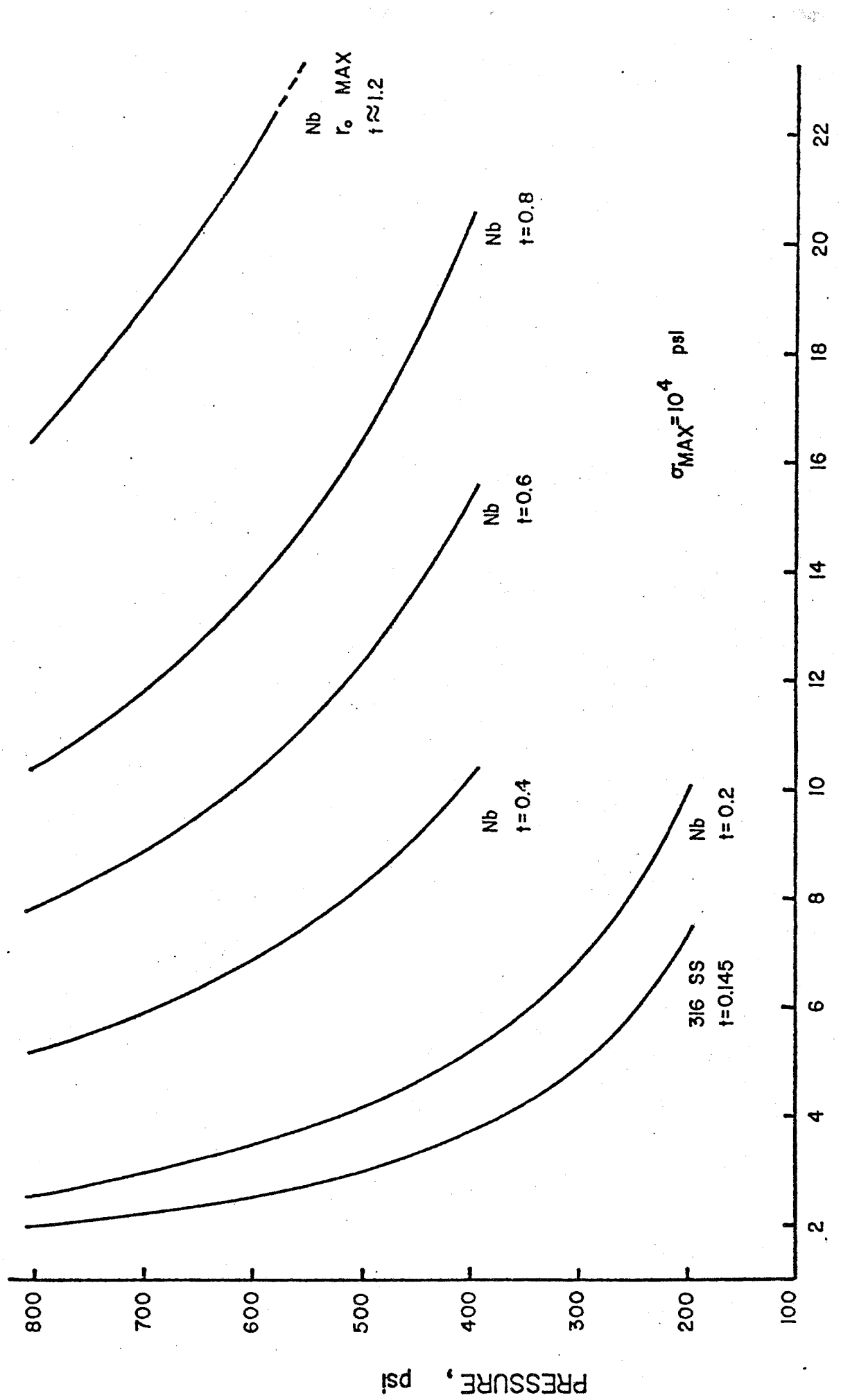

FIG. 8.3 MODULUS MAX OUTSIDE RADIUS

Fig.8.4* FAILURE RATES OF COMPONENTS AND PARTS

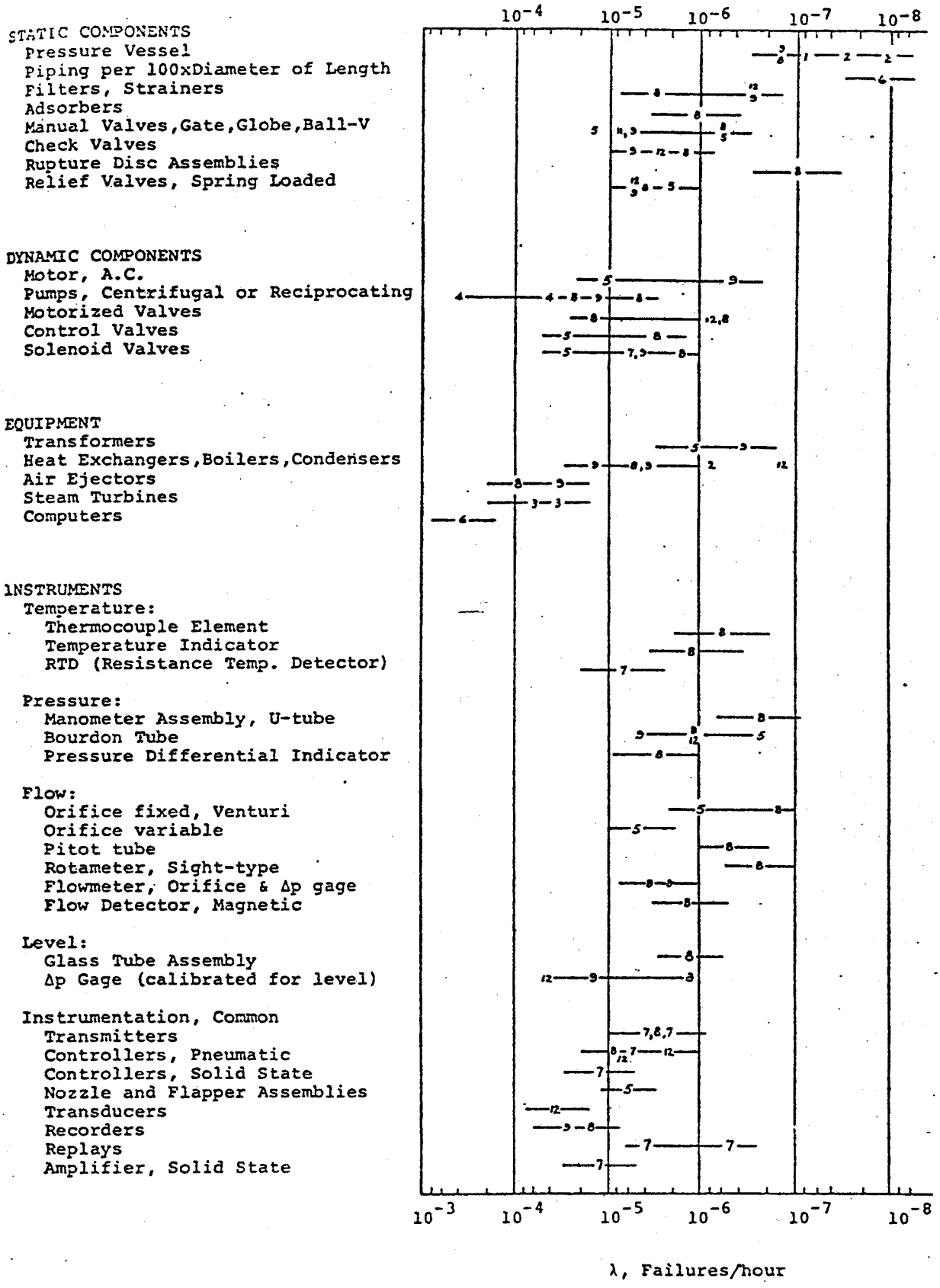

* Table 3.1 Reference 40

Fig.8.4 Con't.

PARTS
- Mechanical
  - Bearings Ball, heavy-light duty
  - Bearings Roller
  - Bearings Sleeve
  - Bolts
  - Clutches Friction
  - Clutches Magnetic
  - Couplings
  - Drive Belt
  - Fulcrums Knife Edge
  - Gears Helical
  - Gears Spur
  - Joints Mechanical
  - Nuts
  - Pins
  - Pivots
  - Screws: Set screws
  - Shafts, heavily-lightly stressed
  - Springs, heavily-lightly stressed
  - Springs Calibration
  - Springs Hair
  - Vibration Mounts

- Pneumatic and Hydraulic
  - Bellows
  - Cylinders
  - Diaphragm, Metal
  - Diaphragm, Rubber
  - Ducts Ventilation
  - Gaskets
  - Hoses, heavily-lightly stressed
  - Joints Pipe
  - Pistons
  - Restrictors
  - Seals "O" Ring
  - Seals Rotating
  - Seals Sliding
  - Unions and Junctions

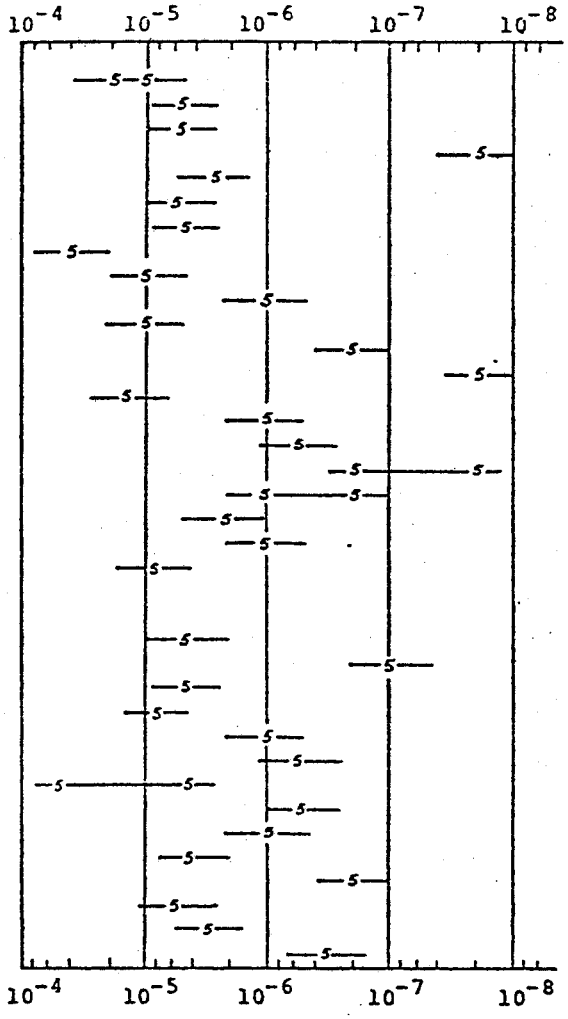

λ, Failures/hour

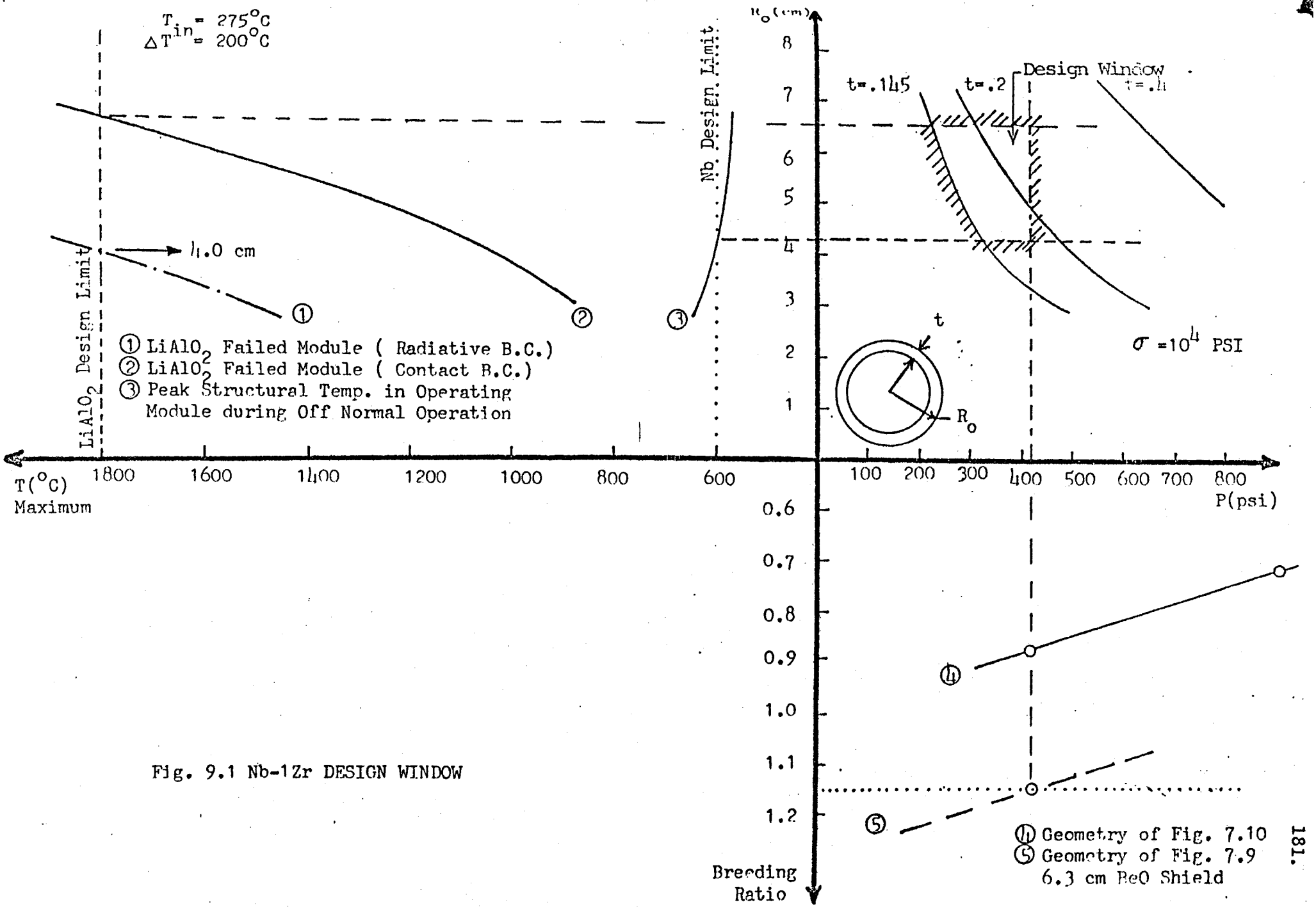

Fig. 9.1 Nb-1Zr DESIGN WINDOW

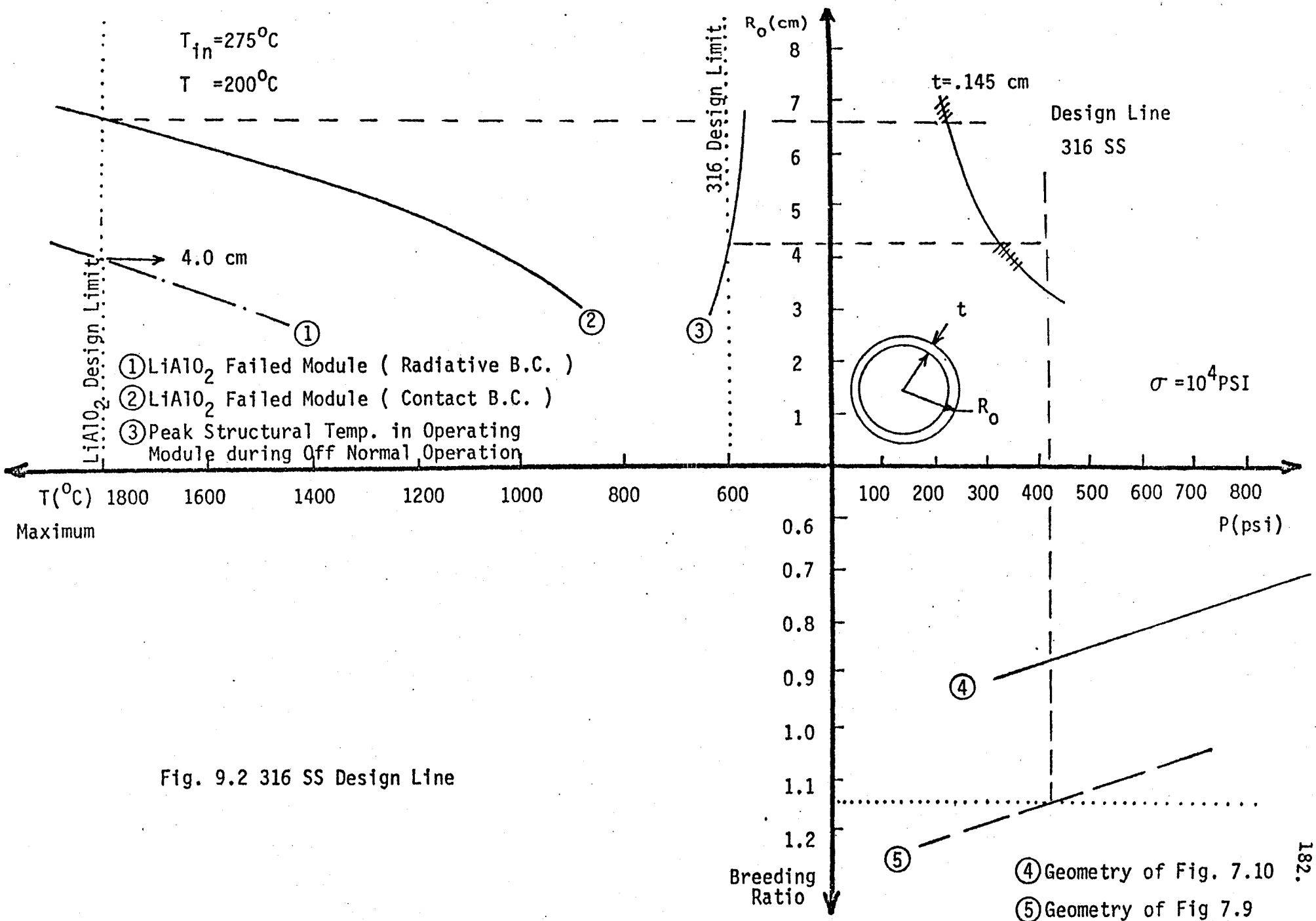

Fig. 9.2 316 SS Design Line

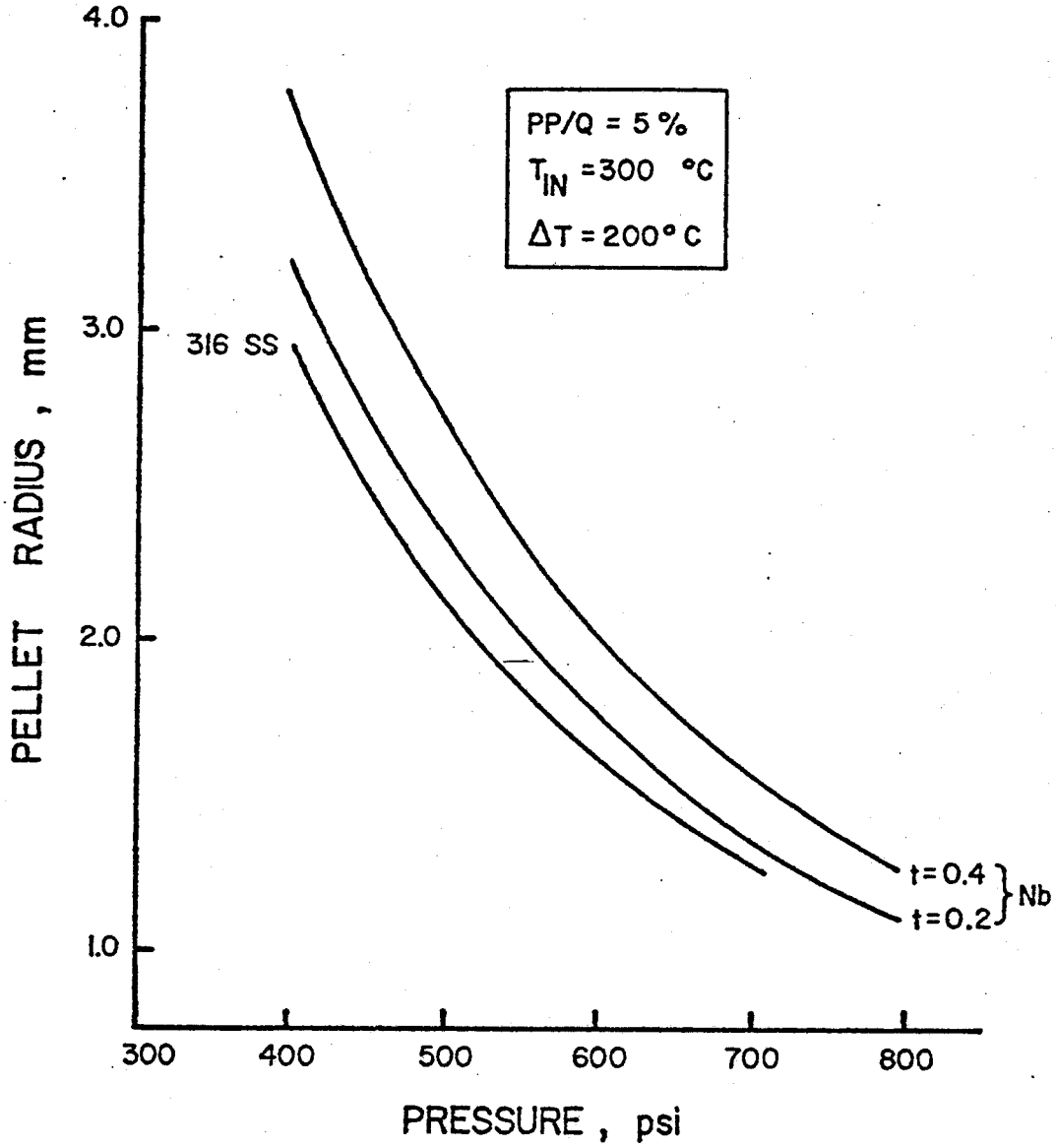

FIG. 9.3 PELLET RADIUS vs. PRESSURE

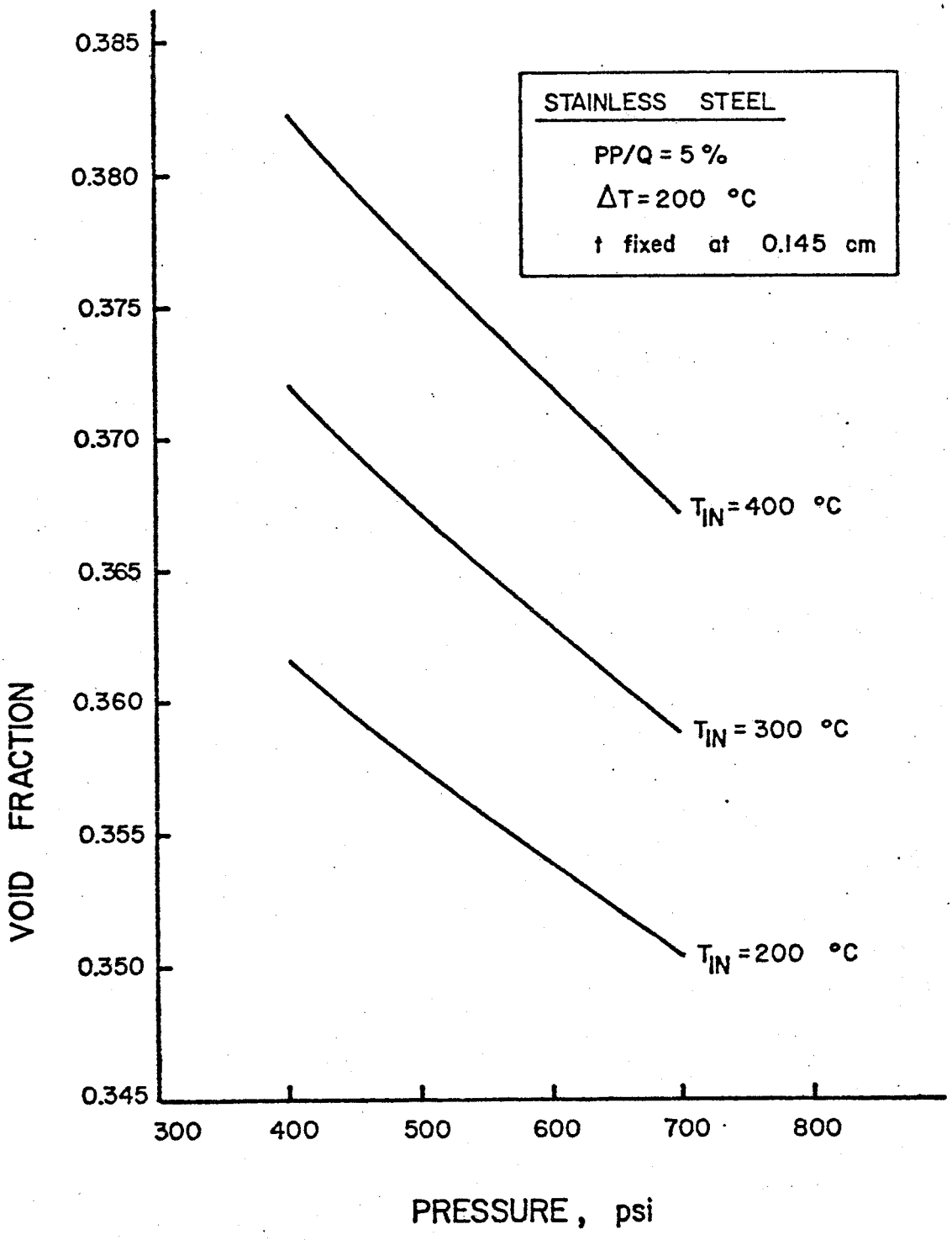

FIG. 9.4 VOID FRACTION vs. PRESSURE

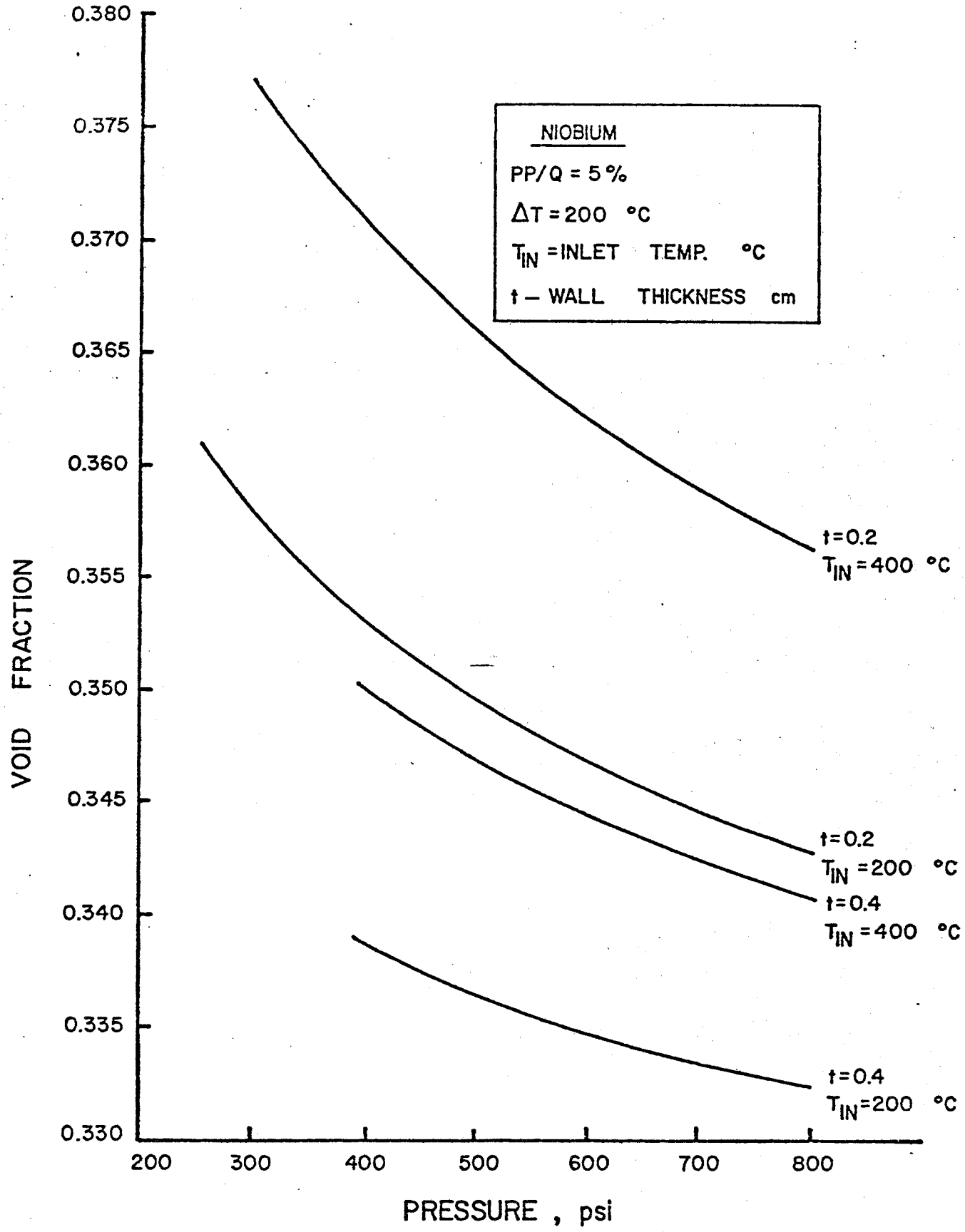
NIOBIUM
PP/Q = 5 %
ΔT = 200 °C
T_{IN} = INLET TEMP. °C
t — WALL THICKNESS cm
t=0.2
T_{IN} = 400 °C
t=0.2
T_{IN} = 200 °C
t=0.4
T_{IN} = 400 °C
t=0.4
T_{IN} = 200 °C
VOID FRACTION
0.380
0.375
0.370
0.365
0.360
0.355
0.350
0.345
0.340
0.335
0.330
200
300
400
500
600
700
800
PRESSURE , psi

FIGURE 9.5

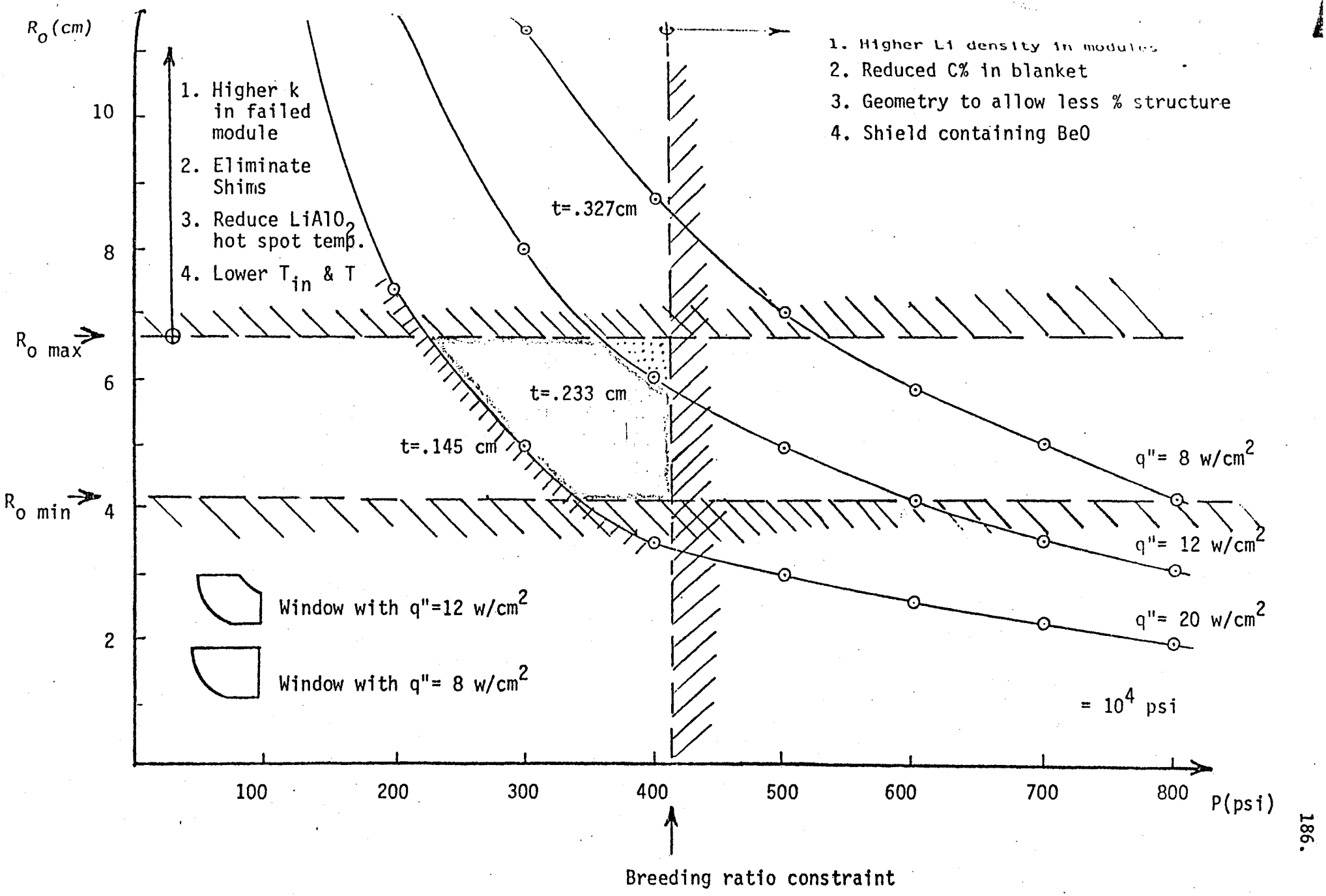

Fig. 11.1 Changes to 316 SS Design Window

APPENDIX A

STRUCTURAL MATERIAL CONSIDERATIONS

Among the primary tasks of reactor design is the identification and selection of suitable structural materials. In the BRSR design, the structure will consist of the breeder rod module and the end cap which is the "first wall" as seen by the plasma. When considering this design, the most important requirement of a structural material is its ability to maintain its integrity in a high temperature (700°C) system. Based on this constraint, the list of candidate materials can be narrowed down to three general classes stainless steel, niobium and niobium alloys, and vanadium and vanadium alloys. Molybedenum was not included due to the serious problems encountered with welding. The following sections will identify the selection criteria and evaluate the candidate materials based on these criteria. The material to be used in the BRSR design will then be selected along with other promising alloys.

A.1 STRUCTURAL MATERIAL SELECTION CRITERIA

Due to thehostile environment in a fusion reactor, a structural material must be able to meet several diversified requirements. These requirements form the criteria by which a material will be selected. The most important criterion are listed below followed by an evaluation of the candidate materials based on these criteria.

1. Mechanical and thermophysical properties
2. Ability to withstand stress at high temperatures
3. Creep strength
4. Irradiation effects on mechanical effects
5. Surface effects of irradiation

TABLE A.1

MECHANICAL AND THERMOPHYSICAL PROPERTIES OF CANDIDATE MATERIALS[a]

Property	316 SS	Niobium	Vanadium
Density (g/cm^3)	7.92	8.7	6.11
Melting point (^oC)	1430.	2468.	1900.
Thermal conductivity at 500^oC (cal/cm-sec^oC)	0.05	0.13	0.088
Linear coefficient of thermal expansion at 500^oC (in/in ^oC)	17.0×10^{-6} (600^oC)	8.3×10^{-6}	9.6×10^{-6}
Modulus of elasticity at R.T. (psi)	29.0×10^6	15.2×10^6 [b]	20.0×10^6
Elongation (%) at 500^oC	49.	19.6	31.3
Poisson's ratio	0.30	0.38	0.36

[a] ref. 42
[b] ref. 43

6. Neutronic characteristics

7. Impurity effects

8. Fabricability, availability and cost

A.2 MECHANICAL AND THERMOPHYSICAL PROPERTIES

The mechanical and thermophysical properties of the three base candidate materials 316 stainless steel, niobium and vanadium are presented in Table A.1. The desirable characteristics are of course, a high melting point, high thermal conductivity to reduce thermal stress due to temperature excursions, a low coefficient of thermal expansion for compatability with blanket goemetry, a ductile material and a material with a high modulus of elasticity. The available data for strength will be compared at appropriate temperatures in the following section. However, after a review of the relevant properties above, none of the candidate materials exhibit characteristics that would eliminate them from consideration as a structural material although the low melting point of 316 SS is not attractive.

A.3 ABILITY TO WITHSTAND STRESS AT HIGH TEMPERATURES

The selected material must be able to withstand high stresses at temperatures in the 800°C range, as might be encountered during a module failure. Pure vanadium is not suited to this type of application but alloying with titanium greatly increases its tensile properties as shown in Table A.2. The VANSTAR alloy and V-Ti alloys show impressive strength at high temperatures. The VANSTAR alloys were developed by the Astronuclear Division of Westinghouse Corporation. The compositions of the alloys are as follows:

TABLE A.2

TENSILE PROPERTIES OF THE CANDIDATE MATERIALS
AT HIGH TEMPERATURES

Material	Temperature (°C)	Yield strength (.2% offset) psi	Ultimate tensile strength (psi)	Total elongation (%)	ref.
V	700	8,500	15,200	22	44
V-10Ti	700	39,900	73,600	21	44
V-20Ti	700	57,200	87,900	21	44
VANSTAR-7	700	28,000	56,200	22	44
VANSTAR-8	700	32,000	60,800	19	44
Nb	600	20,000	34,200	19.6	45
Nb-1Zr	650	12,300	27,000	23.8	45
316 SS	700	20,500	66,500	43	42

VANSTAR-7 (V-9Cr-3Fe-1.3Zr-0.05C)

VANSTAR-8 (V-8Cr-10Ta-1.3Zr-0.05C)

VANSTAR-9 (V-6Fe-5Cb-1.3Zr-0.05C)

Although pure vanadium has a very low yield strength, its alloys have much higher yield strengths providing a wide safety margin. Niobium, Nb-1Zrand 316 stainless steel are not quite as attractive.

A.4 CREEP STRENGTH

The high temperatures and stresses characteristic of the fusion reactor environment demand high creep strength from the alloys used as the first wall material. From the results presented in Tables A.4 and A.5, it is evident that alloying niobium and vanadium has a considerable strengthening effect. Although all creep tests were not conducted under identical experimental conditions, it appears that the VANSTAR alloys are comparable to Nb-1Zr in creep strength. The V-Ti alloys are attractive but are not as creep resistance as the VANSTAR alloys. The addition of titanium adds to the strength but tends to degrade the time-dependent properties with increasing concentration.

A.5 IRRADIATION EFFECTS OF MECHANICAL PROPERTIES

Due to the intense neutron and light ion flux at the first wall, it will be advantageous to know the response of the candidate materials under this irradiation environment. Table A.6 exhibits the effect of irradiation on the tensile properties of the candidate alloys. The data indicates the large amount of radiation hardening that occurs in the vanadium and niobium alloys. It should be noted that although both are embrittled, the Nb-1Zr alloy is most severely embrittled as the total

TABLE A.4

CREEP RATES OF CANDIDATE ALLOYS

Material	Temperature (°C)	Stress (psi)	Min creep rate, %/hr	ref.
Nb-1Zr	982	10,000	.0017	47
	982	20,000	.0058	47
	982	30,000	.040	47
V-10Ti	700	30,000	.006	46
	700	35,000	.023	46
	800	10,000	.18	46
V-20Ti	700	30,000	.09	46
	800	10,000	.09	46
VANSTAR-7	800	10,000	.0017	46
	800	15,000	.0074	46
VANSTAR-8	800	15,000	.0011	46
VANSTAR-9	800	25,000	.0013	46
316 SS	700	24,000	.154	46
	800	9,000	.089	46

TABLE A.5

CREEP RUPTURE PROPERTIES OF CANDIDATE ALLOYS

Material	T (°C)	Stress (psi)	Rupture life, hr	Elongation at rupture %	Time to 1% strain	ref
V-10Ti	800	9,000	147	137	-	46
	800	12,500	105	119	3	46
	800	15,000	71	118	1.7	46
V-20Ti	800	10,000	365	132.5	13	46
	800	18,000	47.5	119	1.8	46
Nb-1Zr	982	10,000	148	50.8	7.8	47
	982	15,000	14.8	29.7	1.2	47
316 SS	815	7,000	1000	-	-	48
	760	10,000	1050	59	-	48

elongation drops to only 8.3% whereas the vanadium alloys retain modest ductility.

A.6 SURFACE EFFECTS OF IRRADIATION

Surface erosion can arise from a number of processes. Among the most important are plasma-particle sputtering, neutron sputtering and the bursting or radiation-induced blisters.

A.6.1 Sputtering

Sputtering yields are heavily dependent on the energy of the light bombarding ions. There is quite a volume of data available and much of it is in only pseudo-agreement. This is largely due to the fact that no real theoretical understanding of neutron sputtering yet exists. Further, sputtering results tend to be very model dependent. Kulcinski et al., estimates the erosion of the 316 stainless steel first wall of the UWMAK-1 due to sputtering to be .20mm/yr[49] Similarly, a niobium wall is expected to erode at a maximum rate of .15 to .22 mm/yr for a plasma-particle energy deposition of 1 MW/m^2[50]. The anticipated erosion rate of vanadium is slightly higher than that for niobium, approximately that of stainless steel. The effect of the erosion of the wall and a reduction in thickness and strength of the first wall on the plasma is mainly in the form of an energy loss due to bremsstrahlung radiation, the energy loss being proportional to the square of the atomic number. However, probably the most meaningful data is that reported by Duchs et al.[51]. Table A.7 gives the sputtering yield in atoms/incident particle due to a 50-50 D-T mixture for various materials. Also included are C_{crit} and C_{crit}/S_H. C_{crit} is the critical impurity

TABLE A.6

IRRADIATION EFFECTS ON THE TENSILE PROPERTIES OF VARIOUS ALLOYS

Material	T (°C)	Fluence (>.1 MeV) $n/cm^2 sec$	Yield strength (psi)	Ultimate tensile strength (psi)	Total elongation (%)	ref.
Vanadium	RT	0	37,500	41,000	27	52
	RT	8.0×10^{17}	45,000	48,000	15	52
V-20Ti	800	0	38,571	47,857	59.4	44
	750	5.2×10^{21}	45,142	51,157	39.4	53
VANSTAR-7	650	0	34,300	61,000	20	45
	650	1.5×10^{22}	81,000	87,600	14	45
Nb-1Zr	650	0	12,300	27,000	23.8	45
	650	3.7×10^{22}	66,300	66,300	8.3	45
316 SS	RT	0	36,500	89,500	66.5	42
	RT	1.0×10^{14} (slow)	35,000	90,000	70.0	42

concentration above which ignition becomes impossible. C_{crit}/S_H gives the time in units of τ_H (particle confinement time of the fuel) after which the critical concentration is reached. It should be noted that niobium has a distinct advantage over stainless steel and vanadium in that the impurity concentration doesn't reach the critical level until a time 60% longer than vanadium or stainless steel. However, even this is an extremely short time that will be unacceptable for actual operation and all results can be considered comparable.

A.6.2 Blistering

The result of Das and Kaminsky will be presented in comparing the blistering of V-20Ti, vanadium and niobium.[54] The degree of blistering will be defined as the ratio of the blistered area to the total specimen area.

Niobium

Niobium was irradiated at room temperature with 0.5 MeV helium ions at a dose of 1 Coulomb/cm^2. The irradiation resulted in large interconnecting blisters of ∿1000 μm in diameter. The blister area was ∿87%. At 600°C, the average blister size was reduced to ∿400 μm and the blister area covered 47% of the specimen. Finally, a temperature increase to 900°C yielded blisters with an average diameter of 15 μm and the blistered area accounted for only 9% of the surface area.

Vanadium

Under identical irradiation conditions at room temperature, blisters an average of 350 μm in diameter were produced in commercially pure vanadium. When the temperature was raised to 900°C, the average diameter was reduced to 10–15 μm in diameter.

TABLE A.7

SPUTTERING YIELD FOR VARIOUS WALL MATERIALS [51]

Material	S_H [a]	C_{crit}	C_{crir}/S_H
Fe (SS)	5×10^{-2}	2.5×10^{-2}	0.5
V	5×10^{-2}	2.5×10^{-2}	0.5
Ti	5×10^{-2}	2.5×10^{-2}	0.5
Nb	1.5×10^{-2}	1.2×10^{-2}	0.8

[a] 2-5 keV.

TABLE A.8

EROSION OF THE 316 SS WALL OF UWMAK-I DUE TO BLISTERING [49]

Ion	Mean energy (keV)	Sputtering yield[a] S	Flux $n/cm^2 sec$	Erosion rate mm/yr
He	23	1	4.7×10^{12}	.017
He	100	3	1.7×10^{11}	.0019
D^+	23	.01	6.4×10^{13}	.0023
T^+	23	.01	6.4×10^{13}	.0023
			Total blistering =	.024 mm/yr

[a] atoms/incident particle.

V-20Ti

Irradiation at room temperature yielded blisters with an average diameter of 10-250 μm. When the temperature was raised to 900°C, the blister size decreased to an average of 8-20 μm with several blisters at 1 μm.

The degree of blistering declines in the order Nb, V, V-20Ti. One possible reason for this is the very low diffusivity of helium in niobium. The correspondingly higher diffusivities in V and V-20Ti may have aided in reducing the degree of blistering in these alloys.

316 Stainless Steel

The expected blistering damage to the 316 SS first wall of the UWMAK-1 is estimated by Kulcinski in Table A.8.[49] As should be noted, helium blistering will account for the majority of the damage. In summary, it can be concluded that V-20Ti and 316 SS are attractive due to their low blister damage.

A.6.3 Gas Production

The gas production rates in the first wall of UWMAK-1 were calculated by Vogelsand et al, Table A.9.[55] The three candidate first wall materials were 316 SS, V-20Ti and Nb-1Zr. It should be noted that in 316 SS, Fe is the main contributor to helium and hydrogen production although Cr, Ni and Si contribute large amounts relative to their abundance in steel. In V-20Ti, vanadium is the dominant contributor to hydrogen and helium production although titanium adds significantly to the hydrogen production (47%). Niobium is the only real concern in the Nz-1Zr alloy, accounting for almost all of the helium and hydrogen production. Atom displacement rates are also presented and are comparable for Nb and V, and are calaculated .

TABLE A.9

MAJOR CONTRIBUTORS TO GAS PRODUCTION IN THE UWMAK-I FIRST WALL [55]

	Element	Original concentration (at %)	amys (appm per MW-yr/m^2)		at % of total		Annual disp/atom[a]
			He	H	He	H	
316 SS	Fe	62.6	154	230	65	45	-
	Cr	18	35	64	15	13	
	Ni	14	23	184	10	36	
	Mn	2	2.6	8	1	2	
	Si	1.5	13	8	5	4	
	C	.28	9.3	-	4	-	
Total			238	505			
V-20Ti	V	79.5	47	94	88	52	22
	Ti	20	3.3	85	6	47	
	O	.26	1	.3	2	.2	
	C	.26	2.1	-	2	-	
Total			53.5	181			
Nb-1Zr	Nb	98.7	27	75	96	98	22
	Zr	1	.1	.9	.3	1	
	C	.03	.9	-	3	-	
Total			28.7	76			

[a] based on neutron wall loading of 1 MW/m^2.

using a secondary displacement model based on the work of Lindhard and Robinson.[55]

From Table A.9, it is evident that 316 SS is the least desirable with Nb-1Zr the most attractive and V-20Ti falling close behind. The large amounts of helium and hydrogen produced may enhance embrittlement at high temperatures and over long times. The results are presented graphically in Figure A.3.[55]

A.6.4 Void Production and Swelling

Vanadium

Swelling has been found to be near a maximum at 550°C in vanadium. Table A.10 gives the swelling in various vanadium alloys at 525°C.[56] The ability of titanium to limit void formation in vanadium could be due to one or a combination of the following reasons.

1) The gettering of impuring interstitial atoms that had been serving as void nuclei
2) The formation of a high number density of coherent precipitates that could serve to limit swelling
3) The addition of a substitutional solute atom that can promote point defect recombination by trapping self-interstitial atoms.

Niobium

Table A.11 gives the effect of neutron irradiation on niobium and Nb-1Zr.[57] Annealing the specimen increases the size of the void but reduces the number density and consequently the volume fraction. In Nb, the voids were annealed out until 1380°C. Annealing at 1230°C increased the size but decreased the number.

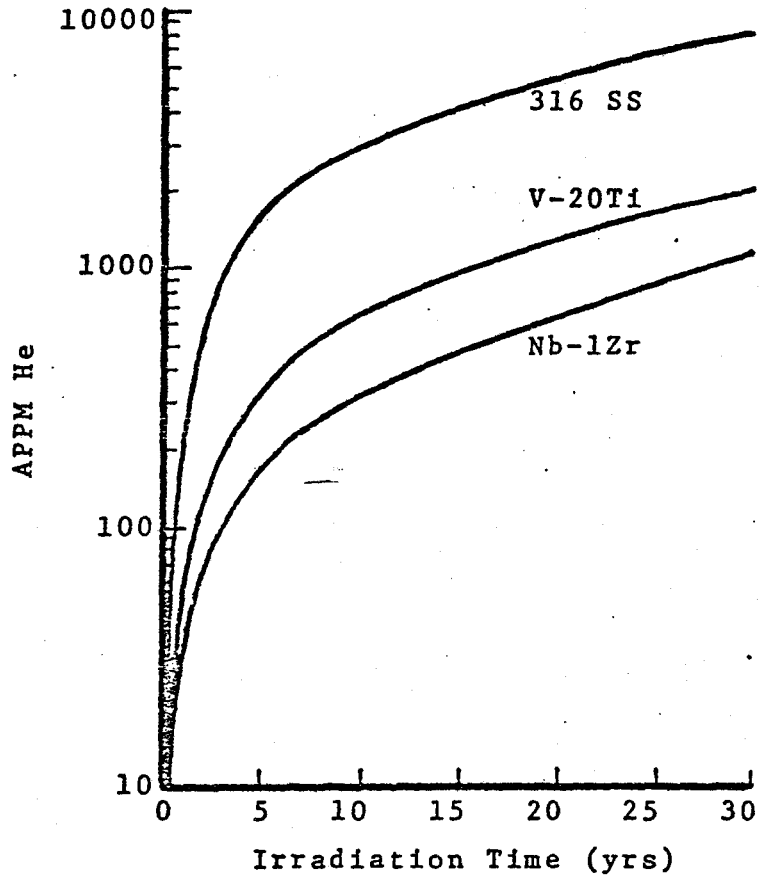

Fig. A3 Helium Buildup in UWMAK-I for 316 SS, Nb-1Zr and V-20Ti Structures.

TABLE A.10

VOID FORMATION IN IRRADIATED V-Ti ALLOYS AT 525°C *

Material	Fluence (> .1 MeV) n/cm^2 sec	Void concentration (voids/cm^3)	Average diameter (Å)	Volume fraction %
Vanadium	1.1×10^{22}	$1.2\text{-}8.0 \times 10^{15}$	102-198	.3-1.1
V-1Ti	"	$.04\text{-}0.5 \times 10^{15}$	60-120	.005-.011
V-5Ti	"			
V-10Ti	"	----- no voids -----		
V-20Ti	"			

* ref. 56

TABLE A.11

VOID FORMATION IN Nb AND Nb-1Zr IRRADIATED AT 790°C[a] 35

Material	Condition	Average void diameter, Å	Void density (voids/cm^3)	volume fraction %
Nb	as-irradiated	152	8.7×10^{14}	.21
	as-irradiated annealed 1230°C	210	1.9×10^{14}	.08
	as-irradiated annealed 1230°C		no voids	
Nb-1Zr	as-irradiated	575	1.8×10^{14}	2.20
	as-irradiated annealed 1230°C	616	8.2×10^{14}	1.16
	as-irradiated annealed 1230°C	663	3.4×10^{13}	.58

[a] fluence = 2.5×10^{22} n/cm^3 sec (E > .1 MeV).

Thus, voids in niobium are stable to .6 T_m. Alloying with 1% zirconium reduces void nucleation resulting in increased diameter and decreased concentration. The presence of voids after 1380°C annealing indicates that voids are stable in Nz-1Zr to .6 T_m.

316 Stainless Steel

Broger et al performed neutron irradiation and swelling measurements on 316 SS at temperatures from 450°C-690°C,[58] Table A.12. The 450°C irradiated specimen contained a moderately high density of voids fairly uniformly distribued throughout the matrix. The speciments irradiated at 535°C and 610°C also contained unusual microstructural features. Void formation at 535°C was very heterogeneous. However, a few regions contained a high concentration f large voids in the form of bands similar to microtwins. Steel irradiated at 610°C exhibited a duplex void size distribution. All of the large voids were attached to $M_{23}C_6$ polyhedral precipitates. The formation of voids near the precipitates may be due to stres field attraction of voids to precipitates. It may be noted that the addition of titanium may reduce void swelling as in the vanadium.

From data presented, it is evident that the swelling is a minimum in vanadium which is most attractive. However the swelling due to irradiation does not appear to be a major problem with either niobium or 316 stainless steel.

A.7 NEUTRONIC CHARACTERISTICS

Nuclear afterheat and induced activity can become a serior problem when considering various structural materials. Steiner[58] and Vogelsang[55] have done extensive work on this problem in vanadium, niobium and 316 SS. The areas that will be considered here are neutron multiplication, nuclear heating, nuclear afterheat, induced activity and biological hazards.

TABLE A.12

SWELLING IN 316 SS DUE TO IRRADIATION *

Temperature (°C)	Fluence (E >.1MeV) n/cm^2 sec	Void diameter, Å min	max	mean	Void density (voids/cm^3)	Void vol. % ($\Delta V/V$)	Swelling ($\%\Delta\rho/\rho$)
454	8.6×10^{22}	117	240	400	2.2×10^{14}	.18	.13
535	8.9×10^{22}	117	347	834	8.6×10^{12}	.03	.42
	"	117	749	1450	6.8×10^{13}	2.0	
609	8.8×10^{22}	133	315	700	4.6×10^{13}	.8	2.30
	"	467	1506	2767	1.1×10^{13}	3.63	
689	9.4×10^{22}	-	-	-	$< 10^{12}$	0.0	-.009

* ref. 58

The information will be presented for vanadium and niobium with some contributions on 316 SS, V-20Ti and Nb-1Zr.

A.7.1 Neutron Multiplication

Table A.13 gives the neutron multiplication and parasitic absorption (including the (n,γ) reaction) of vanadium and niobium in the four structural zones of the breeding blanket considered by Steiner[5a]. All quantities are normalized to a source of one fusion neutron. The following points should be noted:

1) Neutron multiplication (n, 2n) is 45% higher in niobium than in vanadium. However, parasitic absorptions are 68% higher in niobium. Now, comparing the (n,2n) and parasitic absorptions in each structural material, it is noted that the parasitic absorption is greater than the neutron multiplication by only a small amount in vanadium, but by a large margin in niobium.
2) Resonance capture is higher in niobium but thermal capture is higher in vanadium.

Based on these results, vanadium appears to be superior to niobium in neutron economy which will affect tritium breeding.

A.7.2 Nuclear Heating

Nuclear heating rates in vanadium and niobium structural zones of Steiner's blanket analysis are presented in Table A.14 (zone 3 is the first wall). The rates are normalized to a neutron wall loading of 1 MW/m^2. Important points to note are:

1) Nuclear heating in the first wall is 36% lower in vanadium. This reflects vanadium's lower gamma-ray contribution due to its lower atomic number.
2) This effect is somewhat offset by the higher neutron contribution

TABLE A.13

SUMMARY OF (n,2n), (n,γ) AND PARASITIC ABSORPTIONS IN THE BLANKET STRUCTURE [a]

Material	(n,2n)	(n,γ)	Parasitic Absorption [b]
Vanadium	.0242	.0247	.0285
Niobium	.0342	.0466	.0480

[a] ref. 58.
[b] includes (n,γ) reaction.

TABLE A.14

NUCLEAR HEATING RATES IN V AND Nb STRUCTURAL ZONES *

Zone	Heating rate in Vanadium (w/cm^3)			Heating rate in Niobium (w/cm^3)		
	Total	From neutrons	From gamma-rays	Total	From neutrons	From gamma-rays
3	4.12	2.04	2.08	6.43	0.97	5.46
5	2.35	0.81	1.54	3.70	0.22	3.48
7	0.62	0.28	0.34	0.47	0.01	0.46
9	0.16	0.00	0.15	0.22	0.00	0.22

* ref. 58

of vanadium. This is due to the larger cross-section for charged particles as compared with niobium.

3) A comparison of the total energy deposited in a blanket with either niobium or vanadium was made by Abdou[11] and he pointed out that for a 1 Mw/m^2 loading the use of niobium produces about 1 Mev more per fusion than vanadium and about 1.1 Mev more per fusion than 316 SS. It appears possible however to use a higher wall loading with vanadium than with 316 SS and this would make vanadium more attractive economically.

A.7.3 Nuclear Afterheat

Table A.15 gives the afterheat as a function of time for a 1 MW/m^2 neutron wall loading. Here, vanadium exhibits greater afterheat due to the V^{52} isotope. However, as displayed in Table A.16, the afterheat has decayed to approximately 13% of its initial value in only 0.01 days (15 min.). This decay continues until after one day, the afterheat is one order of magnitude below that of niobium. Figures A.4 and A.5[55] illustrate the afterheat after startup and after shutdown following 10 years of operation of UWMAK-I respectively.

A.7.4 Induced Activity

The induced activity is expressed as a function of irradiation time for a 1 MW/m^2 neutron wall loading in Table A.15. Vanadium exhibits a consistently lower activity level than niobium. The rates for UWMAK-1 are given in Table A.17 after 10 years of operation. Again, 316 SS and Nb-1Zr are considerable hotter than V-20Ti. Figures A.6 and A.7[55] gives the activity of 316 SS, Nb-1Zr and V-20Ti at shutdown and after shutdown, respectively.

TABLE A .15

AFTERHEAT AND ACTIVITY AS A FUNCTION OF IRRADIATION TIME*.58

Irradiation time (yrs)	Afterheat % of reactor thermal power		Activity (Ci/w th)	
	Vanadium	Niobium	Vanadium	Niobium
1	.291	.100	.23	.65
2	"	.105	"	.68
3	"	.109	"	.70
4	"	.113	"	.73
5	"	.118	"	.75
6	"	.122	"	.77
7	"	.126	"	.79
8	"	.130	"	.81
9	"	.134	"	.83
10	"	.137	"	.85

* neutron wall loading of .1 MW/m^2.

TABLE A.16

AFTERHEAT AS A FUNCTION OF TIME AFTER SHUTDOWN* [58]

Time after shutdown (days)	Afterheat as % of reactor thermal power	
	Vanadium	Niobium
0.0	.291	.137
.01	.038	.127
.1	.017	.125
1.0	.012	.118
10.0	4.0×10^{-4}	.074
100.0	3.8×10^{-4}	7.13×10^{-3}
1000.0	6.5×10^{-9}	3.23×10^{-4}

* after 10 years operation at a wall loading of 1 MW/m^2 (neutronic).

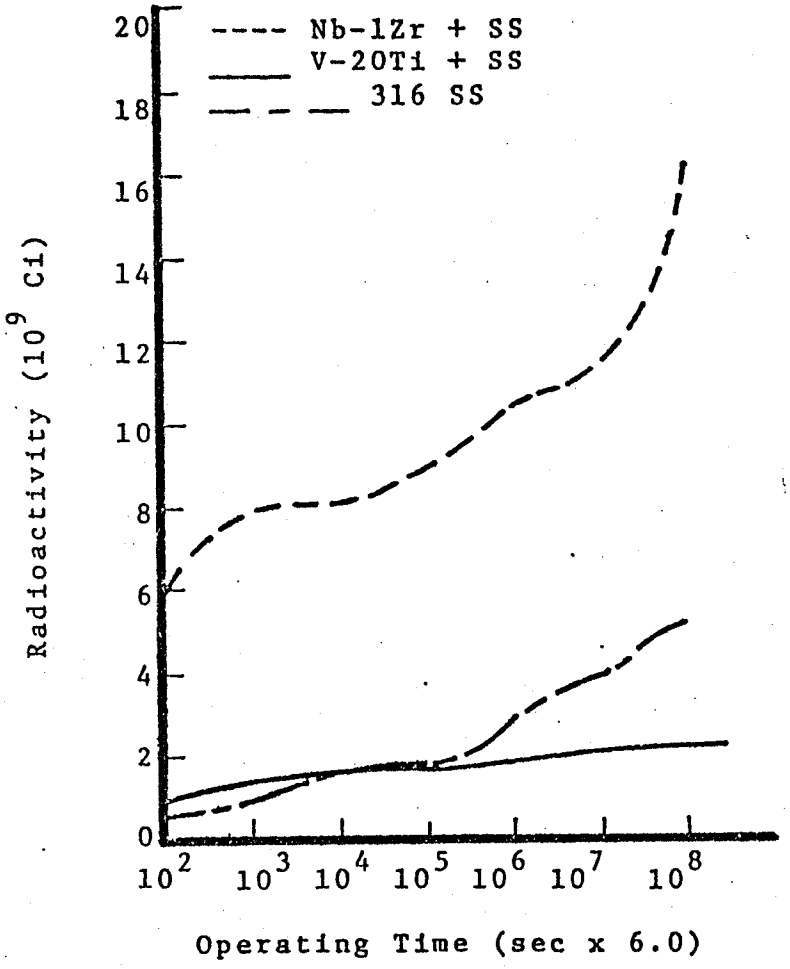

Fig. A.6 Radioactivity at Shutdown of UWMAK-I.

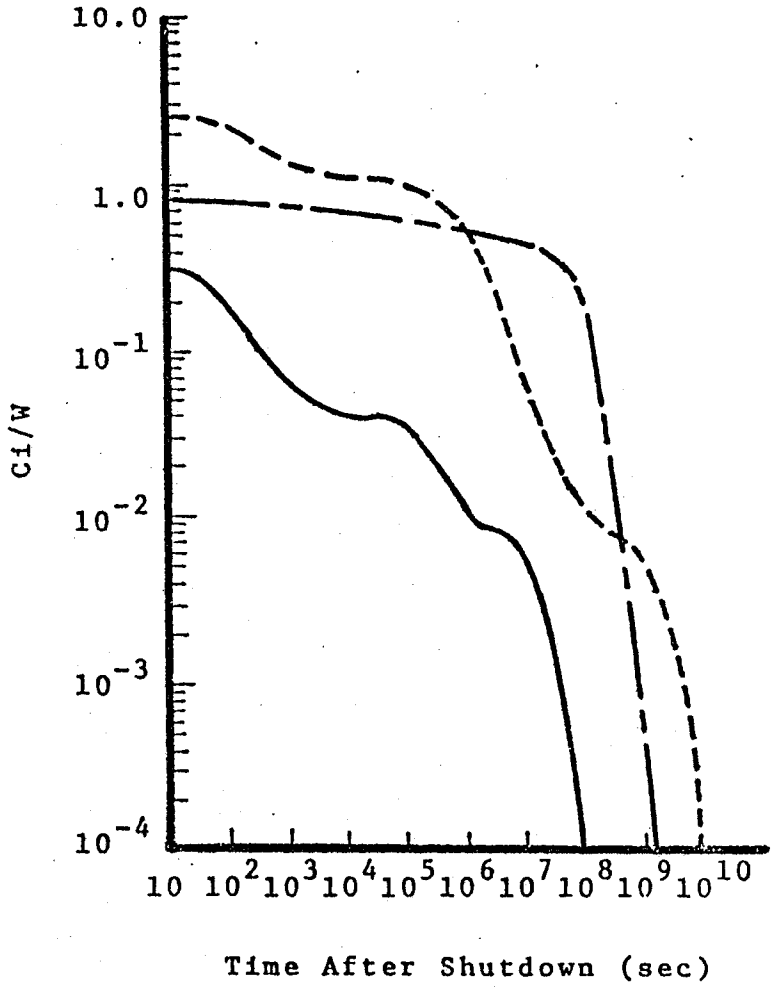

Fig. A.7 Decay of Radioactivity in UWMAK-I After 10 years of operation.

A.7.5 Biological Hazard Potential

A good indication of the biological hazard of the induced activity is the BHP (Biological Hazard Potential) as described by Steiner.[5] The BHP is determined by dividing the activity in Ci/w by the maximum permissible concentration (MPC) for exposure in air. The BHP is equivalent to the volume of air required to dilute the activity per thermal kilowatt to the MPC. As is evident from Table A.16, the BHP for V-20Ti is significantly lower than for Nb-1Zr or 316 SS. However, it is probable that impurities may significantly raise this level.

The following obserations can now be made.

1) The parasitic absorptions in vanadium are significantly less than in niobium and will aid in tritium breeding.
2) Nuclear heating in the first wall is substantially lower in vanadium than in niobium.
3) Vanadium will exhibit an afterheat, activity and biological hazard several orders of mangitude lower than niobium and about 10 times lower than 316 SS.

These results all heavily favor a vanadium alloy as a first wall material as opposed to a niobium alloy or stainless steel.

A.8 EFFECTS OF OXYGEN, HELIUM AND HYDROGEN

It is greatly feared that helium, hydrogen, and oxygen will have severe embrittlement effects in structural materials at high temperatures. Therefore, it may be helpful to present some points of view on this question. First, titanium and zirconium are added as getters to vanadium and niobium, respectively, Further, it has been found that nitrogen and oxygen can improve the creep strength of niobium for $T < 0.5\ T_m$. However, an oxygen substitution for carbide in VANSTAR alloys can greatly reduce the creep strength.

In considering hydrogen embrittlement, it is expected that substantial hydrogen concentrations will be necessary to produce a ductile to brittle transition in niobium and vanadium at CTR operating conditions. For example, an extrapolation would predict that 36 atom % H in niobium and 93 atom % in vanadium would be required to raise the Ductile to Brittle Transition Temperature, DBTT to the CTR operating temperature range.[59] Even if this extrapolation is invalid, the entire problem has not been presented. At various periods during the lifetime of a CTR, the reactor will be brought down near room temperature and the structural integrity must be preserved at these temperatures. The data available concerning impurity effects at high temperatures is sparce, but relevant findings will be presented.

A.8.1 Oxygen Effects

Loomis et al irradiated niobium and Nb-1Zr with 3.5 MeV Ni^{58+} ions.[60] Voids were observed in pure niobium at 600°C. However, after an addition of 900 ppm O_2 the voids were not observed until 700°C. Furthermore, they were smaller and more evenly distributed.

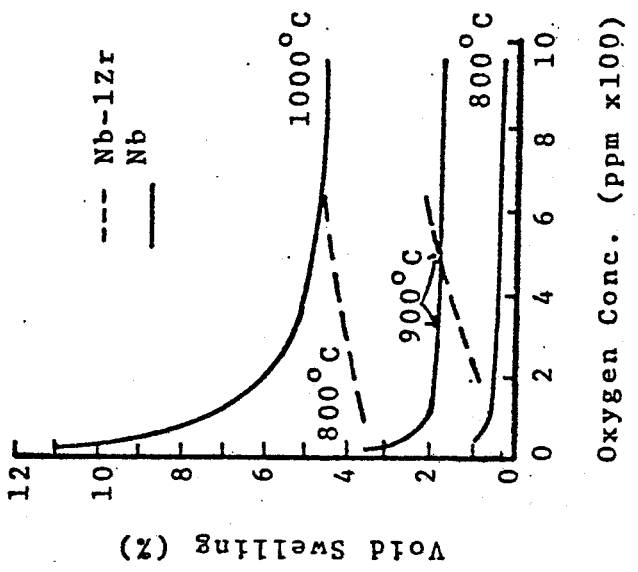

Fig. A.9 Effect of Oxygen on Void Swelling of Nb and Nb-1Zr.

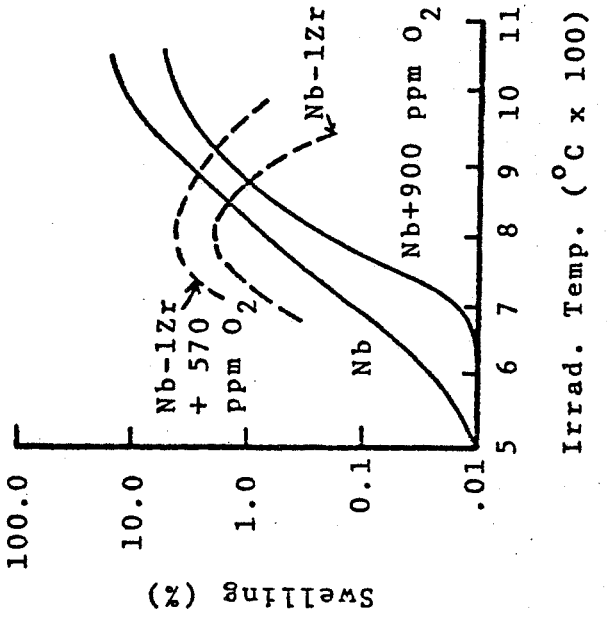

Fig. A.8 Effect of Temperature on Swelling of Nb and Nb-1Zr.

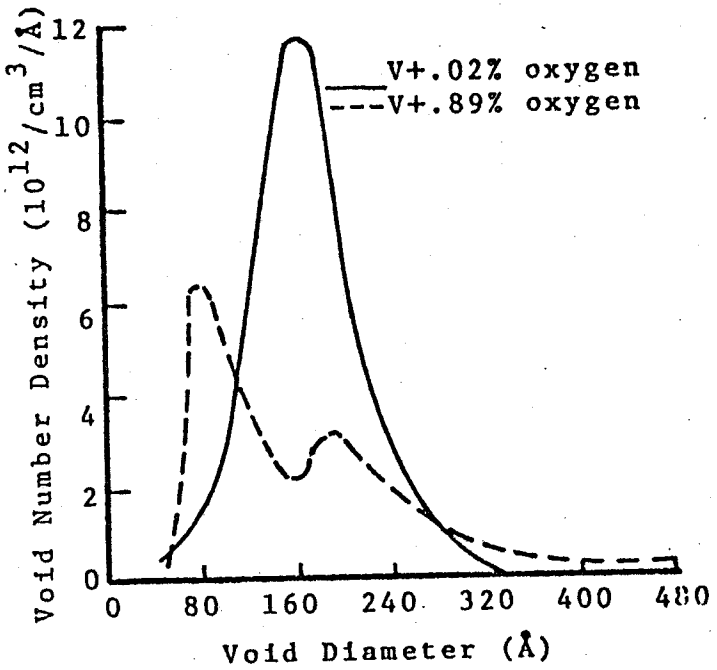

Fig. A.10 Effect of Oxygen on Void Formation in Vanadium.

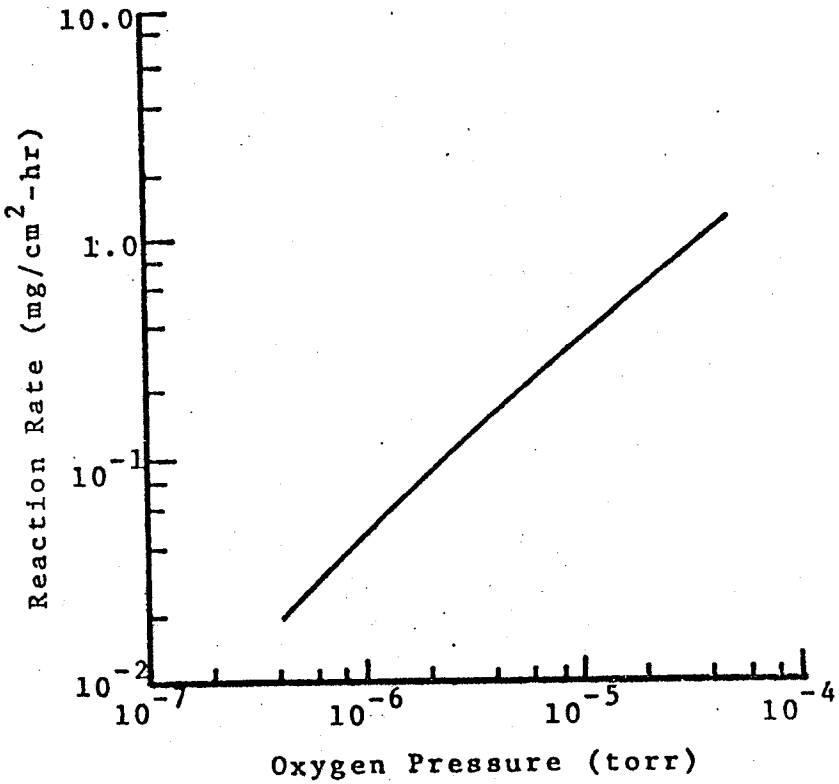

Fig. A.11 Reaction Rate of 1093°C Nb-1Zr with Oxygen.

Pure Nb-1Zr and Nb-1Zr doped with 570 ppm O_2 were irradiated at 800°C and 900°C to the same fluence. The oxygen doped alloy developed ordered bcc super lattices of voids at 25 DPA. This was not observed until 100 DPA in NB or NB with O_2. Figure A.8 shows the effect of temperatures on the void swelling of Nb and Nb-1Zr while Figure A.9 shows the effect of oxygen on swelling.[60]

From this data, it appears that oxygen reduces swelling in niobium and enhances it in Nb-1Zr by promoting a void lattice. It would also appear that for a vacuum wall the swelling could be reduced by increasing the oxygen concentration to the solubility limit which is 4000 ppm at 800°C. However, corrosion and embrittlement may become a problem long before this.

For commerical purity vanadium, the addition of oxygen appears to increase the void diameter and the swelling. Figure A.10 shows the effect of oxygen on void formation in vanadium for specimens irradiated at 525°C to a neutron fluence of 1.1×10^{22} n/cm^2 (E > 0.1 Mev).[56]

The reaction rate of Nb-1Zr at 1093°C with oxygen is given in Fig. A.11[61]. For an oxygen pressure of 10^{-6} torr (immeasurably low in a helium system pressure of 35,700 torr) the reaction rate is about 0.04 mg/cm^{2}hr. This reaction rate is related to a reduction rate of the niobium wall thickness through the number density.

$$0.04 \text{ mg/cm}^2\text{hr} = \frac{4 \times 10^{-5} \text{ g/cm}^2\text{hr}}{8.7 \text{ g/cm}^3} = 4.6 \times 10^{-6} \text{ cm/hr}$$

After 1000 hours, the reduction would amount to 1000 x (4.6×10^{-6}) = .0046 cm or .046 mm. For the 2.0 mm module wall design, this would result in a 2.3% reduction in thickness and a corresponding loss of strength. Clearly this material will not survive long under such conditions.

Vanadium is believed to be even more reactive with oxygen than niobium and this would restrict the maximum operating temperature to a lower value. Fraas stated that a maximum temperature for niobium with a helium coolant would be approximately 600°C and for vanadium approximately 500°C.

A.8.2 Helium Effects

Helium in vanadium has been found to reduce swelling.[62] The reasoning behind this is that since the material has a low dislocation density, the helium bubbles were the predominant sink for the radiation-produced point defects. This would have an effect in low ering the vacancy super-saturation and hence the swelling. Table A.18 shows the effect of helium on swelling in vanadium.

It is also known that helium reduces the ductility of stainless steel. Table A.19. However, it has been observed that doping 316 SS with 100 ppm helium by cyclotron implantation and subjecting the specimen to thermal aging for 1000 hours at 650°C enhances fatigue performance of annealed and 20% cold worked 316 SS by increasing fatigue life and decreasing the crack growth rate.[63] Helium has the effect of supplanting the massive $M_{23}C_6$ precipitate that reduced fatigue life.

TABLE A.18

VOID SWELLING IN VANADIUM AFTER Ni^+ ION IRRADIATION[a] 62

Material	T (°C)	Helium content (atom ppm)	Void concentration (voids/cm^3x10^{15})	Average void size, A	Void volume (%)
HPV[b]	650	10	0.97	120	0.21
HPV		100	1.60	115	0.29
CPV[b]		10	18.0	52	0.22
CPV		100	19.0	45	0.13
HPV	750	10	1.9	206	2.17
HPV		100	1.7	141	0.61
CPV		10	2.1	238	3.45
CPV		100	2.5	100	0.34

[a] dose ~ 60 dpa.

[b] HPV is high-purity vanadium and CPV is commercial-purity vanadium.

TABLE A.19

REDUCTION IN DUCTILITY OF 316 SS DUE TO He CONTENT *

Helium content (appm)	Yield strength (psi)	Elongation %	
		Uniform	Total
0	11,000	9	47
40	12,000	4	6

* ref. 64

There is not one model available to completely explain swelling under the mixed irradiation condition of high DPA and high helium production. However, it appears that helium is the main contributor to swelling. Cold work is effective in suppressing swelling at temperatures below 600°C since in the cold-worked sample the cavity density is greater than in the solution annealed specimen. The increased cavity density will accomodate the increased amount of swelling. However, the helium concentration at the grain boundary may lead to intergrannular failure well before swelling becomes important. Finally, the breakdown of the resistance of cold-worked stainless steel to swelling at 680°C indicates an upper limit of 700°C for reactor operation. The effect of the helium content on 316 stainless steel is given in Table A.20.

A.8.3 Hydrogen Embirttlement

It is well known that hydrogen causes severe embrittlement of vanadium and niobium near room temperature. The suspected embrittlement mechanism is the formation of vanadium-hydride particles at the DBTT[65]. One other possible explanation is that the hydrogen reduces the true surface energy and therefore the associated binding energy or cohesion of vanadium.

However, it is questionable as to whether hydrogen will have a strong effect on vanadium and niobium at such high temperatures as those expected at the first wall. It is quite unlikely that the hydrogen concentration in these metals can push the BDTT to a point near reactor temperature cycling range. Experimental data on permeation and diffusion of hydrogen in niobium and vanadium are extremely sparse, but the general range will be a diffusion coefficient on the order of 10^{-4} cm^2/sec and a permeability of 10^2 $\frac{cc(STP)mm}{atm^{1/2}hr\text{-}cm^2}$ (extremely high). The effect of hydrogen on vanadium is given in Table A.21.

A.9 FABRICABILITY, AVAILABILITY AND COST

Fabrication methods for all three metals are well established but perhaps not yet developed on the industrial scale.[67] Initial hot reduction is usually carried out under the protection of a steel jacket. Westinghouse Astronuclear, developed of the VANSTAR alloys has found that V-20Ti and the VANSTAR alloys are equally fabricable and no unusual problems have been encountered in forging, sheet rolling or swagging.[68]

The amount of vanadium currently used in industry is small when compared with the quantity that would be needed for one fusion reactor.[69] It is doubtful that discoveries could increase world reserves enough to support a fullblown fusion economy at this time, however, this is not within sight for the next several decades. For the purposes of this study and near term use of refractory metals, the available amounts are adequate for experimental purposes and pioneer fusion power reactors. Table A.22 gives reserves of vanadium, niobium and titanium.

Cost is an area in which stainless steel enjoys a tremendous advantage over refractory metals such as niobium or vandium. For example, the cost of one kilogram of stainless steel is approximately $15 while niobium will cost about $65/kg and vanadium even more.[70] Thus, on a small scale, only stainless steel will be economical, and on a large scale, the scarcity of niobium could keep its price prohibitively high.

A.10 CONCLUSION

Based on the preceeding analysis, vanadium alloys as a whole are most attractive. This conclusion was based on several different vanadium alloys evaluated on each criterion. They exhibit good high temperature strength, creep strength, ductility, extremely low swelling, afterheat,

TABLE A.20

SWELLING DUE TO HELIUM CONTENT IN IRRADIATED 316 SS [65]

T (°C)	Fluence (E > 0.1 MeV) n/cm^2 sec	Calculated displacements (dpa)[a]	Calculated helium content (ppm)[b]	Measured swelling %	
				Solution treated	20% cold worked
535	3.79×10^{22}	52	1930	3.5	.52
574	4.21×10^{22}	58	1791[c]	3.3	-
602	8.71×10^{22}	119	5940	8.0	3.3
679	8.74×10^{22}	121	6090	14.1	16.8

[a] DPA calculated from the Lindhard model.

[b] atomic concentration calculated by the formula $C = 9.8 \times 10^{-19} (\phi t)^{1.6}$ atoms He/g Ni, where ϕt is the thermal fluence.

c measured helium content.

TABLE A .21

HYDROGEN EMBRITTLEMENT OF VANADIUM AT ROOM TEMPERATURE *

Condition	Yield strength (psi)	Ultimate tensile strength (psi)	Elongation %	
			Total	Uniform
Annealed	27,571	47,143	42	22
Low H_2 (400 ppm)	36,571	38,143	40	22
High H_2 (10^3 ppm)	38,857	60,000	24.4	18.6

* ref. 66

TABLE A.22

ESTIMATED RESERVES OF SELECTED REFRACTORY METALS *

Material	Inventory for 10^6 MWe capacity (metric megatons)	World reserves (metric megatons)	Ratio of quantity in the Earth's crust to world reserves
Niobium	3.3	10	9.4×10^3
Vanadium	2.4	10	6.6×10^4
Titanium	0.5	150	1.9×10^5

* ref. 50

gas production and induced activity. The areas of concern in the proposed design environment are embrittlement and corrosion by hydrogen and oxygen and the high cost. However, there is no single vanadium alloy that exhibited all of these attractive characteristics. This is in part due to the lack of data available on many of the alloys analyzed. Nevertheless, with the availability of data on vanadium alloys, there appears to be good promise.

While 316 SS enjoys a large cost, availability and fabricability advantage over either niobium or vanadium, it is limited to lower operating temperatures by its comparatively low melting point (1430°C) and low creep-rupture strength. In the case of a failure, temperatures in the 800°C range may be reached which would require stainless steel to operate above 0.5 T_m. Furthermore, it develops high thermal stresses and exhibits a high helium production rate, afterheat and activity.

Niobium-1Zirconium has an advantage over stainless steel in that its melting point and operability limit is the highest of all alloys surveyed. It has high temperature strength, low swelling and gas production. However, Nb-1Zr suffers from the possibility of hydrogen and oxygen embrittlement and corrosion, high afterheat, activity and cost. Nevertheless, all things considered, Nb-1Zr possesses the most characteristics necessary for the structural material of the BRSR. Therefore, Nb1Zr has been used as the reference material for the first wall and module structure of the BRSR.

APPENDIX B

ENERGY GENERATION IN FUSION BLANKETS

B.1 KERMA

A fusion neutron carries 80% of the fusion energy and therefore is the primary energy source in a non-fissioning fusion blanket. Contrary to a fission reactor where most of the energy released is deposited locally, a fusion neutron undergoes a variety of reactions with the blanket materials releasing various amounts of energy in each of the reaction types before its final thermalization and/or its absorption by the breeding materials. Among the neutron reactions, (n,γ) produces a photon which also has high penetrating power and carries a non-negligible amount of energy. For the purpose of calculating the energy generation in a blanket, the heating rate is divided into two types of contribution.

1. Heat generated by the various neutron reactions
2. Heat generated by the absorption of the secondary gamma radiation produced by the neutron reactions.

Therefore, the calculation of the energy generation in a blanket requires the knowledge of energy released per neutron reaction and per gamma reaction. The factor which governs the probable energy released per reaction is the Kerma factor (an acronym for kinectic energy released in material). The neutron kerma factor is defined as

$$k_{ij}(E) \equiv \sigma_{ij}(E)\, E_{ij}(E) \qquad \text{B-1}$$

$$k_{j}(E) \equiv \sum_{i} k_{ij}(E) \qquad \text{B-2}$$

Many investigators [B1, B2, B3] had calculated the neutron kerma factors with the most recent contribution from Abdou [B4], the results of which are documented in DLC-29 [B5] and DLC-37b [B10].

The gamma kerma factor is defined by the following equation

$$k_\gamma^j = \sigma_{pe}^j E_p + \sigma_{pp}^j (E_p - 1.02) + \sigma_{cs}^j E_p \qquad \text{B-3}$$

Equation (B-3) reflects the three processes [B6] that are mainly responsible for the absorption of the gamma radiation, namely the photoelectric absorption, the compton scattering by the electrons in the atoms and the production of electron-positron pairs. In the pair production process, part of the photon energy, though initially absorbed, reappears almost immediately by the production of two 0.511 Mev photons. This is the reason for the correction in the pair production of equation (B-3). The calculation of the gamma kerma was computer coded and is documented in PSR-51 [B7], and the gamma kerma factors are included in DLC-37b [B10].

To facilitate the calculation of the q''' to be discussed later in Appendix B.3, a computer code KERMA was developed to extract the kerma factors from DLC-37b and to create a new data set DISKERMA on disks containing the kerma factors for 26 materials as exhibited in Table B-1.[2]

B.2 ANISN

In addition to the kerma factors, the calculation of the blanket energy production rate also requires the spatial distribution of the neutron flux and the gamma flux. The central problem

of flux determination is the solution of the integral-differential Boltzman Transport equation.[B8] With the exception of a very simple case, the solution to the Boltzmann's equation requires the execution of one of the several computer codes: ANISN, DOT, Monte Carlo, etc. In this study, the ANISN code was used. The group to group transport cross section data sets used with ANISN was DLC-28[B9], which is a coupled neutron/gamma data set with 52 neutron groups from 14.9 Mev to 0.02 Mev and 21 gamma groups from 14.0 Mev to 0.01 Mev. The procedures for the operation of ANISN is documented but a slight variation was adopted in this study. The details of this procedure can be found in Chen's thesis.[21]

B.3 CTRHEATFLUX

With the flux distribution and the kerma factors, the energy generation rate is calculated by the following equation

$$q'''(r) = \int_{\text{all } E} \phi(r,E) \sum_j \sum_i n_j(r)\, k_{ij}(E)\, dE \qquad \text{B-4}$$

CTRHEATFLUX was coded to calculate q''' using the flux from ANISN and the kerma factors from the dataset DISKERMA discussed earlier in Appendix B.1.

B.4 SAMPLE PROBLEM AND OUTPUT

The aforementioned procedures were tested in the sample calculation of a blanket of 40 cm of carbon sandwiched between two 30 cm layers of lithium. This blanket is represented as Figure B-1 where the composition of zones 3 and 5 designates natural lithium. In the ANISN transport calculation, the P3-S4 configuration was used with the ORNL 73-groups coupled cross section dataset DLC-28[B9]. This procedure was checked out by repeating the Steiner benchmark calculation [B12] for a CTR blanket, though, in this case, a 100-groups neutron cross section dataset DLC-2[B13] and a 100-groups reaction cross section dataset DLC-24[B14] were used.

With the kerma factors from the dataset DISKERMA created in Appendix B.1 and the neutron/gamma flux calculated/punched by ANISN for the sample blanket, CTRHEATFLUX was executed to calculate the q'''. It should be pointed out that in the sample blanket there is one interval each in zones 1 and 2, 50 equal intervals of 2 cm in zones 3 to 5. CTRHEATFLUX also plots the neutron flux, the gamma flux and the volumetric heat rate which are included as Figures B-2, B-3 and B-4. In Figure B-2, the conventional energy unit of lethargy is adopted and is defined as the natural logarithm of the inverse of the energy in units of 10 Mev. Curve B of Figure B-2 shows the moderating effect of the carbon on neutrons whereas curve C reflects the 1/v cross section of ^{6}Li (n,t) reaction causing a depletion of low energy neutrons. In Figure B-4, the results calculated by Santoro[B-15] of ORNL using ANISN is included showing favorable agreement with the results calculated by CTRHEATFLUX. The steep rise in heat generation, both before and after the carbon region is primarily due to the moderation of neutron energy by carbon. The carbon in zone 4 reflects a portion of the incoming neutrons back in zone 3 creating a high neutron population just before the graphite and therefore increasing the chance of energy released in that region. Also, because of the moderation of neutrons through zone 4, the frequency of the 1/v exothermic ^{6}Li (n, αt) reaction increases with the availability of the low energy neutrons at the beginning of zone 5 causing the increase in heat generation. Similarly, the procedures developed here were used to calculate the q''' for the blanket discussed in Chapter 2 with the final result from CTRHEATFLUX presented as Figure 5.

A complete listing of the codes used along with sample outputs and user instructions is contained in F. Chen's Thesis.[21]

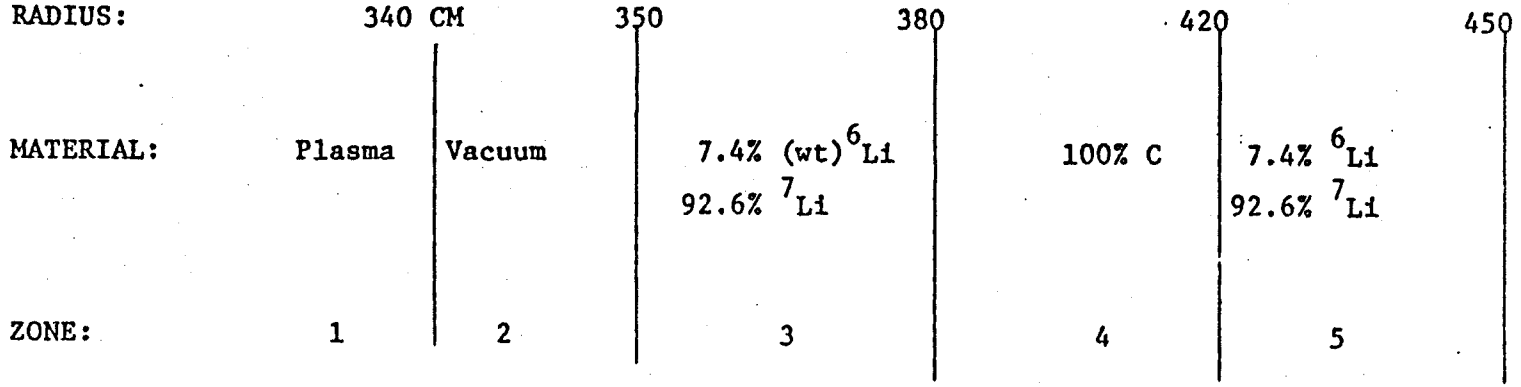

FIGURE B-1: SCHEMATIC OF THE BLANKET USED IN THE SAMPLE CALCULATION

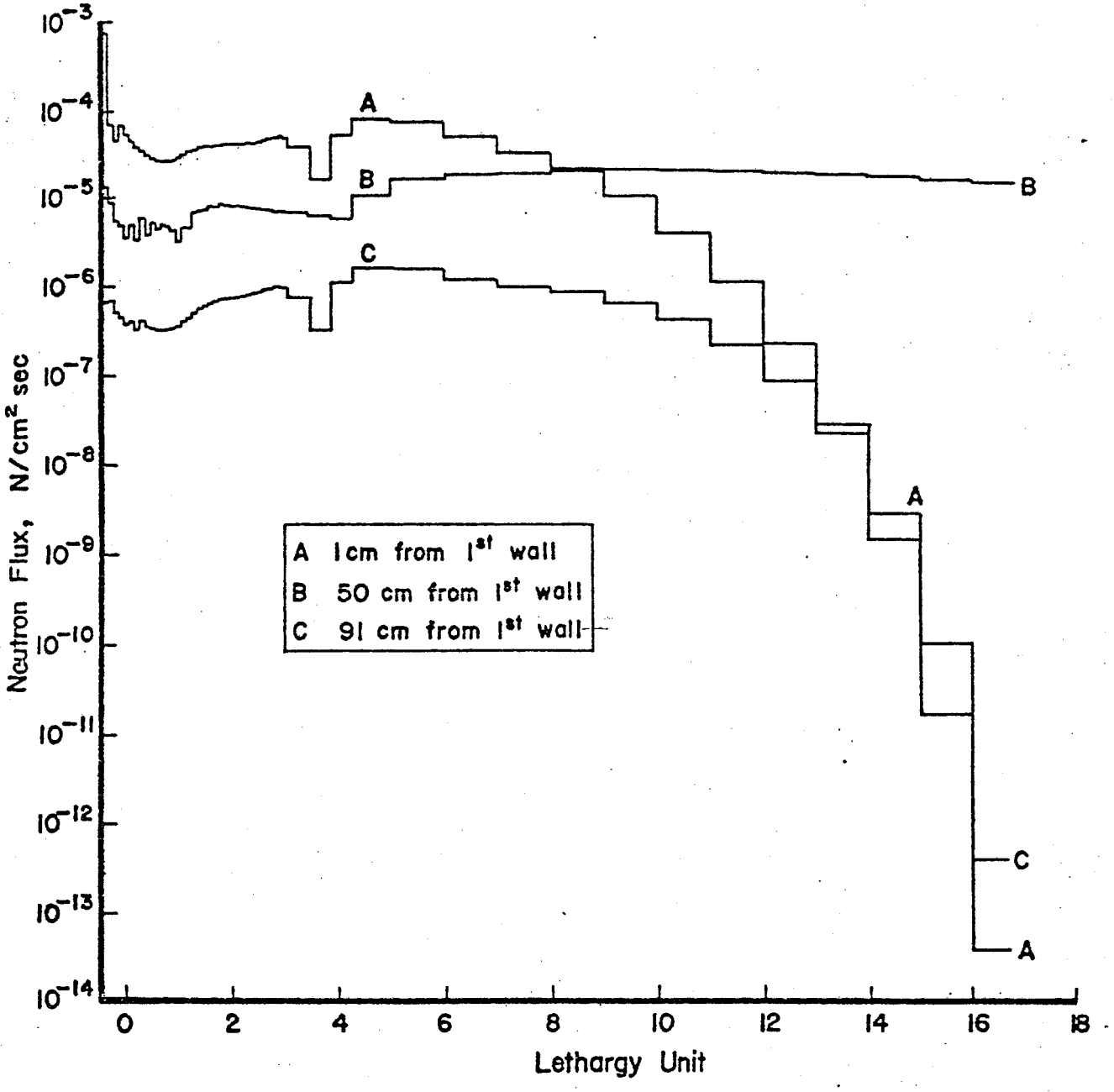

FIG. B-2 NEUTRON FLUX OF THE SAMPLE BLANKET

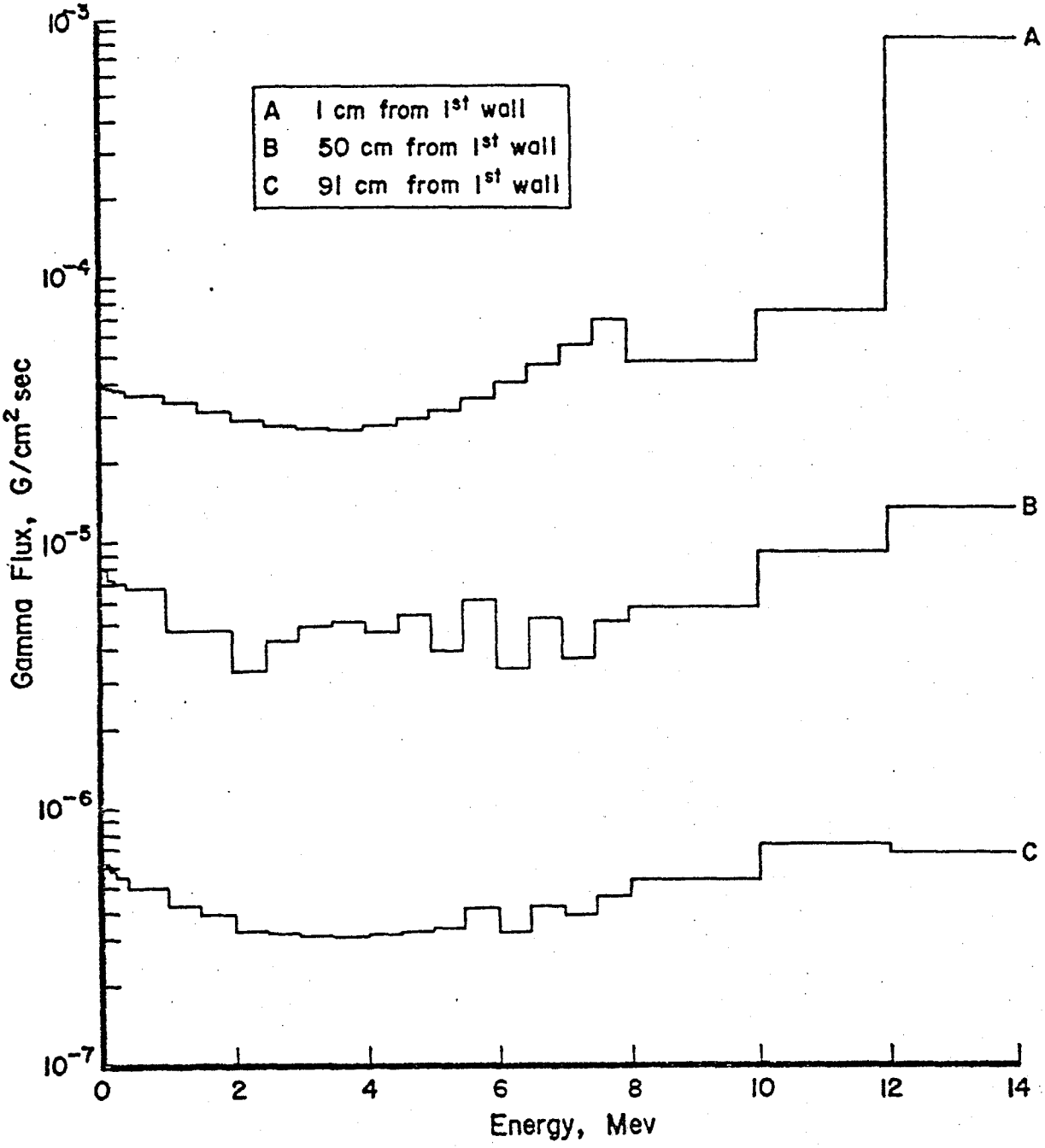

FIG. B-3 GAMMA FLUX OF THE SAMPLE BLANKET

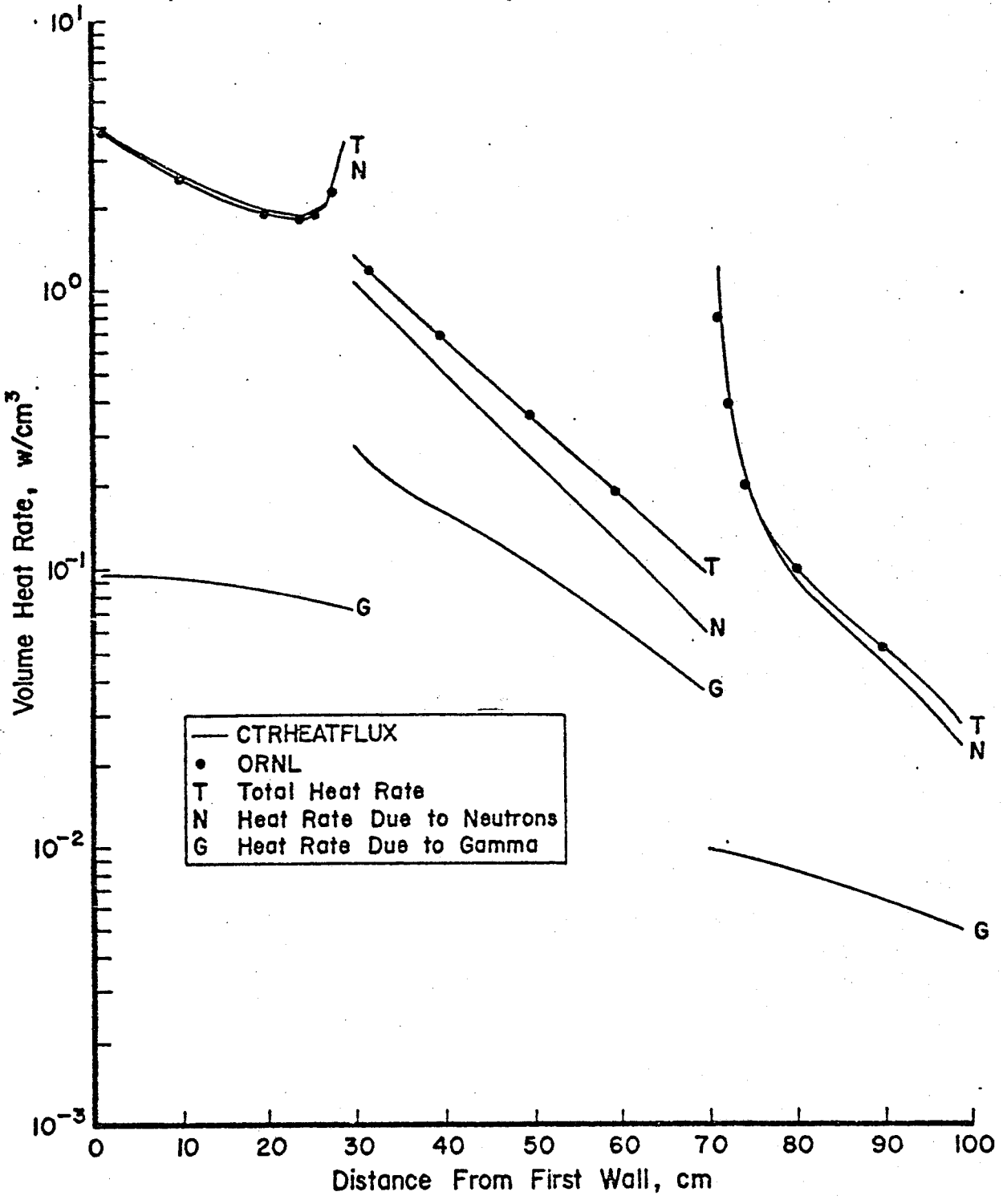

FIG. B-4 VOLUME HEAT RATE OF THE SAMPLE BLANKET

TABLE B-1

CONTENTS OF DATASET DISKERMA

MAT. NO.	MATERIAL	NEUTRON KERMAS (Groups 1-100)	GAMMA KERMAS (groups 101-121)
1	Ni	yes	yes
2	Cr	"	"
3	Fi	"	"
4	^{55}Mn	no	"
5	^{59}Co	no	"
6	Cu	yes	"
7	^{4}He	"	"
8	C	"	"
9	O	"	"
10	Al	"	"
11	Pb	"	"
12	^{6}Li	"	"
13	^{7}Li	"	"
14	^{10}B	"	"
15	H	"	"
16	^{9}Be	"	"
17	V	"	"
18	Nb	"	"
19	^{11}B	"	"
20	Ti	no	yes
21	F	"	"
22	Si	"	"
23	Mg	"	"
24	K	"	"
25	Na	Yes	"
26	W	no	"

References

B1. Williamson, F.S. and Mitacek, P., Jr., "Calculations of Kerma Due to Fast Neutrons in Tissue-Like Materials", Proceedings of the Symposium in Neutron Monitoring Radiological Protection, International Atomic Energy Agency, Vienna, 1967.

B2. Auxier, J.A. and Snyder, W.S., "The Calculation of Kerma as a Function of Neutron Energy", ORNL-4168, Oak Ridge National Laboratory, 1967.

B3. Ritts, J.J., Solomito, M. and Stevens, P.N., "The Calculation of Neutron-Induced Physical Doses In Human Tissues", ORNL-TM-2991, Oak Ridge National Laboratory, 1970.

B4. Abdou, M.A., "Calculational Methods For Nuclear Heating and Neutronics and Photonics Design for CTR Blankets and Shields", Ph.D. Thesis, The University of Wisconsin, Madison, 1973.

B5. Abdou, M.A. and Rosessin, R.W., "Macklib: 100-Group Neutron Fluence-To-Kerma Factors and Reaction Cross Sections Generated By The Mack Computer Program From Data In End Format", ORNL-TM-3995.

B6. Kaplan, I., "Nuclear Physics", Addison Welsley, 1962.

B7. Lucius, J.L. and Ford, W.E. III, "SMUG: Multigroup Photon Cross Section Generator", PSR-51, Oak Ridge National Laboratory, 1973.

B8. Bell, G.Z. and Glasstone, S., "Nuclear Reactor Theory", Van Nostrand Riehold Co., 1970.

B9. Kriese, J.T., "73-Group P_3 Coupled Neutron and Gamma-Ray Cross Sections for Fusion Reactor Calculations", ORNL-TM-4277, Oak Ridge National Laboratory, 1973.

B10. Plaster, D.M., Santoro, R.T. and Ford, W.E., III, "Coupled 100-Group Neutron and 21-Group Gamma-Ray Cross Sections for EPR Calculations", ORNL-TM-4872, Oak Ridge National Laboratory, 1975.

B11. Engle, W.W., Jr., "A Users Manual For ANISN: A One Dimensional Discrete Ordinates Transport Code With Anisotropic Scattering", ORNL-K-1693, Oak Ridge National Laboratory, 1967.

B12. Steiner, D., "Analysis of a Bench-Mark Calculation of Tritium Breeding In a Fusion Reactor Blanket: The United States Contribution", ORNL-TM-4177, Oak Ridge National Laboratory, 1973.

B13. Radiation Shielding Information Center, "100 -Group Neutron Cross Section Data Based on ENDF/B", DLC-2, Oak Ridge National Laboratory, 1972.

B14. Wright, R.Q. and Roussin, R.W., "SINEX: 100-Group Neutron Reaction Cross-Section Data Generated by Supertog From ENDF/B", DLC-24, Oak Ridge National Laboratory, 1973.

B15. Santora, R., Private Communication, January 6, 1976.

APPENDIX C

PERMEABILITY OF THE BREEDER ROD

The permeability of the niobium breeder rod is so high that it appears as a sieve to tritium. A simple calculation will illustrate this fact

PF = tritium permeation in

Ci/sec leaking through the module

$$PF = F \frac{P0_{\frac{cc(STP)mm}{cm^2\ hr\ atm^{1/2}}}}{} \quad \frac{(\sqrt{p_1} - \sqrt{p_2})atm^{1/2}\ WA\ cm^2}{d\ mm}$$

where

$F = 323.6$ Ci/cc (STP)

$$P = \frac{2000}{\sqrt{3}} \exp(-5200/RT) \frac{cc(STP)\ mm}{cm^2\ hr\ atm^{1/2}}$$

p_1 = inside pressure, atm

p_2 = outside pressure, atm

WA = wall area, cm^2

d = wall thickness, mm

Given

$p_1 = 10^{-4}$ torr

$p_2 = 0.0$ torr

$T = 400°C = 673°K$

WA = 45.24 cm^2

d = 2 mm

PF Ci/sec leakage = .017 Ci/sec

Now 10^{-4} torr = 1.395×10^{-7} Ci/cm^3 and 1 segment = 43.676 cm^3
Therefore 1 segment contains 6.09×10^{-6} Ci.

Thus, 1 segment full of tritium will leakout in 3.6×10^{-4} sec = τ_p. The coolant transit time through the module is τ_m = 1.33 sec. Since $\tau_p << \tau_m$, the wall appears as a sieve to tritium.

APPENDIX D

COOLANT LEAKS TO THE PLASMA

The following is a rough estimate of the minimum size of a coolant leak into the plasma which would begin to be of concern.

Consider all the He leaking from a hole to enter the plasma where the He ions are then confined for an average time equal to the particle confinement time.

Let

S = number of He atoms leaking per second

V_p = plasma volume

τ = particle confinement time

A rate balance on helium ions ignoring the production by fusion yields

$$\frac{dn_{He}}{dt} = \frac{S}{V_p} - \frac{n_{He}}{\tau}$$

Integrating and applying the boundary condition $n_{He/t=0} = 0$ yields

$$n_{He} = \frac{\tau S}{V_p}\left(1 - e^{-t/\tau}\right)$$

for $t >> \tau$

$$n_{He} = \frac{\tau S}{V_p}$$

As an arbitrary guide assume that the minimum size leak of concern is one that changes $\bar{Z}$, the average plasma ion charge, by 5%.

$$1.05 = \frac{n_T + n_D + 2\,n_{He}}{n_T + n_D + n_{He}} \qquad \text{or}$$

$$n_{He} = .0526(n_T + n_D)$$

For the reference design the fusion power is 1740 Mw_t. For a uniform density profile at 15 kev $n_T = n_D = 3.5 \times 10^{19}\ m^{-3}$.

Assuming $\tau = 10$ sec and a plasma radius of 3 m we have

$$S = \frac{V_p \cdot n_{He}}{\tau}$$

$$= \frac{(1.86 \times 10^3)(.0526)(7.07 \times 10^{19})}{10}$$

$$= 6.94 \times 10^{20} \text{ atoms/sec}$$

$$S_{MIN} = 4.61 \times 10^{-3} \text{ gms/sec}$$

This is then the size leak which begins to be important. It is nearly equal to the α-particle production rate. To estimate the size hole consider the leak to be from a tube under choke flow conditions. For this case the maximum mass flow is[63]

$$\left(\frac{W}{A}\right)_{MAY} = \sqrt{\frac{k}{R}\left(\frac{2}{k+1}\right)^{\frac{k+1}{k-1}}} \quad \frac{P_o}{\sqrt{T_o}}$$

where

W = mass flow rate

A = cross sectional area

k = 1.66 for He

R = 2.08 J/gm-K for He

P_o = pressure

T_o = temperature

for P_o = 800 Psi

T_o = 600°C

$W = 2.97 \times 10^2 A(cm^2)$ gm/sec

For $W = S_{MIN}$, $A = 1.55 \times 10^{-5}\ cm^2$, or for a circular hole $D = 4.4 \times 10^{-3}$ cm.

APPENDIX E

SOLUTION OF THE TRIPORT DIFFERENTIAL EQUATION

The time dependent inhomogeneous concentration is given as follows

$$\frac{\partial C(r,t)}{\partial t} = D\left(\frac{\partial^2 C}{\partial r^2} + \frac{2}{r}\frac{\partial C}{\partial r}\right) + B \qquad \text{(E.1)}$$

Setting $u = C \cdot r$ we have

$$\frac{1}{D}\frac{\partial C}{\partial t} = \frac{\partial^2 u}{\partial r^2} + \frac{B}{D} \qquad \text{(E.2)}$$

with boundary condition

$$u(0,r) = 0$$

$$\frac{\partial u}{\partial r}(0,t) = 0$$

$$u(t,a) = aC_a$$

Physically $u(r,t)$ can be separated into two functions

$$u(r,t) = \psi(r,t) + \phi(r) \qquad \text{(E.3)}$$

where

$\phi(r)$ represents the steady state solution and

$\psi(r,t)$ represents the transient solution.

Thus we have,

$$\frac{1}{r} = \frac{\partial}{\partial r}\left(r\frac{\partial \phi}{\partial r}\right) = \frac{-B}{D} \quad \text{with B.C. a) } \frac{\partial \phi}{\partial r}(0) = 0 \qquad \text{(E.4)}$$

$$\text{b) } \phi(a) = C_a$$

$$\frac{\partial \psi}{\partial t} = D \frac{\partial^2 \psi}{\partial r^2} \qquad \text{with} \quad \text{B.C. c) } \psi(r,0) = -r\phi(r) \qquad \text{(E.5)}$$

$$\text{d) } \frac{\partial \psi(0,t)}{\partial r} = 0$$

$$\text{e) } \psi(a,t) = 0$$

Solving Eq. (E.4);

$$\frac{1}{r^2} \frac{\partial}{\partial r} \left(r^2 \frac{\partial \phi}{\partial r}\right) = \frac{-B}{D}$$

$$\frac{\partial}{\partial r} \left(r^2 \frac{\partial \phi}{\partial r}\right) = \frac{-B}{D} r^2$$

$$r^2 \frac{\partial \phi}{\partial r} = \frac{-Br^3}{3D} + K_1$$

$$\frac{\partial \phi}{\partial r} = \frac{-Br}{3D} + \frac{K_1}{r^2}$$

$$\phi(r) = \frac{-Br^2}{6D} - \frac{K_1}{r^3} + K_2 \qquad \text{(E.6)}$$

B.C. a) $\frac{\partial \phi(0)}{\partial r} = 0$ gives $K_1 = 0$

B.C. b) $\phi(a) = C_a$ gives $K_2 = C_a + \frac{Ba^2}{6D}$

Therefore

$$\phi(r) = \frac{-B}{6D} r^2 + \frac{B}{6D} a^2 + C_a$$

$$\phi(r) = \frac{B}{6D} (a^2 - r^2) + C_a \qquad \text{(E.7)}$$

$$r\phi(r) = \frac{B}{6D} (a^2 r - r^3) + C_a r \qquad \text{(E.8)}$$

Solving Eq. (E.5)

$$\frac{1}{D} \frac{\partial \psi}{\partial t} = \frac{\partial^2 \psi}{\partial r^2}$$

Using separation of variables $\psi(r,t) = R_t(r)T_t(t)$

$$\frac{1}{D} R_t \frac{\partial T_e}{\partial t} = T_t \frac{\partial^2 R_e}{\partial r^2}$$

$$\frac{1}{DT_t} \frac{\partial T_t}{\partial t} = \frac{1}{R_t} \frac{\partial^2 R_t}{\partial r^2} = -\lambda^2$$

$$\frac{\partial T_t}{\partial t} + \lambda^2 D\lambda T_t = 0 \qquad \text{(E.9)}$$

$$\frac{\partial^2 R_e}{\partial r^2} + \lambda^2 R_t = 0 \qquad \text{(E.10)}$$

Solving Eq. (E.9) gives

$$T_t = C\, e^{-D\lambda^2 t} \qquad \text{(E.11)}$$

Solving Eq. (E.10) gives

$$R_t = P \cos \lambda r + Q \sin \lambda r \qquad \text{(E.12)}$$

Applying B.C. d) $\frac{\partial R_t}{\partial r}(0,t) = 0$ we have $P=0$ and

B.C. e) $\psi(a,t) = 0$ gives $\lambda = \lambda_n = \frac{n\pi}{a}$

therefore

$$R_t(r) = Q_n \sin \lambda_n r$$

$$T_t(t) = C_n\, e^{-D\lambda_n^2 t}$$

Now

$$\psi(r,t) = R_t(r)\, T_t(t)$$

$$\psi(r,t) = \sum_{n=0}^{\infty} a_n\, e^{-D\lambda_n^2 t} \sin \lambda_n r$$

The initial condition (B.C. d) is used to determine a_n.

$$\psi(r,0) = \sum_{n=0}^{\infty} a_n \sin \lambda_n r = -r\phi(r) = \frac{B}{6D}(r^3 - ra^2) - rC_a$$

Thus,

$$a_n = \frac{2}{a}\int_o^a -r\phi(r) \sin \frac{n\pi r}{a}\, dr \qquad \text{(E.13)}$$

or

$$a_n = \frac{2}{a}\int_o^a \left(\frac{B}{6D} r^3 \sin \frac{n\pi r}{a} - \frac{Bra^2}{6D} \sin \frac{n\pi r}{a} - rC_a \sin \frac{n\pi r}{a}\right)dr \qquad \text{(E.14)}$$

Integration gives

$$a_n = (-1)^n \frac{2}{\lambda_n}\left[C_a + \frac{B}{D}\left(\frac{1}{\lambda_n}\right)^2\right] \qquad \text{(E.15)}$$

Thus,

$$\psi(r,t) = \sum_{n=0}^{\infty} (-1)^n \frac{2}{\lambda_n}\left[C_a + \frac{B}{D}\left(\frac{1}{\lambda_n}\right)^2\right]e^{-D\lambda_n^2 t} \sin \lambda_n r \qquad \text{(E.16)}$$

$$u(r,t) = \psi(r,t) + \phi(r) = \frac{B}{6D}(a^2 r - r^3) + C_a$$

$$+ 2\sum_{n=0}^{\infty} \frac{(-1)^n}{\lambda_n}\left[C_a + \frac{B}{D\lambda_n^2}\right]e^{-D\lambda_n^2} \sin \lambda_n r \qquad \text{(E.17)}$$

Finally $C(r,t) = u(r,t)/r$

$$C(r,t) = \frac{B}{6D}(a^2 - r^2) + C_a + \frac{2}{r}\sum_{n=1}^{\infty} \frac{(-1)^n}{\lambda_n}\left(C_a + \frac{B}{D\lambda_n^2}\right)e^{-D\lambda_n^2} \sin \lambda_n r \qquad \text{(E.18)}$$

where $\lambda_n = n\pi/a$

REFERENCES

1. Sako, K., Yamato, H., et al., "Design Study of A Tomamak Reactor", IAEA-CN-331G1-5, Japan Atomic Energy Research Institute, I baraki, Japan, 1974.

2. Powell, J.R., Miles, F.T., Aronson, A., and Winsche, W.E., "Studies of Fusion Reactor Blankets with Minimum Radioactive Inventory and with Tritium Breeding in Solid Lithium Compounds: A Preliminary Report", BNL 18236, Brookhaven National Laboratory, 1973.

.3) 3. Badger, et al, "UWMAK II" UWFDM-112, Nuclear Engineering Department, University of Wisconsin, October 1975.

4. Hopkins, G., "Fusion Reactor Studies: Potential of Low Z Materials for the First Wall", General Atomic Co., San Diego, California, September 1975.

.4) 5. Powell, J.R., Wiswall, R.H., and Wirsing, E., "Tritium Recovery From Fusion Blankets Using Solid Lithium Components", BNL-25063, October 1975.

6. Fraas, A.P., "Comparative Study of the More Promising Combinations
.5) of Blanket Materials, Power Conversion Systems, and Tritium Recovery and Containment Systems for Fusion Reactors", ORNL-TM-4999, Oak Ridge National Laboratory, July 1975.

7. Inouye, H., "Contamination of Refractory Metals by Residual Gases in
.6) Vacuum Below 10^{-6} Torr", ORNL-3674, September 1964.

8. Roche, T.K., "Effect of Degree of Vacuum on the Slow-Bend Creep Behavior of Columbium -0.6% Zirconium at 1000°C", in "Refractory Metals and Alloys III: Applied Aspects", 30, 901-916, Gordon and Breach Science publishers, New York 1966.

9. DeVan, J.H., "Compatability", in "Fusion Reactor First Wall Materials,
.7) WASH-1206", p. 25, 1972.

10. Mills, R.G., "Princeton Reactor Studies Program", Technology of Controlled Thermonuclear Fusion Experiments and the Engineering Aspects of Fusion Reactors, Editor E.L. Draper, Jr., p. 9, April 1974.

11. Abdou, M., "Calculational Method for Nuclear Heating and Neutronics and and Photonics Design for CTR Blankets and Shields", Ph.D. Thesis, Department of Nuclear Engineering, University of Wisconsin, July 1973.

8)

12. Steiner, D., Tobias, M., "Cross-Section Sensitivity of Tritium Breeding in a Fusion Reactor Blanket: Effects of Uncertainties in Cross-Sections of 6Li, 7Li, 93Nb", Nuclear Fusion, Vol. 14, April 1974.

13. Ohkawa, T., "Conceptual Design Study for a Fusion Experimental Power Reactor", General Atomic Co., San Diego, Cal., GA-A13534, 1975.

14. Lefkowitz,Sheldon, "Thermal Hydraulic Assessment of Recent Blanket Designs For Tokomak Fusion Reactors", M.S. Thesis , Department of Mechanical Engineering, M.I.T. 1975

15. Carlson, G.A., Moir, R.W., University of California, Livermore, Trans. Am. Nucl. Soc., 22, 59, November 1975.

16. Steiner, D., "The Neutron Induced Activity and Decay Power of the Niobium Structure of a D-T Fusion Reactor Blanket", ORNL-TM-3094, Oak Ridge National Laboratory, August 1970.

17. Goppage, J.E. and London, A.L., "Heat Transfer and Flow Friction Characteristics of Porous Media", Chemical Engineering Progress, Vol. 52., No. 2, February 1956.

18. Eckert, E.R.G., "Introduction to Heat and Mass Transfe r", McGraw-Hill, New York, 1950.

19. Kunii, D., and Levinspiel, O., "Fluidization Engineering", John Wiley and Sonds, Inc., 1969.

20. Rohsenow, W.M. and Choi, H.Y., "Heat, Mass and Momentum Transfer", Prentice-Hall, Inc. 1961.

21. Chen, F., "Thermal and Hydraulic Considerations for the Designing of a Solid Tokamak Blanket", Ph.D. Thesis, Department of Mechanical Engineering, M.I.T.

22. Conn, R.W., Kulcinski, G.L, Avci, H., and El-Magrabi, M., "New Concepts for Controlled Fusion Reactor Blanket Design", Nuclear Technology, Vol. 26, June 1975.

23. Kunii, D., and Levinspiel, O., "Fluidization Engineering", John Wiley and Sons, Inc. 1969.

24. Coultas, T.A., "First Wall Bumper Concepts," Presented at 1974 Winter ANS Meeting, Washington, D.C., October 1974.

25. Fraas, A.P., "Comparative Study of the More Promising Combinations of Blanket Materials, Power Conversion Systems, and Tritium Recovery and Containment Systems for Fusion Reactors", ORNL-TM-4999, Oak Ridge National Laboratory, July 1975.

26. Rohsenow, W.M. and Choi, H.Y., "Heat, Mass and Momentum Transfer", Prentice-Hall, Inc., 1961.

27. Leval, M., "Fluidization", McGraw-Hill, N.Y., 1959.

28. Ergun, S., "Fluid Flow Through Packed Columns", Chemical Engineering Progress, 48, 93 (89), 1952.

29. El-Wakil, "Nuclear Heat Transport", International Textbook Company, 1971.

30. Kingery, W.D., "Property Measurements at High Temperatures", John Wiley and Sons, Inc. New York, 1959.

31. R.H. Wiswall and E. Wirsing, "Removal of Tritium from Solid CTR Blanket Materials", BNL-19766, February 1975.

32. J.R. Powell, R.H. Wiswall and E. Wirsing, "Tritium Recovery from Fusion Blankets Using Solid Lithium Compounds", BNL-25063, October 1975.

52.,

33. W. Jost, "Diffusion in Solids, Liquids, Gases", Academic Press, New York, 1952.

34. Was, G.S., "A Material Evaluation of a Gas-Cooled Solid-Breeding Fusion Reactor Blanket", S.M. Thesis, M.I.T., September 1976.

35. Stark, W.A., Jr., "Diffusion Analysis for Systems of Spherical Particles," Nuclear Technology, 26, 35, May 1975.

36. Touloukian, Y.S., ed., "Thermophysical Properties of Matter, Volume 2, Thermal Conductivity, Non Metallic Solids", Plenum, New York, Washington, 1970.

37. "Reactor Handbook, Materials: General Properties," USAEC, McGraw-Hill, New York, 1955.

38. White, D.W. and Burke, J.E., eds., "The Metal Beryllium," American Society for Metals, Cleveland, 1955.

39. Williams, M., Santoro, R., Gabriel, T., "The Calculated Performance of Various Structural Materials in Fusion-Reactor Blankets", ORNL-TM-5036, December 1975.

40. McLvin, J.G., Hauck, D., Mile, F., "Component R & M", Sec. 3., "Reliability and Maintainability Manual Process Systems", Ed, J.McLvin, R. Maxwell, AECL-4607, January 19, 1974.

41. Stickney, R.E., "Hydrogen Isotopes in Fusion Reactors", in "The Chemistry of Fusion Technology, Proceedings", Plenum Press, New York, 1972.

42. Tyson, C.R., Jr., ed., "Reactor Handbook Materials", 1, Interscience Publishers Inc., New York, 1960.

43. Hamped, C.A., ed., "Rare Metals Handbook," Reinhold Publishing Corp., London, 1961.

44.* Yaggee, F.L., "Some Mechanical and Physical Properties of Vanadium and Vanadium Alloys", ANL, Vanadium-Alloy Development Group.

45. Wiffen, F.W., "Tensile Properties of Fast Reactor Neutron Irradiated BCC Metals and Alloys," Conf. 730813-4, ORNL.

46. Pollack, W., Buckman, R.W., Begley, R.T., Thomas, K.C. and Bishop, E.C., "Development of High Strength Vanadium Alloys", WCAP-3487-16, June 1967.

47. Conway, Flagella, "Creep-Rupture Data for the Refractory Metals to High Temperatures", Gordon and Breach Science Publishers, New York, 1971.

48. Davis, M.V., "Selected Properties of Materials with Application to CTR Design", ANL/CTR-72-01, December 1972.

49. Kulcinski, G.L, Emmal, G.A., "First Wall Surface Problems for a D-T Tokamak Reactor", J. of Nuclear Materials, 53, 31-38, 1974.

50. Steiner, D., "The Technological Requirements for Power by Fusion", Nuclear Science and Engineering, 58, 107-165, 1975.

51. Duchs, D., Haas, G., Pfusch, D. and Vernickel, "On the Impurity Problem in Quasi Steady-State Torodal Plasma Experiments and Fusion Reactors", J. of Nuclear Materials, 53, 102-106, 1974.

52.* Smolik, G. and Chen, C.W., "Radiation Embrittlement of Vanadium", Presented at the Vanadium-Working Group Meeting, AEC, Germantown, Md., March 27, 1968.

53.* Carlander, R. "The Effects of Irradiation on the Mechanical Properties of V-20 Ti and V-15 Ti - 7.5 Cr Alloys", Vanadium-Alloy Development Group Meeting, Germantown, Md., March 27, 1968.

54. Das, S.K. and Kaminsky, M., "Comparative Study of Blistering in Nb, V and V-20 Ti", Proc. of the Symposium of Technology of Controlled Thermonuclear Fusion Experiments and the Engineering Aspects of Fusion Reactors, Austin, Texas, 1974, Conf. 72111.

55. Vogelsang, W.F., Kulcinski, G.L., Lott, R.T., and Sung, T.Y., "Transmutation Radioactivity and Afterheat in a Deuterium-Tritium Tokamak Fusion Reactor", Nuclear Technology, 22, No. 3, 379, June 1974.

56. Carlander, R., Harkness, S.C. and Santhanam, A.T., "Effects of Fast-Neutron Irradiation on Tensile Properties and Swelling Behavior of Vanadium Alloys", in "Effects of Radiation on Substructure and Mechanical Properties of Metals and Alloys", ASTM STP 529, 399-414, 1974.

57. Michel, D.J. and Moteff, J., "Voids in Neutron Irradiated and Annealed Niobium and Niobium-1% Zirconium", Radiation Effects, 21, No. 4, 235-243, 1974.

58. Steiner, D., "The Nuclear Performance of Vanadium as a Structural Material in Fusion Reactor Blankets", Nuclear Fusion, 14, No. 1, 33-44, Jan. 1975.

59. Mather, J.C., "Effect of Hydrogen on the Creep Properties of Vanadium, Niobium and Molybdenum", M.S. Thesis, Iowa State University, IS-T-658, 1975.

60. Loomis, B.A., Taylor, A. and Gerber, "Void Swelling of Niobium and Niobium +1 w/o Zirconium Alloy", Proc. of the Fifth Symposium on Engineering Problems of Fusion Research," Princeton University, p. 46, Nov. 5-9, 1973.

61. Hogan, J.F., Limoncelli and Cleary, R.E., "Reaction Rate of Columbium-1 Zirconium Alloy with Oxygen at Low Pressure", in "Refractory Metals and Alloys", 2, Gordon and Breach, New York, 1967.

62. Santhanam, A.T., "Effect of Helium on High-Temperature Tensile Properties and Swelling of Vanadium and its Alloys", Proc. of the Fifth Symposium on Fusion Research, Princeton University, p. 54, November 5-9, 1973.

63. Michel, D.J., Serpan, C.Z.,Jr., Smith, H.H. and Preper, A.G., "Effect of Cyclotron-Implanted Helium on the Fatigue Behavior and Microstructure of 316 SS at 650°C", Naval Research Laboratory, Washington, D.C.

64. Kramer, D., "Helium Embrittlement", in "Fusion First Wall Materials, WASH-1206," 1972.

65. Wiffen and Bloom, E.E., "Effects of High Helium Content on Stainless Steel Swelling", ORNL-TM-4541, May 1974.

66. "Fatigue of Vanadium", Annual Report, COO-3459-7, RPI, 1975.

67. B.R.T. Frost, "Refractory Metals-Alloys and Properties", in "Fusion Reactor First Wall Materials, WASH-1206", p. 21, 1972.

68.* "Vanadium Cladding Alloy Development", Vanadium-Alloy Development Group Meeting, Germantown, Md., March 27, 1968.

69.* Carlander, R., "The Effects of Irradiation on the Mechanical Properties of V-20 Ti and V-15 Ti - 7.5 CR Alloys", Vanadium-Alloy Development Group Meeting, Germantown, Md., March 27, 1968.

70. Fraas, A.P., "Comparative Study of the More Promising Combinations of Blanket Materials, Power Conversion Systems, and Tritium Recovery and Containment Systems for Fusion Reactors", ORNL-TM-4899, November 1975.

71. Green,A.E.;Bourne, A.J., "Safety Assessment with Reference to Automatic Protective System for Nuclear Reactors", Report UKAEA AHSB(S) R.117

72. A.P. Fraas, "Estimating the Reliability of Systems", USAEC Report ORNL-TM-2200 Oak Ridge National Laboratory, May 1968

*Permission to reference these reports granted by R.W. Buckman, Advanced Energy Systems Laboratory, Westinghouse Corporation.